MIMO Channel Modelling and Simulation for Cellular and Mobile-to-Mobile Communication Systems

by

Xiang Cheng

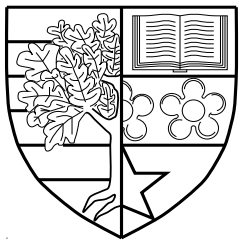

A thesis submitted in partial fulfilment for the degree of
Doctor of Philosophy

at

Heriot-Watt University
School of Engineering and Physical Science

October 2009

Abstract

Recently, mobile-to-mobile (M2M) communications have received much attention due to several emerging applications, such as wireless mobile ad hoc networks, relay-based cellular networks, and dedicated short range communications (DSRC) for intelligent transportation systems (e.g., IEEE 802.11p standard). Different from conventional fixed-to-mobile (F2M) cellular systems, in M2M systems both the transmitter (Tx) and receiver (Rx) are in motion and often equipped with low elevation antennas. Multiple-input-multiple-output (MIMO) technologies, employing multiple antennas at both the Tx and Rx, have widely been adopted for the third generation (3G) and beyond-3G (B3G) F2M cellular systems due to their potential benefits of improving coverage, link reliability, and overall system capacity. More recently, MIMO has been receiving more and more attention for M2M systems as well.

Reliable knowledge of the propagation channel obtained from channel measurements and corresponding channel models serve as the enabling foundation for the design and analysis of MIMO F2M and M2M systems. Furthermore, the development of accurate MIMO F2M and M2M channel simulation models plays a major role in the practical simulation and performance evaluation of these systems. These form the primary motivation behind our research on MIMO channel modelling and simulation for F2M cellular and M2M communication systems.

In this thesis, we first propose a new wideband theoretical multiple-ring based MIMO regular-shaped geometry-based stochastic model (RS-GBSM) for non-isotropic scattering F2M macro-cell scenarios and then derive a generic space-time-frequency (STF) correlation function (CF). The proposed theoretical reference wideband model can be reduced to a narrowband one-ring model, a new closed-form STF CF of which is derived as well. Narrowband and wideband sum-of-sinusoids (SoS) simulation models are then developed, demonstrating a good agreement with the corresponding reference models in terms of correlation functions.

Secondly, based on a well-known narrowband two-ring single-input single-output (SISO) M2M channel reference model, we propose new deterministic and stochastic SoS simulation models for non-isotropic scattering environments. The proposed deterministic simulator is the first SISO M2M deterministic simulator with good performance, while the proposed stochastic simulator outperforms the existing one in terms of fitting the desired statistical properties of the corresponding reference model.

Thirdly, a new adaptive narrowband MIMO M2M RS-GBSM is proposed for non-isotropic scattering environments. To the best of our knowledge, the proposed M2M model is the first RS-GBSM that has the ability to study the impact of the vehicular traffic density on channel statistics. From the proposed theoretical reference model, we comprehensively investigate some important M2M channel statistics including the STF CF, space-Doppler-frequency power spectral density, envelope level crossing rate, and average fade duration. A close agreement between some channel statistics obtained from the proposed reference model and measurement data is observed, confirming the utility of our model.

Finally, we extend the above narrowband model to a new wideband MIMO M2M RS-GBSM with respect to the frequency-selectivity. The proposed wideband reference model is validated by observing a good match between some statistical properties of the theoretical model and available measurement data. From the wideband reference model, we further design new wideband deterministic and stochastic SoS simulation models. The proposed wideband simulators can be easily reduced to narrowband ones. The utilities of the newly derived narrowband and wideband simulation models are validated by comparing their statistical properties with those of the corresponding reference models.

The proposed channel reference models and simulators are expected to be useful for the design, testing, and performance evaluation of future MIMO cellular and M2M communication systems.

Dedicated to my loving grandmother: Huizhen, my loving parents: Fanmin & Lisheng, and my lovely wife: Lily.

Acknowledgements

Three years ago, I made a tough decision to come to Edinburgh and pursue my PhD degree at the Advanced Wireless Technologies (AWiTec) Group, School of Engineering and Physical Sciences, Heriot-Watt University. Now looking back these three years, I am very glad that I have made a right decision at that moment, even though I have experienced some tough moments (especially at the early beginning of my PhD study) that have tested the limits of my determination. As this journey has almost reached its destination, I would like to explore this opportunity and express my deepest gratitude to a number of people without whom I could not have completed this dissertation.

First of all, I am truly indebted to my supervisor Dr. Cheng-Xiang Wang for his priceless help, excellent guidance, and ceaseless encouragement. He has been not only my academic adviser but also my life mentor. The generous help from him and his wife, Qi Yao, is an indispensable factor that supports me in passing through some tough moments during the last three years and will never be forgotten in my heart. His influence in shaping me and my career will be ever-lasting.

My sincere thanks must also go to my second supervisor, Dr. David I. Laurenson, from the University of Edinburgh, for his insightful guidance and proof reading. I am also grateful to Prof. Athanasios V. Vasilakos, Prof. Sana Salous, and Prof. Hsiao-Hwa Chen for the discussions and co-publishing original papers.

My friends and colleagues in AWiTec Group deserve my sincere thanks: Xumin Hong, Dayong Xu, Omar Saeed Salih, Zengmao Chen, Margaret Uzunma Anyaegbu, Raul Jose Hernandez Fernandez, and Chui Choon Ivan Ku. I really enjoy the time we spent together on discussions, conversations, chats, seminars, lunches, dinners, coffees, parties, and so on.

During the last three years in Edinburgh, I had the fortune to have some people around me that made this period fly by memorably. Just a few of the names are: Sanliang Lin, Yufei Liu, George Dobbie, Tom, and many more. All my long-time friends back in China deserve my warm thanks as well but unfortunately the list is too long to name all of them!

The financial support from the Scottish Funding Council for the Joint Research Institute in Signal and Image Processing between the University of Edinburgh and

Heriot-Watt University which is a part of the Edinburgh Research Partnership in Engineering and Mathematics (ERPem), is gratefully acknowledged.

Life is not just work and without a life besides work, work is impossible and meaningless. Research is not always fun and even if it is, there is nothing more valuable than having a family to share the life with, which doubles the fun and halves the misery. My endless gratefulness goes to my mother Fanmin, my father Lisheng, and my grandparents for reasons that are beyond what words can describe. I hope I have not disappointed you. Finally, I would like to thank my beloved wife, Lily, for her love, understanding, patience, and support. I really appreciate your unshakable trust and wait, which are the most important driving force that supports me in passing through the last three years.

Granny, hope you can see in heaven... I miss you so much...

Xiang Cheng
Edinburgh, September 2009.

Declaration of Authorship

I, Xiang Cheng, declare that this thesis titled, 'MIMO Channel Modelling and Simulation for Cellular and Mobile-to-Mobile Communication Systems' and the work presented in it are my own. I confirm that:

- This work was done wholly while in candidature for a research degree at Heriot-Watt University.
- Where I have consulted the published work of others, this is always clearly attributed.
- Where I have quoted from the work of others, the source is always given. With the exception of such quotations, this thesis is entirely my own work.
- I have acknowledged all main sources of help.
- Where the thesis is based on work done by myself jointly with others, I have made clear exactly what was done by others and what I have contributed myself.

Signed: _____

Date: _____

Contents

List of Figures

List of Tables

Abbreviations

2D	2-Dimensional
3D	3-Dimensional
3G	Third Generation
3GPP SCM	Third Generation Partnership Project Spatial Channel Model
AFD	Average Fade Duration
AoA	Angle of Arrival
AoD	Angle of Departure
ARA	Acceptance Rejection Algorithm
B3G	Beyond Third Generation
BS	Base Station
CDF	Cumulative Distribution Function
CF	Correlation Function
COST	European Cooperative in Science and Technology
DSRC	Dedicated Short Range Communications
DoA	Direction of Arrival
DoD	Direction of Departure
F2M	Fixed-to-Mobile
FCC	Federal Communications Commission
FCF	Frequency Correlation Function
GBDM	Geometry-Based Deterministic Model
GBSM	Geometry-Based Stochastic Model
IMMEA	Improved Modified Method of Equal Area
i.i.d.	Independent and Identically Distributed
IS-GBSM	Irregular-Shape Geometry-Based Stochastic Model

LCR	Level Crossing Rate
LoS	Line-of-Sight
M2M	Mobile-to-Mobile
MEA	Method of Equal Area
MEDS	Method of Exact Doppler Spread
MIMO	Multiple-Input Multiple-Output
MMEA	Modified Method of Equal Area
MS	Mobile Station
NGSM	Non-Geometrical Stochastic Model
NLoS	Non-Line-of-Sight
OFDM	Orthogonal Frequency Division Multiplexing
PDF	Probability Density Function
PDP	Power Delay Profile
PSD	Power Spectral Density
QoS	Quality of Service
RS-GBSM	Regular-Shape Geometry-Based Stochastic Model
Rx	Receiver
SD	Space-Doppler
SDF	Space-Doppler-Frequency
SISO	Single-Input Single-Output
SoS	Sum-of-Sinusoids
ST	Space-Time
STF	Space-Time-Frequency
TDL	Tapped Delay Line
Tx	Transmitter
US	Uncorrelated Scattering
VTD	Vehicular Traffic Density
WINNER	Wireless World Initiative New Radio
WSS	Wide Sense Stationary
WSSUS	Wide Sense Stationary Uncorrelated Scattering

Symbols

$(\cdot)^*$	complex conjugate operation
$\tilde{(\cdot)}$	corresponding parameters of deterministic simulation models
$\hat{(\cdot)}$	corresponding parameters of stochastic simulation models
$\langle\cdot\rangle$	time average operator
a	major axis of the ellipse model
a_l	major axis of the lth ellipse
$a_{l,n}(t)$	complex amplitudes
A_s	space separation between any two antenna elements
b	semi-minor axis of an ellipse
B_c	coherence bandwidth
c	speed of light
c_l	gain of the lth tap
$\vec{d}_R$	vector of the chosen element position measured from an arbitrary but fixed reference points on the Rx arrays
$\vec{d}_T$	vector of the chosen element position measured from an arbitrary but fixed reference points on the Tx arrays
D	Tx-Rx distance
D_c	coherence distance
$\mathbf{E}[\cdot]$	statistical expectation operator
$E_{\cdot}^{(p)}$	L_p-norm
f	frequency
f	half length of the distance between the two focal points of an ellipse
f_c	carrier frequency

f_D	maximum Doppler frequency
$f_{D,l,n}(t)$	Doppler frequency
$f_{R_{max}}$	maximum Doppler frequency due to the motion of the Rx
$f_{T_{max}}$	maximum Doppler frequency due to the motion of the Tx
$f(\cdot)$	von Mises probability density function
$F_{T/R}(\cdot)$	von Mises cumulative distribution functions
$F_{T/R}^{-1}(\cdot)$	inverse functions of $F_{T/R}(\cdot)$
$F_{R_l}(\cdot)$	von Mises cumulative distribution functions
$F_{R_l}^{-1}(\cdot)$	inverse functions of $F_{T/R}(\cdot)$
$g(f_D, \tau', \Omega)$	Doppler-direction-spread impulse response (spread function)
G_l	propagation delay subintervals
G_R	receive antenna gain
G_T	transmit antenna gain
$G'(t, f)$	time-variant transfer function
$G(t, f_c, x)$	time-space-variant transfer function
$h(t)$	complex fading envelope of Rayleigh fading channels
$h_i(t)$	in-phase component of $h(t)$
$h_q(t)$	quadrature component of $h(t)$
$h_l(t)$	time-variant complex fading envelope associated with the lth resolvable multipath component
$h^{DIF}(t)$	complex fading envelope of the diffuse component
$h^{LoS}(t)$	complex fading envelope of the LoS component
$h^{SB}(t)$	complex fading envelope of the single-bounced rays
$h^{DB}(t)$	complex fading envelope of the double-bounced rays
$h_{oq}(t)$	complex fading envelope between the oth BS and the qth MS
$h_{oq}^{LoS}(t)$	complex fading envelope of the LoS component
$h_{oq}^{SB}(t)$	complex fading envelope of the single-bounced rays
$h_{oq}^{DB}(t)$	complex fading envelope of the double-bounced rays
$h_{1,oq}(t)$	complex fading envelope of the first tap
$h_{1,oq}^{LoS}(t)$	complex fading envelope of the LoS component in the first tap
$h_{1,oq}^{SB_i}(t)$	complex fading envelope of the single-bounced rays in the first tap

$h_{1,oq}^{DB}(t)$	complex fading envelope of the double-bounced rays in the first tap
$h_{l',oq}(t)$	complex fading envelope of the l'th tap
$h_{l',oq}^{LoS}(t)$	complex fading envelope of the LoS component in the l'th tap
$h_{l',oq}^{SB_i}(t)$	complex fading envelope of the single-bounced rays in the l'th tap
$h_{l',oq}^{DB}(t)$	complex fading envelope of the double-bounced rays in the l'th tap
$h'(t,\tau')$	complex channel impulse response for non-directional channels
$h_{oq}(t,\tau')$	complex channel impulse response
	between the oth BS and the qth MS
$h_{l,oq}(t)$	complex time-variant tap coefficient of the lth tap
$h(t,\tau',\Omega)$	time-variant direction-spread impulse response
	(channel impulse response)
$h(t,\tau',\Omega_T,\Omega_R)$	double-directional time-variant complex impulse response
$H(f_D,f_c,\Omega)$	direction-Doppler-spread transfer function
$\mathbf{H}(t)$	MIMO channel matrix
$I_V(\cdot)$	V^{th}-order modified Bessel function of the first kind
j	$j=\sqrt{-1}$
k	parameter of von Mises distribution that controls
	the angle spread of the angle of arrival
$k_{l,i,r}$	parameter of truncated von Mises distribution
	that controls the angle spread of the angle of arrival
k_R	parameter of von Mises distribution
	of the angle of arrival ϕ_R that controls the angle spread
k_T	parameter of von Mises distribution that controls the angle spread
	of the angle of departure ϕ_T
k_R^{TR}	parameter of von Mises distribution that controls the angle spread
	of the angle of arrival $\phi_R^{SB_2}$
k_T^{TR}	parameter of von Mises distribution that controls the angle spread
	of the angle of departure $\phi_T^{SB_1}$
k_R^{EL}	parameter of von Mises distribution that controls the angle spread
	of the angle of arrival $\phi_R^{SB_3}$
$k_T^{(1,1)}$	parameter of von Mises distribution that controls the angle spread

	of the angle of departure $\phi_T^{(1,1)}$
$k_R^{(1,2)}$	parameter of von Mises distribution that controls the angle spread of the angle of arrival $\phi_R^{(1,2)}$
$k_R^{(l,3)}$	parameter of von Mises distribution that controls the angle spread of the angle of arrival $\phi_R^{(l,3)}$
$\vec{k}$	wave vector
K	Ricean factor
K_{oq}	Ricean factor
L	total number of resolvable path
L	total number of virtual confocal ellipses
$L_\xi(r_l)$	envelope level crossing rate
m	mth effective scatterers
$m_{i/q}$	$m_{i/q}$th effective scatterers
$m'_{i/q}$	$m'_{i/q}$th effective scatterers
$m(f_D, \tau', x)$	Doppler-spread space-variant impulse response
M	number of independent effective scatterers
$M_{i/q}$	number of effective scatterers located on the ring around the Tx
M_R	receiver antenna array
M_T	transmitter antenna array
$M(t, f_c, \Omega)$	time-variant direction-spread transfer function
n	nth effective scatterers
$n_{i/q}$	$n_{i/q}$th effective scatterers
$n'_{i/q}$	$n'_{i/q}$th effective scatterers
N	number of independent effective scatterers
N_1	number of effective scatterers around the Tx lying on a ring
N_2	number of effective scatterers around the Rx lying on a ring
N_3	number of effective scatterers lying on an ellipse
$N_{1,1}$	number of effective scatterers around the Tx lying on a ring
$N_{1,2}$	number of effective scatterers around the Rx lying on a ring
$N_{l,3}$	number of effective scatterers lying on the lth ellipse
$N_{i/q}$	number of effective scatterers located on the ring around the RX

N_{stat}	number of simulation trials
N_{ARA}	number of harmonic functions used in the ARA simulation model
$Q_{l,i,r}$	normalisation coefficient
P_R	received signal power
P_T	transmitted power
R	radius of a ring in the one-ring model
$R_{l,i}$	radius of the ith ring in the concentric multiple-ring
R_c	number of effective cluster for one ring in each tap
R_R	radius of a ring around the Rx in the two-ring model
R_T	radius of a ring around the Tx in the two-ring model
$s(t, \tau', x)$	time- and space-variant impulse response
S_n	nth effective scatterer
$s^{(n_1)}$	n_1th effective scatterer located on a ring around the Tx
$s^{(n_2)}$	n_2th effective scatterer located on a ring around the Rx
$s^{(n_3)}$	n_3th effective scatterer located on an ellipse
$s^{(n_{1,1})}$	$n_{1,1}$th effective scatterer located on a ring around the Tx
$s^{(n_{1,2})}$	$n_{1,2}$th effective scatterer located on a ring around the Rx
$s^{(n_{l,3})}$	$n_{l,3}$th effective scatterer located on the lth ellipse
$S_{l,i}$	effective cluster
$S_{l,i,n}$	nth effective scatterer in one effective cluster
$S_{h_{oq}h'_{o'q'}}(f_D, \chi)$	space-Doppler-frequency power spectral density of complex fading envelope
$S_{h_{oq}^{LoS}h'^{LoS}_{o'q'}}(f_D, \chi)$	space-Doppler-frequency power spectral density of LoS component
$S_{h_{oq}^{SB_i}h_{o'q'}^{SB_{i'}}}(f_D, \chi)$	space-Doppler-frequency power spectral density of single-bounced rays
$S_{h_{oq}^{DB}h'^{DB}_{o'q'}}(f_D, \chi)$	space-Doppler-frequency power spectral density of double-bounced rays
$S_{h_{l,oq}h_{l,o'q'}}(f_D)$	space-Doppler power spectral density of the first tap coefficient
$S_{h_{1,oq}^{LoS}h_{1,o'q'}^{LoS}}(f_D)$	space-Doppler power spectral density of the LoS component in the first tap

$S_{h_{1,oq}^{SB_i} h_{1,o'q'}^{SB_i}}(f_D)$	space-Doppler power spectral density of the single-bounced rays in the first tap
$S_{h_{1,oq}^{DB} h_{1,o'q'}^{DB}}(f_D)$	space-Doppler power spectral density of the double-bounced rays in the first tap
$S_{h_{l',oq} h_{l',o'q'}}(f_D)$	space-Doppler power spectral density of the l'th tap coefficient
$S_{h_{l',oq}^{SB_3} h_{l',o'q'}^{SB_3}}(f_D)$	space-Doppler power spectral density of the single-bounced rays in the l'th tap
$S_{h_{l',oq}^{DB_{1/2}} h_{l',o'q'}^{DB_{1/2}}}(f_D)$	space-Doppler power spectral density of the double-bounced rays in the l'th tap
$S_{H_{oq}H_{o'q'}}(\tau')$	power delay profile
t	time
T_c	coherence time
T_f	frame duration
T_s	symbol duration
T_s	sampling period
$T_{\xi-}(r_l)$	envelope average fade duration
$T(f_D, f_c, x)$	Doppler-spread space-variant transfer function
$v(t)$	relative velocity
x	location of an antenna element
$z_l(t)$	persistence process
λ	carrier wavelength
Λ_l	total number of concentric rings in the lth tap
Ω	direction of an antenna element
Ω_p	mean squared envelope level
Ω_l	average direction
$\Omega_{R,l}\,(t)$	direction of arrival
$\Omega_{T,l}\,(t)$	direction of departure
Ω_{oq}	total power of the $T_o{-}R_q$ link
τ	time separation
τ'	time delay
τ_l'	average time delay

τ'_n	propagation delay
$\tau'_{\max}$	maximum propagation delay
τ_{oq}	travel time of the wave through the link T_o–R_q
$\tau_{oq,n}$	travel time of the wave through the link $T_o - S_n - R_q$
τ_{oq,n_i}	travel time of the wave through the link T_o–$s^{(n_i)}$–R_q
τ_{oq,n_1,n_2}	travel time of the wave through the link T_o–$s^{(n_1)}$–$s^{(n_2)}$–R_q
$\tau_{oq,n_{1,i}}$	travel time of the wave through the link T_o–$s^{(n_{1,i})}$–R_q
$\tau_{oq,n_{1,1},n_{1,2}}$	travel time of the wave through the link T_o–$s^{(n_{1,1})}$–$s^{(n_{1,2})}$–R_q
$\tau_{oq,n_{l',3}}$	travel time of the wave through the link T_o–$s^{(n_{l',3})}$–R_q
$\tau_{oq,n_{1,1(2)},n_{l',3}}$	travel time of the wave through the link T_o–$s^{(n_{1,1})}(s^{(n_{l',3})})$–$s^{(n_{l',3})}(s^{(n_{1,2})})$–$R_q$
$\tau_{l,i.oq,n}$	travel time of the wave through the link T_o–$S_{l,i,n}$–R_q
$\tau'_l(t)$	excess delay
μ	mean angle of arrival of the scatterers located on a ring around the Rx
μ_R	mean angle of arrival of the scatterers located on a ring around the Rx
μ_T	mean angle of departure of the scatterers located on a ring around the Tx
μ_R^{TR}	mean angle of arrival of the scatterers located on a ring around the Rx
μ_T^{TR}	mean angle of departure of the scatterers located on a ring around the Tx
μ_R^{EL}	mean angle of arrival of the scatterers located on an ellipse
$\mu_R^{(1,2)}$	mean angle of arrival of the scatterers located on a ring around the Rx
$\mu_T^{(1,1)}$	mean angle of departure of the scatterers located on a ring around the Tx
$\mu_R^{(l,3)}$	mean angle of arrival of the scatterers located on the lth ellipse
$\mu_{l,i,r}$	mean angle of arrival of the effective cluster in each tap
μ_{Ω_p}	area mean

σ_Ω	direction spread
σ_{Ω_p}	standard deviation of the shadowing
σ_{f_D}	Doppler spread
$\sigma_{\tau'}$	delay spread
ϕ	azimuth angle
θ	elevation angle
$\theta_{T/R}$	random variable uniformly distributed on the interval $[-1/2, 1/2)$
$\theta_{R,l,n}(t)$	direction of arrival
$\theta_{T,l,n}(t)$	direction of departure
Θ	angle spread seen at the BS (Tx)
$\Theta_{l.i}$	angle spread seen at the BS (Tx)
δ_R	antenna element spacing at the MS (Rx)
δ_T	antenna element spacing at the BS (Tx)
Δ	$\Delta = R/D$
Δ_R	$\Delta_R = R_R/D$
Δ_T	$\Delta_T = R_T/D$
β_R	multi-element antenna array angles at the MS (Rx)
β_T	multi-element antenna array angles at the BS (Tx)
$\beta_{l,n}(t)$	aggregate phase angle of the nth subpath
ϕ_R	angle of arrival of the scatterers located on a ring around the Rx
ϕ_T	angle of departure of the scatterers located on a ring around the Rx
ϕ^{LoS}	angle of arrival of a LoS path
ϕ_n^R	angle of arrival of nth scatterer
$\phi_{T(R)}$	azimuth angle
$\phi_{l,i,r}^R$	angle of arrival of the effective cluster located on a multiple-ring model
ϕ_R^n	angle of arrival of the scatterers located on a ring around the Rx
ϕ_T^m	angle of departure of the scatterers located on a ring around the Tx
$\phi_R^{(n_i)}$	angle of arrival of the nth scatterer located on

	a ring around the Rx (or an ellipse)
$\phi_T^{(n_i)}$	angle of departure of the nth scatterer located on
	a ring around the Tx (or an ellipse)
$\phi_R^{(SB_i)}$	angle of arrival of the scatterers located on
	a ring around the Rx (or an ellipse)
$\phi_T^{(SB_i)}$	angle of departure of the scatterers located on
	a ring around the Tx (or an ellipse)
$\phi_T^{(1,1)}$	angle of departure of the scatterers located on
	a ring around the Tx
$\phi_R^{(1,2)}$	angle of arrival of the scatterers located on a ring around the Rx
$\phi_R^{(l,3)}$	angle of arrival of the scatterers located on the lth ellipse
$\tilde{\phi}_R^{n_{i/q}}$	discrete realisations of the random variable ϕ_R
$\tilde{\phi}_T^{m_{i/q}}$	discrete realisations of the random variable ϕ_T
ψ_n	phase of nth effective scatterer
$\psi_{l,i,n}$	phase of nth effective scatterer in one effective cluster
ψ_{nm}	random phase of the double-bounced rays
ψ_{n_i}	random phase of the single-bounced rays
ψ_{n_1,n_2}	random phase of the double-bounced rays
$\psi_{n_{1,i}}$	random phase of the single-bounced rays in the first tap
$\psi_{n_{1,1},n_{1,2}}$	random phase of the single-bounced rays in the first tap
$\psi_{n_{l',3}}$	random phase of the single-bounced rays in the l'th tap
$\psi_{n_{1,1(2)},n_{l',3}}$	random phase of the single-bounced rays in the l'th tap
$\tilde{\psi}_{n_{i/q}m_{i/q}}$	single outcome of the random phases ψ_{nm}
$\delta(\cdot)$	Dirac delta function
$\varphi_{T(R)}$	elevation angle
γ	angle of motion
γ_R	angle of motion of the Rx
γ_T	angle of motion of the Tx
$\Delta\mu_{l,i}$	angle spread of the effective cluster in each tap
$\Delta\tau_l'$	time difference between difference time delays
$\rho_{h^{DIF}}(\tau)$	time correlation function of the diffuse component

$\rho_{oq,o'q'}(\tau,\chi)$	space-time-frequency correlation function of complex channel impulse response
$\rho_{l,oq;l,o'q'}(\tau,\chi)$	space-time-frequency correlation function of complex channel fading envelope
$\rho_{hh}(\tau)$	autocorrelation function of the reference model $h(t)$
$\rho_{h_{oq}h'_{o'q'}}(\tau,\chi)$	space-time-frequency correlation function of complex channel fading envelope
$\tilde{\rho}_{h_{oq}h'_{o'q'}}(\tau,\chi)$	space-time-frequency correlation function of complex channel fading envelope
$\rho_{h_{oq}^{LoS}h'^{LoS}_{o'q'}}(\tau,\chi)$	space-time-frequency correlation function of the LoS component
$\rho_{h_{oq}^{SB_i}h'^{SB_i}_{o'q'}}(\tau,\chi)$	space-time-frequency correlation function of the single-bounced rays
$\rho_{h_{oq}^{DB}h'^{DB}_{o'q'}}(\tau,\chi)$	space-time-frequency correlation function of the double-bounced rays
$\rho_{h_{l,oq}h_{l,o'q'}}(\tau)$	space-time correlation function of the first tap coefficient
$\rho_{h_{1,oq}^{LoS}h_{1,o'q'}^{LoS}}(\tau)$	space-time correlation function of the LoS component in the first tap
$\rho_{h_{1,oq}^{SB_i}h_{1,o'q'}^{SB_i}}(\tau)$	space-time correlation function of the single-bounced rays in the first tap
$\rho_{h_{1,oq}^{DB}h_{1,o'q'}^{DB}}(\tau)$	space-time correlation function of the double-bounced rays in the first tap
$\rho_{h_{l',oq}h_{l',o'q'}}(\tau)$	space-time correlation function of the l'th tap coefficient
$\rho_{h_{l',oq}^{SB_3}h_{l',o'q'}^{SB_3}}(\tau)$	space-time correlation function of the single-bounced rays in the l'th tap
$\rho_{h_{l',oq}^{DB_{1/2}}h_{l',o'q'}^{DB_{1/2}}}(\tau)$	space-time correlation function of the double-bounced rays in the l'th tap
$\rho_{H_{oq}H_{o'q'}}(\Delta f')$	frequency correlation of complex channel impulse response
χ	frequency separation
υ_R	speed of movement of the RX
υ_T	speed of movement of the TX
η_{SB_i}	power of single-bounced rays
η_{DB}	power of double-bounced rays

$\eta_{SB_{1,i}}$	power of single-bounced rays in the first tap
η_{DB_1}	power of double-bounced rays in the first tap
$\eta_{SB_{l',3}}$	power of single-bounced rays in the l'th tap
$\eta_{DB_{l',1(2)}}$	power of double-bounced rays in the l'th tap
$\xi(t)$	signal envelope

Chapter 1

Introduction

1.1 Background and Motivation

Cellular technology has revolutionarily changed the manner that people communicate with each other. A typical cellular network connects different mobile users to one another through a fixed (stationary) based station (BS). In this sense, cellular radio links are mobile at one end (user end) only, while the service provider end is stationary [1, 2]. Therefore, cellular communication systems are normally referred to as fixed-to-mobile (F2M) cellular systems.

Recently, the increasing demand for better quality of service (QoS) and increased mobility support leads to some new applications, where mobile users can communicate directly with each other. The conventional F2M cellular system cannot support such new applications, thus driving the emergence of a new communication architecture: mobile-to-mobile (M2M) communication system, where both the transmitter (Tx) and receiver (Rx) are in motion and equipped with low elevation antennas. The potential applications of M2M systems include mobile ad-hoc wireless networks [3], intelligent transportation systems[4], and future cellular systems employing cooperative diversity technologies [5].

One of the most promising technologies in mobile radio communications is multiple-input multiple-output (MIMO), in which multiple antennas are deployed at both the Tx and Rx [6, 7]. Information theory has shown that the capacity of a wireless channel can be increased significantly if the spatial domain of multipath propagation is properly exploited by using MIMO technologies [8, 9]. Considering the demand for high-speed wireless services, MIMO technologies have widely been adopted for the third generation (3G) and beyond-3G (B3G) F2M cellular systems and have been receiving more and more attention for M2M systems as well.

Reliable knowledge of the propagation channel obtained from channel measurements and corresponding channel models serve as the enabling foundation for the design and analysis of any wireless communication system. Furthermore, the development of accurate channel simulation models plays a major role in the practical simulation and performance evaluation of a wireless communication system. This philosophy has been the driving force behind more than four decades of research into wireless channels and also forms the primary motivation behind our research on MIMO channel modelling and simulation for F2M cellular and M2M communication systems.

MIMO F2M (cellular) channel modelling and simulation have generated considerable interests among the researchers and thus have been extensively investigated [10, 11, 12, 13] in the past decade. These researches have led to standardized channel models for MIMO F2M cellular systems, such as European Cooperation in Science and Technolgy (COST) 259 [14, 15, 16], COST 273 [17], Third Generation Partnership Project (3GPP) Spatial Channel Model (SCM) [18, 19, 20], and Wireless World Initiative New Radio (WINNER) [21] channel models. Among numerous MIMO F2M channel models, the one-ring model [22, 23] has been widely used to model narrowband MIMO F2M channels in a macro-cell scenario due to its close agreement with the measured data [24] and its mathematical tractability. Due to the increasing demand for high-speed wireless services, future communication systems tend to be wideband. Therefore, it is desirable to extend the traditional narrowband one-ring model to wideband applications. The first part of this thesis is to propose a new wideband

MIMO F2M mathematical reference model and its corresponding simulation model for macro-cell scenarios.

Unlike a rich and fascinating history of the research in F2M channels, the investigation of M2M channel modelling and simulation is still in its infancy. Up till now, only few theoretical research have focused on the M2M channels as described in [25, 26, 27, 28, 29, 30], and even fewer measurement campaigns have been conducted to investigate these channels as provided in [31, 32, 33, 34, 35]. Moreover, standardized M2M channel models or methods to simulate them are yet to be developed. Therefore, the second part of this thesis, also the main part of this thesis, focuses on the investigation of M2M channel modelling and simulation for non-isotropic scattering environments. Taking a two-ring M2M theoretical model [36] as a mathematical reference model, we propose new deterministic and stochastic sum-of-sinusoids (SoS) simulation models for narrowband single-input single-output (SISO) M2M channels under a more realistic scenario of non-isotropic scattering. In order to further improve this traditional two-ring M2M theoretical model [36], some works have been done in the M2M channel modelling [28, 29, 30, 37] and simulation [27, 28, 30, 38, 39, 40]. However, it can be observed that there are still some flaws in the previously reported models. This motivated us to propose new M2M mathematical reference models for non-isotropic scattering narrowband and wideband MIMO Ricean fading channels and the corresponding simulation models.

1.2 Contributions of the thesis

The key contributions of the thesis are summarised as follows:

- Propose a new wideband multiple-ring based MIMO channel mathematical reference model for macro-cell scenarios. From the proposed model, we derive the generic space-time-frequency (STF) correlation function (CF), which can be reduced to a compact closed-form expression for narrowband MIMO channels by removing the frequency-selectivity. Based on the proposed mathematical

reference model, a deterministic SoS simulation model is then developed. Similarly, a corresponding narrowband simulation model can be obtained from the developed wideband simulator by removing the frequency-selectivity.

- Review the state-of-the-art in M2M channel measurements and modelling. Some important M2M channel measurement campaigns and models are briefly described and classified.

- Propose novel deterministic and stochastic SoS simulation models for non-isotropic scattering SISO M2M Rayleigh fading channels by taking a narrowband two-ring M2M regular-shaped geometry-based stochastic model (RS-GBSM) as a mathematical reference model. The proposed simulation models extensively consider the distributions of the angle of arrival (AoA) and angle of departure (AoD), and thus provide a good approximation to the desired statistical properties of the mathematical reference model.

- Propose a generic and adaptive RS-GBSM for non-isotropic scattering narrowband MIMO M2M Ricean fading channels. The proposed model is sufficiently generic and adaptable to a variety of M2M scenarios (macro-, micro-, and pico-cells). More importantly, our model is the first RS-GBSM that has the ability to study the impact of the vehicular traffic density (VTD) on channel statistics. From this model, the STF CF and the corresponding space-Doppler-frequency (SDF) power spectral density (PSD) are derived.

- Derive the envelope level crossing rate (LCR) and average fade duration (AFD) for non-isotropic scattering M2M Ricean fading channels. From the derived LCR and AFD, we investigate for the first time the impact of the VTD on the LCR and AFD.

- Propose a novel RS-GBSM for non-isotropic scattering wideband MIMO M2M Ricean fading channels according to the tapped delay line (TDL) structure. The proposed wideband model can easily match any specified power delay profile (PDP) and is the first RS-GBSM that has the ability to study the impact of the VTD on channel statistics for different time delays, i.e., for every tap in our

model. From the proposed mathematical reference model, the space-time (ST) CF, space-Doppler (SD) PSD, frequency CF, and PDP are derived.

- Propose new deterministic and stochastic SoS simulation models for MIMO M2M Ricean fading channels under the condition of non-isotropic scattering by taking the proposed narrowband and wideband RS-GBSM as mathematical reference models. The developed wideband simulation models can be easily reduced to narrowband simulation models by removing the frequency-selectivity.

1.3 Organisation of the thesis

The remainder of this thesis is organised as follows:

Chapter 2 covers the background related to the propagation channel modelling and reviews existing important methods for channel modelling and simulation of MIMO F2M channels and M2M channels.

Chapter 3 presents a new wideband multiple-ring based MIMO channel mathematical reference model for macro-cell scenarios, which is an extension of the traditional narrowband on-ring model. Closed-form expressions of the STF CFs are derived for both non-isotropic scattering narrowband and wideband MIMO channels. Moreover, a wideband deterministic SoS simulation model is derived, which can be reduced to a narrowband simulator by removing the frequency-selectivity.

Chapter 4 proposes novel deterministic and stochastic SoS simulation models using a non-isotropic scattering narrowband two-ring SISO M2M Rayleigh fading channel model as a mathematical reference model. Closed-form expressions of the time CF for both the proposed deterministic and stochastic simulation models are derived.

Chapter 5 proposes a generic and adaptive RS-GBSM for non-isotropic scattering narrowband MIMO M2M Ricean fading channels. From the proposed model, we further investigate the important channel statistics, including the STF CF, SDF PSD, envelope LCR, and AFD.

Chapter 6 describes a novel wideband MIMO M2M RS-GBSM for non-isotropic scattering Ricean fading channels, which is an extension of our narrowband MIMO M2M model in Chapter 5 to wideband applications. From the proposed wideband model, some important channel statistics are derived, such as ST CF, SD PSD, frequency CF, and PDP. In addition, corresponding wideband simulation models are developed, which can be easily reduced to narrowband simulators by removing the frequency-selectivity.

Chapter 7 concludes the thesis by summarising our key findings and addressing open directions of research in wireless channel modelling and simulation.

1.4 Original publications

The work presented in this thesis includes the following original publications:

Refereed Journal Papers

1. **X. Cheng**, C.-X. Wang, D. I. Laurenson, and A. V. Vasilakos, "An investigation on envelope level crossing rate and average fade duration of non-isotropic mobile-to-mobile Ricean fading channels," *IEEE Transactions on Vehicular Technology*, to be submitted.

2. **X. Cheng**, C.-X. Wang, and D. I. Laurenson, "Modeling and simulation of wideband MIMO mobile-to-mobile channels," *IEEE Transactions on Vehicular Technology*, submitted for publication.

3. **X. Cheng**, C.-X. Wang, D. I. Laurenson, S. Salous, and A. V. Vasilakos, "New deterministic and stochastic simulation models for non-isotropic scattering mobile-to-mobile Rayleigh fading channels," *Wireless Communications and Mobile Computing, John Wiley and Sons*, accepted for publication.

4. C.-X. Wang, **X. Cheng**, and D. I. Laurenson, "Vehicle-to-vehicle channel modeling and measurements: recent advances and future challenges", *IEEE Communication Magazine*, vol. 47, no. 11, Nov. 2009.

5. **X. Cheng**, C.-X. Wang, D. I. Laurenson, S. Salous, and A. V. Vasilakos, "An adaptive geometry-based stochastic model for non-isotropic MIMO mobile-to-mobile channels," *IEEE Transaction on Wireless Communications*, vol. 8, no. 9, pp. 4824–4835, Sept. 2009.

Refereed Conference Papers

1. D. I. Laurenson, M. Matthaiou, **X. Cheng**, and C.-X. Wang, "Modelling for Vehicle to Vehicle Applications," *Proc. IEEE Loughborough Antennas and Propagation Conference (LAPC'09)*, Loughborough, UK, 16 - 17 Nov. 2009, accepted for publication (**invited paper**).

2. **X. Cheng**, C.-X. Wang, and D. I. Laurenson, "A Geometry-based stochastic model for wideband MIMO mobile-to-mobile channels", *Proc. IEEE Globe Communications Conference (GLOBECOM'09)*, Hawaii, USA, 30 Nov.–4 Dec. 2009, accepted for publication.

3. **X. Cheng**, C.-X. Wang, and D. I. Laurenson, "New deterministic and stochastic simulation models for non-isotropic scattering MIMO channels", *Proc. ACM International Wireless Communications and Mobile Computing Conference (IWCMC'09)*, Leipzig, Germany, 21–24 June 2009, pp. 1365–1369.

4. **X. Cheng**, C.-X. Wang, D. I. Laurenson, S. Salous, and A. V. Vasilakos, "New simulation models for non-isotropic scattering mobile-to-mobile Rayleigh fading channels", *Proc. The First International Workshop on Vehicular Communication Technologies (VehiCom'09), co-located with IWCMC'09*, Leipzig, Germany, 21–24 June 2009, pp. 1289–1294.

5. **X. Cheng**, C.-X. Wang, and D. I. Laurenson, "Multiple-ring based modeling and simulation of wideband space-time-frequency MIMO channels", *Proc. IEEE*

International Conference on Communications (ICC'09), Dresden, Germany, 14–18 June 2009.

6. **X. Cheng**, C.-X. Wang, D. I. Laurenson, and A. V. Vasilakos, "Second order statistics of non-isotropic mobile-to-mobile Ricean fading channels", *Proc. IEEE International Conference on Communications (ICC'09)*, Dresden, Germany, 14–18 June 2009.

7. **X. Cheng**, C.-X. Wang, D. I. Laurenson, H. H. Chen, and A. V. Vasilakos, "A generic geometrical-based MIMO mobile-to-mobile channel model", *Proc. IEEE International Wireless Communications and Mobile Computing Conference (IWCMC'08)*, Chania Crete Island, Greece, 6–8 August 2008, pp. 1000–1005.

8. **X. Cheng**, C.-X. Wang, D. I. Laurenson, H. H. Chen, and A. V. Vasilakos, "Space-time-frequency characterization of non-isotropic MIMO mobile-to-mobile multicarrier Ricean fading channels", *Proc. IEEE International Wireless Communications and Mobile Computing Conference (IWCMC'08)*, Chania Crete Island, Greece, 6–8 August 2008, pp. 994–999.

9. **X. Cheng**, C.-X. Wang, and D. I. Laurenson, "A generic space-time-frequency correlation model and its corresponding simulation model for narrowband MIMO channels," *Proc. European Conference on Antennas and Propagation (EuCAP'07)*, Edinburgh, UK, 11–16 November 2007, pp. 1–6.

Chapter 2

Wireless Propagation Channel Modelling and Simulation

Successful design of wireless communication systems requires a detailed understanding of the multipath propagation environment. This underlines the importance of developing physically meaningful yet easy-to-use methods to model and simulate the wireless channels. Moreover, in order to design highly reliable and high-speed wireless communication systems with limited bandwidth, MIMO technologies that efficiently exploit the spatial domain of propagation channels have become the most promising candidates. This chapter provides a brief overview of some important concepts of propagation modelling (e.g., path loss, shadowing, multipath fading) and describes existing important methods for the modelling and simulation of MIMO F2M channels and M2M channels.

2.1 Propagation Channel Modelling

Fading refers to the time variation of the received signal power induced by changes in the transmission medium or path. Generally speaking, fading can be categorised as large-scale fading and small-scale fading. Path loss and shadowing belong to large-scale fading since they are dominant when the mobile station moves over distances of

several tens of wavelengths. Large-scale fading is very important for the system design at the network level. For example, the cell coverage area, outage, and handoffs are influenced by these effects. On the other hand, small-scale fading appears due to the multipath propagation. Small-scale fading plays an important role in determining the link level performance according to bit error rates, average fade durations, etc. It must be noted that throughout this thesis, we constrain our interests in the investigation of small-scale fading for different types of channels, e.g., F2M channels and M2M channels.

2.1.1 Path Loss and Shadowing

Path loss is the attenuation in the transmitted signal while propagating from the Tx and Rx. This attenuation is caused by the effects such as free-space loss, refraction, diffraction, and reflection. Significant variations in the path loss are observed over distance of several hundred or thousand wavelengths.

The simplest path loss model corresponds to a propagation in free space, i.e., line-of-sight (LoS) link between the Tx and Rx. In this case, the received signal power can be expressed as [41]

$$P_R = P_T G_T G_R \frac{\lambda^2}{4\pi D^2} \tag{2.1}$$

where P_T is the transmitted power, G_T and G_R are the transmit and receive antenna gains, respectively, λ is the carrier wavelength, and D is the distance between the Tx and Rx. Note that the path loss exponents (i.e., the power of the distance dependence D) are 2 for free-space propagation. Therefore, the received power decreases with a factor of distance-squared under free-space propagation. (2.1) also shows the path loss dependency on the carrier wavelength λ. Shorter the wavelength, higher the path loss.

However, in a real environment, the wireless signals seldom experience the free-space propagation. Therefore, several different models such as the Okumura-Hata [42, 43], Lee [44], Walfish-Ikegami [45], etc., have been proposed to model path loss in different

propagation environments such as urban, rural, and indoor areas. Experiments show that the actual path loss exponents are around 3 – 8, suggesting higher attenuation than free-space propagation conditions. A detailed description of different path loss models can be found in [41].

The aforementioned path loss models assume that the path loss is constant at a given distance. However, the presence of obstacles, e.g., buildings and trees, leads to random variations of the received power at a given distance. This effects is termed shadowing (shadow fading).

Experiments illustrate that shadowing can be modeled as a log-normal random variable. Thus, the shadowing distribution is given by [41]

$$f_{\Omega_p}(x) = \frac{10}{x\sigma_{\Omega_p}\sqrt{2\pi}\ln 10} \exp\left[-\frac{\left(10\log_{10} x - \mu_{\Omega_p(dBm)}\right)^2}{2\sigma^2_{\Omega_p}}\right] \tag{2.2}$$

where Ω_p denotes the mean squared envelope level, μ_{Ω_p} designates the area mean expressed in dBm, and σ_{Ω_p} is the standard deviation of the shadowing. Typical values of σ_{Ω_p} range from 5 to 10 dB. Detailed discussions of shadowing can be found in [41].

2.1.2 Multipath Fading

Multipath propagation is the propagation mechanism manifested when the transmitted signal reaches the Rx by two or more paths. The presence of local scatterers, e.g., mountains and buildings, often obstructs a direct wave path between the Tx and Rx (i.e., the LoS). Therefore, a non-LoS (NLoS) propagation path will appear between the Tx and Rx. Consequently, the waves must propagate through reflection, diffraction, and scattering. This results in the received waves from various directions with different delays. The multiple waves combine vectorially at the receiver antenna (a phenomenon called multipath fading) to produce a composite received signal.

As mentioned above, the presence of local scatterers gives rise to NLoS scenarios, where Rayleigh distribution is the most popular distribution used to describe the

fading envelope. Some types of scattering environments have a specular component, i.e., LoS or a strong reflected path. These scattering environments are called LoS scenarios, where Ricean distribution is used to describe the fading envelope.

A non-directional channel can be characterised by one of the four system functions also termed as the first set of Bello's functions [46]. Whereas for a directional channel, eight system functions [47], which are extended from the traditional four system functions by incorporating another two terms (direction and space), can be used. Considering that the system functions of directional channels include those of non-directional channels as special cases and directional channel description (strictly speaking, double-directional channel description) is very useful for MIMO systems, here we give a brief overview of directional channels and invite interested readers to refer to [47, 48]. The eight system functions of directional channels are the

- Time-variant direction-spread impulse response (channel impulse response) $h(t, \tau', \Omega)$
- Time- and space-variant impulse response $s(t, \tau', x)$
- Direction-Doppler-spread transfer function $H(f_D, f_c, \Omega)$
- Doppler-spread space-variant transfer function $T(f_D, f_c, x)$
- Doppler-direction-spread impulse response (spread function) $g(f_D, \tau', \Omega)$
- Doppler-spread space-variant impulse response $m(f_D, \tau', x)$
- Time-variant direction-spread transfer function $M(t, f_c, \Omega)$
- Time-space-variant transfer function $G(t, f_c, x)$

where t denotes the time, τ' designates the time delay, f_c and f_D are the carrier frequency and Doppler shift, respectively, x denotes the location of an antenna element in the antenna array in the Tx/Rx, and Ω is the direction of a antenna element in the antenna array in the Tx/Rx including both azimuth angle ϕ and elevation angle θ. The Fourier relationship between the system functions is shown in FIGURE 2.1. These system functions lay emphasis upon different aspects of the channels. For example, the

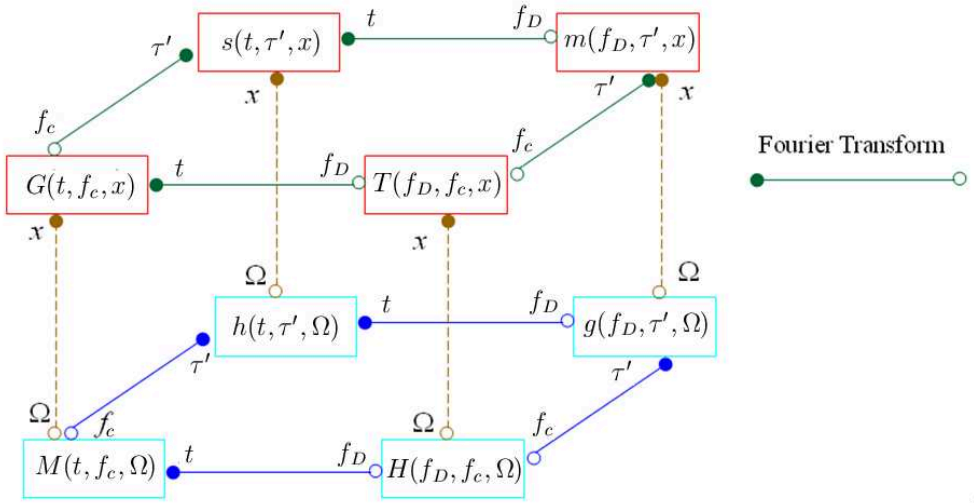

FIGURE 2.1: Fourier relationship between the system functions of directional channels.

channel impulse response $h(t,\tau',\Omega)$ focuses on the description of channels in the time-direction domain, while the time-space-variant transfer function $G(t,f_c,x)$ describes the channels in the frequency-space domain. However, since the channel impulse response $h(t,\tau',\Omega)$ can directly relate the multipath components, it is the most often-used system function and thus will be used throughout this thesis. The channel impulse response $h(t,\tau',\Omega)$ is given by

$$h(t,\tau',\Omega) = \sum_{l=1}^{L} h_l(t)\delta(\tau'-\tau_l')\delta(\Omega-\Omega_l) \tag{2.3}$$

where L is the total number of resolvable multipath components, $h_l(t)$ is the time-variant complex fading envelope associated with the lth resolvable multipath component arriving with an average time delay τ_l' and an average direction Ω_l. Each time-variant complex fading envelope $h_l(t)$ is either Rayleigh or Ricean faded.

Selectivity and dispersion are basic and important properties in radio channels. Moreover, they have the so-called dual relationship, which means that they allow one to investigate the channels from different domains [49]. Time-selectivity refers to the property that the channel changes over time due to the motion of the Tx, the Rx,

and/or the scatterers. When viewed in the frequency domain, time-selectivity appears as Doppler shifts in the transmitted signal, resulting in a broadening of the transmitted signal spectrum. This effect is termed frequency-dispersion. Therefore, time-selectivity and frequency-dispersion are one type of selectivity-dispersion duality. Normally, coherence time T_c and its approximate reciprocal, Doppler spread σ_{f_D}, are used to measure the time-selectivity and frequency-dispersion, respectively. When the Doppler spread σ_{f_D} is sufficiently large to result in the coherence time T_c being smaller than the transmitted symbol duration T_s, the channel changes within the transmitted symbol duration T_s. This kind of channel is named fast fading channel. Otherwise, if the Doppler spread σ_{f_D} is sufficiently small to lead to the coherence time T_c being larger than the transmitted frame duration T_f, the channel is approximately constant within the transmitted frame duration T_f. In this case, the channel is termed slow fading channel.

Frequency-selectivity refers to the property that the channel changes over frequency. Multipath components that arrive with different time delays results in this frequency-selectivity. From the time domain, multipath components with different time delays lead to the spread of the transmitted signal. This effect is called time-dispersion. Therefore, frequency-selectivity and time-dispersion are another type of selectivity-dispersion duality. To measure the frequency-selectivity and time-dispersion, we use the coherence bandwidth B_c and its reciprocal, delay spread $\sigma_{\tau'}$, respectively. When the delay spread $\sigma_{\tau'}$ is larger than the symbol duration T_s, which corresponds to the coherence bandwidth B_c being smaller than the signal bandwidth B_s, the transmitted frequencies experience different amplitude and phase changes, the channel is termed frequency-selective (or wideband) channel. On the other hand, if the delay spread $\sigma_{\tau'}$ is smaller than the symbol duration T_s, i.e., the coherence bandwidth B_c is larger than the signal bandwidth B_s, the transmitted frequencies undergo approximately identical amplitude and phase changes, the channel is called frequency flat (narrowband) channel.

Space-selectivity refers to the fluctuations of the channel that result because the waves interfere successively in a destructive and constructive fashion as location changes.

When viewed in the direction domain, these space-variant fluctuations are caused by multipath components with different directions over the location. This effect is termed direction-dispersion. Therefore, space-selectivity and direction-dispersion are another type of selectivity-dispersion duality. Similar to the above mentioned two dualities, the space-selectivity and direction-dispersion are measured by the coherence distance D_c and its reciprocal, direction spread σ_Ω, respectively. When the direction spread σ_Ω is sufficiently large to result in the coherence distance D_c being smaller than the space separation between any two antenna elements A_s, the antennas are uncorrelated. This kind of channel is named space-uncorrelated channel. Otherwise, if the direction spread σ_Ω is sufficiently small to lead to the coherence space D_c being larger than the space separation between any two antenna elements A_s, the antennas are correlated. In this case, the channel is termed space-correlated channel.

In context with mobile radio channels usually wide sense stationary uncorrelated scattering (WSSUS) is assumed. WSSUS has originally been defined for non-directional (SISO) channels, where it means that wide sense stationary (WSS) property with respect to both time t and frequency f when regarding the properties of time-variant transfer function $G'(t, f)$ [2, 46]. When regarding the complex channel impulse response for non-directional channels $h'(t, \tau')$, the WSSUS assumption represents WSS with respect to time t and uncorrelated scattering (US) with respect to the time delay τ'. This leads to the designation "WSSUS" since this describes the properties of a WSSUS channel completely in the time domain. From the duality between the time-Doppler relation, the frequency-delay relation, and the distance-direction relation described before, the aforementioned WSSUS concept for non-directional channels can be extended straightforwardly for directional channels [47, 48]. In this case, a directional WSSUS channel shows US with respect to not only the time delay τ' and Doppler shift f_D but also the direction Ω. Since US with respect to the time delay τ' is equivalent to WSS property with respect to the carrier frequency f_c, US with respect to the direction Ω will result in WSS property with respect to the distance x. WSSUS, in a strict sense, is never fulfilled since it requires the channel statistics to stay constant for infinite time. However, the WSSUS assumption is fulfilled for many

channels over short periods of time or distance (e.g., in the order of tens of wavelengths) [41]. Therefore, to significantly simplify the modelling complexity, WSSUS assumption is widely used to model many radio channels [1, 2, 41].

2.2 MIMO Cellular Channel Modelling

Throughout this thesis, our investigations on MIMO F2M cellular channels focus on macro-cell scenarios, while the MIMO F2M channels for other scenarios, e.g., micro-cell or pico-cell, are out of the scope of this thesis. A MIMO F2M cellular channel for macro-cell scenarios is a channel between a BS with multiple antennas, which is stationary, elevated, and relatively free of local scattering, and a mobile station (MS) with multiple antennas that is mobile, low elevated, and surrounded by local scatterers, as illustrated in FIGURE 2.2. In the past roughly ten years, several modelling and simulation approaches for MIMO F2M cellular channels have been proposed.

Within the past decade, MIMO F2M cellular channel modelling has been received extremely high attention and thus many different types of MIMO F2M channel models have been proposed. These different types of MIMO channel models can be classified in many different manners, such as wideband models vs. narrowband models, time-variant models vs. time-invariant models, 2-dimensional (2D) propagation environment models vs. 3-dimensional (3D) propagation environment models, stationary models vs. non-stationary models, etc. Recently, another very popular manner to classify the MIMO F2M channel models was described in [11], where the models are categorised as physical models vs. analytical models based on the modelling approach taken. Physical models are independent of antenna configurations (antenna pattern, number of antenna elements, array geometry, polarisation) and system bandwidth, while analytical models characterise the channel impulse response between individual transmit and receive antennas in a mathematical way without explicitly accounting for wave propagation. In general, physical models are suitable for an accurate reproduction of radio propagation, while analytical models are preferable for synthesising

MIMO matrix in the context of system and algorithm (e.g., space-time codes) design and verification [11].

Physical MIMO F2M channel models can further be classified as deterministic models, geometry-based stochastic models (GBSMs), and non-geometric stochastic models [11]. In deterministic models, the environment (positions of Tx, Rx and scatterers) is prescribed in a completely fixed (deterministic) manner. In a GBSM, the location of the scatterers is chosen stochastically assuming a certain probability density function (PDF) and the model is derived from the position of the scatterers by applying the fundamental laws of reflection, diffraction and scattering. The non-geometric stochastic models describe paths from Tx to Rx by statistical parameters only, without reference to the geometry of the physical environment. In the following of this section, we only give a brief introduction of the widely used one-ring MIMO F2M GBSM and invite interested readers to refer to [11, 50, 51, 52].

A one-ring narrowband MIMO F2M GBSM was first proposed in [23] and further developed in [22]. The one-ring model has been widely used for narrowband MIMO F2M channels under the condition of the scenario as presented in FIGURE 2.2 (i.e., macro-cell scenario) due to its close agreement with the measured data [24] and mathematical tractability. Let us consider a one-ring narrowband MIMO channel model shown in FIGURE 2.3, where the effective scatterers are located on a ring surrounding the MS with radius R. Here the effective scatterers, which is the terminology first proposed in Lee's model [53], are used to represent the effect of many scatterers with similar spatial location. The BS and MS have M_T and M_R omni-directional antenna elements in the horizontal plane, respectively. Without loss of generality, we consider uniform linear antenna arrays with $M_T = M_R = 2$ (a 2×2 MIMO channel). The antenna element spacing at the BS and MS are designated by δ_T and δ_R, respectively. It is usually assumed that the radius R is much smaller than D, denoting the distance between the BS and MS. Furthermore, it is assumed that both R and D are much larger than the antenna element spacing δ_T and δ_R, i.e., $D \gg R \gg \max\{\delta_T, \delta_R\}$. The multi-element antenna array angles are denoted by β_T and β_R. The MS moves with a

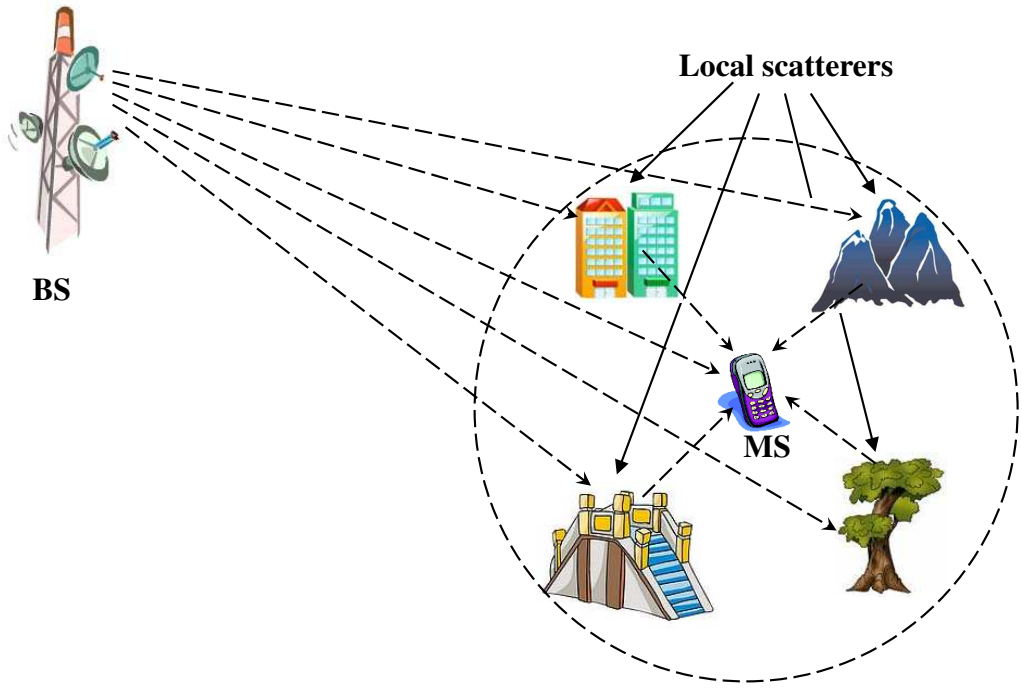

FIGURE 2.2: A typical F2M cellular propagation environment for macro-cell scenarios.

speed in the direction determined by the angle of motion γ. The angle spread seen at the BS is denoted by Θ, which is related to R and D by $\Theta \approx \arctan(R/D) \approx R/D$.

The MIMO fading channel can be described by a matrix $\mathbf{H}(t) = [h_{oq}(t)]_{M_R \times M_T}$ of size $M_R \times M_T$. Without a LoS component, the sub-channel complex fading envelope between the oth ($o = 1, ..., M_T$) BS and the qth ($q = 1, ..., M_R$) MS at the carrier frequency f_c can be expressed as

$$h_{oq}(t) = \lim_{N\to\infty} \frac{1}{\sqrt{N}} \sum_{n=1}^{N} \exp\left\{ j \left[\psi_n - 2\pi f_c \tau_{oq,n} + 2\pi f_D t \cos\left(\phi_n^R - \gamma\right) \right] \right\} \tag{2.4}$$

with $\tau_{oq,n} = (\varepsilon_{on} + \varepsilon_{nq})/c$, where $\tau_{oq,n}$ is the travel time of the wave through the link $T_o - S_n - R_q$ scattered by the nth scatterer S_n and c is the speed of light. The AoA of the wave travelling from the nth scatterer towards the MS is denoted by ϕ_n^R, while

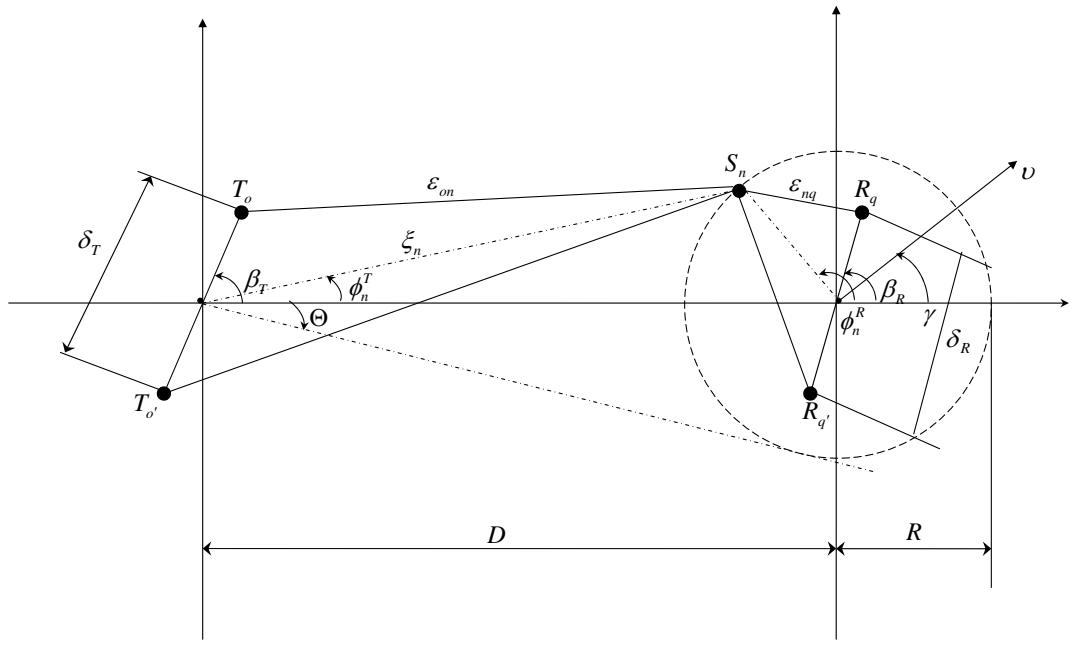

FIGURE 2.3: Geometrical configuration of a narrowband one-ring channel model with local scatters around the mobile user.

ε_{on} and ε_{nq} can be expressed as the function of ϕ_n^R as

$$\varepsilon_{on} \approx \xi_n - \delta_T[\cos(\beta_T) + \Theta \sin(\beta_T)\sin(\phi_n^R)]/2 \tag{2.5a}$$

$$\varepsilon_{no} \approx R - \delta_R \cos(\phi_n^R - \beta_R)/2 \tag{2.5b}$$

where $\xi_n \approx D + R\cos(\phi_n^R)$. The phases ψ_n are independent and identically distributed (i.i.d.) random variables with uniform distributions over $[0, 2\pi)$, f_D is the maximum Doppler frequency, and N is the number of independent effective scatterers S_n around the MS.

The above described one-ring model is a narrowband MIMO F2M cellular channel model. To reach the high demand for high-speed communications, wideband MIMO cellular systems have been suggested in many communication standards, leading to the increasing requirement for wideband MIMO F2M channel models. However, the one-ring model that assumes effective scatterers located on a one-ring is overly simplistic

and thus unrealistic for modeling wideband channels [54]. How to properly extend the narrowband one-ring model to wideband applications is still an open problem.

2.3 Mobile-to-Mobile Channel Measurements and Modelling

In contrast to conventional F2M cellular channels, in M2M channels, both the Tx and Rx are in motion and equipped with low elevation antennas, as shown in FIGURE 2.4. Therefore, M2M channels have characteristics that are widely different from F2M cellular channels. The first detailed description of M2M channels can be obtained from [25] and [26], where the authors presented that the received signal envelope of M2M channels is Rayleigh fading under NLoS conditions, but the statistical properties differ from F2M channels.

2.3.1 Recent Advances in Mobile-to-Mobile Channel Measurements

Knowledge of the M2M propagation channel for different scenarios is of great importance for the design and analysis of M2M systems. However, due to the large difference between the F2M and M2M channels, the channel knowledge obtained from conventional F2M cellular systems cannot be directly used for M2M systems. So far, some measurement campaigns have been conducted and others are ongoing to investigate the M2M propagation channels for different application scenarios. Here, we will briefly review and classify some recent typical measurement campaigns according to carrier frequencies, frequency-selectivity, antennas, environments, Tx/Rx direction of motion, and channel statistics, as shown in Table 2.1.

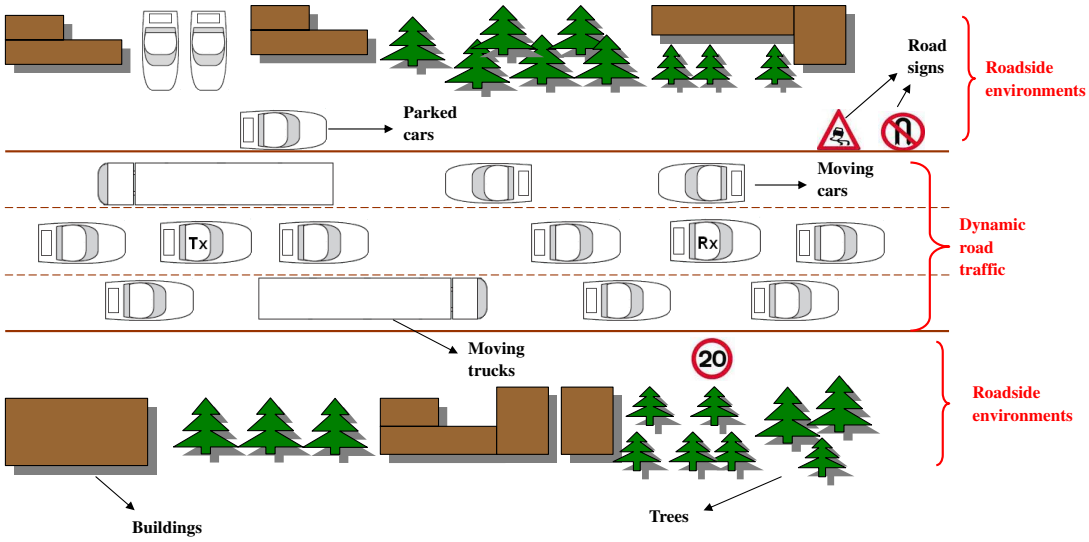

FIGURE 2.4: A typical M2M environment and the corresponding geometrical description of the geometry-based deterministic model.

- **Carrier Frequencies**

The IEEE 802.11p standard is proposed as part of the intelligent transportation system for dedicated short range communications (DSRC) in the USA [5]. The IEEE 802.11p radio technology is directly derived from IEEE 802.11a with some modifications to adapt to vehicular environments. It occupies 75 MHz of the licensed spectrum, from 5.85 to 5.925 GHz. Before the IEEE 802.11p standard was proposed, some measurement campaigns were conducted at carrier frequencies outside the 5.9 GHz DSRC band. In [33, 55], M2M measurements were carried out at 2.4 GHz, i.e., the IEEE 802.11b/g band. Some measurements were done around the IEEE 802.11a frequency band, e.g., at 5 GHz in [32] and at 5.2 GHz in [34]. Measurements at 5.9 GHz were presented in [31, 35] for narrowband and wideband M2M channels, respectively. Based on the aforementioned measurement campaigns, we can observe that propagation phenomenon in similar environment with different frequencies can vary significantly. Therefore, more measurement campaigns are expected to be conducted at 5.9 GHz for the better design of safety applications for M2M systems following the IEEE 802.11p standard. On the other hand, for improved design of non-safety applications for M2M

Measurements	Carrier Frequency	Antenna	Frequency-Selectivity	Tx/Rx Direction of Motion	Environments	Channel Statistics
Ref. [33]	2.4 GHz	SISO	wideband	same	SS/EW (Pico), LVTD	PDP, DD power profile
Ref. [55]	2.4 GHz	MIMO	wideband	same	UC/EW (Pico), LVTD	STF CF, LCR, SDF PSD
Ref. [32]	5 GHz	SISO	wideband	same	UC/SS/EW, (Micro/Pico), H(L)VTD	amplitude PDF, frequency CF, PDP
Ref. [34]	5.2 GHz	MIMO	wideband	opposite	EW (Pico), LVTD	PL, PDP, DD power profile
Ref. [35]	5.9 GHz	SISO	narrowband	same	SS, (Micro/Pico) LVTD	PL, CT, amplitude CDF, Doppler PSD
Ref. [31]	5.9 GHz	SISO	wideband	same+ opposite	UC/SS/EW, (Micro/Pico) LVTD	amplitude PDF, DD power profile

SS: suburban street; EW: expressway; UC: urban canyon; Micro: Micro-cell; Pico: Pico-cell; H(L)VTD: high (low) vehicular traffic density; PDP: power delay profile; DD: Doppler-delay; PSD: power spectrum density; STF: space-time-frequency; CF: correlation function; LCR: level crossing rate; SDF: space-Doppler-frequency; PDF: probability density function; PL: path loss; CDF: cumulative distribution function; CT: coherence time.

TABLE 2.1: Important M2M channel measurements.

systems, measurement campaigns performed at other frequency bands, e.g., 2.4 GHz or 5.2 GHz, are still required.

- **Frequency-Selectivity and Antennas**

In 1999, the Federal Communications Commission (FCC) allocated 75 MHz of licensed spectrum, including seven channels, each with approximately 10 MHz instantaneous bandwidth, for DSRC in the USA. Such M2M channels are often frequency-selective (wideband) channels. A narrowband fading channel characterisation based on measurement results, e.g., in [35], is not sufficient for such M2M DSRC applications. Wideband measurement campaigns, e.g., in [31, 32, 33, 34, 55], are therefore essential for understanding the frequency-selectivity features of M2M channels and further designing high-performance M2M systems.

Most M2M measurement campaigns so far have focused on single-antenna applications, resulting in SISO systems, e.g., in [31, 32, 33, 35]. MIMO systems, with multiple

antennas at both ends, are very promising candidates for future communication systems and are gaining more importance in IEEE 802.11 standards. Moreover, MIMO technology becomes more attractive for M2M systems since multiple antenna elements can be easily placed on large vehicle surfaces. However, until now only a few measurement campaigns, e.g., in [34, 55], were conducted for MIMO M2M channels. Hence, more MIMO M2M wideband measurement campaigns are needed for future M2M system developments.

- **Environments and Tx/Rx Direction of Motion**

Similar to conventional F2M cellular systems, M2M scenarios can be classified as macro-cell, micro-cell, and pico-cell according to the Tx–Rx distance. For macro-cell scenarios or micro-cell scenarios, where the Tx–Rx distance is normally larger than 1 km or ranges from 300 meters to 1 km, M2M systems are mainly used for broadcasting or geocasting, i.e., geographic broadcasting [56]. Whereas for pico-cell scenarios, where the Tx–Rx distance is usually smaller than 300 meters, the applications of M2M systems can be broadcasting, geocasting, or unicasting. Since most M2M applications fall into micro-cell or pico-cell scenarios, these two scenarios are currently receiving more and more attention with several current measurement campaigns taking place, e.g., in [31, 32, 33, 34, 35, 55]. However, there are still a few applications that need communications between two vehicles separated by large distances (larger than 1 km, i.e., macro-cell scenarios), e.g., M2M decentralised environmental notification, which means that vehicles or drivers in a certain area share information with each other about observed events or roadway features. These applications have not gained much attention and thus no measurement results are available that explore M2M channels for macro-cell scenarios.

M2M scenarios can also be categorised as urban canyon, suburban street, and expressway in terms of roadside environments, i.e., buildings, bridges, trees, parked cars, etc., located on the roadside. Many measurement campaigns, e.g., in [31, 32, 33, 55], were conducted to study the channel statistics for various types of roadside environments. Due to the unique feature of M2M environments, the VTD also significantly affects

the channel statistics, especially for micro-cell and pico-cell scenarios. In general, the smaller Tx–Rx distance, the larger impact of the VTD. Note that M2M channels usually exhibit non-isotropic scattering except in cases of high VTD. To the best of the authors' knowledge, only one measurement campaign [32] was carried out to study the impact of the VTD for expressway micro-cell and pico-cell scenarios.

Directions of motion of the Tx and Rx also affect channel statistics, e.g., Doppler effects. Many measurement campaigns e.g., [32, 33, 35, 55], have focused on studying channel characteristics when the Tx and Rx are moving in the same direction. Few M2M measurement campaigns, e.g., in [31, 34], have investigated channel characteristics when the Tx and Rx are moving in opposite directions.

In summary, it is desirable to conduct more measurement campaigns for micro-cell and pico-cell scenarios with various VTDs when the Tx and Rx move in opposite directions. In addition, measurement campaigns for macro-cell scenarios are indispensable for some M2M applications that need communications between two vehicles with a large distance.

- **Channel Statistics**

Knowledge of channel statistics is essential for the analysis and design of a communication system. As shown in Table 2.1, many different M2M channel statistics have been studied in recent measurement campaigns [31, 32, 33, 34, 35, 55]. Here, we only concentrate on two important statistics, amplitude distribution and Doppler PSD. Analysis of amplitude distributions has been reported in [31, 32, 35]. In [31], the authors modeled the amplitude PDF of the received signal as either Rayleigh or Ricean. In [35], it was observed that the received amplitude distribution in a dedicated M2M system with a carrier frequency of 5.9 GHz gradually transits from near-Ricean to Rayleigh as the vehicle separation increases. When the LoS component is intermittently lost at large distances, the channel fading can become more severe than Rayleigh. A similar conclusion has been drawn in [32], where the amplitude PDF is modeled as Weibull distribution and this "worse than Rayleigh" fading is called severe fading. The reason behind the severe fading is the rapid transitions of multipath

components induced by the higher velocity and lower height of the Tx/Rx and the faster moving scatterers [57].

The Doppler PSD has been investigated in [31, 33, 34, 35, 55]. Joint Doppler-delay PSD measurements for wideband M2M channels at 2.4 GHz, 5.2 GHz, and 5.9 GHz were reported in [33], [34], and [31], respectively. It was demonstrated that Doppler PSDs can vary significantly with different time delays in a wideband M2M channel. In [35], the authors analyzed the Doppler spread and coherence time of narrowband M2M channels and presented their dependence on both velocity and vehicle separation. Recently, the SD PSD, which is the Fourier transform of the ST CF in terms of time, was investigated in [34, 55]. It is worth noting that for isotropic scattering environments the Doppler PSD for M2M channels is completely different from the traditional U-shaped Doppler PSD for F2M channels.

2.3.2 Recent Advances in Mobile-to-Mobile Channel Modelling

In this subsection, we will give a brief overview of recent advances of M2M channel models. Table 2.2 lists some recent important M2M channel models. In terms of the modeling approach, these models can be categorized as geometry-based deterministic models (GBDMs) [58] and stochastic models, while the latter can be further classified as non-geometrical stochastic models (NGSMs) [31, 32] and GBSMs [25, 26, 27, 28, 29, 30, 55, 59]. In the following, we will first present a general expression of the complex impulse response for M2M channels and then analyse each category of M2M models in more detail.

Based on the expression in (2.3), the double-directional time-variant complex impulse response of a M2M channel can be modeled as the superposition of L resolvable paths or taps

$$h\left(t,\tau',\Omega_T,\Omega_R\right)=\sum_{l=1}^{L}h_l\left(t\right)\delta\left(\tau'-\tau'_l\left(t\right)\right)\delta\left(\Omega_T-\Omega_{T,l}\left(t\right)\right)\delta\left(\Omega_R-\Omega_{R,l}\left(t\right)\right) \tag{2.6}$$

Channel Model	Antenna and FS	Stationarity	Impact of VTD	Per-tap CS	Scatterer region/ Distribution	Scattering Assumptions	Applicable Scenarios
Ref. [58] GBDM	MIMO wideband	non-stationary	yes	no	3D non-isotropic (deterministic)	SB+MB	site-specific
Ref. [31] NGSM	SISO wideband	stationary	no	yes	2D non-isotropic (N/A)	N/A	Micro Pico
Ref. [32] NGSM	SISO wideband	non-stationary	yes	yes	2D non-isotropic (N/A)	N/A	Micro Pico
Ref. [25] RS-GBSM	SISO narrowband	stationary	no	no	2D isotropic (two-ring)	DB	Macro
Ref. [27] RS-GBSM	MIMO narrowband	stationary	no	no	2D non-isotropic (two-ring)	DB	Marco Micro
Ref. [28] RS-GBSM	MIMO narrowband	stationary	no	no	2D non-isotropic (two-ring)	SB+DB	Macro Micro
Ref. [29] RS-GBSM	MIMO narrowband	stationary	no	no	3D non-isotropic (two-cylinder)	SB+DB	Macro Micro
Ref. [30, 55] RS-GBSM	MIMO wideband	stationary	no	no	3D non-isotropic (two concentric-cylinder)	SB+DB	Macro Micro
Ref. [59] IS-GBSM	MIMO wideband	non-stationary	yes	no	2D non-isotropic (randomly)	SB	Micro Pico

FS: frequency-selectivity; CS: channel statistics; SB: single-bounced; MB: multiple-bounced; DB: double-bounced; Macro: Macro-cell; Micro: Micro-cell; Pico: Pico-cell; N/A: not-applicable.

TABLE 2.2: Important M2M channel models.

where $\tau_l'(t)$, $\Omega_{T,l}(t)$, and $\Omega_{R,l}(t)$ represent the excess delay, direction of departure (DoD), and direction of arrival (DoA) of the lth resolved path at time t, respectively, and $\delta(\cdot)$ denotes Dirac delta function, and $h_l(t)$ denotes the complex fading envelope of the lth ($l = 1, \ldots, L$) resolved path and can be expressed as

$$h_l(t) = \sum_{n=1}^{N} a_{l,n}(t)\, e^{j2\pi f_{D,l,n}(t)t} e^{j\vec{k}\left(\theta_{T,l,n}(t)\right)\vec{d}_T} e^{j\vec{k}\left(\theta_{R,l,n}(t)\right)\vec{d}_R}. \tag{2.7}$$

From (2.7), it is clear that each resolvable path $h_l(t)$ also consists of multiple unresolvable subpaths with complex amplitudes represented by $a_{l,n}(t)$ ($n = 1, 2, ..., N$). Here, $f_{D,l,n}(t) = v(t) f_c \cos\beta_{l,n}(t)/c$ is the Doppler frequency of the nth unresolvable subpath within the lth resolvable path at time t induced by the motion of both the Tx and Rx, $v(t)$ denotes the relative velocity, f_c is the carrier frequency, $\beta_{l,n}(t)$ is the aggregate phase angle of the nth subpath, and c is the speed of light.

The terms $e^{j\vec{k}\left(\theta_{T,l,n}(t)\right)\vec{d}_T}$ and $e^{j\vec{k}\left(\theta_{R,l,n}(t)\right)\vec{d}_R}$ are the corresponding distance-induced phase shifts, where $\theta_{T,l,n}(t)$ and $\theta_{R,l,n}(t)$ denote the DoD and DoA of the nth sub-path within the lth path at time t, respectively, $\vec{d}_T$ and $\vec{d}_R$ are the vectors of the chosen element position measured from an arbitrary but fixed reference points on the corresponding arrays, and $\vec{k}$ is the wave vector so that $\vec{k}\left(\theta_{T(R),l,n}(t)\right)\vec{d}_{T(R)} = \frac{2\pi}{\lambda}\big(x\cos\varphi_{T(R)}(t)\cos\phi_{T(R)}(t)+y\cos\varphi_{T(R)}(t)\sin\phi_{T(R)}(t)+z\sin\varphi_{T(R)}(t)\big)$, where $\varphi_{T(R)}$ and $\phi_{T(R)}$ denote elevation and azimuth angles, respectively.

- **Geometry-Based Deterministic Models**

GBDMs characterise M2M physical channel parameters in a completely deterministic manner. A GBDM based on the ray-tracing method for M2M channels was proposed in [58]. It aims at reproducing the actual physical radio propagation process for a given environment. As illustrated in FIGURE 2.4, the representation of the real environment duplication includes two major parts: the modeling of the dynamic road traffic (e.g., moving cars, vans, trucks, etc.) and the modeling of the roadside environments (e.g., buildings, packed cars, road signs, trees, etc.). Then, an accurate modeling of the wave propagation in the aforementioned real environment is implemented by generating possible paths (rays) from the Tx to the Rx according to geometric considerations and the rules of geometrical optics. In [58], a 3D ray-tracing approach was used in a wave propagation model. The resulting complex impulse response incorporates the complete channel information, e.g., the statistical non-stationarity of the channel, the impact of the VTD on channel statistics, and the impact of the elevation angle on channel statistics, and thus agrees very well with measurements. However, GBDM require a detailed and time-consuming description of site-specific propagation environments and consequently cannot be easily generalised to a wide class of scenarios.

- **Non-Geometrical Stochastic Models**

A NGSM determines physical parameters of a M2M channel in a completely stochastic manner without presuming any underlying geometry. The SISO NGSM proposed in

[31] is the origin of the M2M channel model standardized by IEEE 802.11p. The complex impulse response of the SISO M2M channels in [31] can be modeled from (2.6) and (2.7) by removing the terms $\delta(\Omega_T - \Omega_{T,l}(t))$, $\delta(\Omega_R - \Omega_{R,l}(t))$ and the corresponding distance-induced phase shift $e^{j\vec{k}\left(\theta_{T,l,n}(t)\right)\vec{d}_T}$ and $e^{j\vec{k}\left(\theta_{R,l,n}(t)\right)\vec{d}_R}$ while the aggregate phase angle $\beta_{l,n}(t)$ is placed in a 2D plane, i.e., has zero elevation. Based on the TDL structure, this model consists of L taps, with tap amplitude PDF being either Ricean or Rayleigh, and thus has the ability to study per-tap channel statistics. Furthermore, each tap contains N unresolvable subpaths that have different types of Doppler spectra, e.g., flat shape, round shape, classic 3 dB shape, and classic 6 dB shape. This allows the synthesis of almost arbitrary Doppler spectra for each tap. However, this NGSM is still based on the WSSUS assumption and has not investigated the impact of the VTD on channel statistics.

Recently, a SISO NGSM was proposed in [32] which takes into account the non-stationarity of the channel by modelling multipath component persistence via Markov chains. Moreover, in this study, the impact of the VTD on channel statistics was investigated. The complex impulse response of the SISO M2M channels in [32] can be obtained from the complex impulse response in [31] by adding an additional term, named as the persistence process, $z_l(t)$, which accounts for the finite lifetime of the lth resolvable path. The NGSM in [32] can easily capture the effect of a sudden disappearance of strong multipaths, mainly caused by rapid blockage or obstruction from another vehicle or other obstacles. However, the model did not consider the drift of scatterers into different delay bins (resolvable paths) and therefore the transitional probabilities of the Markov model for the persistence processes may not be accurate. This may reduce the ability of the NGSM [32] to accurately capture the non-stationarity of real M2M channels and thus deserves more investigations.

- **Geometry-Based Stochastic Models**

A GBSM is derived from a predefined stochastic distribution of effective scatterers by applying the fundamental laws of wave propagation. Such models can be easily adapted to different scenarios by changing the shape of the scattering region and/or

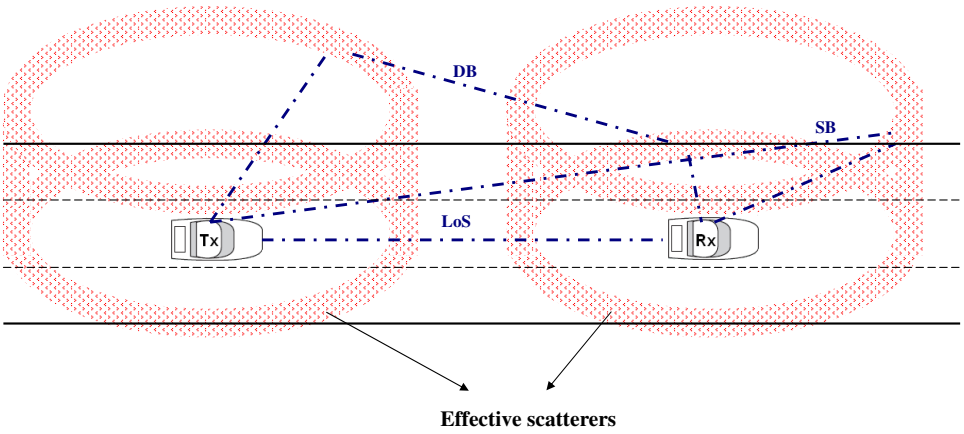

FIGURE 2.5: The geometrical description of the RS-GBSM according to the typical M2M environment in FIGURE 2.4. SB: single-bounced; DB: double-bounced.

the PDF of the location of the scatterers. GBSMs can be further classified as regular-shaped GBSMs (RS-GBSMs) and irregular-shaped GBSMs (IS-GBSMs) depending on whether effective scatterers are placed on regular shapes (e.g., one/two-ring, ellipse, etc.) or irregular shapes (randomly). Therefore, the one-ring MIMO F2M channel model described in Section 2.2 actually belongs to RS-GBSMs.

In general, RS-GBSMs are used for the theoretical analysis of channel statistics and theoretical design and comparison of communication systems. Therefore, to preserve the mathematical tractability, RS-GBSMs assume all effective scatterers are located on a regular shape. Akki and Haber [25, 26] were the first to propose a 2D two-ring RS-GBSM with only double-bounced rays for narrowband isotropic scattering SISO M2M Rayleigh fading channels in macro-cell scenarios. In [27], a two-ring RS-GBSM considering only double-bounce rays was presented for non-isotropic scattering MIMO M2M Rayleigh fading channels in macro-cell scenarios. In [28], the authors proposed a general 2D two-ring RS-GBSM with both single- and double-bounced rays for non-isotropic scattering MIMO M2M Ricean channels in both macro-cell and micro-cell scenarios. The 2D two-ring narrowband model in [28] was further extended to a 3D two-cylinder narrowband model in [29] and a 3D two-concentric-cylinder wideband model in [30, 55]. Based on the real M2M environment in FIGURE 2.4, FIGURE 2.5 shows the geometrical description of the 3D two-concentric-cylinder wideband model that consists of LoS, single-, and double-bounced rays. The complex impulse response

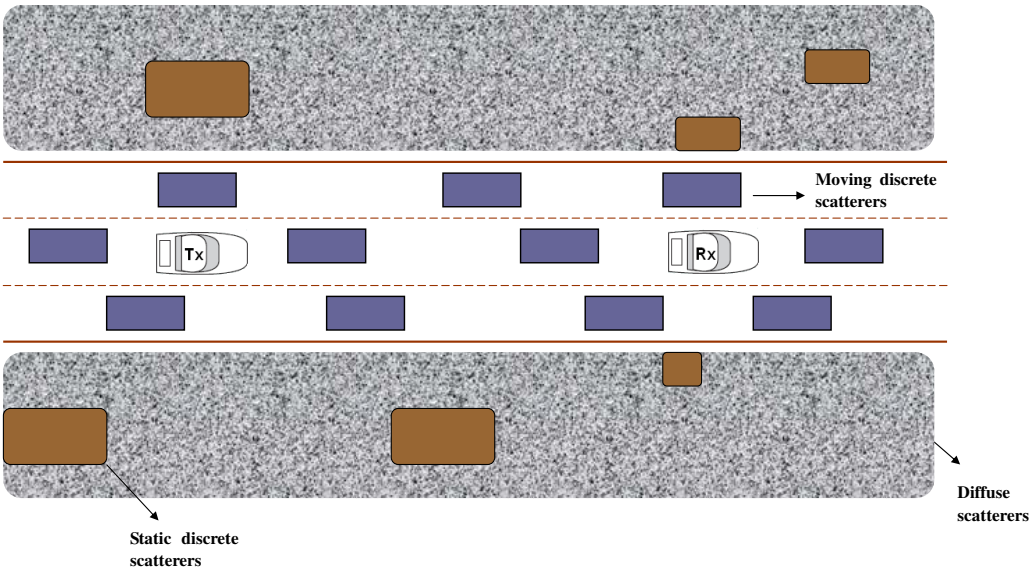

FIGURE 2.6: The geometrical description of the IS-GBSM according to the typical M2M environment in FIGURE 2.4.

of this wideband model can be easily obtained from (2.6) and (2.7). In agreement with real M2M environments, the authors in [30, 55] divide the complex impulse response into three parts: 1) the LoS component; 2) the single-bounced rays generated from the effective scatterers located on either of the two cylinders; and 3) the double-bounced rays produced from the effective scatterers located on both cylinders, as illustrated in FIGURE 2.5. However, all the aforementioned RS-GBSMs cannot study the impact of the VTD on channel statistics and investigate per-tap channel statistics in wideband cases. Furthermore, a RS-GBSM does not have the ability to study the non-stationarity due to the static nature of the geometry in RS-GBSMs.

Unlike RS-GBSMs, IS-GBSMs intend to reproduce the physical reality and thus need to modify the location and properties of the effective scatterers of RS-GBSMs. IS-GBSMs place the effective scatterers with specified properties at random locations with certain statistical distributions. The signal contributions of the effective scatterers are determined from a greatly-simplified ray-tracing method and finally the total signal is summed up to obtain the complex impulse response, which can be expressed as (2.6) and (2.7) with the assumption of the elevation angle $\varphi_{T(R)} = 0$. In [59], to provide better agreement with the measurement results presented in [34], the impulse

response is further divided into four parts: 1) the LoS component; 2) discrete components from reflections of mobile scatterers (e.g., moving cars); 3) discrete components from reflections of significant (strong) static scatterers (e.g., building and road signs located on the roadside); and 4) diffuse components from reflections of weak static scatterers located on the roadside, as depicted in FIGURE 2.6. Therefore, IS-GBSMs are actually a greatly-simplified version of GBDMs while suitable for a wide variety of M2M scenarios by properly adjusting the statistical distributions of the location of the effective scatterers. With the ray-tracing approach, the IS-GBSM in [59] can easily handle the non-stationarity of M2M channels by prescribing the motion of the Tx, Rx, and mobile scatterers. Note that only single-bounced rays are considered in this IS-GBSM due to the fairly low VTD of the measurements in [34]. For a high VTD environment, it is possible that double-bounced rays should be considered as well. Compared to the NGSM in [32], the IS-GBSM in [59] can easily handle the drift of scatterers into different delay bins but with relatively higher complexity.

2.4 Simulation Models for Fading Channels

As mentioned in Chapter 1, accurate simulation models play an important role in the practical simulation and performance evaluation of a wireless communication system. Simulation of fading channels is commonly used as opposed to field trials, because it allows for less expensive and more reproducible system tests and evaluations. In contrast to the so-called mathematical reference model [13] that assumes an infinite number of effective scatterers (i.e., has an infinite complexity) and thus cannot be directly implemented in practice, a simulation model has a finite complexity and thereby is realisable in practice. Note that the previously described narrowband one-ring MIMO F2M RS-GBSM and M2M RS-GBSMs are actually mathematical reference models since they assume an infinite number of effective scatterers, as shown in (2.4) where the number of effective scatterers N tends to be infinite. As mentioned in [41], a mathematical reference model can be used for theoretical analysis and design of a wireless communication system, and also is a starting point to design a realisable simulation model that has the reasonable complexity, i.e., finite numbers of effective scatterers.

Therefore, the development of a simulation model aims to design a simulator with a reasonable complexity while representing the desired statistical properties of the mathematical reference model as faithfully as possible.

There are several different methods for simulating fading channels. The most accepted methods are filter methods [3, 60, 61, 62, 63] and SoS methods [13, 36, 39, 64, 65, 66, 67, 68, 69, 70]. The filter methods filter Gaussian noise through properly designed filters to generate the channel waveform with the desired Doppler PSD. The main limitation of this approach is that only the waveform with rational forms of the Doppler PSD can be produced exactly. However, as mentioned in [41], the non-rational Doppler PSD is the typical form of Doppler PSD in reality. In order to approximate the waveform with the non-rational Doppler PSD, the filter models have to include high-order filters, which lead to this approach being significantly complicated and time-consuming. Moreover, the Doppler PSD obtained by using this approach is not band-limited since it is difficult to implement the filters with sharp stop-bands in practice. On the other hand, the SoS methods generate the channel waveform by superimposing a finite number of properly designed sinusoids. In contrast to filter simulation models, SoS simulation models have low complexity and produce channel waveforms with high accuracy and a perfectly band-limited Doppler PSD. Furthermore, it is easy to extend the SoS models to develop ST correlated simulators for MIMO systems. Due to the aforementioned advantages, our research focuses on SoS simulation models.

A SoS simulation model can be either deterministic or stochastic in terms of the underlying parameters (gains, frequencies, and phases) [70]. For a deterministic model, all the parameters are fixed for all simulation trials. In contrast, a stochastic model has at least one parameter (gains, frequencies, or phases) as a random variable which varies for each simulation trial. Therefore, the relevant statistical properties of a stochastic model vary for each simulation trial but converge to the desired ones when averaged over a sufficient number of trials. It is worth noting that a stochastic model with only phases as random variables is actually an ergodic process. Due to the ergodicity, such a stochastic simulation model needs only one simulation trial to converge

to the desired statistical properties.

2.4.1 Sum-of-Sinusoids Simulation Models for Cellular Channels

Many approaches have been suggested for SoS simulation of SISO F2M Rayleigh fading channels. Jakes [65] was among the first to propose a deterministic simulation model for SISO F2M Rayleigh fading channels. However, Jakes' model does not satisfy most of the statistical properties of Rayleigh fading channels [71] and it is not WSS [66]. Therefore, various modifications of Jakes' model have been proposed in the literature [13, 66, 70]. Pop and Beaulieu have proposed a new deterministic simulation model [66] to solve the non-stationarity of Jakes' model. However, this model still cannot satisfy most of the other statistical properties of Rayleigh fading channels. Pätzold and his co-workers have developed several deterministic simulation models with different parameter computation methods [72, 73, 74, 75]. The method of equal area (MEA) [72, 73] is characterised by the fact that the area under the Doppler PSD between two neighbouring discrete frequencies are equal area. This parameter computation method presents acceptable performance with low complexity. A quasi-optimal procedure is the method of exact Doppler spread (MEDS) [74, 75]. This method outperforms the MEA and even shows the very similar performance to the optimisation method (i.e., L_p-norm method) [74, 75]. Compared to the MEA and MEDS, the arising numerical complexity of the optimisation method is comparatively high, so that the simulation of such isotropic scattering Rayleigh fading channels is often not worth the effort [13]. More recently, the drawback of the MEDS in generating multiple uncorrelated Rayleigh fading waveforms has been resolved by Wang and his co-workers in [70, 76].

In order to satisfy more statistical properties and/or match the desired properties over longer time delays, Zheng and Xiao have proposed several new stochastic simulation models [67, 68, 77]. By allowing all three parameters (gains, frequencies, and phases) to be random variables, Zheng and Xiao's model obtain the statistical properties

similar to the ones of Rayleigh fading channels. Since the models are no longer ergodic process, the statistical properties of these models vary for each simulation trial, but they converge to the desired properties over sufficient number of simulation trials (normally 50 to 100). A detailed comparison of the statistical properties for Zheng and Xiao's models is presented in [78].

However, all the aforementioned deterministic and stochastic simulation models are limited to isotropic scattering SISO F2M Rayleigh fading channels, while simulation models for MIMO F2M channels under a more realistic scenario of non-isotropic scattering are scarce in the current literature. In [79], a narrowband MIMO F2M deterministic simulation was proposed for macro-cell scenarios. In [80], new deterministic simulation models were developed for both narrowband and wideband MIMO F2M channels of micro-cell scenarios. Up to now, only one wideband MIMO F2M deterministic simulation model was proposed in [81] for macro-cell scenarios. However, since the mathematical reference model based on which the wideband simulation model [81] was proposed has several drawbacks (see Chapter 3 for more details), the proposed simulation cannot capture the statistical properties of real wideband MIMO F2M channels for macro-cell scenarios.

2.4.2 Sum-of-Sinusoids Simulation Models for Mobile-to-Mobile Channels

Several methods for the simulation of M2M channels have been proposed in the current literature. Among them, Patel *et al.* [36] were the first to propose new SoS simulation models for SISO M2M Rayleigh fading channels. They first modified the MEDS proposed in [74, 75] for F2M channels and propose a new deterministic simulation model. However, the proposed deterministic model matches the desired statistical properties of the mathematical reference model only for a small range of normalised time delays. Therefore, Patel *et al.* also modified a stochastic model developed in [67] for F2M channels and propose a new stochastic simulation model for M2M channels. This stochastic model can match the desired statistical properties over a

large range of normalised time delays at the expense of simulation complexity (need 50 simulation trials). The stochastic model in [36] was further improved in [39] by choosing orthogonal functions for in-phase and quadrature components of the complex fading envelope. More recently, in [40] the Rayleigh M2M stochastic simulation model in [36] was extended to include a LoS component, i.e., for Ricean fading channels.

However, it is worth noting that all the aforementioned simulation models limit their applications to isotropic scattering environments. So far, only one stochastic simulation model [82] has been proposed for the simulation of non-isotropic scattering M2M Rayleigh fading channels. However, this model has a notable difficulty in reproducing the desired statistical properties of the mathematical reference model and a comparatively high computational complexity, which is brought forward in detail in Chapter 4. Furthermore, accurate deterministic simulation models for non-isotropic scattering M2M Rayleigh fading channels are not available in the current literature.

Regarding the simulation of MIMO M2M channels, Pätzold *et al.* [38] proposed a new deterministic SoS simulation model under the condition of isotropic scattering. This model was further improved and extended to include a LoS component in [28]. To simulate MIMO M2M channels under a more realistic scenario of non-isotropic scattering, in [27] the authors modified the narrowband deterministic simulation model in [38] for isotropic scattering environments and proposed a new parameter computation method. This new parameter computation method is termed modified MEA (MMEA) since it is originated from the MEA in [72, 73] for isotropic scattering F2M channels. In [29], new deterministic and stochastic simulation models were developed for non-isotropic scattering narrowband MIMO M2M channels. More recently, the authors in [30] developed a new wideband deterministic simulation model for MIMO M2M channels under non-isotropic scattering conditions. However, all the previously reported non-isotropic scattering MIMO M2M deterministic simulation models have several flaws in reproducing properly the statistical properties of the mathematical reference model, which is detailed in Chapter 6. Moreover, stochastic simulation models for non-isotropic scattering wideband MIMO M2M channels are surprisingly unavailable in the current literature.

Chapter 3

MIMO Cellular Channels for Macro-Cell Scenarios: Modelling and Simulation

3.1 Introduction

Chapter 2 briefly described the well-known one-ring MIMO F2M RS-GBSM [22], which is widely used for the analysis and design of narrowband MIMO cellular systems for macro-cell scenarios. To reach the high demand for high-speed communications, wideband MIMO cellular systems have been suggested in many communication standards, leading to the increasing requirement for wideband MIMO F2M channel models.

However, the one-ring structure that assumes effective scatterers located on a one-ring is overly simplistic and thus unrealistic for modeling wideband channels [54]. Therefore, in [54] the authors for the first time extended the narrowband one-ring model to a wideband model by extending the location of effective scatterers on a one-ring to a circular-ring. However, it is not trivial to use this model to match any given or measured PDP since many parameters need adjustments via a complicated approach. In addition, the integral expressions of the derived STF CFs based on this

model can only be numerically evaluated as no closed-form expressions were found. In contrast to [54], in [81] the one-ring model was extended to a wideband application by dividing the one-ring into several segments in terms of different time of arrivals (ToAs). This makes the model easier to match any specific PDPs due to the TDL structure. However, the one-ring structure was still applied in this model, which causes this model to exhibit an unrealistic structure in that certain ToAs (or propagation delays) are always related to a certain proportion of AoAs. To obtain closed-form expressions of STF CFs, the model in [81] further applied an unrealistic assumption that the mean AoA and the corresponding angle spread are exactly the same for all the scatterers in different segments. Moreover, neither of the two models considered the interaction of the AoA, AoD, and ToA, the importance of which was described in [83]. More importantly, frequency correlation of sub-channels with different carrier frequencies, studied in [69] for SISO channels, has not been investigated yet for MIMO channels. Chapter 2 showed that the frequency correlation appears when the coherence bandwidth B_c is larger than the frequency separation of different sub-channels. This frequency-correlated MIMO channel is commonly encountered in frequency-diversity MIMO communication systems, such as frequency-hopping MIMO systems and MIMO-orthogonal frequency division multiplexing (MIMO-OFDM) systems. For convenience, researchers investigating these systems have typically assumed that different frequency-separated channels are uncorrelated [65], which leads to positively biased performance results for the investigated systems. Therefore, accurate theoretical analysis and simulations of frequency-correlated MIMO channels are of great importance in investigating the impact of the frequency correlation on the performance of real frequency-diversity MIMO systems.

The goals of this chapter are three-fold. First, we propose a new wideband MIMO F2M RS-GBSM that represents a reasonable compromise between physical reality and analytical tractability. The proposed model uses a concentric multiple-ring instead of one-ring around the MS to avoid the one-ring structure. Also, to easily match any specified or measured PDP, the model utilises a virtual confocal multiple-ellipse to construct a TDL structure. Moreover, this model has the ability to consider the interaction of the AoA, AoD, and ToA. Secondly, from the proposed model, a closed-form

expression of the STF CF between any two sub-channels with different carrier frequencies for each time-bin signal is derived. For simplicity, the spatial and frequency correlations were assumed to be independent in [54, 81]. On the contrary, in this chapter we derive the STF CF by taking into account the dependency between them, which is a unique characteristic of frequency-correlated MIMO channels [84]. Therefore, the derived STF CF can explicitly relate the frequency correlation to various environment parameters (e.g., mean AoA and angle spread of the AoA). Moreover, based on the derived CF, we reveal the inherent frequency correlation within the spatial correlation, which is important for the design of frequency-diversity MIMO systems [85, 86]. In addition, the proposed wideband model can be reduced to the traditional one-ring model by removing the frequency-selectivity. In this case, the derived STF CF shows a compact closed-form expression that is a generalisation of many existing CFs [22, 23, 24, 65, 87, 88]. Since the proposed wideband RS-GBSM is a mathematical reference model that assumes an infinite number of effective scatterers, it cannot be implemented directly in practice. Therefore, the third goal of this chapter is to derive a wideband deterministic SoS simulation model based on the proposed mathematical reference model. Closed-form expressions are provided for the STF CF of the simulation model. Similarly, the corresponding narrowband simulation model can be obtained by removing the frequency-selectivity from the wideband simulation model. The statistical properties of our simulation models are verified by comparing with the corresponding statistical properties of the mathematical reference models.

The rest of this chapter is organized as follows. Section 3.2 describes the new wideband multiple-ring based MIMO F2M channel mathematical reference model for non-isotropic scattering macro-cell scenarios. In Section 3.3, based on the proposed new model, the generic STF CF is derived, which can be reduced to a compact closed-form expression for narrowband MIMO channels by removing the frequency-selectivity. Section 3.4 details the proposed deterministic SoS simulation models. Numerical results and analysis are given in Section 3.5. Finally, Section 3.6 summarises this chapter.

3.2 A New Wideband Multiple-ring Based MIMO Channel Mathematical Reference Model

A narrowband one-ring MIMO model is suitable for describing a narrowband channel in macro-cell scenarios, where the BS is elevated and unobstructed, while the MS is surrounded by a large number of local scatterers as shown in FIGURE 2.2. For narrowband systems, since the propagation delays τ'_n of all N ($N \to \infty$) incoming waves are much smaller than the transmitted symbol duration T_s, i.e., $\tau'_{\max} = \max\{\tau'_n\}_{n=1}^{N} \ll T_s$, the delay differences caused by different local scatterers randomly around the MS can be neglected in comparison to T_s. Therefore, it is reasonable to use the effective scatterers located on a one-ring instead of the real local scatterers to construct the low complexity one-ring model at the minor expense of accuracy [24]. However, in high data rate wideband systems, T_s is much smaller than that in narrowband systems. In this case, the propagation delay differences cannot be neglected and thus the channel becomes a wideband channel. Therefore, the one-ring structure violates the basic characteristics of wideband channels as mentioned in [54].

To extend the one-ring model to wideband applications in macro-cell scenarios, the primary task is to modify the oversimple one-ring structure. To this end, we replace the one ring of effective scatterers by concentric multiple rings of effective scatterers around the MS to capture the basic characteristics of wideband channels. To make our model easier to match any specified or measured PDP, we utilise the confocal multiple virtual ellipses with the BS and MS located at the foci to represent the TDL structure, where different delays correspond to different virtual confocal ellipses (i.e., taps). Note that the total number of virtual confocal ellipses L and the values of major axes a_l of different ellipses are determined according to the specified or measured PDP. The newly developed structure is shown in FIGURE 3.1. For clarity, FIGURE 3.1 only presents the effective scatterers from three concentric rings (the total number of concentric rings in the lth tap is Λ_l) belong to the lth tap ($l = 1, 2, ..., L$). Notice that the total number and radii of the concentric multiple rings for different taps (i.e., Λ_l and $R_{l,i}$) can be different in terms of different propagation environments for different

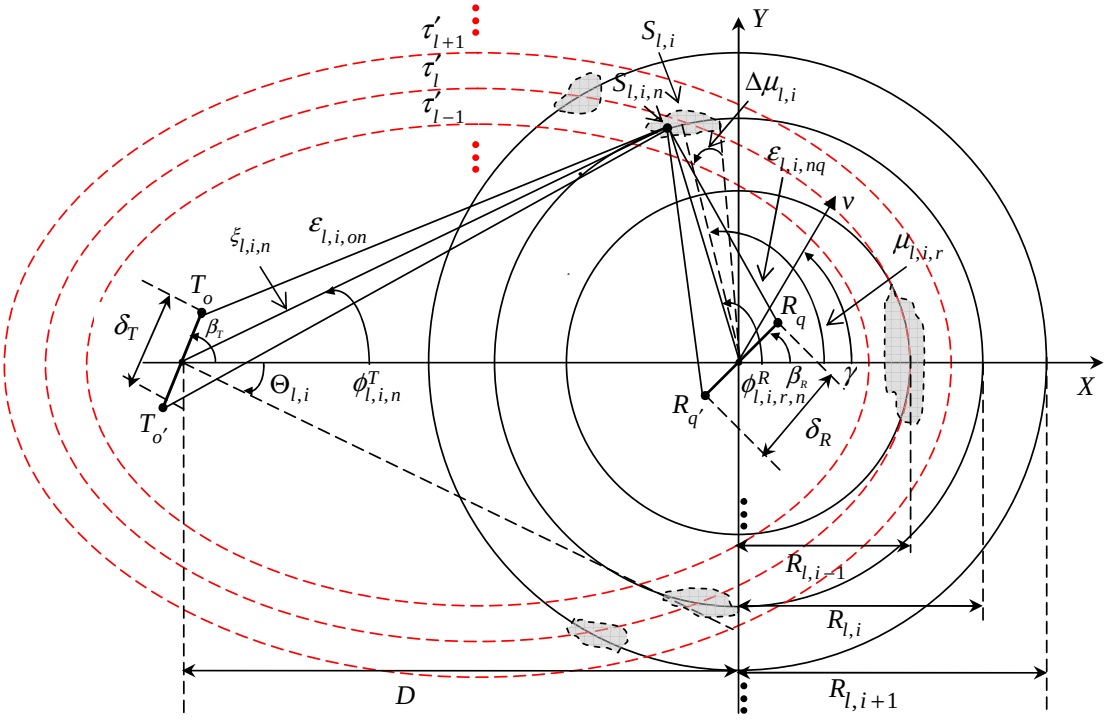

FIGURE 3.1: A new wideband multiple-ring based MIMO F2M channel model.

delays. Therefore, the new wideband model with the appropriate number and major axes of virtual confocal multiple ellipses (i.e., L and a_l), and the appropriate number and radii of concentric multiple rings (i.e., Λ_l and $R_{l,i}$) should be suitable for any macro-cell scenario. We assume that uniform linear antenna arrays are used with M_T=M_R=2 antennas. The symbols δ_T and δ_R designate the antenna element spacing at the BS and MS, respectively, and D denotes the distance between the BS and MS. The effective scatterers are located on $\sum_{l=1}^{L}\Lambda_l$ rings with radii $R_{l,i}$ (i=0, 1, ..., Λ_l-1). It is usually assumed that the assumption $D \gg R_{l,i} \gg \max\{\delta_T, \delta_R\}$ is fulfilled. The multi-element antenna array angles are denoted by β_T and β_R. The MS moves with speed in the direction determined by the angle of motion γ. The angle spread seen at the BS is denoted by $\Theta_{l.i}$, which is related to $R_{l,i}$ and D by $\Theta_{l,i} \approx \arctan(R_{l,i}/D) \approx R_{l,i}/D$.

The received complex impulse response at the carrier frequency f_c for the link $T_o - R_q$ can be expressed as

$$h_{oq}(t,\tau') = \sum_{l=1}^{L} h_{l,oq}(t) \times \delta(\tau' - \tau'_l) \tag{3.1}$$

with $o = 1, 2, ..., M_T$ and $q = 1, 2, ..., M_R$, where $h_{l,oq}(t)$ and τ'_l denote the complex time-variant tap coefficient and the discrete propagation delay of the lth tap, respectively. Similar to the concept of effective scatterers in the narrowband one-ring model, the concept of an effective cluster is introduced in the new wideband multiple-ring model. From FIGURE 3.1, it is obvious that the position of the effective cluster $S_{l,i}$ is identified by the intersection of the virtual ellipses and multiple rings, and the lth tap includes $2\Lambda_l$ effective clusters. The mean angle of the effective cluster in each tap is $\mu_{l,i,r}$ (r=1, 2) and the corresponding angle spread is $\Delta\mu_{l,i}$ as illustrated in FIGURE 3.1. Therefore, the effective cluster can be completely determined by $\mu_{l,i,r}$ and $\Delta\mu_{l,i}$. Note that the angular range of $\mu_{l,i,r}$ in each tap is over $[0, 2\pi)$, which means the effective cluster can be located around the MS over $[0, 2\pi)$ for each tap. The setting of these two parameters follows a fixed rule. To establish this rule, firstly, we need to define the propagation delay subintervals G_l. The propagation delay interval $G = [0, \tau'_{\max}]$ is partitioned into L mutually disjoint sub-intervals G_l. Here, we utilise the definition of subintervals as [69]

$$G_l = \begin{cases} \left[0, \Delta\tau'_{l+1}/2\right), & l=1 \\ \left[\tau'_l - \Delta\tau'_l/2, \tau'_l + \Delta\tau'_{l+1}/2\right), & l=2, 3, ..., L-1 \\ \left[\tau'_l - \Delta\tau'_l/2, \tau'_{\max}\right], & l=L \end{cases} \tag{3.2}$$

where $\Delta\tau'_l = \tau'_l - \tau'_{l-1}$ and $\tau'_{\max} = 2R_{L-1,\Lambda_{L-1}-1}/c$ (c is the speed of light). The propagation delay τ'_l of the lth tap can be expressed according to the corresponding AoA $\phi^R_{l,i,r}$ ($r = 1, 2$) as $\tau'_l \approx \tau'_{\max}(1+\cos\phi^R_{l,i,r})/2$ [81]. Solving this equation for $\phi^R_{l,i,r}$ gives $\phi^R_{l,i,r} = \pm\arccos(2\tau'_l/\tau'_{\max} - 1)$. According to (3.2), the expression of $\phi^R_{l,i,r}$, and the geometrical relationship in FIGURE 3.1, the expression of the mean angle $\mu_{l,i,r}$ and the corresponding angle spread $\Delta\mu_{l,i}$ of the effective cluster in the lth tap are given

as

$$\begin{aligned}\mu_{l,i,r} &= \left(\phi^R_{l,i-1,r}+2\phi^R_{l,i,r}+\phi^R_{l,i+1,r}\right)/4=\pm\big[\arccos\left(2\tau'_{l-1}/\tau'_{\max}-1\right)\\ &\quad +2\arccos\left(2\tau'_l/\tau'_{\max}-1\right)+\arccos\left(2\tau'_{l+1}/\tau'_{\max}-1\right)\big]/4 \qquad (3.3)\\ \Delta\mu_{l,i} &= \left|\left(\phi^R_{l,i-1,r}-\phi^R_{l,i+1,r}\right)/4\right|\\ &= \big[\arccos\left(2\tau'_{l-1}/\tau'_{\max}-1\right)-\arccos\left(2\tau'_{l+1}/\tau'_{\max}-1\right)\big]/4. \qquad (3.4)\end{aligned}$$

Following the definition of the subintervals G_l and some geometrical relationship shown in FIGURE 3.1, we can determine the effective cluster in each tap according to the propagation delay τ'_l. The time-variant tap coefficient at the carrier frequency f_c of lth tap can be expressed as

$$h_{l,oq}(t)=\lim_{N\to\infty}\frac{1}{\sqrt{N}}\sum_{i=0}^{\Lambda_l-1}\sum_{r=1}^{R_c}\sum_{n=1}^{N}\exp\left\{j\left[\psi_{l,i,n}-2\pi f_c\tau_{l,i,oq,n}+2\pi f_D t\cos\left(\phi^R_{l,i,r,n}-\gamma\right)\right]\right\} \qquad (3.5)$$

with $\tau_{l,i,oq,n}=(\varepsilon_{l,i,on}+\varepsilon_{l,i,nq})/c$. Here, $\tau_{l,i.oq,n}$ is the travel time of the wave through the link $T_o-S_{l,i,n}-R_q$ scattered by the nth scatterer, $S_{l,i,n}$, R_c is the number of effective cluster for one ring in each tap (here $R_c=2$), and N is the number of effective scatterers $S_{l,i,n}$ in the effective cluster $S_{l,i}$. The AoA of the wave traveling from the nth scatterer in the effective cluster $S_{l,i}$ towards the MS is denoted by $\phi^R_{l,i,r,n}$. The phases $\psi_{l,i,n}$ are i.i.d. random variables with uniform distributions over $[0,2\pi)$ and f_D is the maximum Doppler frequency. As shown in [22], the distance $\varepsilon_{l,i,on}$ and $\varepsilon_{l,i,nq}$ can be expressed as the function of $\phi^R_{l,i,r,n}$ as

$$\begin{aligned}\varepsilon_{l,i,on} &\approx \xi_{l,i,n}-\delta_T[\cos(\beta_T)+\Theta_{l,i}\sin(\beta_T)\sin(\phi^R_{l,i,r,n})]/2 \qquad (3.6a)\\ \varepsilon_{l,i,nq} &\approx R_{l,i}-\delta_R\cos(\phi^R_{l,i,r,n}-\beta_R)/2 \qquad (3.6b)\end{aligned}$$

respectively, where $\xi_{l,i,n}\approx D+R_{l,i}\cos(\phi^R_{l,i,r,n})$.

Since we assume that the number of effective scatterers in one effective cluster in this mathematical reference model tends to infinite (as shown in (3.5)), the discrete AoA $\phi^R_{l,i,r,n}$ can be replaced by the continuous expressions $\phi^R_{l,i,r}$. In the literature, many different scatterer distributions have been proposed to characterise the AoA $\phi^R_{l,i,r}$,

such as the uniform [89], Gaussian [90], wrapped Gaussian [91], and cardioid PDFs [92]. In this chapter, the von Mises PDF [24] is used, which can approximate all the above mentioned PDFs. The von Mises PDF is defined as

$$f(\phi) \triangleq \exp\left[k\cos(\phi-\mu)\right]/2\pi I_0(k) \tag{3.7}$$

where $\phi \in [-\pi, \pi)$, $I_0(\cdot)$ is the zeroth-order modified Bessel function of the first kind, $\mu \in [-\pi, \pi)$ accounts for the mean value of the angle ϕ, and k ($k \geq 0$) is a real-valued parameter that controls the angle spread of the angle ϕ. For $k=0$ (isotropic scattering), the von Mises PDF reduces to the uniform distribution, while for $k>0$ (non-isotropic scattering), the von Mises PDF approximates different distributions based on the values of k [22]. To better characterise the AoA in one effective cluster $S_{l,i}$, we further modify the general expression of von Mises PDF as

$$f_c\left(\phi_{l,i,r}^R\right) = Q_{l,i,r}\exp\left[k_{l,i,r}\cos\left(\phi_{l,i,r}^R-\mu_{l,i,r}\right)\right]/2\pi I_0\left(k_{l,i,r}\right) \tag{3.8}$$

where $\phi_{l,i,r}^R \in [\mu_{l,i,r}-\Delta\mu_{l,i}, \mu_{l,i,r}+\Delta\mu_{l,i})$ and $Q_{l,i,r}$ is the normalisation coefficient. Here we name the PDF in (3.8) the truncated von Mises PDF. Here, truncated means that the range of AoA in this PDF is only defined within a limited interval $[\mu_{l,i,r}-\Delta\mu_{l,i}, \mu_{l,i,r}+\Delta\mu_{l,i})$. Therefore, the expression of the 'tapped' PDF of AoA in the lth tap of the proposed wideband multiple-ring channel model is given by

$$f_g\left(\phi_{l,i,r}^R\right) = \sum_{i=0}^{\Lambda_l-1}\sum_{r=1}^{R_c}\frac{Q_{l,i,r}\exp\left[k_{l,i,r}\cos\left(\phi_{l,i,r}^R-\mu_{l,i,r}\right)\right]}{2\pi I_0\left(k_{l,i,r}\right)} w\left(\phi_{l,i,r}^R, \mu_{l,i,r}-\Delta\mu_{l,i}, \mu_{l,i,r}+\Delta\mu_{l,i}\right)$$
$$\text{where} \quad \mathrm{w}(\phi, \phi_\mathrm{l}, \phi_\mathrm{u}) = \begin{cases} 1, & \text{if } \phi_l < \phi < \phi_u \\ 0, & \text{otherwise.} \end{cases} \tag{3.9}$$

Here, $Q_{l,i,r}$ are computed in such a way that the 'tapped' PDF $f_g(\phi_{l,i,r}^R)$ is equal to 1, i.e., $\int_{-\pi}^{\pi} f_g(\phi_{l,i,r}^R)d\phi_{l,i,r}^R = 1$.

Note that the proposed wideband model allows one to consider the interaction of AoA, AoD, and ToA in a sensible manner. The interaction between the AoA and AoD is obtained in terms of the exact geometrical relationship, while the interaction between the AoA/AoD and ToA is calculated according to the TDL structure that

allows one to investigate the correlation properties in each tap. Therefore, inspired by [83], the interaction between the AoA/AoD and ToA can be considered via setting the appropriate parameter $k_{l,i,r}$ for the PDF of AoA/AoD in each tap according to the PDF of ToA.

3.3 New Generic Space-Time-Frequency Correlation Function

In this section, from the proposed model we first derive a new generic STF CF for wideband MIMO channels. As shown at the end of this section, the derived STF CF can be reduced to a compact closed-form STF CF for narrowband MIMO channels by removing the frequency-selectivity, which includes many existing CFs as special cases.

3.3.1 Space-Time-Frequency Correlation Function for Wideband MIMO Channels

From the proposed wideband model, we derive the STF CF for each tap. The correlation properties of two arbitrary links $h_{oq}(t,\tau')$ and $h'_{o'q'}(t,\tau')$ at different frequency f_c and f'_c of a MIMO channel are completely determined by the correlation properties of $h_{oq}(t)$ and $h'_{o'q'}(t)$ in each tap since we assume that no correlations exist between the underlying processes in different taps. Therefore, we can restrict our investigations to the following STF CF

$$\rho_{l,oq;l,o'q'}(\tau,\chi) := \mathbf{E}[h_{l,oq}(t)h'^{*}_{l,o'q'}(t-\tau)] \tag{3.10}$$

where $(\cdot)^*$ denotes the complex conjugate operation and $\mathbf{E}[\cdot]$ designates the statistical expectation operator. Note that the above defined CF is a function of the time separation τ, space separation δ_T and δ_R, and frequency separation $\chi = f'_c - f_c$. As shown in Appendix A, the closed-form expression of STF CF $\rho_{l,oq;l,o'q'}(\tau,\chi)$ can be

presented as

$$\rho_{l,oq;l,o'q'}(\tau,\chi)=\frac{2}{\pi I_0(k)}\sum_{i=0}^{\Lambda_l-1}\sum_{r=1}^{R_c}Q_{l,i,r}e^{jC_{l,i}}\{\Delta\mu_{l,i}I_0(A_{l,i,r})\,I_0(B_{l,i,r})/2+I_0(B_{l,i,r})\sum_{\ell=1}^{\infty}$$
$$\times I_\ell(A_{l,i,r})\sin(\ell\Delta\mu_{l,i})\cos(\ell\mu_{l,i,r})/\ell+I_0(A_{l,i,r})\sum_{\ell'=1}^{\infty}(-1)^{\ell'}I_{\ell'}(B_{l,i,r})\sin(\ell'\Delta\mu_{l,i})$$
$$\times\cos(\ell'\mu_{l,i,r}+\ell'\pi/2)/\ell'+\sum_{\ell=1}^{\infty}(-1)^{\ell}I_\ell(A_{l,i,r})\,I_\ell(B_{l,i,r})[\Delta\mu_{l,i}\cos(\ell\pi/2)+\sin(2\ell\Delta\mu_{l,i})$$
$$\times\cos(2\ell\mu_{l,i,r}+\ell\pi/2)/2\ell]+\sum_{\ell=1}^{\infty}\sum_{\substack{q=1\\(\ell\neq q)}}^{\infty}(-1)^{\ell'}I_\ell(A_{l,i,r})\,I_{\ell'}(B_{l,i,r})[\sin[(\ell+\ell')\Delta\mu_{l,i}]$$
$$\times\frac{\cos\left[(\ell+\ell')\mu_{l,i,r}+\ell'\pi/2\right]}{\ell+\ell'}+\frac{\sin\left[(\ell-\ell')\Delta\mu_{l,i}\right]\cos\left[(\ell-\ell')\mu_{l,i,r}-\ell'\pi/2\right]}{\ell-\ell'}\Bigg]\Bigg\} \tag{3.11}$$

where

$$A_{l,i,r} = a_{l,i,r}+j(\mathrm{X}U_{l,i}+y\cos\beta_R+x\cos\gamma) \tag{3.12a}$$
$$B_{l,i,r} = b_{l,i,r}+j(\mathrm{X}V_{l,i}+y\sin\beta_R+z\Theta_{l,i}\sin\beta_T+x\sin\gamma) \tag{3.12b}$$
$$C_{l.i} = z\cos\beta_T+\mathrm{X}T_{l.i} \tag{3.12c}$$

with $x=2\pi f_D\tau$, $y=2\pi f_c\delta_R/c$, $z=2\pi f_c\delta_T/c$, $\mathrm{X}=2\pi\chi/c$, $a_{l,i,r}=k_{l,i,r}\cos\mu_{l,i,r}$, $b_{l,i,r}=k_{l,i,r}\sin\mu_{l,i,r}$, $T_{l,i}=(\delta_T/2)\cos\beta_T+D+R_{l,i}$, $U_{l,i}=R_{l,i}+(\delta_R/2)\cos\beta_R$, and $V_{l,i}=(\delta_T/2)\Theta_{l,i}\sin\beta_T+(\delta_R/2)\sin\beta_R$. Consequently, the STF CF between $h_{oq}(t,\tau')$ and $h'_{o'q'}(t,\tau')$ can be shown as

$$\rho_{oq,o'q'}(\tau,\chi)=\frac{1}{L}\sum_{l=1}^{\mathrm{L}}\rho_{l,oq;l,o'q'}(\tau,\chi). \tag{3.13}$$

Note that (3.11) and (3.13) are the generic expressions which apply to the STF CF and the subsequently two-variable or one-variable CFs (e.g., ST CF, frequency CF, etc.) differ only in values of $A_{l,i,r}$, $B_{l,i,r}$, and $C_{l,i}$. The corresponding expressions of these three parameters for the two-variable or one-variable CFs can be easily obtained by setting relevant terms (τ, δ_T and δ_T, and χ) to zero.

3.3.2 Space-Time-Frequency Correlation Function for Narrowband MIMO Channels

A special case of the proposed model described by (3.1) is given when L=1 and Λ_l=1. Consequently, we have $h_{oq}(t,\tau')$=$h_{oq}(t)\,\delta(\tau')$, which is the complex fading envelope of the narrowband one-ring channel model. To make this evident, we express the complex fading envelop $h_{oq}(t)$ similarly to (3.5) by removing the subscripts $(\cdot)_l$, $(\cdot)_i$, and $(\cdot)_r$, i.e.,

$$h_{oq}(t)=\lim_{N\to\infty}\frac{1}{\sqrt{N}}\sum_{n=1}^{N}\exp\left\{j\left[\psi_n-2\pi f_c\tau_{oq,n}+2\pi f_D t\cos\left(\phi_n^R-\gamma\right)\right]\right\} \tag{3.14}$$

with $\tau_{oq,n}$=$(\varepsilon_{on}+\varepsilon_{nq})/c$, where ε_{on} and ε_{nq} can be expressed as the function of ϕ_n^R as

$$\varepsilon_{on} \approx \xi_n-\delta_T[\cos(\beta_T)+\Theta\sin(\beta_T)\sin(\phi_n^R)]/2 \tag{3.15a}$$

$$\varepsilon_{nq} \approx R-\delta_R\cos(\phi_n^R-\beta_R)/2 \tag{3.15b}$$

where $\xi_n\approx D+R\cos(\phi_n^R)$. In order to consistent with the proposed wideband model, the von Mises PDF (3.7) is employed to characterise the AoA ϕ_n^R of the narrowband model. In such a case, the angle spread $\Delta\mu_{l,i}$=π, which means the AoA range is over $[0,2\pi)$. As shown in Appendix B, the STF CF of the narrowband one-ring model can be obtained from (3.11) after some manipulation

$$\rho_{oq,o'q'}(\tau,\chi)=e^{jC}I_0\left[\left(A^2+B^2\right)^{1/2}\right]\Big/I_0(k) \tag{3.16}$$

where

$$A = a+j(\mathrm{X}U+y\cos\beta_R+x\cos\gamma) \tag{3.17a}$$

$$B = b+j(\mathrm{X}V+y\sin\beta_R+z\Theta\sin\beta_T+x\sin\gamma) \tag{3.17b}$$

$$C = z\cos\beta_T+\mathrm{X}T \tag{3.17c}$$

with $a=k\cos\mu$, $b=k\sin\mu$, $T=(\delta_T/2)\cos\beta_T+D+R$, $U=R+(\delta_R/2)\cos\beta_R$, and $V=(\delta_T/2)\Theta\sin\beta_T+(\delta_R/2)\sin\beta_R$. The parameters x, y, z, and X are the same as

defined in (3.11). It is worth stressing that (3.16) is the generic expressions which applies to the STF CF and the subsequently two-variable or one-variable CFs with the difference only in values of A, B, and C. The corresponding expressions of A, B, and C for the two-variable or one-variable CFs can be easily obtained from (3.17) by setting relevant terms to zero.

The derived generic STF CF (3.16) includes many existing CFs as special cases. For a SISO case, the time CF given in [24] is obtained by setting $\delta_T = \delta_R = 0$ and $\chi = 0$ in (3.16) with $k \neq 0$. If further setting $k = 0$ (isotropic scattering) in (3.16), the Clarke's time CF in [65] is obtained. For a SIMO case, the Lee's ST CF in [88] is obtained by substituting $\delta_T = 0$, $\chi = 0$, $\beta_R = 0$, and $k = 0$ into (3.16). For a MISO case, the ST CF in [23] is obtained by substituting $\delta_R = 0$, $\chi = 0$, and $k = 0$ into (3.16). If further substituting $f_D = 0$ into (3.16), the space CF given in [87] is obtained. For a MIMO case, the ST CF shown in [22] is obtained by setting $\chi = 0$ in (3.16) with $k \neq 0$.

3.4 MIMO Simulation Models

In this section, based on the proposed wideband MIMO channel mathematical reference model, we propose an efficient deterministic SoS simulation model for wideband MIMO channels. The proposed wideband simulation model can be further reduced to a narrowband one by removing the frequency-selectivity.

3.4.1 A Deterministic Simulation Model for Wideband MIMO Channels

The wideband deterministic simulation model is proposed also based on the TDL structure. The impulse response of the simulation model at the carrier frequency f_c for the T_o–R_q link are again composed of L discrete taps according to

$$\tilde{h}_{oq}(t, \tau') = \sum_{l=1}^{L} \tilde{h}_{l,oq}(t) \times \delta(\tau' - \tau'_l). \tag{3.18}$$

In (3.18), the complex fading envelope $\tilde{h}_{l,oq}(t)$ is modeled by utilising only a finite number of scatterers N and keeping all the model parameters fixed as

$$\tilde{h}_{l,oq}(t)=\frac{1}{\sqrt{N}}\sum_{i=0}^{\Lambda_l-1}\sum_{r=1}^{R_c}\sum_{n=1}^{N}\exp\left\{j\left[\tilde{\psi}_{l,i,n}-2\pi f_c\tau_{l,i,oq,n}+2\pi f_D t\cos\left(\tilde{\phi}^R_{l,i,r,n}-\gamma\right)\right]\right\} \tag{3.19}$$

where the phases $\tilde{\psi}_{l,i,n}$ are simply the outcomes of a random generator uniformly distributed over $[0,2\pi)$, the discrete AoAs $\tilde{\phi}^R_{l,i,r,n}$ will be kept constant during simulation, and the other symbol definitions are the same as those in (3.5). Therefore, we can analyse the properties of the deterministic channel simulator by time averages instead of statistical averages. The STF CF is defined as

$$\tilde{\rho}_{l,oq;l,o'q'}(\tau,\chi):=\left\langle\tilde{h}_{l,oq}(t)\,\tilde{h}'^{*}_{l,o'q'}(t-\tau)\right\rangle \tag{3.20}$$

where $\langle\cdot\rangle$ denotes the time average operator. Substituting (3.19) into (3.20), we can get the closed-form STF CF as

$$\tilde{\rho}_{l,oq;l,o'q'}(\tau,\chi)=\frac{1}{N}\sum_{i=0}^{\Lambda_l-1}\sum_{r=1}^{R_c}\sum_{n=1}^{N}e^{j(C_{l,i}+P_{l,i}\cos\tilde{\phi}^R_{l,i,r,n}+J_{l,i}\sin\tilde{\phi}^R_{l,i,r,n})} \tag{3.21}$$

with

$$P_{l,i} = \mathrm{X}U_{l,i}+y\cos\beta_R+x\cos\gamma \tag{3.22a}$$

$$J_{l,i} = \mathrm{X}V_{l,i}+y\sin\beta_R+z\Delta\sin\beta_T+x\sin\gamma \tag{3.22b}$$

where $C_{l,i}$, x, y, z, X, $U_{l,i}$, and $V_{l,i}$ are the same as defined in (3.11). By analogy to (3.13), we can further get the STF CF between $\tilde{h}_{oq}(t,\tau')$ and $\tilde{h}'_{o'q'}(t,\tau')$ as

$$\tilde{\rho}_{oq,o'q'}(\tau,\chi)=\frac{1}{L}\sum_{l=1}^{L}\tilde{\rho}_{l,oq;l,o'q'}(\tau,\chi). \tag{3.23}$$

Similar to (3.11) and (3.13), (3.21) and (3.23) are the generic expressions which apply to all the CFs of the deterministic simulation model with different $C_{l,i}$, $P_{l,i}$, and $J_{l,i}$. Comparing the expressions of $A_{l,i,r}$ and $B_{l,i,r}$ with $P_{l,i}$ and $J_{l,i}$, respectively, we have $A_{l,i,r}=a_{l,i,r}+jP_{l,i}$ and $B_{l,i,r}=b_{l,i,r}+jJ_{l,i}$. From (3.21) and (3.23), it is obvious that only

$\{\tilde{\phi}^R_{l,i,r,n}\}_{n=1}^N$ needs to be determined for this deterministic simulation model.

As addressed in Chapter 2, the MEA and MEDS have been widely used to compute the important parameters of deterministic simulation models for isotropic scattering environments. However, these two methods fail to reproduce the desired statistical properties of the mathematical reference model under the condition of non-isotropic scattering [80, 81]. Therefore, the optimisation method (i.e., L_p-norm method) [13] is utilised here to calculate the model parameters $\{\tilde{\phi}^R_{l,i,r,n}\}_{n=1}^N$ of the deterministic simulation model based on corresponding properties of the mathematical reference model. The time CF $\rho_{l,oq;l,oq}(\tau)$, frequency CF $\rho_{l,oq;l,oq}(\chi)$, and space CF $\rho_{l,oq;l,o'q'}$ are identified as key properties. Then the optimisation method requires the numerical minimization of the following three L_p-norms

$$E^{(p)}_{1,l} := \left\{ \int_0^{\tau_{\max}} |\rho_{l,oq;l,oq}(\tau) - \tilde{\rho}_{l,oq;l,oq}(\tau)|^p \, d\tau / \tau_{\max} \right\}^{1/p} \tag{3.24}$$

$$E^{(p)}_{2,l} := \left\{ \int_0^{\chi_{\max}} |\rho_{l,oq;l,oq}(\chi) - \tilde{\rho}_{l,oq;l,oq}(\chi)|^p \, d\chi / \chi_{\max} \right\}^{1/p} \tag{3.25}$$

$$E^{(p)}_{3,l} := \left\{ \int_0^{\delta_T^{\max}} \int_0^{\delta_R^{\max}} |\rho_{l,oq;l,o'q'} - \tilde{\rho}_{l,oq;l,o'q'}|^p \, d\delta_T d\delta_R / (\delta_T^{\max} \delta_R^{\max}) \right\}^{1/p} \tag{3.26}$$

where $p = 1, 2, ...$ Note that τ_{max}, χ_{max}, δ_T^{max}, and δ_R^{max} define the upper limits of the ranges over which the approximations $\tilde{\rho}_{l,oq;l,oq}(\tau) \approx \rho_{l,oq;l,oq}(\tau)$, $\tilde{\rho}_{l,oq;l,oq}(\chi) \approx \rho_{l,oq;l,oq}(\chi)$, and $\tilde{\rho}_{l,oq;l,o'q'} \approx \rho_{l,oq;l,o'q'}$ are of interest. For $\tilde{\rho}_{l,oq;l,oq}(\chi)$ and $\tilde{\rho}_{l,oq;l,o'q'}$, if we replace $\tilde{\phi}^R_{l,i,r,n}$ by $\tilde{\phi}'^R_{l,i,r,n}$ and $\tilde{\phi}''^R_{l,i,r,n}$, respectively, the three error norms $E^{(p)}_{1,l}$, $E^{(p)}_{2,l}$, and $E^{(p)}_{3,l}$ can be minimized independently.

3.4.2 A Deterministic Simulation Model for Narrowband MIMO Channels

Analogous to Section 3.3.2, if we impose $L=1$ and $\Lambda_l=1$ on the wideband simulation model in (3.18), it reduces to a narrowband MIMO channel simulator. It follows that $\tilde{h}_{oq}(t, \tau') = \tilde{h}_{oq}(t)\,\delta(\tau')$ holds. The complex fading envelope $\tilde{h}_{oq}(t)$ of the deterministic

simulation model is then given by

$$\tilde{h}_{oq}(t) = \frac{1}{\sqrt{N}} \sum_{n=1}^{N} \exp\left\{ j \left[\tilde{\psi}_n - 2\pi f_c \tau_n + 2\pi f_D t \cos\left(\tilde{\phi}_n^R - \gamma \right) \right] \right\} \tag{3.27}$$

where the phases $\tilde{\psi}_n$ are simply the outcomes of a random generator uniformly distributed over $[0, 2\pi)$, the discrete AoAs $\tilde{\phi}_n^R$ will be kept constant during simulation, and the other symbol definitions are the same as those in (3.14). The correlation properties of this narrowband simulation model can be obtained from (3.21) by simply neglecting the subscripts $(\cdot)_l$, $(\cdot)_i$, and $(\cdot)_r$ in all the affected symbols. Thus

$$\tilde{\rho}_{oq;o'q'}(\tau, \chi) = \frac{1}{N} \sum_{n=1}^{N} e^{j(C + P\cos\tilde{\phi}_n^R + J\sin\tilde{\phi}_n^R)} \tag{3.28}$$

with

$$P = \mathrm{X}U + y\cos\beta_R + x\cos\gamma \tag{3.29a}$$

$$J = \mathrm{X}V + y\sin\beta_R + z\Delta\sin\beta_T + x\sin\gamma \tag{3.29b}$$

where other parameters are the same as defined in (3.16). Similar to the wideband simulation model, we have $A = a + jP$ and $B = b + jJ$. From (3.28), it is clear that only $\{\tilde{\phi}_n^R\}_{n=1}^N$ needs to be determined for this deterministic simulation model. The model parameters $\{\tilde{\phi}_n^R\}_{n=1}^N$ can be calculated by using the same optimisation method as the wideband simulation model. Therefore, by removing the subscript $(\cdot)_l$ in (3.24)–(3.26), the model parameters can be obtained as follows

$$E_1^{(p)} := \left\{ \int_0^{\tau_{\max}} |\rho_{oq;oq}(\tau) - \tilde{\rho}_{oq;oq}(\tau)|^p \, d\tau / \tau_{\max} \right\}^{1/p} \tag{3.30}$$

$$E_2^{(p)} := \left\{ \int_0^{\chi_{\max}} |\rho_{oq;oq}(\chi) - \tilde{\rho}_{oq;oq}(\chi)|^p \, d\chi / \chi_{\max} \right\}^{1/p} \tag{3.31}$$

$$E_3^{(p)} := \left\{ \int_0^{\delta_T^{\max}} \int_0^{\delta_R^{\max}} |\rho_{oq;o'q'} - \tilde{\rho}_{oq;o'q'}|^p \, d\delta_T d\delta_R / (\delta_T^{\max} \delta_R^{\max}) \right\}^{1/p}. \tag{3.32}$$

Similarly, for $\tilde{\rho}_{oq;oq}(\chi)$ and $\tilde{\rho}_{oq;o'q'}$, if we replace $\tilde{\phi}_n^R$ by $\tilde{\phi}_n'^R$ and $\tilde{\phi}_n''^R$, respectively, the three error norms $E_1^{(p)}$, $E_2^{(p)}$, and $E_3^{(p)}$ can be minimized independently.

3.5 Numerical Results and Analysis

In this section, based on the derived STF CFs for wideband and narrowband MIMO channels in Section 3.3, the two-variable or one-variable CFs are numerically analysed in detail. In addition, verification of the proposed wideband and narrowband deterministic SoS simulation models is carried out by comparing the correlation properties of the simulation models with those of the corresponding mathematical reference models. All the results presented in this section are obtained using the following basic parameters: f_c=5 GHz, f_D=463 Hz, D=2000 m, β_T=$\pi/6$, β_R=$\pi/3$, and γ=$7\pi/12$.

3.5.1 Correlation Properties of Wideband MIMO Channel Models

Without loss of any generality, we constrain our investigation on the correlation properties of the second tap ($l = 2$) with Λ_2=4 and $\{R_{2,i}\}_{i=0}^{3}$=$\{50, 100, 400, 750\}$ m based on (3.11). The discrete COST 207 TU channel model with $\{\tau_l'\}_{l=0}^{5}$=$\{0, 0.2, 0.5, 1.6, 2.3, 5\}$ μs will be applied. For simplicity, we assume that $k_{l,i,r}$=k for all effective clusters in the tap.

FIGURES 3.2 and 3.3 show the resulting frequency CF and space-frequency (SF) CF with $\delta_T = 0$, respectively. As a good trade off between the complexity and performance of the wideband simulation model, the number of effective scatterers $N = 45$ and the parameter of L_p-norm $p = 2$ are used in both figures. Moreover, the parameter of L_p-norm $\chi_{\max} = 10$ MHz is used in FIGURE 3.2, while the parameter of L_p-norm $\delta_R^{\max} = 3\lambda$ is applied in FIGURE 3.3. From FIGURE 3.2, it is clear that the trend of frequency CFs decreases with the increase of the frequency separation χ. FIGURE 3.2 also illustrates that the frequency correlations vary according to the environment parameter k that controls the angle spread of the AoA. It can be observed that the frequency correlations increase with the increase of k (i.e., with the decrease of angle spread of AoA).

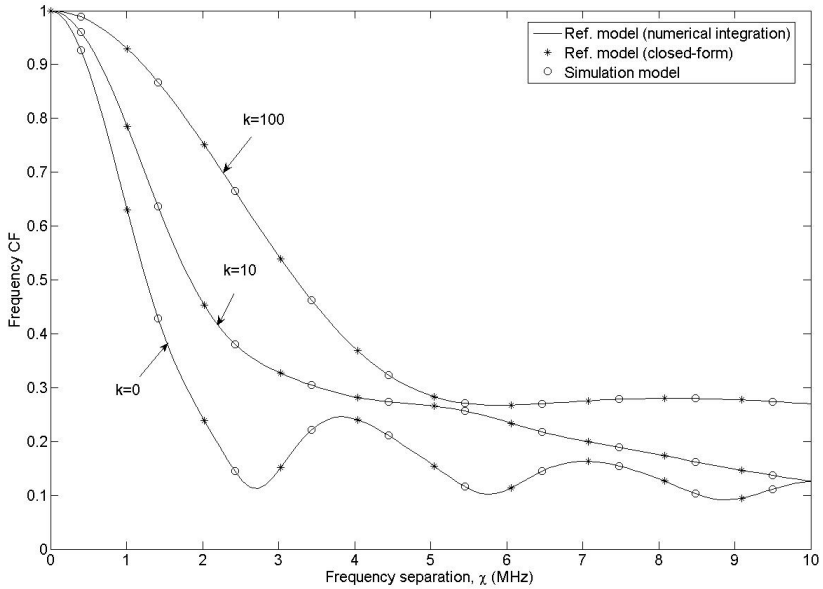

FIGURE 3.2: The frequency CFs $|\rho_{l,oq;l,oq}(\chi)|$ (mathematical reference model) and $|\tilde{\rho}_{l,oq;l,oq}(\chi)|$ (simulation model, $N = 45$) for different values of the parameter k.

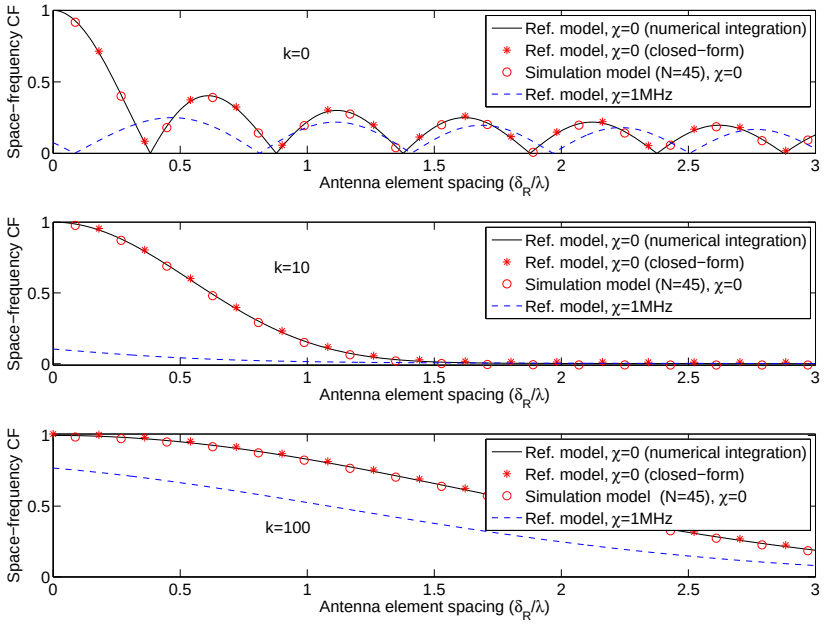

FIGURE 3.3: The SF CFs $\left|\rho_{l,oq;l,o'q'}\right|$ (mathematical reference model) and $\left|\tilde{\rho}_{l,oq;l,o'q'}\right|$ (simulation model, $N = 45$) for different values of the parameter k.

FIGURE 3.3 shows that the trend of SF CFs decreases with the increase of the space separation δ_R. FIGURE 3.3 also depicts the impact of the environment parameter k on the SF correlations. It is obvious that the SF correlations increase with the increase of k. From FIGURE 3.3, we can also observe the impact of frequency separation on spatial correlations. It is clear that the frequency separation decreases the spatial correlation. Therefore, we can conclude that in such a case, the resulting correlation is jointly contributed to by the actual spatial correlation (i.e., due to the spatial distance/geometry of arrays only) and inherent frequency correlation. Note that this resulting correlation is important for the appropriate design of STF coded MIMO-OFDM systems [85] and is also useful for the sensible utilisation of the SF diversity [86].

In addition, we depict in both FIGURES 3.2 and 3.3 the CFs of the mathematical reference model with both the closed-form expression and the numerical integration method, and the simulation model. Clearly, all these results match very well, demonstrating the validity of our derivation and excellent performance of our simulation model.

3.5.2 Correlation Properties of Narrowband MIMO Channel Models

In this subsection, we will investigate the correlation properties for narrowband MIMO channels based on (3.16) and evaluate the performance of the proposed narrowband simulation model. All the results presented in this subsection are obtained by using $k = 3$ and $\mu = \pi$.

FIGURES 3.4 (a) and (b) illustrate the SF CFs against the frequency separation and space separation at the BS and MS, respectively. Comparing them, we find that the impact of the normalised antenna spacing at the MS is greater than the one at the BS. This is because that the angular spread Θ at the BS is generally small for macro-cell scenarios. FIGURES 3.4 (a) and (b) also show that the trend of relevant CFs decreases with the increase of the frequency separation χ and space separation δ_T and δ_R.

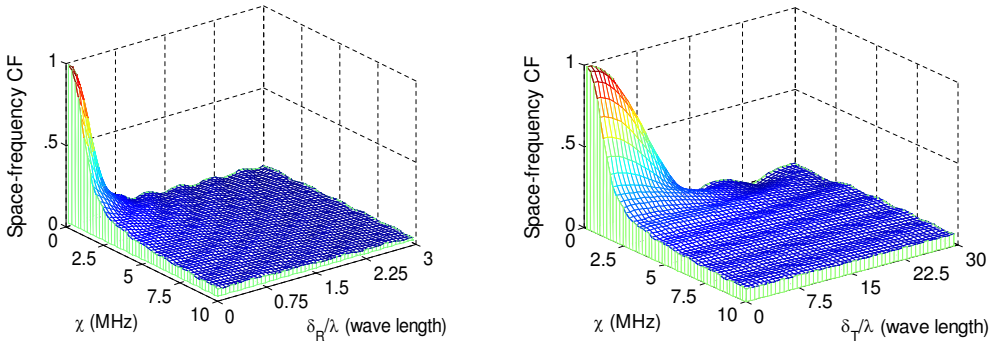

FIGURE 3.4: (a) The SF CF $\left|\rho_{oq;o'q'}(\chi)\right|$ versus the frequency separation χ and the normalised antenna spacing at the MS δ_R with $\delta_T = 0$; (b) the SF CF $\left|\rho_{oq;o'q'}(\chi)\right|$ versus the frequency separation χ and the normalised antenna spacing at the BS δ_T with $\delta_R = 0$.

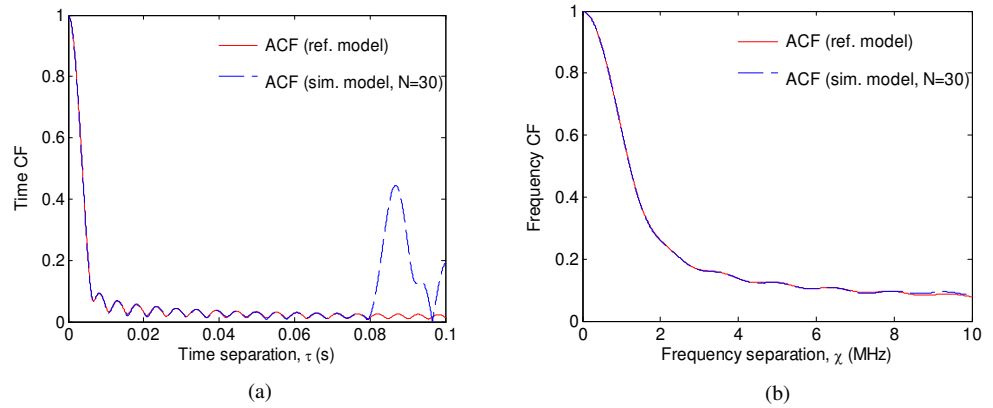

FIGURE 3.5: (a) The time CF $|\rho_{oq;oq}(\tau)|$ of the mathematical reference model and the time CF $|\tilde{\rho}_{oq;oq}(\tau)|$ of the corresponding simulation model with $N = 30$; (b) the frequency CF $|\rho_{oq;oq}(\chi)|$ of the mathematical reference model and the time CF $|\tilde{\rho}_{oq;oq}(\chi)|$ of the corresponding simulation model with $N = 30$.

A plot of the time CF of the mathematical reference model is shown in FIGURE 3.5 (a). This figure also depicts the resulting time CF of the simulation model designed with the L_p-norm using $p = 2$ and $\tau_{\max} = 0.08$ s, and the number of effective scatterers $N = 30$. FIGURE 3.5 (b) illustrates the frequency CF of the mathematical reference model and the one of the simulation model, when applying the L_p-norm with $p = 2$ and $\chi_{\max} = 8$ MHz, and the number of effective scatterers $N = 30$. FIGURES 3.6 (a) and (b) depict the space CF of the mathematical reference model and the one of

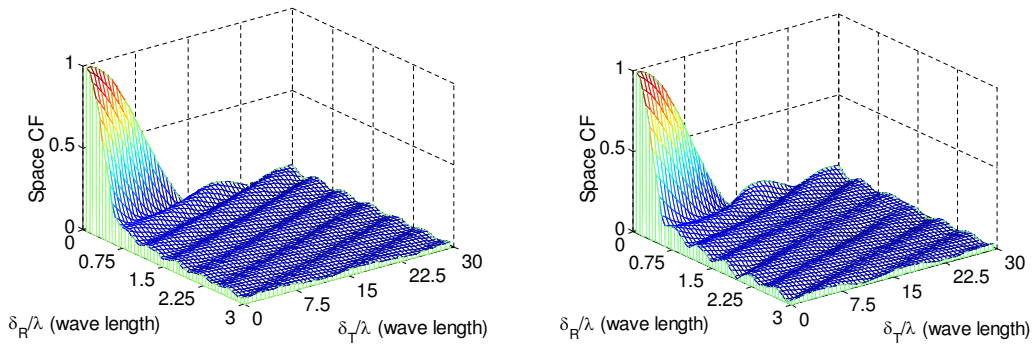

FIGURE 3.6: (a) The space CF $\left|\rho_{oq;o'q'}\right|$ of the mathematical reference model and (b) the space CF $\left|\tilde{\rho}_{oq;o'q'}\right|$ of the corresponding simulation model with $N = 30$.

the simulation model with $N = 30$, respectively. The discrete AoAs $\tilde{\phi}_n^{''R}$ have been obtained by using the L_p-norm with $p = 2$, $\delta_T^{\max} = 30\lambda$, and $\delta_R^{\max} = 3\lambda$. FIGURES 3.5 and 3.6 clearly demonstrate that the proposed deterministic simulation model can fit the underlying mathematical reference model very well in terms of time, frequency, and space correlation properties.

3.6 Summary

In this chapter, we have extended the narrowband one-ring MIMO model to a new wideband multi-ring based MIMO RS-GBSM. According to the TDL structure of our model, the closed-formed expression of the STF CF for each tap has been derived. We have demonstrated that the traditional narrowband one-ring model is actually a special case of the proposed wideband model. Therefore, the derived generic STF CF for wideband MIMO channels can be reduced to the STF CF with a compact closed-from expression for narrowband MIMO channels by removing the frequency-selectivity. From the proposed wideband multi-ring based MIMO mathematical reference model and the traditional narrowband one-ring MIMO mathematical reference model, corresponding wideband and narrowband deterministic SoS simulation models have been proposed. Numerical results have revealed the impact of the environment parameter k on frequency correlations and the inherent frequency correlations within

spatial correlations. Finally, the excellent agreement of correlation properties between the mathematical reference models and simulation models has validated the utility of the proposed deterministic simulation models. The proposed multi-ring based MIMO mathematical reference model and deterministic simulation models are very useful for the theoretical analysis and practical simulation, respectively, of frequency-correlated MIMO channels, such as frequency-hopping MIMO and MIMO-OFDM channels.

Chapter 4

Novel Simulation Models for Non-Isotropic Scattering Narrowband SISO Mobile-to-Mobile Rayleigh Fading Channels

4.1 Introduction

The previous chapter concentrated on the investigation of MIMO channel modelling and simulation for cellular channels. From this chapter, we turn our attention to M2M channels. As mentioned in Chapter 2, most available simulation models [3, 36, 39, 40] for narrowband SISO M2M channels limit their applications to isotropic scattering environments. The simulation models for M2M Rayleigh fading channels under a more realistic scenario of non-isotropic scattering are scarce in the current literature. So far, only one stochastic SoS simulation model [82] has been proposed for the simulation of non-isotropic scattering M2M Rayleigh fading channels. However, this model only considered the symmetrical property of the distributions of the AoA and AoD and was designed based on the acceptance rejection algorithm (ARA). This leads to the

ARA model having a notable difficulty in reproducing the desired statistical properties of the mathematical reference model and a comparatively high computational complexity. Moreover, as addressed in Chapter 2, no deterministic simulation models for non-isotropic scattering M2M Rayleigh fading channels are available in the current literature.

To fill the above gap, in this chapter, taking the traditional two-ring M2M RS-GBSM [36] as a mathematical reference model, we first propose a new M2M deterministic SoS based simulation model. By allowing at least one parameter (frequencies and/or gains) to be a random variable, our deterministic model can be further modified to be a stochastic model. It is worth noting that the proposed simulation models incorporate the PDFs of the AoA and AoD, and thus can approximate the desired statistical properties of the mathematical reference model for any non-isotropic scattering M2M Rayleigh fading channel. Moreover, compared to the ARA stochastic model in [82], our stochastic model presents better approximation to the desired properties of the mathematical reference model with an even smaller number of harmonic functions.

The chapter is structured as follows. Section 4.2 gives a brief description of the two-ring mathematical reference model for non-isotropic scattering M2M Rayleigh fading channels. In Section 4.3, we propose two new SoS simulation models (deterministic and stochastic models). The performance evaluation of our models is presented in Section 4.4. Finally, concluding remarks are drawn in Section 4.5.

4.2 A Two-Ring SISO Mobile-to-Mobile Mathematical Reference Model

FIGURE 4.1 shows the geometry of a two-ring SISO M2M RS-GBSM [36] that has two rings of effective scatterers, one around the Tx and the other around the Rx. Based on this two-ring model and considering the direction of movement of the Tx and Rx, we can express the complex fading envelope of our mathematical reference model, under a narrowband non-isotropic scattering M2M Rayleigh fading assumption, as

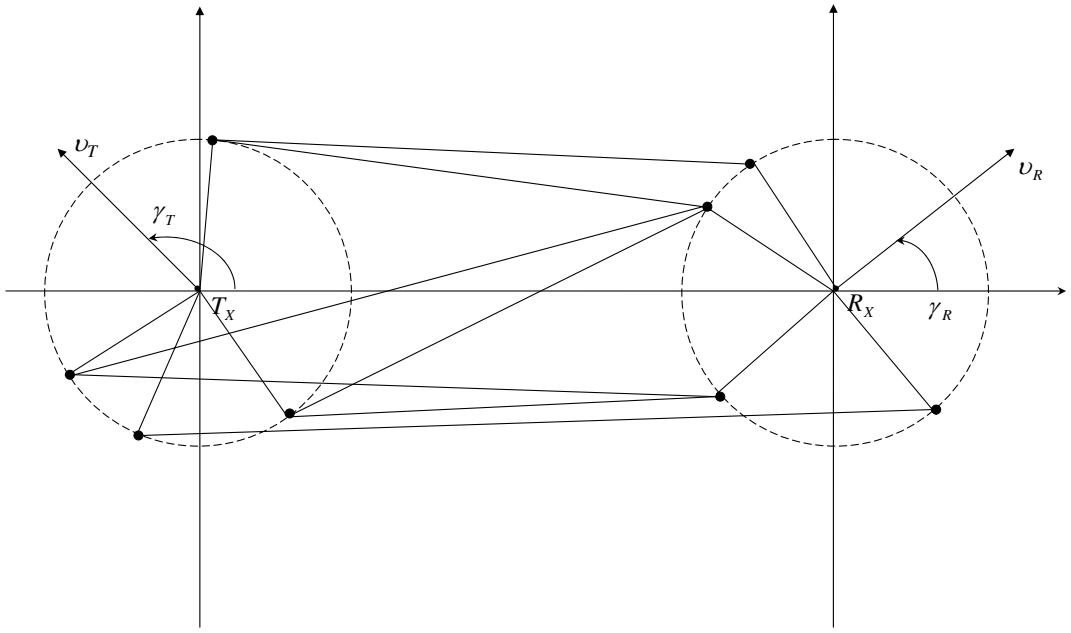

FIGURE 4.1: Geometrical two-ring model for SISO M2M channels.

$$\begin{aligned} h(t) &= h_i(t) + jh_q(t) \\ &= \lim_{N,M\to\infty} \frac{1}{\sqrt{NM}} \sum_{n,m=1}^{N,M} e^{j\psi_{nm}} e^{j\left[2\pi f_{T_{max}} t\cos(\phi_T^m-\gamma_T)+2\pi f_{R_{max}} t\cos(\phi_R^n-\gamma_R)\right]} \end{aligned} \quad (4.1)$$

where $h_i(t)$ and $h_q(t)$ are in-phase and quadrature components of the complex fading envelope $h(t)$, respectively, $j=\sqrt{-1}$, N and M are the number of harmonic function representing effective scatterers (propagation paths) located on the ring around the Rx and Tx, respectively, $f_{T_{max}}$ and $f_{R_{max}}$ are the maximum Doppler frequency due to the motion of the Tx and Rx, respectively. The Tx and Rx move in directions determined by the angles of motion γ_T and γ_R, respectively. The random AoA and AoD of the nth path are denoted by ϕ_R^n and ϕ_T^m, respectively, and ψ_{nm} is the random phase uniformly distributed on $[-\pi,\pi)$. It is assumed that ϕ_R^n, ϕ_T^m, and ψ_{nm} are mutually independent random variables.

Since the number N and M of effective scatterers in the mathematical reference model

$h(t)$ tends to infinity, the discrete expressions of the AoA $\phi_R^{(n)}$ and AoD $\phi_T^{(m)}$ can be replaced by the continuous expressions ϕ_R and ϕ_T, respectively. Note that since $h(t)$ describes a non-isotropic scattering M2M Rayleigh fading channel, the AoA ϕ_R and AoD ϕ_T exhibit nonuniform distributions. To characterise the AoA and AoD, we use the von Mises PDF given in (3.7) due to its advantage addressed in Chapter 3. Applying the von Mises PDF to the AoA ϕ_R and AoD ϕ_T, we obtain $f(\phi_R) \triangleq \exp[k_R \times \cos(\phi_R - \mu_R)]/[2\pi I_0(k_R)]$ and $f(\phi_T) \triangleq \exp[k_T \cos(\phi_T - \mu_T)]/[2\pi I_0(k_T)]$, respectively.

The autocorrelation function (ACF) of the mathematical reference model $h(t)$ can be expressed as

$$\rho_{hh}(\tau) = \mathbf{E}[h(t)\, h^*(t-\tau)] = \frac{1}{I_0(k_T) I_0(k_R)} I_0\Big[\left(A_T^2 + B_T^2\right)^{1/2}\Big]\, I_0\Big[\left(A_R^2 + B_R^2\right)^{1/2}\Big] \quad (4.2)$$

with

$$A_T = k_T \cos(\mu_T) + j2\pi\tau f_{T_{max}} \cos(\gamma_T) \quad (4.3a)$$

$$B_T = k_T \sin(\mu_T) + j2\pi\tau f_{T_{max}} \sin(\gamma_T) \quad (4.3b)$$

$$A_R = k_R \cos(\mu_R) + j2\pi\tau f_{R_{max}} \cos(\gamma_R) \quad (4.3c)$$

$$B_R = k_R \sin(\mu_R) + j2\pi\tau f_{R_{max}} \sin(\gamma_R) \quad (4.3d)$$

where τ is the time separation, $(\cdot)^*$ denotes the complex conjugate operation, and $\mathbf{E}[\cdot]$ is the statistical expectation operator.

4.3 New Simulation Models

In this section, based on the mathematical reference model introduced in Section 4.2, we propose the corresponding deterministic and stochastic SoS simulation models.

4.3.1 A New Deterministic Simulation Model

Based on the two-ring mathematical reference model, we can then design a new deterministic simulation model, which needs only one simulation trial to obtain the desired

statistical properties, as

$$\tilde{h}(t)= \tilde{h}_i(t)+ j\tilde{h}_q(t) \tag{4.4}$$

$$\tilde{h}_i(t)=\frac{1}{\sqrt{N_i M_i}}\sum_{n_i,m_i=1}^{N_i,M_i}\cos\Big[\tilde{\psi}_{n_i m_i}+2\pi f_{T_{max}} t\cos(\tilde{\phi}_T^{m_i}-\gamma_T)+2\pi f_{R_{max}} t\cos(\tilde{\phi}_R^{n_i}-\gamma_R)\Big] \tag{4.5}$$

$$\tilde{h}_q(t)=\frac{1}{\sqrt{N_q M_q}}\sum_{n_q,m_q=1}^{N_q,M_q}\sin\Big[\tilde{\psi}_{n_q m_q}+2\pi f_{T_{max}} t\cos(\tilde{\phi}_T^{m_q}-\gamma_T)+2\pi f_{R_{max}} t\cos(\tilde{\phi}_R^{n_q}-\gamma_R)\Big] \tag{4.6}$$

where $\tilde{h}_i(t)$ and $\tilde{h}_q(t)$ are in-phase and quadrature components of the complex fading envelope $\tilde{h}(t)$, respectively, $N_{i/q}$ is the number of effective scatterers located on the ring around the RX, $M_{i/q}$ is the number of effective scatterers located on the ring around the Tx, the AoA $\tilde{\phi}_R^{n_{i/q}}$ and the AoD $\tilde{\phi}_T^{m_{i/q}}$ are discrete realisations of the random variables ϕ_R and ϕ_T, respectively, the phases $\tilde{\psi}_{n_{i/q}m_{i/q}}$ are the single outcomes of the random phases ψ_{nm} in (4.1). It is assumed that $\tilde{\phi}_R^{n_{i/q}}$, $\tilde{\phi}_T^{m_{i/q}}$, and $\tilde{\psi}_{n_{i/q}m_{i/q}}$ are mutually independent. Note that the AoA $\tilde{\phi}_R^{(n_{i/q})}$ and the AoD $\tilde{\phi}_T^{(m_{i/q})}$ remain constant for different simulation trials due to the deterministic nature of the proposed simulation model.

From the above proposed deterministic simulation model, it is obvious that the key issue in designing a M2M deterministic simulation model is to find the sets of AoAs $\left\{\tilde{\phi}_R^{n_{i/q}}\right\}_{n_{i/q}=1}^{N_{i/q}}$ and AoDs $\left\{\tilde{\phi}_T^{m_{i/q}}\right\}_{m_{i/q}=1}^{M_{i/q}}$ that make the simulation model reproduce the desired statistical properties of the mathematical reference model as faithfully as possible with reasonable complexity, i.e., with a finite number of $N_{i/q}$ and $M_{i/q}$. Under the condition of non-isotropic scattering environments, the PDFs of the AoA ϕ_R and AoD ϕ_T should be used to design the sets of AoAs $\left\{\tilde{\phi}_R^{n_{i/q}}\right\}_{n_{i/q}=1}^{N_{i/q}}$ and AoDs $\left\{\tilde{\phi}_T^{m_{i/q}}\right\}_{m_{i/q}=1}^{M_{i/q}}$ that guarantee the uniqueness of the sine and cosine functions related to the AoA $\phi_R^{(n)}$ and AoD $\phi_T^{(n)}$ in the mathematical reference model (4.1). This means that the design of the sets of AoAs and AoDs of the simulation model $\tilde{h}(t)$ in (4.4) should meet the following two conditions: 1) $\cos(\tilde{\phi}_R^{n_{i/q}}-\gamma_R)\neq\cos(\tilde{\phi}_R^{n'_{i/q}}-\gamma_R)$, $n_{i/q}\neq n'_{i/q}$; and 2) $\cos(\tilde{\phi}_T^{m_{i/q}}-\gamma_T)\neq\cos(\tilde{\phi}_T^{m'_{i/q}}-\gamma_T)$, $m_{i/q}\neq m'_{i/q}$.

Considering the non-isotropic scattering M2M environments, we now design the sets of AoAs and AoDs of our deterministic simulation model. Via extensive investigation

of the PDFs of the AoA ϕ_R and AoD ϕ_T, we find that unlike isotropic scattering M2M environments [36], it is difficult to obtain the sets of AoAs and AoDs that meet the two conditions for all non-isotropic scattering M2M environments. Therefore, we divide the non-isotropic scattering M2M environment into the following three categories in terms of the mean AoA μ_R and mean AoD μ_T (i.e., the PDFs of the AoA and AoD), and the angles of motion γ_R and γ_T, and then design the sets of AoAs and AoDs separately for these three cases: 1) *Case I*: the main transmitted and received powers come from the same direction as or opposite direction to the movements of the Tx and Rx, respectively, i.e., $|\mu_T - \gamma_T| = |\mu_R - \gamma_R| = 0^\circ$ or π; 3) *Case II*: the main transmitted and received powers come from the directions that are perpendicular to those of the movements of the Tx and Rx, respectively, i.e., $|\mu_T - \gamma_T| = |\mu_R - \gamma_R| = 90^\circ$; and 3) *Case III*: different from *Cases I* and *II*.

For *Case I*, the in-phase component $h_i(t)$ and quadrature component $h_q(t)$ of the mathematical reference model $h(t)$ in (4.1) are correlated. Therefore, to meet this correlation, we set $N_i = N_q = N$ and $M_i = M_q = M$ and thereby the AoA $\tilde{\phi}_R^{n_{i/q}}$ and AoD $\tilde{\phi}_T^{m_{i/q}}$ can be replaced by the $\tilde{\phi}_R^n$ and $\tilde{\phi}_T^m$, respectively. Inspired by the modified MEA (MMEA) proposed in [93] for non-isotropic scattering F2M channels, we design the AoA and AOD of our model as

$$\frac{n - 1/4}{N} = \int_{\tilde{\phi}_R^{n-1}}^{\tilde{\phi}_R^n} f\left(\tilde{\phi}_R^n\right) d\tilde{\phi}_R^n, \qquad \tilde{\phi}_R^n \in [-\pi, \pi) \qquad n = 1, 2, ..., N \tag{4.7a}$$

$$\frac{m - 1/4}{M} = \int_{\tilde{\phi}_T^{m-1}}^{\tilde{\phi}_T^m} f\left(\tilde{\phi}_T^m\right) d\tilde{\phi}_T^m, \qquad \tilde{\phi}_T^m \in [-\pi, \pi) \qquad m = 1, 2, ..., M \tag{4.7b}$$

where $\tilde{\phi}_R^0 = -\pi$ and $\tilde{\phi}_T^0 = -\pi$, $f\left(\tilde{\phi}_R^n\right)$ and $f\left(\tilde{\phi}_T^m\right)$ denote the PDFs of the AoA $\tilde{\phi}_R^n$ and the AoD $\tilde{\phi}_T^m$, respectively. The cumulative distribution functions (CDFs) of the AoA $\tilde{\phi}_R$ and the AoD $\tilde{\phi}_T$ are defined as $F_R(x) = \int_{-\infty}^{x} f\left(\tilde{\phi}_R^n\right) d\tilde{\phi}_R^n$ and $F_T(x) = \int_{-\infty}^{x} f\left(\tilde{\phi}_T^m\right) d\tilde{\phi}_T^m$, respectively. If the inverse functions $F_R^{-1}(\cdot)$ of $F_R(\cdot)$ and $F_T^{-1}(\cdot)$ of $F_T(\cdot)$ exist, (4.7a) and (4.7b) become

$$\tilde{\phi}_R^n = F_R^{-1}\left(\frac{n - 1/4}{N}\right) \tag{4.8a}$$

$$\tilde{\phi}_T^m = F_T^{-1}\left(\frac{m - 1/4}{M}\right). \tag{4.8b}$$

Note that the value of 1/4 used in (4.8a) and (4.8b) guarantees that the designed sets of AoAs and AoDs can meet the aforementioned two conditions ($\tilde{\phi}_R^n \neq -\tilde{\phi}_R^{(n')} + 2\gamma_R$, $n \neq n'$ and $\tilde{\phi}_T^m \neq -\tilde{\phi}_T^{m'} + 2\gamma_T$, $m \neq m'$) for *Case I*. The proof of the above statement is omitted here since one can easily prove it by following the procedure provided in [93]. The performance of this design will be validated in Section 4.4.

Under the condition of *Case II*, the cross-correlation between the in-phase component $h_i(t)$ and quadrature component $h_q(t)$ of the complex fading envelope $h(t)$ in (4.1) is equal to zero. Therefore, by setting $N_i \neq N_q$ and $M_i \neq M_q$ in this case, we can directly use the expression of our simulation model itself to guarantee the aforementioned cross-correlation is equal to zero rather than through the design of the AoAs and AoDs. This makes for a more efficient use of the number of harmonic functions and thus results in better performance of the model. Following the similar parameter computation method of *Case I*, we design the AoA and AoD of our model as

$$\tilde{\phi}_R^{n_{i/q}} = F_R^{-1}\left(\frac{n_{i/q} - 1/2}{N_{i/q}}\right), \quad \tilde{\phi}_R^{n_{i/q}} \in [-\pi, \pi) \quad n_{i/q} = 1, 2, ..., N_{i/q} \tag{4.9a}$$

$$\tilde{\phi}_T^{m_{i/q}} = F_T^{-1}\left(\frac{m_{i/q} - 1/2}{M_{i/q}}\right), \quad \tilde{\phi}_T^{m_{i/q}} \in [-\pi, \pi) \quad m_{i/q} = 1, 2, ..., M_{i/q}. \tag{4.9b}$$

Note that the value of 1/2 is applied in (4.9a) and (4.9b) instead of the value of 1/4 in (4.8a) and (4.8b). The reason is that unlike *Case I*, for *Case II* it is difficult to design the sets of AoAs and AoDs that meet the two conditions. Although it is difficult to find one value that can guarantee the designed sets of AoAs and AoDs have the best approximation to the two conditions. Based on simulations and motivated by the modified MEDS in (37) and (38) in [36] for the simulation of isotropic scattering M2M channels, we found that with the value of 1/2, the proposed simulation model presents better performance than the one with other values, e.g., 1/4. The performance of this design will be validated in Section 4.4.

For *Case III*, since the in-phase and quadrature components of the mathematical reference model $h(t)$ in (4.1) are correlated (similarly to *Case I*) we set $N_i = N_q = N$ and $M_i = M_q = M$ as well and thus the AoA $\tilde{\phi}_R^{n_{i/q}}$ and AoD $\tilde{\phi}_T^{m_{i/q}}$ can be replaced by the $\tilde{\phi}_R^n$ and $\tilde{\phi}_T^m$, respectively. Following the similar parameter computation method of

Case I, we design the AoA and AoD of our model as

$$\tilde{\phi}_R^n = F_R^{-1}\left(\frac{n-1/2}{N}\right), \quad \tilde{\phi}_R^n \in [-\pi,\pi) \quad n=1,2,...,N \tag{4.10a}$$

$$\tilde{\phi}_T^m = F_T^{-1}\left(\frac{m-1/2}{M}\right), \quad \tilde{\phi}_T^m \in [-\pi,\pi) \quad m=1,2,...,M. \tag{4.10b}$$

Note that the value of 1/2 is used in (4.10a) and (4.10b) due to the same reason as *Case II*.

The correlation properties of the proposed deterministic simulation model must be analysed by using time average rather than statistical average. The time-average ACF of the proposed simulation model $\tilde{h}(t)$ is defined as

$$\tilde{\rho}_{\tilde{h}\tilde{h}}(\tau) = \left\langle \tilde{h}(t)\,\tilde{h}^*(t-\tau) \right\rangle \tag{4.11}$$

where $\langle\cdot\rangle$ denotes the time average operator. Substituting (4.4) into (4.11), we have

$$\tilde{\rho}_{\tilde{h}\tilde{h}}(\tau) = 2\tilde{\rho}_{\tilde{h}_i\tilde{h}_i}(\tau) - 2j\tilde{\rho}_{\tilde{h}_i\tilde{h}_q}(\tau) \tag{4.12}$$

where

$$\tilde{\rho}_{\tilde{h}_i\tilde{h}_i}(\tau) = \frac{1}{2N_iM_i}\sum_{n_i,m_i=1}^{N_i,M_i}\cos\Big[2\pi f_{T_{max}}\tau\cos(\tilde{\phi}_T^{m_i}-\gamma_T) + 2\pi f_{R_{max}}\tau\cos(\tilde{\phi}_R^{n_i}-\gamma_R)\Big] \tag{4.13a}$$

$$\tilde{\rho}_{\tilde{h}_i\tilde{h}_q}(\tau) = \begin{cases} -\dfrac{1}{2NM}\displaystyle\sum_{n,m=1}^{N,M}\sin\Big[2\pi f_{T_{max}}\tau\cos(\tilde{\phi}_T^{m}-\gamma_T) + 2\pi f_{R_{max}}\tau\cos(\tilde{\phi}_R^{n}-\gamma_R)\Big], \\ \qquad N_i=N_q=N \text{ and } M_i=M_q=M \ (\textit{Case I and III}) \\ 0, \qquad N_i\neq N_q \text{ and } M_i\neq M_q \ (\textit{Case II}). \end{cases} \tag{4.13b}$$

In Appendix C, we give a brief outline of the derivations of (4.13a) and (4.13b). From (4.13b), and based on the corresponding derivation in Appendix C, it is clear that by setting $N_i \neq N_q$ and $M_i \neq M_q$, the cross-correlation between the in-phase

component $\tilde{h}_i(t)$ and quadrature component $\tilde{h}_q(t)$ of the proposed simulation model $\tilde{h}(t)$ is equal to zero no matter how the sets of AoAs and AoDs are designed. When N (N_i) and M (M_i) tend to infinity, it is straightforward that the time-average ACF in (4.12) matches the ensemble average ACF in (4.2). This allows us to conclude that for $\{N(N_i), M(M_i)\} \rightarrow \infty$, our deterministic simulation model can represent the correlation properties of the mathematical reference model.

4.3.2 A New Stochastic Simulation Model

Our deterministic model can be further modified to a stochastic simulation model by allowing both the phases and frequencies to be random variables. Unlike the deterministic model, the properties of the stochastic model vary for each simulation trial, but will converge to the desired ones when averaged over a sufficient number of simulation trials. A hat is used to distinguish this model from the deterministic one, thus

$$\hat{h}(t) = \hat{h}_i(t) + j\hat{h}_q(t) \tag{4.14}$$

$$\hat{h}_i(t) = \frac{1}{\sqrt{N_i M_i}} \sum_{n_i,m_i=1}^{N_i,M_i} \cos\Big[\hat{\psi}_{n_i m_i} + 2\pi f_{T_{max}} t \cos(\hat{\phi}_T^{m_i} - \gamma_T) + 2\pi f_{R_{max}} t \cos(\hat{\phi}_R^{n_i} - \gamma_R)\Big] \tag{4.15}$$

$$\hat{h}_q(t) = \frac{1}{\sqrt{N_q M_q}} \sum_{n_q,m_q=1}^{N_q,M_q} \sin\Big[\hat{\psi}_{n_q m_q} + 2\pi f_{T_{max}} t \cos(\hat{\phi}_T^{m_q} - \gamma_T) + 2\pi f_{R_{max}} t \cos(\hat{\phi}_R^{n_q} - \gamma_R)\Big] \tag{4.16}$$

where $\hat{h}_i(t)$ and $\hat{h}_q(t)$ are in-phase and quadrature components of the complex fading envelope $\hat{h}(t)$, respectively, $\hat{\phi}_R^{n_{i/q}}$ and $\hat{\phi}_T^{m_{i/q}}$ denote the AoA and AoD of our stochastic simulation model, respectively, and the phases $\hat{\psi}_{n_{i/q}m_{i/q}}$ are random variables uniformly distributed on the interval $[-\pi, \pi)$. Parameters $\hat{\phi}_R^{n_{i/q}}$, $\hat{\phi}_T^{m_{i/q}}$, and $\hat{\psi}_{n_{i/q}m_{i/q}}$ are independent of each other. Note that unlike the AoA and AoD in a deterministic simulation model, the AoA $\hat{\phi}_R^{n_{i/q}}$ and AoD $\hat{\phi}_T^{m_{i/q}}$ are random variables and thus vary for different simulation trials. The fundamental issue for the design of the sets of AoAs $\left\{\hat{\phi}_R^{n_{i/q}}\right\}_{n_{i/q}=1}^{N_{i/q}}$ and AoDs $\left\{\hat{\phi}_T^{m_{i/q}}\right\}_{m_{i/q}=1}^{M_{i/q}}$ is how to incorporate a random term into the AoA and AoD. In this chapter, to deal with this fundamental issue, we apply the method proposed in [67] for the simulation of isotropic scattering F2M channels.

According to the comparative analysis in [78], we can conclude that the smaller (but sufficient) range on which the AoA $\hat{\phi}_R^{n_{i/q}}$ and AoD $\hat{\phi}_T^{m_{i/q}}$ are designed, the better performance the stochastic model that will be obtained. Based on the extensive investigation of the PDFs of the AoA ϕ_R and AoD ϕ_T, we find that unlike isotropic scattering M2M environments [36], the appropriate range on which the AoA and AoD are designed varies for different non-isotropic scattering M2M environments. Therefore, similarly to our deterministic model, we design the sets of AoAs and AoDs of our stochastic model separately for the following three cases: 1) *Case I*: the main transmitted and received powers come from the same direction as the movements of the Tx and Rx that is along x axis, i.e., $\mu_T{=}\gamma_T{=}\mu_R{=}\gamma_R{=}0^\circ$ or π; 2) *Case II*: the main transmitted and received powers come from the directions that are perpendicular to those of the movements of the Tx and Rx, respectively, i.e., $|\mu_T{-}\gamma_T|{=}|\mu_R{-}\gamma_R|{=}90^\circ$; and 3) *Case III*: different from *Cases I* and *II*.

For *Case I*, due to the same reason as the design of our deterministic model for *Case I* we have $N_i{=}N_q{=}N$ and $M_i{=}M_q{=}M$ and thus the AoA $\hat{\phi}_R^{n_{i/q}}$ and AoD $\hat{\phi}_T^{m_{i/q}}$ can be replaced by the $\hat{\phi}_R^n$ and $\hat{\phi}_T^m$, respectively. In this case, we found that the PDFs of the AoA and AoD are symmetric with respect to the origin. Therefore, the appropriate ranges for the design of both AoA and AoD are from 0 to π because the rest of the range is redundant (i.e., the range $[-\pi, 0)$ provides us with the same infomation as $[0, \pi)$). Inspired by the method in [67] for isotropic scattering F2M channels, we design the AoA and AoD of our model as

$$\hat{\phi}_R^n = F_R^{-1}\left(\frac{n-1/2+\theta_R}{N}\right), \quad \hat{\phi}_R^n \in [0,\pi) \quad n=1,2,...,N \tag{4.17a}$$

$$\hat{\phi}_T^m = F_T^{-1}\left(\frac{m-1/2+\theta_T}{M}\right), \quad \hat{\phi}_T^m \in [0,\pi) \quad m=1,2,...,M \tag{4.17b}$$

where θ_R and θ_T are random variables uniformly distributed on the interval $[-1/2, 1/2)$ and are independent to each other. It is worth stressing that the interval $[-1/2, 1/2)$ and the constant value of $1/2$ are chosen to guarantee that the design of the AoA and AoD is based on the desired range (here is $[0, \pi)$). This indicates that any interval and the corresponding constant value can be chosen only if they can fulfill the aforementioned guarantee (e.g., the interval is $[0, 1)$ and constant value is 1). Note

that the introduction of the random terms θ_R and θ_T in the AoA $\hat{\phi}_R^n$ and AoD $\hat{\phi}_T^m$, respectively, leads to the AoA and AoD being random variables and thus varying for different simulation trials.

For *Case II*, analogous to our deterministic model for *Case II*, we impose $N_i \neq N_q$ and $M_i \neq M_q$ in our stochastic model to guarantee the cross-correlation between the in-phase component $\hat{h}_i(t)$ and quadrature component $\hat{h}_q(t)$ of the proposed stochastic model $\hat{h}(t)$ for one simulation trial is equal to zero. In this case, since the PDFs of the AoA and AoD are asymmetric with respect to the origin, the full range (i.e., from $-\pi$ to π) is needed for the design of the AoA and AoD. Therefore, we can express the AoA and AoD as

$$\hat{\phi}_R^{n_{i/q}} = F_R^{-1}\left(\frac{n_{i/q}-1/2+\theta_R}{N_{i/q}}\right), \quad \hat{\phi}_R^{n_{i/q}} \in [-\pi,\pi) \quad n_{i/q}=1,2,...,N_{i/q} \tag{4.18a}$$

$$\hat{\phi}_T^{m_{i/q}} = F_T^{-1}\left(\frac{m_{i/q}-1/2+\theta_T}{M_{i/q}}\right), \quad \hat{\phi}_T^{m_{i/q}} \in [-\pi,\pi) \quad m_{i/q}=1,2,...,M_{i/q}. \tag{4.18b}$$

For *Case III*, due to the same reason as *Case I* we have $N_i=N_q=N$ and $M_i=M_q=M$ and thus the AoA $\hat{\phi}_R^{n_{i/q}}$ and AoD $\hat{\phi}_T^{m_{i/q}}$ can be replaced by the $\hat{\phi}_R^n$ and $\hat{\phi}_T^m$, respectively. In this case, analogous to *Case II*, we know that the full range (i.e., from $-\pi$ to π) is necessary for the design of the AoA and AoD. Therefore, the AoA and AoD can be designed as

$$\hat{\phi}_R^n = F_R^{-1}\left(\frac{n-1/2+\theta_R}{N}\right), \qquad \hat{\phi}_R^n \in [-\pi,\pi) \qquad n=1,2,...,N \tag{4.19a}$$

$$\hat{\phi}_T^m = F_T^{-1}\left(\frac{m-1/2+\theta_T}{M}\right), \qquad \hat{\phi}_T^m \in [-\pi,\pi) \qquad m=1,2,...,M. \tag{4.19b}$$

Unlike our deterministic simulation model, the time ACF of our stochastic simulation model should be computed according to $\hat{\rho}_{\hat{h}\hat{h}}(\tau)=\mathbf{E}\left[\hat{h}\,(t)\,\hat{h}^*(t-\tau)\right]$. It can be shown that our stochastic model exhibits correlation properties of the mathematical reference model irrespective of the values of $N_{i/q}$ and $M_{i/q}$, i.e., for any $N_{i/q}$ and $M_{i/q}$. Appendix D outlines the derivation of the ACF $\hat{\rho}_{\hat{h}\hat{h}}\,(\tau)$ for the model $\hat{h}(t)$.

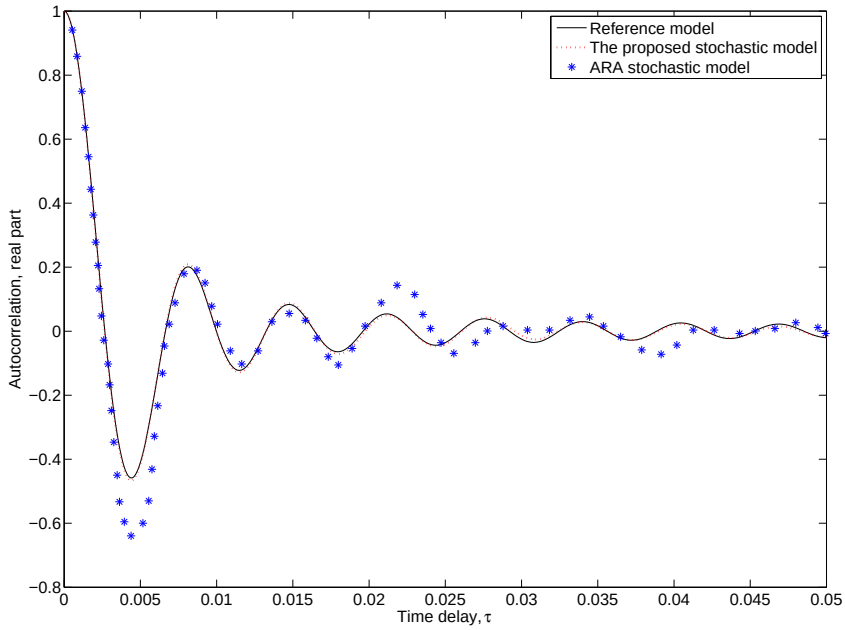

FIGURE 4.2: Comparison between the proposed stochastic model and the ARA stochastic model.

It is worth noting that the proposed stochastic model shows better performance and has lower complexity than the ARA model [82]. Since in [82] the authors did not give the detailed explanation on how to generate the AoAs and AoDs for their model by using the ARA, it is impossible to reproduce this model. Therefore, to validate the above statement, in FIGURE 4.2 we compare the ACF of the real part of the ARA model obtained from FIGURE 5 in [82] with the one of our model. For a fair comparison, the same parameters as those used in FIGURE 5 in [82] are used, namely $f_{T_{max}}=100$ Hz, $f_{R_{max}}=50$ Hz, $\mu_T=\pi/4$, $\mu_R=-\pi/4$, $k_T=k_R=3$, $\gamma_T=\gamma_R=0°$, and the number of simulation trials $N_{stat}=10$. Note that the number of harmonic functions used in the ARA model is $N_{ARA}=144$, while in our model is $N_i=M_i=10$. From FIGURE 4.2, it is obvious that our model outperforms the ARA model with an even smaller number of harmonic functions, i.e., $N_i \times M_i=100<N_{ARA}$.

4.4 Numerical Results and Analysis

In this section, we first validate the newly proposed deterministic model by using the squared error between the correlation properties of the simulation model and those of the mathematical reference model. Then the validation of the proposed stochastic simulation model is performed by utilising the difference in the time average properties of a single simulation trial for the stochastic model from the desired ensemble average properties. Furthermore, the performance evaluation of the proposed models is carried out by comparing the correlation properties of the proposed simulation models with those of the mathematical reference model. Unless otherwise specified, all the results presented here are obtained using $f_{T_{max}} = f_{R_{max}} = 100$ Hz, $N_i = M_i = N_q = M_q = 20$ for *Cases I*, *III* and $N_i = M_i = 20$, $N_q = M_q = 21$ for *Case II* of the deterministic model, $N_i = M_i = N_q = M_q = 10$ for *Cases I*, *III* and $N_i = M_i = 10$, $N_q = M_q = 11$ for *Case II* of the stochastic model, and the normalised sampling period $f_{T_{max}} T_s = 0.005$ (T_s is the sampling period).

To validate our deterministic model, in FIGURE 4.3 we compare the difference in the ACF $\tilde{\rho}_{\tilde{h}\tilde{h}}(\tau)$ from the desired $\rho_{hh}(\tau)$ using the squared error $|\tilde{\rho}_{\tilde{h}\tilde{h}}(\tau) - \rho_{hh}(\tau)|^2$ for different non-isotropic M2M scenarios. Similarly, to validate our stochastic model, FIGURE 4.4 compares the difference in the time averaged ACF of a single simulation trial $\breve{\rho}_{hh}(\tau)$ from the desired ACF $\rho_{hh}(\tau)$ as $\mathbf{E}\left[|\breve{\rho}_{hh}(\tau) - \rho_{hh}(\tau)|^2\right]$ for different non-isotropic M2M scenarios. As pointed out in [78], this provides a measure of the utility of the stochastic model in simulating the desired channel waveform using a finite harmonic functions $N_{i/q}$ and $M_{i/q}$. The results in FIGURE 4.4 are obtained by averaging over 10^4 simulation trials for each value of time delay τ. Note that for the sake of the readability of figures, the difference of our models for *Case II* is only shown in FIGURES 4.3 (a) and 4.4 (a) since it is extremely large for other cases. In addition, for longer time delays, the deviation of our simulation model for all cases become extremely large due to the insufficient number of harmonic functions. To maintain readability of the figures, we have removed the longer time delays and only presented shorter time delays, which is typically of interest for most communication

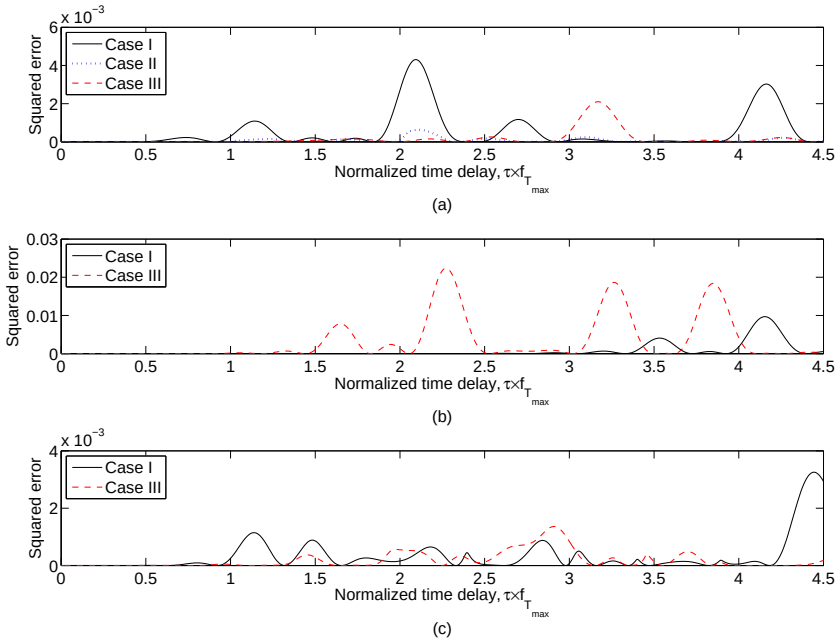

FIGURE 4.3: Squared error in the CF of the proposed deterministic simulation model with k=1 for different non-isotropic scattering M2M Rayleigh fading channels: (a) μ_T=μ_R=110° and γ_T=γ_R=20°; (b) μ_T=μ_R=γ_T=γ_R=0°; (c) μ_T=30°, μ_R=160°, γ_T=10°, and γ_R=20°.

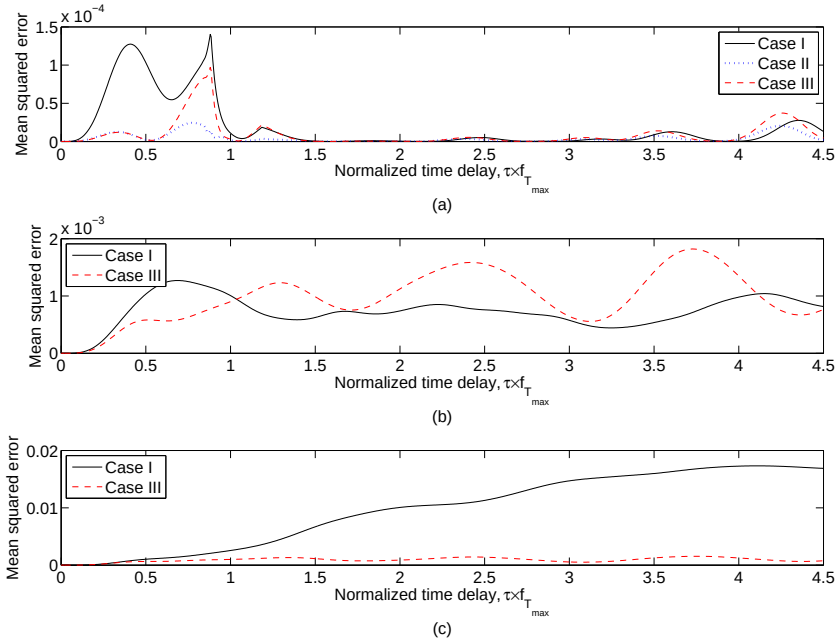

FIGURE 4.4: Mean squared error in the CF of the proposed stochastic simulation model with k=5 for different non-isotropic scattering M2M Rayleigh fading channels: (a) μ_T=μ_R=110° and γ_T=γ_R=20°; (b) μ_T=μ_R=γ_T=γ_R=0°; (c) μ_T=20°, μ_R=10°, γ_T=10°, and γ_R=20°.

systems [36]. From FIGURES 4.3 and 4.4, it is clear that due to the impact of non-isotropic scattering, no one parameter computation method in our models consistently outperforms others for all non-isotropic M2M scenarios. This, hence, validates the utility of our models that include three different sets of model parameters rather than only one.

To evaluate the performance of our simulation models, in FIGURES 4.5–4.7 we give a comparison between the ACF of the mathematical reference model and the one of our simulation models for various values of k_T, k_R, μ_T, and μ_R. The results obtained for the stochastic model are averaged over $N_{stat} = 10$ simulation trials. It is obvious that the deterministic model provides a fairly good approximation to the ACF of the mathematical reference model in a shorter normalised time-delay range, while the stochastic model presents much better approximation even with a smaller number of harmonic functions $N_{i/q}$ and $M_{i/q}$. Compared to our deterministic model, our stochastic model has a higher complexity since it requires several simulation trials to achieve the desired properties. Notice that the quality of the approximation between the ACFs of our deterministic model and the mathematical reference model can be improved by increasing the values of $N_{i/q}$ and $M_{i/q}$, while the quality of the approximation between the ACF of our stochastic model and the one of the mathematical reference model can be improved by increasing the values of $N_{i/q}$ and $M_{i/q}$, and/or the value of N_{stat}. More interestingly, from FIGURE 4.5, we observe that the increase of the values of $|\mu_T - \gamma_T|$ and $|\mu_R - \gamma_R|$ decreases the difficulty of our simulation model in approximating the correlation properties of the mathematical reference model. Similarly, FIGURE 4.6 shows that the difficulty of our simulation model in approximating the correlation properties of the mathematical reference model increases with the increase of the values of k_T and k_R. More importantly, FIGURES 4.5–4.7 show that when the values of $|\mu_T - \gamma_T|$ and $|\mu_R - \gamma_R|$ are small and/or the values of k_T and k_R are large, the proposed deterministic simulation model cannot even approximate the correlation properties of the mathematical reference model for short time-delays. In the aforementioned situations, to obtain an acceptable approximation between the correlation properties of our deterministic model and the ones of the mathematical reference model, a large number of harmonic functions (here $N_i{=}M_i{=}N_q{=}M_q{=}60$ as depicted

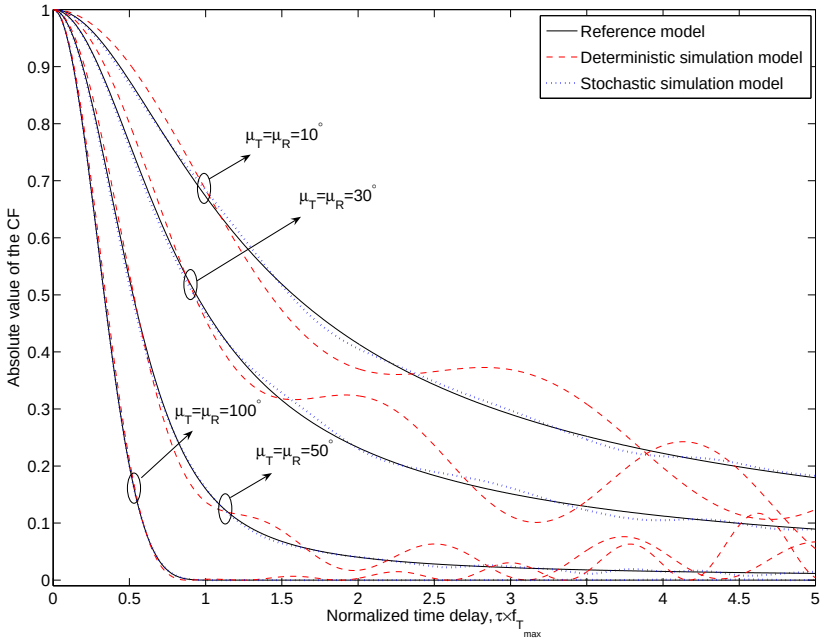

FIGURE 4.5: Comparison between the CF of the mathematical reference model and the one of the proposed simulation models with $k_T = k_R = 6$ and $\gamma_T = \gamma_R = 10°$ for various values of the mean AoD μ_T and mean AoA μ_R.

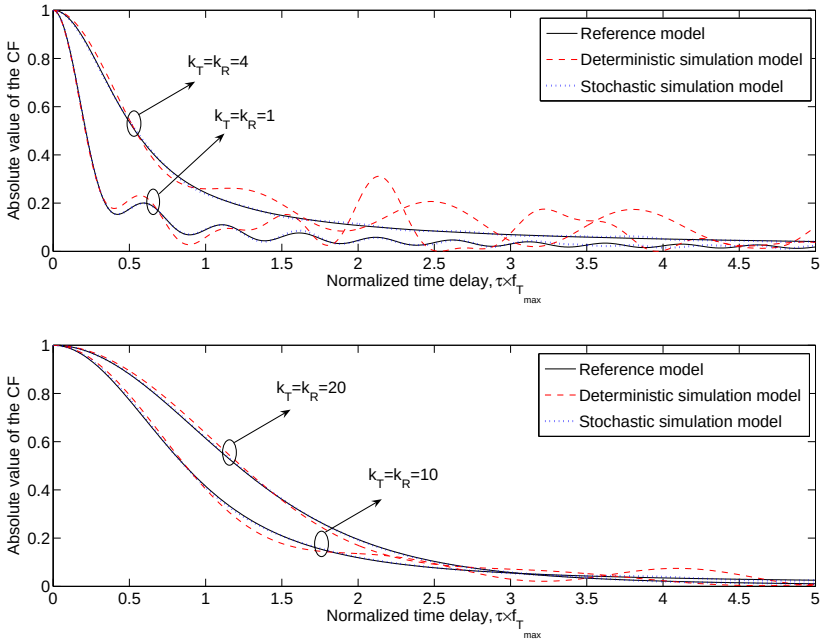

FIGURE 4.6: Comparison between the CF of the mathematical reference model and the one of the proposed simulation models with $\mu_T = \mu_R = 60°$ and $\gamma_T = \gamma_R = 30°$ for various values of k_T and k_R.

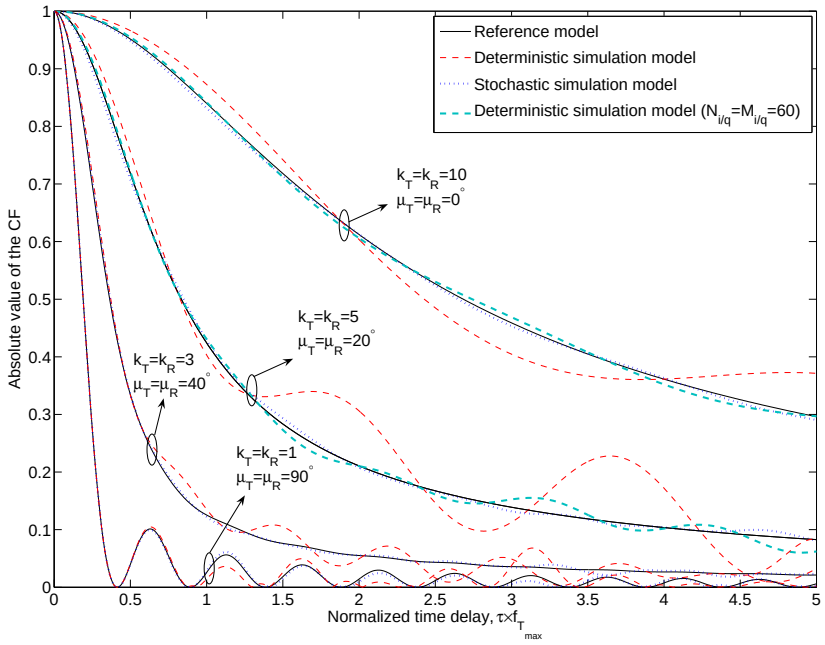

FIGURE 4.7: Comparison between the CF of the mathematical reference model and the one of the proposed simulation models with $\gamma_T = \gamma_R = 0°$ for various values of k_T, k_R, the mean AoD μ_T, and mean AoA μ_R.

in FIGURE 4.7) is necessary. This allows us to conclude that the stochastic simulation model is more suitable than the deterministic model for such a non-isotropic scattering M2M scenario where the differences between the angles of motion γ_T and γ_R, and the mean AoA μ_T and AoD μ_R are small (i.e., the value of $|\mu_T - \gamma_T|$ and $|\mu_R - \gamma_R|$ are small) and/or the received powers are more concentrated in one direction (i.e., the value of k_T and k_R are large).

4.5 Summary

In this chapter, based on the traditional two-ring SISO M2M mathematical reference model and the comprehensive analysis of the PDFs of the AoA and AoD, new deterministic and stochastic SoS simulation models have been proposed for non-isotropic scattering M2M Rayleigh fading channels. The performance of the proposed simulation models has been verified in terms of the CF through the theoretical and simulation results. Results have shown that compared to the proposed deterministic model, the

proposed stochastic model provides better approximation to the mathematical reference model with an even smaller number of harmonic functions. Moreover, our analysis has revealed that the proposed stochastic model performs better than the ARA stochastic model. Finally, either the proposed deterministic (lower complexity) model or stochastic (higher accuracy) model can be used for the simulation of M2M systems.

Chapter 5

A New Narrowband MIMO Mobile-to-Mobile Channel Mathematical Reference Model

5.1 Introduction

The mathematical reference model applied in Chapter 4 (i.e., the two-ring RS-GBSM) is over-simple and thus cannot capture some important features of M2M channels. Therefore, as reviewed in Chapter 2, several important RS-GBSMs for narrowband MIMO M2M channels have been provided in [25, 26, 27, 28, 29]. However, none of the previously reported RS-GBSMs is sufficiently general to characterise a wide variety of M2M scenarios, especially for pico-cell scenarios, and has the ability to take the impact of the VTD on channel statistics into account. Although the Doppler PSD, envelope LCR, and AFD are the most important statistics that significantly distinguish M2M channels from F2M channels, more detailed investigations of these statistics in non-isotropic scattering environments are surprisingly lacking in the open literature. Moreover, frequency correlations of sub-channels with different carrier frequencies, studied in Chapter 3 for F2M channels, in M2M communications have

not been studied so far, although OFDM has already been suggested for use in IEEE 802.11p.

Motivated by the above gaps, in this chapter we propose a new narrowband RS-GBSM that addresses all the aforementioned shortcomings of the existing RS-GBSMs. Based on the proposed model, some important channel statistics, such as the STF CF, SDF PSD, envelope LCR, and AFD, are derived. The contributions and novelties of this chapter are summarised as follows.

1) We propose a generic RS-GBSM for narrowband non-isotropic scattering MIMO M2M Ricean fading channels. The proposed model can be adapted to a wide variety of scenarios, e.g., macro-, micro-, and pico-cell scenarios, by adjusting some model parameters.

2) By distinguishing between the moving cars and the stationary roadside environment in micro- and pico-cell scenarios, our model is the first RS-GBSM to consider the impact of the VTD on M2M channel characteristics.

3) We propose a new general method to derive the exact relationship between the AoA and AoD for any known shapes of the scattering region, e.g., one-ring, two-ring, or ellipse, in a wide variety of scenarios.

4) We point out that the widely used CF definition in [22, 27, 28, 29] is incorrect and is actually the complex conjugate of the correct CF definition as given in Stochastic Processes [94].

5) From the proposed model, we derive the STF CF and the corresponding SDF PSD, which are sufficiently general and can be reduced to many existing CFs and PSDs, respectively, e.g., those in [22, 25, 27, 28]. In addition, our analysis shows that the SD PSD of a single-bounce two-ring model for non-isotropic scattering MIMO M2M fading channels derived in [28] is incorrect.

6) Considering the simplified version (SISO) of our proposed MIMO model, we derive the envelope LCR and AFD, which include many existing LCRs and AFDs as special cases, e.g., those in [24, 26, 41, 95]. Our analysis shows several

flaws in the derivation and investigation of the LCR and AFD in [96] and [55], revealing some easily neglected but important issues.

7) Based on the derived STF CF, SDF PSD, envelope LCR, and AFD, we study in more detail these channel statistics in terms of some important parameters and thus obtain some interesting observations. These observations and conclusions can be considered as the guidance for adjusting important parameters of our model properly and setting up more purposeful M2M channel measurement campaigns in the future. Finally, the some obtained theoretical results (e.g., Doppler PSDs, LCR, and AFD) and measurement data in [31] are compared. Excellent agreement between them demonstrates the utility of the proposed model.

The remainder of this chapter is outlined as follows. Section 5.2 describes the new adaptive RS-GBSM for narrowband MIMO M2M Ricean fading channels. In Section 5.3, based on the proposed new model, the STF CF and the corresponding SDF PSD are derived. Section 5.4 investigates the envelope LCR and AFD of M2M Ricean fading channels according to the simplified version (SISO) of the proposed new model. Numerical results and analysis are presented in Section 5.5. Finally, concluding remarks are drawn in Section 5.6.

5.2 A New Adaptive Model for Non-Isotropic Scattering MIMO Mobile-to-Mobile Ricean Fading Channels

Let us now consider a narrowband single-user MIMO M2M multicarrier communication system with M_T transmit and M_R receive omnidirectional antenna elements. Both the Tx and Rx are equipped with low elevation antennas. FIGURE 5.1 illustrates the geometry of the proposed RS-GBSM, which is the combination of a single- and double-bounce two-ring model, a single-bounce ellipse model, and the LoS component.

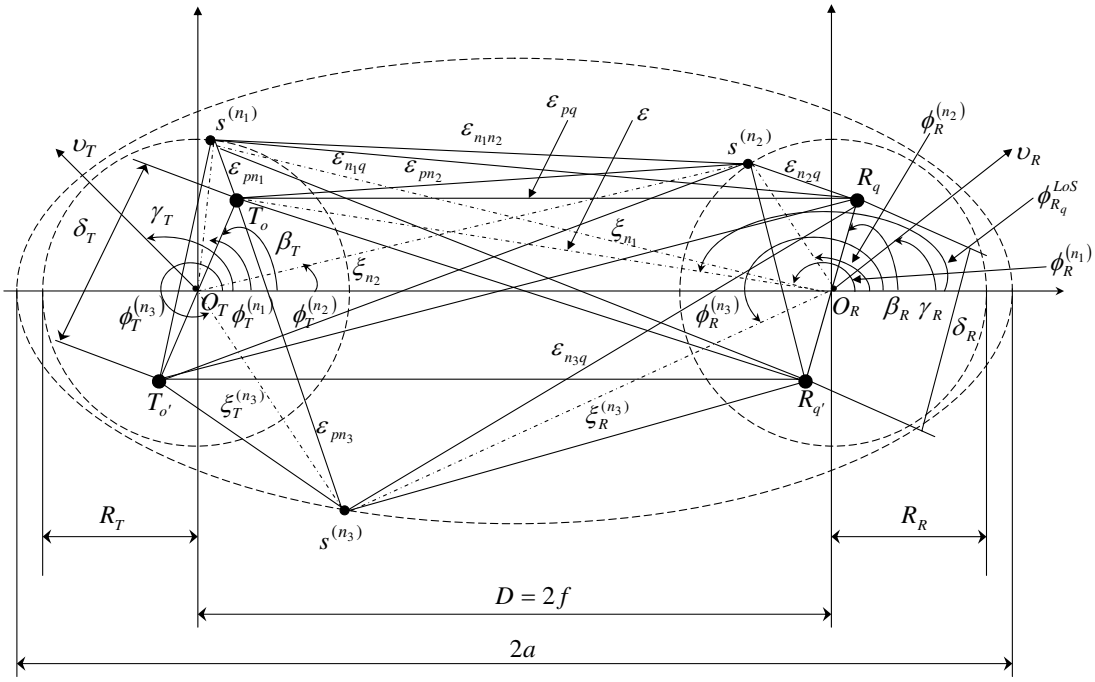

FIGURE 5.1: A generic channel model combining a two-ring model and an ellipse model with LoS components, single- and double-bounced rays for a MIMO M2M channel ($M_T = M_R = 2$).

As an example, uniform linear antenna arrays with $M_T = M_R = 2$ were used here. The two-ring model defines two rings of effective scatterers, one around the Tx and the other around the Rx. Suppose there are N_1 effective scatterers around the Tx lying on a ring of radius R_T and the n_1th ($n_1 = 1, ..., N_1$) effective scatterer is denoted by $s^{(n_1)}$. Similarly, assume there are N_2 effective scatterers around the Rx lying on a ring of radius R_R and the n_2th ($n_2 = 1, ..., N_2$) effective scatterer is denoted by $s^{(n_2)}$. For the ellipse model, N_3 effective scatterers lie on an ellipse with the Tx and Rx located at the foci. The semi-major axis of the ellipse and the n_3th ($n_3 = 1, ..., N_3$) effective scatterer are denoted by a and $s^{(n_3)}$, respectively. The distance between the Tx and Rx is $D = 2f$ with f denoting the half length of the distance between the two focal points of the ellipse. The antenna element spacings at the Tx and Rx are designated by δ_T and δ_R, respectively. It is normally assumed that the radii R_T and R_R, and the difference between the semi-major axis a and the parameter f, are all much greater

than the antenna element spacings δ_T and δ_R, i.e., $\min\{R_T, R_R, a-f\} \gg \max\{\delta_T, \delta_R\}$. The multi-element antenna tilt angles are denoted by β_T and β_R. The Tx and Rx move with speeds υ_T and υ_R in directions determined by the angles of motion γ_T and γ_R, respectively. The AoA of the wave traveling from an effective scatterer $s^{(n_i)}$ ($i \in \{1,2,3\}$) toward the Rx is denoted by $\phi_R^{(n_i)}$. The AoD of the wave that impinges on the effective scatterer $s^{(n_i)}$ is designated by $\phi_T^{(n_i)}$. Note that $\phi_{R_q}^{LoS}$ denotes the AoA of a LoS path.

The MIMO fading channel can be described by a matrix $\mathbf{H}(t) = [h_{oq}(t)]_{M_R \times M_T}$ of size $M_R \times M_T$. The received complex fading envelope between the oth ($o = 1, ..., M_T$) Tx and the qth ($q = 1, ..., M_R$) Rx at the carrier frequency f_c is a superposition of the LoS, single-, and double-bounced components, and can be expressed as

$$h_{oq}(t) = h_{oq}^{LoS}(t) + h_{oq}^{SB}(t) + h_{oq}^{DB}(t) \tag{5.1}$$

where

$$h_{oq}^{LoS}(t) = \sqrt{\frac{K_{oq}\Omega_{oq}}{K_{oq}+1}} e^{-j2\pi f_c \tau_{oq}} e^{j\left[2\pi f_{T_{max}} t \cos\left(\pi - \phi_{R_q}^{LoS} + \gamma_T\right) + 2\pi f_{R_{max}} t \cos\left(\phi_{R_q}^{LoS} - \gamma_R\right)\right]} \tag{5.2a}$$

$$h_{oq}^{SB}(t) = \sum_{i=1}^{I} h_{oq}^{SB_i}(t) = \sum_{i=1}^{I} \sqrt{\frac{\eta_{SB_i}\Omega_{oq}}{K_{oq}+1}} \lim_{N_i \to \infty} \sum_{n_i=1}^{N_i} \frac{1}{\sqrt{N_i}} e^{j\left(\psi_{n_i} - 2\pi f_c \tau_{oq,n_i}\right)} \times e^{j\left[2\pi f_{T_{max}} t \cos\left(\phi_T^{(n_i)} - \gamma_T\right) + 2\pi f_{R_{max}} t \cos\left(\phi_R^{(n_i)} - \gamma_R\right)\right]} \tag{5.2b}$$

$$h_{oq}^{DB}(t) = \sqrt{\frac{\eta_{DB}\Omega_{oq}}{K_{oq}+1}} \lim_{N_1, N_2 \to \infty} \sum_{n_1, n_2 = 1}^{N_1, N_2} \frac{1}{\sqrt{N_1 N_2}} e^{j\left(\psi_{n_1,n_2} - 2\pi f_c \tau_{oq,n_1,n_2}\right)} \times e^{j\left[2\pi f_{T_{max}} t \cos\left(\phi_T^{(n_1)} - \gamma_T\right) + 2\pi f_{R_{max}} t \cos\left(\phi_R^{(n_2)} - \gamma_R\right)\right]}. \tag{5.2c}$$

In (5.2), $\tau_{oq} = \varepsilon_{oq}/c$, $\tau_{oq,n_i} = (\varepsilon_{on_i} + \varepsilon_{n_i q})/c$, and $\tau_{oq,n_1,n_2} = (\varepsilon_{on_1} + \varepsilon_{n_1 n_2} + \varepsilon_{n_2 q})/c$ are the travel times of the waves through the link T_o–R_q, T_o–$s^{(n_i)}$–R_q, and T_o–$s^{(n_1)}$–$s^{(n_2)}$–R_q, respectively. Here, c is the speed of light and I=3. The symbols K_{oq} and Ω_{oq} designate the Ricean factor and the total power of the $T_o - R_q$ link, respectively. Parameters η_{SB_i} and η_{DB} specify how much the single- and double-bounced rays contribute to the total scattered power $\Omega_{oq}/(K_{oq}+1)$. Note that these energy-related parameters satisfy $\sum_{i=1}^{I} \eta_{SB_i} + \eta_{DB} = 1$. The phases ψ_{n_i} and ψ_{n_1,n_2} are i.i.d. random variables

with uniform distributions over $[-\pi, \pi)$, $f_{T_{max}}$ and $f_{R_{max}}$ are the maximum Doppler frequencies with respect to the Tx and Rx, respectively. Note that the AoD $\phi_T^{(n_i)}$ and AoA $\phi_R^{(n_i)}$ are independent for double-bounced rays, while they are interdependent for single-bounced rays.

From FIGURE 5.1 and based on the application of the law of cosines in appropriate triangles, the distances ε_{oq}, ε_{on_i}, ε_{n_iq}, and $\varepsilon_{n_1n_2}$ in (5.2) for any scenario (macro-cell ($D \geq 1000$ m), micro-cell ($300 < D < 1000$ m), or pico-cell ($D \leq 300$ m) scenario) can be expressed as

$$\varepsilon_{oq} \approx \varepsilon - k_q \delta_R \cos(\phi_{R_q}^{LoS} - \beta_R) \tag{5.3}$$

$$\varepsilon_{on_1} \approx R_T - k_o \delta_T \cos(\phi_T^{(n_1)} - \beta_T) \tag{5.4}$$

$$\varepsilon_{n_1q} \approx \xi_{n_1} - k_q \delta_R \cos(\phi_R^{(n_1)} - \beta_R) \tag{5.5}$$

$$\varepsilon_{on_2} \approx \xi_{n_2} - k_o \delta_T \cos\left(\phi_T^{(n_2)} - \beta_T\right) \tag{5.6}$$

$$\varepsilon_{n_2q} \approx R_R - k_q \delta_R \cos\left(\phi_R^{(n_2)} - \beta_R\right) \tag{5.7}$$

$$\varepsilon_{on_3} \approx \xi_T^{(n_3)} - k_o \delta_T \cos\left(\phi_T^{(n_3)} - \beta_T\right) \tag{5.8}$$

$$\varepsilon_{n_3q} \approx \xi_R^{(n_3)} - k_q \delta_R \cos\left(\phi_R^{(n_3)} - \beta_R\right) \tag{5.9}$$

$$\varepsilon_{n_1n_2} \approx D - R_T \cos\phi_T^{(n_1)} + R_R \cos\phi_R^{(n_2)} \tag{5.10}$$

where $\phi_{R_q}^{LoS} \approx \pi$, $\varepsilon \approx D - k_o \delta_T \cos\beta_T$, $\xi_{n_1} = \left(D^2 + R_T^2 - 2D \times R_T \cos\phi_T^{(n_1)}\right)^{-1/2}$, $\xi_{n_2} = \sqrt{D^2 + R_R^2 + 2DR_R \cos\phi_R^{(n_2)}}$, $\xi_T^{(n_3)} = \left(a^2 + f^2 + 2af\cos\phi_R^{(n_3)}\right) / \left(a + f\cos\phi_R^{(n_3)}\right)$, $\xi_R^{(n_3)} = b^2 / \left(a + f\cos\phi_R^{(n_3)}\right)$, $k_o = (M_T - 2o + 1)/2$, and $k_q = (M_R - 2q + 1)/2$. Here b denotes the semi-minor axis of the ellipse and the equality $a^2 = b^2 + f^2$ holds. As shown in Appendix E, based on the newly proposed general method to derive the exact relationship between the AoA and AoD for any shape of the scattering region, we have

$$\sin\phi_R^{(n_1)} = R_T \sin\phi_T^{(n_1)} / \sqrt{R_T^2 + D^2 - 2R_T D\cos\phi_T^{(n_1)}} \tag{5.11}$$

$$\cos\phi_R^{(n_1)} = -\left(D - R_T\cos\phi_T^{(n_1)}\right) / \sqrt{R_T^2 + D^2 - 2R_T D\cos\phi_T^{(n_1)}} \tag{5.12}$$

$$\sin\phi_T^{(n_2)} = R_R \sin\phi_R^{(n_2)} / \sqrt{R_R^2 + D^2 + 2R_R D\cos\phi_R^{(n_2)}} \tag{5.13}$$

$$\cos\phi_T^{(n_2)} = \left(D + R_R\cos\phi_R^{(n_2)}\right) / \sqrt{R_R^2 + D^2 + 2R_R D\cos\phi_R^{(n_2)}} \tag{5.14}$$

$$\sin\phi_T^{(n_3)} = b^2 \sin\phi_R^{(n_3)} / \left(a^2 + f^2 + 2af\cos\phi_R^{(n_3)}\right) \tag{5.15}$$

$$\cos\phi_T^{(n_3)} = \left(2af + (a^2 + f^2)\cos\phi_R^{(n_3)}\right) / \left(a^2 + f^2 + 2af\cos\phi_R^{(n_3)}\right). \tag{5.16}$$

Note that the above derived expressions in (5.3)–(5.16) are sufficiently general and suitable for various scenarios. For macro- and micro-cell scenarios, the assumption $D \gg \max\{R_T, R_R\}$, which is invalid for pico-cell scenarios, is fulfilled. Then, the general expressions of ξ_{n_1} and ξ_{n_2} can further reduce to the widely used approximate expressions as $\xi_{n_1} \approx D - R_T \cos\phi_T^{(n_1)}$ and $\xi_{n_2} \approx D + R_R \cos\phi_R^{(n_2)}$. In addition, the general expressions (5.11)–(5.14) for the two-ring model can further reduce to the widely used approximate expressions as $\phi_R^{(n_1)} \approx \pi - \Delta_T \sin\phi_T^{(n_1)}$ and $\phi_T^{(n_2)} \approx \Delta_R \sin\phi_R^{(n_2)}$ with $\Delta_T \approx R_T/D$ and $\Delta_R \approx R_R/D$. Moreover, the relationships (5.15) and (5.16) for the ellipse model obtained by using our method significantly simplify the relationships derived based on pure ellipse properties, such as (A1)–(A3) in [97] and (27), (28), and (32) in [98].

Since the number of effective scatterers are assumed to be infinite, i.e., $N_i \to \infty$, the proposed model is actually a mathematical reference model and results in the Ricean PDF. For our mathematical reference model, the discrete expressions of the AoA, $\phi_R^{(n_i)}$, and AoD, $\phi_T^{(n_i)}$, can be replaced by the continuous expressions $\phi_R^{(SB_i)}$ and $\phi_T^{(SB_i)}$, respectively. To characterise AoD $\phi_T^{(SB_i)}$ and AoA $\phi_R^{(SB_i)}$ we use the von Mises PDF given in (3.7).

As mentioned in the introduction, the proposed model is adaptable to a wide variety of M2M propagation environments by adjusting model parameters. It turns out that these important model parameters are the energy-related parameters η_{SB_i} and η_{DB}, and the Ricean factor K_{oq}. For a macro-cell scenario, the Ricean factor K_{oq} and the energy parameter η_{SB_3} related to the single-bounce ellipse model are very small or even close to zero. The received signal power mainly comes from single- and double-bounced rays of the two-ring model, in which we assume that double-bounced rays bear more energy than single-bounced rays due to the large distance D (larger distance D results in the independence of the AoD and AoA), i.e., $\eta_{DB} > \max\{\eta_{SB_1}, \eta_{SB_2}\} \gg \eta_{SB_3}$. This means that a macro-cell scenario can be well characterised by using a two-ring model with a negligible LoS component. In contrast to macro-cell scenarios, in micro- and pico-cell scenarios, the VTD significantly affects the channel characteristics as presented in [32]. To consider the impact of the VTD on channel statistics, we need

to distinguish between the moving cars around the Tx and Rx and the stationary roadside environments (e.g., buildings, trees, parked cars, etc.). Therefore, we use a two-ring model to mimic the moving cars and an ellipse model to depict the stationary roadside environments. Note that ellipse models have been widely used to model F2M channels in micro- and pico-cell scenarios [97], [98]. However, to the best of the authors' knowledge, this is the first time that an ellipse model is used to mimic M2M channels. For a low VTD, the value of K_{oq} is large since the LoS component can bear a significant amount of power. Also, the received scattered power is mainly from waves reflected by the stationary roadside environments described by the scatterers located on the ellipse. The moving cars represented by the scatterers located on the two rings are sparse and thus more likely to be single-bounced, rather than double-bounced. This indicates that $\eta_{SB_3} > \max\{\eta_{SB_1}, \eta_{SB_2}\} > \eta_{DB}$ holds. For a high VTD, the value of K_{oq} is smaller than that in the low VTD scenario. Also, due to the large amount of moving cars, the double-bounced rays of the two-ring model bear more energy than single-bounced rays of two-ring and ellipse models, i.e, $\eta_{DB} > \max\{\eta_{SB_1}, \eta_{SB_2}, \eta_{SB_3}\}$. Therefore, micro-cell and pico-cell scenarios with consideration of the VTD can be well characterised by utilising a combined two-ring model and ellipse model with a LoS component.

5.3 New Generic Space-Time-Frequency Correlation Function and Space-Doppler-Frequency Power Spectral Density

In this section, based on the proposed channel model in (5.1), we will derive the STF CF and the corresponding SDF PSD for a non-isotropic scattering environment.

5.3.1 New Generic Space-Time-Frequency Correlation Function

As mentioned in Chapter 2, WSS channels have fading statistics that remain constant over short periods of time or distance (e.g., in the order of tens of wavelengths). In our channel model, we have used the WSS assumption. This means that we study the M2M channel over a short distance, when the WSS condition is fulfilled. Under the WSS condition, the normalised STF CF between any two complex fading envelopes $h_{oq}(t)$ and $h'_{o'q'}(t)$ with different carrier frequencies f_c and f'_c, respectively, is defined as [95]

$$\begin{aligned}\rho_{h_{oq}h'_{o'q'}}(\tau,\chi) &= \frac{\mathbf{E}\left[h_{oq}(t)\,h'^{*}_{o'q'}(t-\tau)\right]}{\sqrt{\Omega_{oq}\Omega_{o'q'}}} \\ &= \rho_{h_{oq}^{LoS}h'^{LoS}_{o'q'}}(\tau,\chi)+\sum_{i=1}^{I}\rho_{h_{oq}^{SB_i}h'^{SB_i}_{o'q'}}(\tau,\chi)+\rho_{h_{oq}^{DB}h'^{DB}_{o'q'}}(\tau,\chi) \qquad (5.17)\end{aligned}$$

where $(\cdot)^*$ denotes the complex conjugate operation, $\mathbf{E}[\cdot]$ is the statistical expectation operator, $o,o' \in \{1,2,...,M_T\}$, and $q,q' \in \{1,2,...,M_R\}$. It should be observed that (5.17) is a function of time separation τ, space separation δ_T and δ_R, and frequency separation $\chi = f'_c - f_c$. Note that the CF definition in (5.17) is different from the following definition widely used in other mathematical references, e.g., [22, 27, 28, 29]

$$\tilde{\rho}_{h_{oq}h'_{o'q'}}(\tau,\chi) = \mathbf{E}\left[h_{oq}(t)\,h'^{*}_{o'q'}(t+\tau)\right]/\sqrt{\Omega_{oq}\Omega_{o'q'}}. \qquad (5.18)$$

The CF definition in (5.17) is actually the correct one following the CF definition given in Stochastic Processes (see Equation (9-51) in [94]). It can easily be shown that the expression (5.18) equals the complex conjugate of the correct CF in (5.17), i.e., $\tilde{\rho}_{h_{oq}h'_{o'q'}}(\tau,\chi) = \rho^{*}_{h_{oq}h'_{o'q'}}(\tau,\chi)$. Therefore, strictly speaking, (5.18) is an incorrect definition. Only when $\rho^{*}_{h_{oq}h'_{o'q'}}(\tau,\chi)$ is a real function (no imaginary part), $\tilde{\rho}_{h_{oq}h'_{o'q'}}(\tau,\chi) = \rho_{h_{oq}h'_{o'q'}}(\tau,\chi)$ holds.

Substituting (5.2a) and (5.3) into (5.17), we can obtain the STF CF of the LoS component as

$$\begin{aligned}\rho_{h_{oq}^{LoS}h_{o'q'}^{\prime LoS}}(\tau,\chi) &= \sqrt{\frac{K_{oq}K_{o'q'}}{(K_{oq}+1)(K_{o'q'}+1)}}e^{j\frac{2\pi\chi}{c}\left(D-k_{o'}\delta_T\cos\beta_T+k_{q'}\delta_R\cos\beta_R\right)} \\ &\times e^{j2\pi(O\cos\beta_T-Q\cos\beta_R)}e^{j2\pi\tau(f_{T_{max}}\cos\gamma_T-f_{R_{max}}\cos\gamma_R)}\end{aligned} \tag{5.19}$$

where $O=(o'-o)\,\delta_T/\lambda$, $Q=(q'-q)\,\delta_R/\lambda$, $k'_o=(M_T-2o'+1)/2$, and $k'_q=(M_R-2q'+1)/2$.

Applying the von Mise PDF to the two-ring model, we obtain $f\left(\phi_T^{SB_1}\right)=\exp\left[k_T^{TR}\cos\left(\phi_T^{SB_1}-\mu_T^{TR}\right)\right]/\left[2\pi I_0\left(k_T^{TR}\right)\right]$ for the AoD $\phi_T^{SB_1}$ and $f\left(\phi_R^{SB_2}\right)=\exp\left[k_R^{TR}\cos\left(\phi_R^{SB_2}-\mu_R^{TR}\right)\right]/\left[2\pi I_0\left(k_R^{TR}\right)\right]$ for the AoA $\phi_R^{SB_2}$. Substituting (5.2b) and (5.4)–(5.7) into (5.17), we can express the STF CF of the single-bounce two-ring model as

$$\begin{aligned}\rho_{h_{oq}^{SB_{1(2)}}h_{o'q'}^{\prime SB_{1(2)}}}(\tau,\chi) &= \frac{\eta_{SB_{1(2)}}}{2\pi I_0\left(k_{T(R)}^{TR}\right)\sqrt{(K_{oq}+1)(K_{o'q'}+1)}}\int_{-\pi}^{\pi}e^{k_{T(R)}^{TR}\cos\left(\phi_{T(R)}^{SB_{1(2)}}-\mu_{T(R)}^{TR}\right)} \\ &\times e^{j2\pi\tau\left[f_{T_{max}}\cos\left(\phi_T^{SB_{1(2)}}-\gamma_T\right)+f_{R_{max}}\cos\left(\phi_R^{SB_{1(2)}}-\gamma_R\right)\right]}e^{j2\pi\left[O\cos\left(\phi_T^{SB_{1(2)}}-\beta_T\right)+Q\cos\left(\phi_R^{SB_{1(2)}}-\beta_R\right)\right]} \\ &\times e^{\frac{j2\pi\chi}{c}\left[R_{T(R)}+\xi_{n_{1(2)}}-k_{o'}\delta_T\cos\left(\phi_T^{SB_{1(2)}}-\beta_T\right)-k_{q'}\delta_R\cos\left(\phi_R^{SB_{1(2)}}-\beta_R\right)\right]}d\phi_{T(R)}^{SB_{1(2)}}\end{aligned} \tag{5.20}$$

where the parameters $\sin\phi_R^{SB_1}$, $\cos\phi_R^{SB_1}$, $\sin\phi_T^{SB_2}$, and $\cos\phi_T^{SB_2}$ follow the expressions in (5.11)–(5.14), respectively. For the macro- and micro-cell scenarios, (5.20) can be further simplified as the following closed-form expression

$$\rho_{h_{oq}^{SB_{1(2)}}h_{o'q'}^{\prime SB_{1(2)}}}(\tau,\chi)=\eta_{SB_{1(2)}}e^{jC_{T(R)}^{SB_{1(2)}}}\frac{I_0\left\{\sqrt{\left(A_{T(R)}^{SB_{1(2)}}\right)^2+\left(B_{T(R)}^{SB_{1(2)}}\right)^2}\right\}}{\sqrt{(K_{oq}+1)(K_{o'q'}+1)}I_0\left(k_{T(R)}^{TR}\right)} \tag{5.21}$$

where

$$\begin{aligned}A_{T(R)}^{SB_{1(2)}} &= k_{T(R)}^{TR}\cos\mu_{T(R)}^{TR}+j2\pi\tau f_{T(R)_{max}}\cos\gamma_{T(R)} \\ &\quad +j2\pi O(Q)\cos\beta_{T(R)}-j2\pi\chi X_{A_{T(R)}}/c\end{aligned} \tag{5.22a}$$

$$B_{T(R)}^{SB_{1(2)}} = k_{T(R)}^{TR}\sin\mu_{T(R)}^{TR}+j2\pi\tau(f_{T(R)_{max}}\sin\gamma_{T(R)}+f_{R(T)_{max}}\Delta_{T(R)}\sin\gamma_{R(T)}) +j2\pi(O(Q)\sin\beta_{T(R)}+Q(O)\Delta_{T(R)}\sin\beta_{R(T)}-\chi X_{B_{T(R)}}/c) \quad (5.22b)$$

$$C_{T(R)}^{SB_1} = \mp 2\pi\tau f_{R(T)_{max}}\cos\gamma_{R(T)}\mp 2\pi Q(O)\cos\beta_{R(T)}+2\pi\chi X_{C_{T(R)}}/c \quad (5.22c)$$

with $X_{A_T}=R_T-k_{o'}\delta_T\cos\beta_T$, $X_{B_T}=-k_{o'}\delta_T\sin\beta_T-k_{q'}\delta_R\Delta_T\sin\beta_R$, $X_{C_T}=R_T+D-k_{q'}\delta_R\cos\beta_R$, $X_{A_R}=-R_R-k_{q'}\delta_R\cos\beta_R$, $X_{B_R}=-k_{q'}\delta_R\sin\beta_R-k_{o'}\delta_T\Delta_R\sin\beta_T$, and $X_{C_R}=R_R+D+k_{o'}\delta_T\cos\beta_T$.

Applying the von Mises PDF to the ellipse model, we get $f\left(\phi_R^{SB_3}\right)=\exp\left[k_R^{EL}\cos\left(\phi_R^{SB_3}-\mu_R^{EL}\right)\right]/\left[2\pi I_0\left(k_R^{EL}\right)\right]$. Performing the substitution of (5.2b), (5.8), and (5.9) into (5.17), we can obtain the STF CF of the single-bounce ellipse model as

$$\rho_{h_{oq}^{SB_3}h_{o'q'}^{SB_{3'}}}(\tau,\chi)=\frac{\eta_{SB_3}}{2\pi I_0\left(k_R^{EL}\right)\sqrt{\left(K_{oq}+1\right)\left(K_{o'q'}+1\right)}}\int_{-\pi}^{\pi}e^{k_R^{EL}\cos\left(\phi_R^{SB_3}-\mu_R^{EL}\right)} \times e^{j2\pi\tau\left[f_{T_{max}}\cos\left(\phi_T^{SB_3}-\gamma_T\right)+f_{R_{max}}\cos\left(\phi_R^{SB_3}-\gamma_R\right)\right]}e^{j2\pi\left[O\cos\left(\phi_T^{SB_3}-\beta_T\right)+Q\cos\left(\phi_R^{SB_3}-\beta_R\right)\right]} \times e^{\frac{j2\pi\chi}{c}\left[2a-k_{o'}\delta_T\cos\left(\phi_T^{SB_3}-\beta_T\right)-k_{q'}\delta_R\cos\left(\phi_R^{SB_3}-\beta_R\right)\right]}d\phi_R^{SB_3} \quad (5.23)$$

where the parameters $\sin\phi_T^{SB_3}$ and $\cos\phi_T^{SB_3}$ follow the expressions in (5.15) and (5.16), respectively.

The substitution of (5.2c), (5.4), (5.7), and (5.10) into (5.17) results in the following STF CF for the double-bounce two-ring model

$$\rho_{h_{oq}^{DB}h_{o'q'}^{\prime DB}}(\tau,\chi)=\eta_{DB}e^{jC^{DB}}\frac{I_0\left\{\sqrt{\left(A_T^{DB}\right)^2+\left(B_T^{DB}\right)^2}\right\}I_0\left\{\sqrt{\left(A_R^{DB}\right)^2+\left(B_R^{DB}\right)^2}\right\}}{\sqrt{\left(K_{oq}+1\right)\left(K_{o'q'}+1\right)}I_0\left(k_T^{TR}\right)I_0\left(k_R^{TR}\right)} \quad (5.24)$$

where

$$A_{T(R)}^{DB} = k_{T(R)}^{TR}\cos\mu_{T(R)}^{TR}+j2\pi\tau f_{T(R)_{max}}\cos\gamma_{T(R)}+j2\pi O(Q)\cos\beta_{T(R)} \mp j2\pi\chi\left(R_{T(R)}\mp k_{o'(q')}\cos\beta_{T(R)}\right)/c \quad (5.25a)$$

$$B_{T(R)}^{DB} = k_{T(R)}^{TR}\sin\mu_{T(R)}^{TR}+j2\pi\tau f_{T(R)_{max}}\sin\gamma_{T(R)} +j2\pi O(Q)\sin\beta_{T(R)}+j2\pi\chi k_{o'(q')}\sin\beta_{T(R)}/c \quad (5.25b)$$

$$C^{DB} = 2\pi\chi\left(R_T+R_R+D\right)/c. \tag{5.25c}$$

Since the derivations of (5.19)–(5.21), (5.23), and (5.24) are similar, only the brief outline of the derivation of (5.21) is given in Appendix F, while others are omitted for brevity.

The derived STF CF in (5.17) includes many existing CFs as special cases. If we only consider the two-ring model ($\eta_{SB_3}=0$) for a M2M channel in a macro- or micro-cell scenario ($D \gg \max\{R_T, R_R\}$) with the frequency separation $\chi=0$, then the CF in (5.17) will be reduced to the CF in (18) of [28], where the time separation τ should be replaced by $-\tau$ since the CF definition (5.18) is used in [28]. Consequently, the derived STF CF in (5.17) also includes other CFs listed in [28] as special cases, when τ is replaced by $-\tau$. If we consider the one-ring model only around the Rx for a F2M channel in a macro-cell scenario ($\eta_{SB_1}=\eta_{SB_3}=\eta_{DB}=f_{T_{max}}=0$) with non-LoS (NLoS) condition ($K_{oq}=0$), the derived STF CF in (5.17) includes the CF (3.16) in Chapter 3 and, subsequently, other CFs listed in Chapter 3 as special cases, when τ is replaced by $-\tau$. Furthermore, the CF (7) in [95] can be obtained from (5.17) with $K_{oq}=f_{T_{max}}=\chi=\eta_{SB_3}=\eta_{DB}=0$. Consequently, other CFs listed in [95] can also be obtained from (5.17).

5.3.2 New Generic Space-Doppler-Frequency Power Spectral Density

Applying the Fourier transform to the STF CF in (5.17) in terms of τ, we can obtain the corresponding SDF PSD as

$$\begin{aligned} S_{h_{oq}h'_{o'q'}}(f_D,\chi) &= \mathcal{F}\left\{\rho_{h_{oq}h'_{o'q'}}(\tau,\chi)\right\} = \int_{-\infty}^{\infty} \rho_{h_{oq}h'_{o'q'}}(\tau,\chi)\, e^{-j2\pi f_D\tau} d\tau \\ &= S_{h_{oq}^{LoS}h_{o'q'}^{\prime LoS}}(f_D,\chi) + \sum_{i=1}^{I} S_{h_{oq}^{SB_i}h_{o'q'}^{SB_{i'}}}(f_D,\chi) + S_{h_{oq}^{DB}h_{o'q'}^{\prime DB}}(f_D,\chi) \end{aligned} \tag{5.26}$$

where f_D is the Doppler frequency. The integral in (5.26) must be evaluated numerically in the case of the single-bounce two-ring and ellipse models. Whereas for other cases, we can obtain the following closed-form solutions.

1) In the case of the LoS component, substituting (5.19) into (5.26) we have

$$S_{h_{oq}^{LoS}h_{o'q'}^{\prime LoS}}(f_D,\chi)=\mathcal{F}\left\{\rho_{h_{oq}^{LoS}h_{o'q'}^{\prime LoS}}(\tau,\chi)\right\}=\sqrt{\frac{K_{oq}K_{o'q'}}{(K_{oq}+1)(K_{o'q'}+1)}}e^{j2\pi O\cos\beta_T}$$
$$\times e^{j2\pi Q\cos\beta_R}e^{j\frac{2\pi\chi}{c}\left(D-k_{o'}\delta_T\cos\beta_T+k_{q'}\delta_R\cos\beta_R\right)}\delta\left(f_D-f_{T_{max}}\cos\gamma_T+f_{R_{max}}\cos\gamma_R\right). \quad (5.27)$$

where $\delta(\cdot)$ denotes the Dirac delta function.

2) In terms of the single-bounce two-ring model for macro- and micro-cell scenarios, substituting (5.21) into (5.26) we have

$$S_{h_{oq}^{SB_{1(2)}}h_{o'q'}^{\prime SB_{1(2)}}}(f_D,\chi)=\mathcal{F}\left\{\rho_{h_{oq}^{SB_{1(2)}}h_{o'q'}^{\prime SB_{1(2)}}}(\tau,\chi)\right\}=\frac{\eta_{SB_{1(2)}}2e^{jU_{T(R)}^{SB_{1(2)}}}}{I_0\left(k_{T(R)}^{TR}\right)}$$
$$\times\frac{e^{jO_{T(R)}^{SB_{1(2)}}\frac{D_{T(R)}^{SB_{1(2)}}}{W_{T(R)}^{SB_{1(2)}}}}\cos\left(\frac{E_{T(R)}^{SB_{1(2)}}}{W_{T(R)}^{SB_{1(2)}}}\sqrt{W_{T(R)}^{SB_{1(2)}}-\left(O_{T(R)}^{SB_{1(2)}}\right)^2}\right)}{\sqrt{(K_{oq}+1)(K_{o'q'}+1)}\sqrt{W_{T(R)}^{SB_{1(2)}}-\left(O_{T(R)}^{SB_{1(2)}}\right)^2}} \quad (5.28)$$

where $O_{T(R)}^{SB_{1(2)}}=2\pi\left(f_D\pm f_{R(T)_{max}}\cos\gamma_{R(T)}\right)$

$$U_{T(R)}^{SB_{1(2)}} = \mp 2\pi Q(O)\cos\beta_{R(T)}+2\pi\chi\left(R_{T(R)}+D\pm k_{q'(o')}\delta_{R(T)}\cos\beta_{R(T)}\right)/c \quad (5.29a)$$

$$W_{T(R)}^{SB_{1(2)}} = 4\pi^2 f_{T(R)_{max}}^2+4\pi^2 f_{R(T)_{max}}^2\Delta_{T(R)}^2\sin^2\gamma_{R(T)}+8\pi^2 f_{T_{max}}f_{R_{max}}$$
$$\times\Delta_{T(R)}\sin\gamma_T\sin\gamma_R \quad (5.29b)$$

$$D_{T(R)}^{SB_{1(2)}} = -j2\pi k_{T(R)}^{TR}J_{T(R)}+4\pi^2 O(Q)(f_{T(R)_{max}}\cos(\beta_{T(R)}-\gamma_{T(R)})+\Delta_{T(R)}f_{R(T)_{max}}$$
$$\times\sin\beta_{T(R)}\sin\gamma_{R(T)})+4\pi^2 Q(O)(\Delta_{T(R)}f_{T(R)_{max}}\sin\beta_{R(T)}\sin\gamma_{T(R)}$$
$$+\Delta_{T(R)}^2 f_{R(T)_{max}}\sin\beta_{R(T)}\sin\gamma_{R(T)})-4\pi^2\chi\left(f_{T(R)_{max}}Y_{TD_{T(R)}}\right.$$
$$\left.+f_{R(T)_{max}}\Delta_{T(R)}\sin\gamma_{R(T)}Y_{RD_{T(R)}}\right)/c \quad (5.29c)$$

$$E_{T(R)}^{SB_{1(2)}} = -j2\pi k_{T(R)}^{TR}(f_{T(R)_{max}}\sin\left(\gamma_{T(R)}-\mu_{T(R)}^{TR}\right)+f_{R(T)_{max}}\Delta_{T(R)}\sin\gamma_{R(T)} \times\cos\mu_{T(R)}^{TR}) -4\pi^2O(Q)(f_{T(R)_{max}}\sin\left(\beta_{T(R)}-\gamma_{T(R)}\right)-\Delta_{T(R)}f_{R(T)_{max}} \times\cos\beta_{T(R)}\sin\gamma_{R(T)}) -4\pi^2Q(O)\Delta_{T(R)}f_{T(R)_{max}}\sin\beta_{R(T)}\cos\gamma_{T(R)} -4\pi^2\chi\left(f_{T(R)_{max}}Y_{TE_{T(R)}}+f_{R(T)_{max}}\Delta_{T(R)}\sin\gamma_{R(T)}Y_{RE_{T(R)}}\right)/c \quad (5.29d)$$

with

$$J_{T(R)} = f_{T(R)_{max}}\cos\left(\gamma_{T(R)}-\mu_{T(R)}^{TR}\right)-f_{R(T)_{max}}\Delta_{T(R)}\sin\gamma_{R(T)}\sin\mu_{T(R)}^{TR} \quad (5.30a)$$

$$Y_{TD_{T(R)}} = \pm R_{T(R)}\cos\gamma_{T(R)}-k_{o'(q')}\delta_{T(R)}\cos\left(\beta_{T(R)}-\gamma_{T(R)}\right) -k_{q'(o')}\delta_{R(T)}\Delta_{T(R)}\sin\beta_{R(T)}\sin\gamma_{T(R)} \quad (5.30b)$$

$$Y_{TE_{T(R)}} = \pm R_{T(R)}\sin\gamma_{T(R)}+k_{o'(q')}\delta_{T(R)}\sin\left(\beta_{T(R)}\mp\gamma_{T(R)}\right) +k_{q'(o')}\delta_{R(T)}\Delta_{T(R)}\sin\beta_{R(T)}\cos\gamma_{T(R)} \quad (5.30c)$$

$$Y_{RD_{T(R)}} = -k_{o'(q')}\delta_{T(R)}\sin\beta_{T(R)}-k_{q'(o')}\delta_{R(T)}\Delta_{T(R)}\sin\beta_{R(T)} \quad (5.30d)$$

$$Y_{RE_{T(R)}} = \pm R_{T(R)}-k_{o'(q')}\delta_{T(R)}\cos\beta_{T(R)}. \quad (5.30e)$$

For the Doppler PSD in (5.28), the range of Doppler frequencies is limited by $|f_D+f_{R_{max}}\times\cos\gamma_R|\le\sqrt{W_T^{SB_1}}/(2\pi)$ and $|f_D-f_{T_{max}}\cos\gamma_T|\le\sqrt{W_R^{SB_2}}/(2\pi)$. Note that the expression of (5.28) corrects the ones of (40) and (41) in [28].

3) In the case of the double-bounce two-ring model, substituting (5.24) into (5.26) we have

$$S_{h_{oq}^{DB}h_{o'q'}^{\prime DB}}(f_D,\chi)=\mathcal{F}\left\{\rho_{h_{oq}^{DB}h_{o'q'}^{\prime DB}}(\tau,\chi)\right\}=\frac{\eta_{DB}e^{jC^{DB}}}{\sqrt{(K_{oq}+1)(K_{o'q'}+1)}I_0(k_T^{TR})I_0(k_R^{TR})} \times2e^{jO^{DB}\frac{D_T^{DB}}{W_T^{DB}}}\frac{cos\left(\frac{E_T^{DB}}{W_T^{DB}}\sqrt{W_T^{DB}-(O^{DB})^2}\right)}{\sqrt{W_T^{DB}-(O^{DB})^2}}\odot2e^{jO^{DB}\frac{D_R^{DB}}{W_R^{DB}}}\frac{cos\left(\frac{E_R^{DB}}{W_R^{DB}}\sqrt{W_R^{DB}-(O^{DB})^2}\right)}{\sqrt{W_R^{DB}-(O^{DB})^2}} \quad (5.31)$$

where $\odot$ denotes convolution, $O^{DB}=2\pi f_D$, $W_{T(R)}^{DB}=4\pi^2f_{T(R)_{max}}^2$

$$D_{T(R)}^{DB} = 4\pi^2O(Q)f_{T(R)_{max}}\cos\left(\beta_{T(R)}-\gamma_{T(R)}\right)-j2\pi k_{T(R)}^{TR}f_{T(R)_{max}} \times\cos\left(\gamma_{T(R)}-\mu_{T(R)}^{TR}\right)-\frac{4\pi^2\chi f_{T(R)_{max}}Y_{D_{T(R)}}}{c} \quad (5.32a)$$

$$E_{T(R)}^{DB} = \pm 4\pi^2 O(Q) f_{T(R)_{max}} \sin\left(\beta_{T(R)} - \gamma_{T(R)}\right) \pm j 2\pi k_{T(R)}^{TR} f_{T(R)_{max}} \times \sin\left(\gamma_{T(R)} - \mu_{T(R)}^{TR}\right) + \frac{4\pi^2 \chi f_{T(R)_{max}} Y_{E_{T(R)}}}{c} \tag{5.32b}$$

with $Y_{D_T} = R_T \cos\gamma_T - k_{o'}\delta_T \cos(\beta_T - \gamma_T)$, $Y_{E_T} = R_T \sin\gamma_T + k_{o'}\delta_T \sin(\beta_T - \gamma_T)$, $Y_{D_R} = -R_R \cos\gamma_R - k_{q'}\delta_R \cos(\beta_R - \gamma_R)$, and $Y_{E_R} = -R_R \sin\gamma_R + k_{q'}\delta_R \sin(\beta_R - \gamma_R)$. For the Doppler PSD in (5.31), the range of Doppler frequencies is limited by $|f_D| \leq f_{T_{max}} + f_{R_{max}}$. Due to the similar derivations of (5.27), (5.28), and (5.31), Appendix G only gives the brief outline of the derivation of (5.28), while others are omitted here.

Many existing Doppler PSDs are special cases of the derived SDF PSD in (5.26). The simplest case is Clarke's Doppler PSD $1/\left(2\pi f_D \sqrt{1-(f_D/f_{R_{max}})^2}\right)$ ($|f_D| \leq f_{R_{max}}$) [41], which can be obtained from (5.26) by setting $K_{oq} = 0$ (NLoS condition), $k_R^{TR} = 0$ (isotropic scattering around the Rx), $\chi = 0$ (no frequency separation), $f_{T_{max}} = \eta_{SB_1} = \eta_{SB_3} = \eta_{DB} = 0$ (fixed Tx, no scattering around the Tx), and applying $D \gg \max\{R_T, R_R\}$ (macro- and micro-cell scenarios). The Doppler PSD for isotropic M2M fading channels presented as (41) in [25] can be obtained from (5.26) by setting $K_{oq} = k_T^{TR} = k_R^{TR} = \delta_T = \delta_R = \chi = \eta_{SB_1} = \eta_{SB_2} = \eta_{SB_3} = 0$ and using $D \gg \max\{R_T, R_R\}$. Similarly, the space-Doppler PSD for non-isotropic double-bounce two-ring model shown as (42)[1] in [28] can be obtained from (5.26) by setting $K_{oq} = \chi = \eta_{SB_1} = \eta_{SB_2} = \eta_{SB_3} = 0$ and utilizing $D \gg \max\{R_T, R_R\}$, when D_T^{TR} and D_R^{TR} are replaced by $-D_T^{TR}$ and $-D_R^{TR}$, respectively, due to applying the different CF definitions.

To further demonstrate that the CF definition in (5.17) is correct, in Appendix H we compare the Doppler PSDs with different CFs (5.17) and (5.18). Appendix H demonstrates that (5.17) leads to the Doppler PSD being capable of capturing the underlying physical phenomena of real channels for any scenarios, while the widely used expression (5.18) is only applicable to certain scenarios where the Doppler PSD is a real function and symmetrical to the origin (i.e., the corresponding CF is a real function), e.g., Clarke's scenario. In [22, 27, 28, 29], the commonly used formula (5.18) was misapplied to non-isotropic F2M or M2M scenarios.

[1] Note that the expression of (42) in [28] is inaccurate. The corrected expression should replace the terms $-jk_T \cos(\gamma_T - \mu_T)$ and $-jk_R \cos(\gamma_R - \mu_R)$ by $+jk_T \cos(\gamma_T - \mu_T)$ and $+jk_R \cos(\gamma_R - \mu_R)$, respectively.

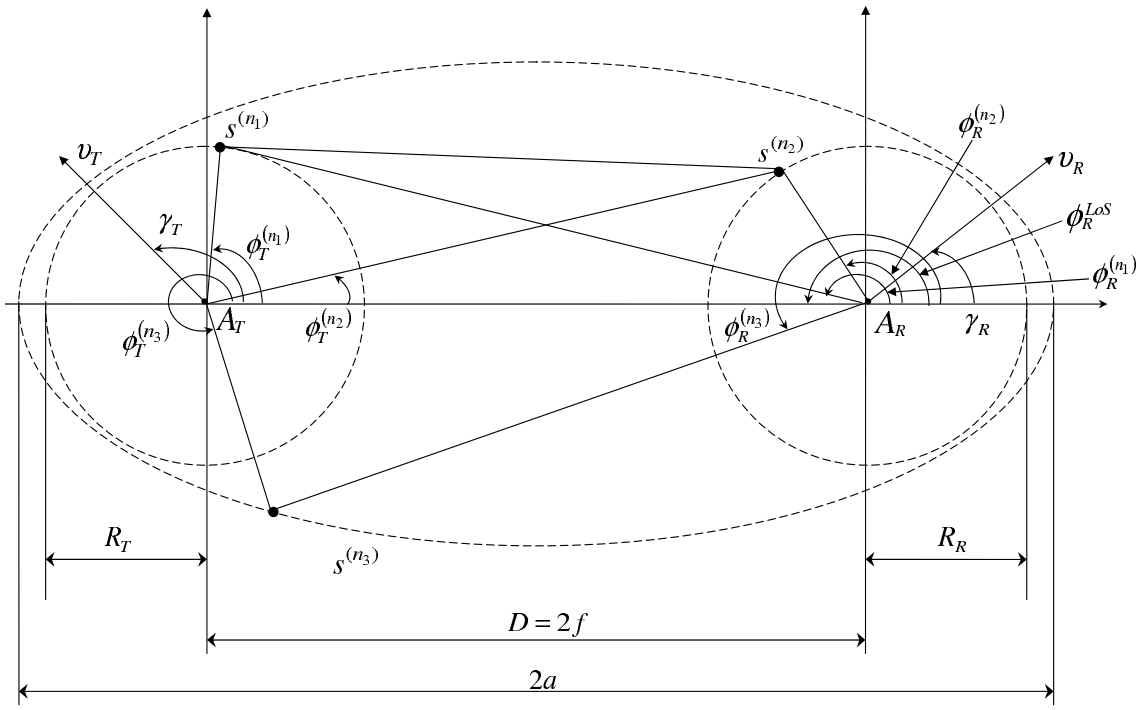

FIGURE 5.2: A generic channel model combining a two-ring model and an ellipse model with LoS components, single- and double-bounced rays for a SISO M2M channel.

5.4 Envelope Level Crossing Rate and Average Fade Duration

In this section, we will derive the envelope LCR and AFD for non-isotropic M2M fading channels based on the narrowband SISO M2M channel model, which is a simplified version of the proposed MIMO M2M model in Section 5.2.

5.4.1 A Narrowband SISO Mobile-to-Mobile Mathematical Reference Model

FIGURE 5.2 shows the geometry of the corresponding SISO M2M RS-GBSM, which is a simplified version of the MIMO M2M RS-GBSM proposed in Section 5.2. This SISO M2M RS-GBSM is also the combination of a LoS component, a single- and double-bounce two-ring model, and a single-bounce ellipse model. In order to keep consistent, all the parameters shown in FIGURE 5.2 are the same as those presented

in FIGURE 5.1 (definitions of these parameters are detailed in Section 5.2). Therefore, from the SISO M2M model, the received complex fading envelope is a superposition of the LoS component and diffuse component, which consists of single-, and double-bounced rays, and can be expressed as

$$h\left(t\right) = h^{LoS}\left(t\right) + h^{DIF}\left(t\right) = h^{LoS}\left(t\right) + h^{SB}\left(t\right) + h^{DB}\left(t\right) \tag{5.33}$$

where

$$h^{LoS}\left(t\right) = \sqrt{\frac{K\Omega}{K+1}} e^{j\left[2\pi f_{T_{max}} t\cos\left(\pi-\phi_R^{LoS}+\gamma_T\right)+2\pi f_{R_{max}} t\cos\left(\phi_R^{LoS}-\gamma_R\right)\right]} \tag{5.34a}$$

$$\begin{aligned} h^{SB}(t) &= \sum_{i=1}^{I} h^{SB_i}(t) = \sum_{i=1}^{I} \sqrt{\frac{\eta_{SB_i}\Omega}{K+1}} \lim_{N_i\to\infty} \sum_{n_i=1}^{N_i} \frac{1}{\sqrt{N_i}} \\ &\quad \times e^{j\psi_{n_i}} e^{j\left[2\pi f_{T_{max}} t\cos\left(\phi_T^{(n_i)}-\gamma_T\right)+2\pi f_{R_{max}} t\cos\left(\phi_R^{(n_i)}-\gamma_R\right)\right]} \end{aligned} \tag{5.34b}$$

$$\begin{aligned} h^{DB}\left(t\right) &= \sqrt{\frac{\eta_{DB}\Omega}{K+1}} \lim_{N_1,N_2\to\infty} \sum_{n_1,n_2=1}^{N_1,N_2} \frac{1}{\sqrt{N_1 N_2}} \\ &\quad \times e^{j\psi_{n_1,n_2}} e^{j\left[2\pi f_{T_{max}} t\cos\left(\phi_T^{(n_1)}-\gamma_T\right)+2\pi f_{R_{max}} t\cos\left(\phi_R^{(n_2)}-\gamma_R\right)\right]}. \end{aligned} \tag{5.34c}$$

Note that (5.34a)–(5.34c) can be obtained by removing the term related to τ_{oq} in (5.2a), the term related to τ_{oq,n_i} in (5.2b), and the term related to τ_{oq,n_1,n_2} in (5.2c), respectively. Therefore, all the parameters in (5.34) are the same as those in (5.2). Since the numbers of effective scatterers N_i tend to be infinite as shown in (5.34b) and (5.34c), the discrete expressions of the AoA, $\phi_R^{(n_i)}$, and AoD, $\phi_T^{(n_i)}$, can be replaced by the continuous expressions $\phi_R^{SB_i}$ and $\phi_T^{SB_i}$, respectively. To characterise the AoD $\phi_T^{SB_i}$ and AoA $\phi_R^{SB_i}$, the von Mises PDF given in (3.7) is used. Analogous to our MIMO M2M model, for the angle of interest in this SISO M2M model, i.e., the AoD $\phi_T^{SB_1}$ for the one ring around the Tx, the AoA $\phi_R^{SB_2}$ for the one ring around the Rx, and the AoA $\phi_R^{SB_3}$ for the ellipse, we use appropriate parameters of the von Mises PDF as μ_T^{TR} and k_T^{TR}, μ_R^{TR} and k_R^{TR}, and μ_R^{EL} and k_R^{EL}, respectively.

5.4.2 Envelope Level Crossing Rate and Average Fade Duration for Non-Isotropic Scattering M2M Ricean Fading Channels

In this section, based on the developed model in (5.33) and (5.34), we will derive the LCR and AFD for a non-isotropic scattering environment. The LCR, $L_\xi(r_l)$, is by definition the average number of crossings per second that the signal envelope, $\xi(t) = |h(t)|$, crosses a specified level r_l with positive/negative slope. Using the traditional PDF-based method [99], we derive the general expression of the LCR for M2M Ricean fading channels as

$$\begin{aligned} L_\xi(r_l) &= \frac{2r_l}{\pi^{3/2}}\sqrt{\frac{B(K+1)}{b_0}}e^{-K-(K+1)r_l^2}\int_0^{\pi/2}\cosh\left(2\sqrt{K(K+1)}r_l\cos\theta\right) \\ &\times \left[e^{-\left(\frac{\varsigma\zeta\sin\theta}{\sqrt{2B}}\right)^2}+\sqrt{\frac{\pi}{2B}}\varsigma\zeta\sin\theta\cdot\operatorname{erf}\left(\frac{\varsigma\zeta\sin\theta}{\sqrt{2B}}\right)\right]d\theta \end{aligned} \tag{5.35}$$

where $\cosh(\cdot)$ is the hyperbolic cosine, $\operatorname{erf}(\cdot)$ denotes the error function, and parameters B, ζ, and ς are $B = b_2 - b_1^2/b_0$, $\zeta = \sqrt{K\Omega/(K+1)}$, and $\varsigma = E + b_1/b_0$, respectively, with $E{=}2\pi f_{T_{max}}\cos(\pi{-}\phi_R^{LoS}{+}\gamma_T){+}2\pi f_{R_{max}}\cos(\phi_R^{LoS}{-}\gamma_R)$. Finally, the key parameters b_m $(m = 0, 1, 2)$ are defined as

$$b_m = \frac{d^m\rho_{h^{DIF}}(\tau)}{2j^m d\tau^m}\Big|_{\tau=0} \tag{5.36}$$

with $\rho_{h^{DIF}}(\tau) = \mathbf{E}\left[h^{DIF}(t)\,h^{DIF*}(t-\tau)\right]/\Omega$, where $j^2 = -1$, $\rho_{h^{DIF}}(\tau)$ is the time ACF of the diffuse component $h^{DIF}(t)$ of the complex fading envelope, $(\cdot)^*$ denotes the complex conjugate operation, and $\mathbf{E}[\cdot]$ designates the statistical expectation operator. Note that (5.35) is actually the same as (29) in [100]. By setting $E = 0$, the general expression (5.35) can be reduced to (6) in [96] and (43) in [55]. Considering that the parameter E refers to Doppler shift of the LoS component, we can conclude that (5.35) can be used for a non-isotropic environment with a time-variant LoS component ($E \neq 0$), while (6) in [96] or (43) in [55] is suitable only for a non-isotropic environment with a time-invariant LoS component ($E = 0$). We believe that the expression (6) in

[96] or (43) in [55] was misapplied to study the LCR for a non-isotropic environment with a time-variant LoS component.

- **Derivation of b_m for A Wide Variety of Scenarios**

Based on the presented model in Subsection 5.4.1, we now derive the key parameters b_m for a wide variety of scenarios. Substituting (5.34b) into (5.36) and setting $m = 0$, we can obtain the parameter b_0 as

$$b_0 = b_0^{SB_1} + b_0^{SB_2} + b_0^{SB_3} + b_0^{DB} = \frac{1}{2(K+1)} \tag{5.37}$$

where $b_0^{SB_1} = \frac{\eta_{SB_1}}{2(K+1)}$, $b_0^{SB_2} = \frac{\eta_{SB_2}}{2(K+1)}$, $b_0^{SB_3} = \frac{\eta_{SB_3}}{2(K+1)}$, and $b_0^{DB} = \frac{\eta_{DB}}{2(K+1)}$. Similarly, we can express the parameters b_1 and b_2 as

$$b_m = b_m^{SB_1} + b_m^{SB_2} + b_m^{SB_3} + b_m^{DB}, \qquad m = 1, 2. \tag{5.38}$$

Considering the von Mise PDFs for the two-ring model, we can express the parameters $b_m^{SB_{1(2)}}$ $(m{=}1, 2)$ as

$$\begin{aligned} b_1^{SB_{1(2)}} &= b_0^{SB_{1(2)}} \int_{-\pi}^{\pi} \frac{f_{T_{max}} \cos(\phi_T^{SB_{1(2)}} - \gamma_T) + f_{R_{max}} \cos(\phi_R^{SB_{1(2)}} - \gamma_R)}{I_0(k_{T(R)}^{TR})} \\ &\quad \times e^{k_{T(R)}^{TR} \cos(\phi_{T(R)}^{SB_{1(2)}} - \mu_{T(R)}^{TR})} d\phi_{T(R)}^{SB_{1(2)}} \end{aligned} \tag{5.39a}$$

$$\begin{aligned} b_2^{SB_{1(2)}} &= b_0^{SB_{1(2)}} \int_{-\pi}^{\pi} \frac{2\pi \left[f_{T_{max}} \cos(\phi_T^{SB_{1(2)}} - \gamma_T) + f_{R_{max}} \cos(\phi_R^{SB_{1(2)}} - \gamma_R) \right]^2}{I_0(k_{T(R)}^{TR})} \\ &\quad \times e^{k_{T(R)}^{TR} \cos(\phi_{T(R)}^{SB_{1(2)}} - \mu_{T(R)}^{TR})} d\phi_{T(R)}^{SB_{1(2)}}. \end{aligned} \tag{5.39b}$$

Based on the general relationships in (5.11)–(5.14), the parameters $\phi_R^{SB_1}$ and $\phi_T^{SB_2}$ in (5.39a) and (5.39b) can be expressed by $\phi_T^{SB_1}$ and $\phi_R^{SB_2}$, respectively. Similarly, considering the von Mises PDF for the ellipse model, we can express the parameters

$b_m^{SB_3}$ $(m=1,2)$ as

$$b_1^{SB_3} = b_0^{SB_3}\int_{-\pi}^{\pi}\frac{f_{T_{max}}\cos(\phi_T^{SB_3}-\gamma_T)+f_{R_{max}}\cos(\phi_R^{SB_3}-\gamma_R)}{I_0(k_R^{EL})} \times e^{k_R^{EL}\cos(\phi_R^{SB_3}-\mu_R^{EL})}d\phi_R^{SB_3} \tag{5.40a}$$

$$b_2^{SB_3} = b_0^{SB_3}\int_{-\pi}^{\pi}\frac{2\pi\left[f_{T_{max}}\cos(\phi_T^{SB_3}-\gamma_T)+f_{R_{max}}\cos(\phi_R^{SB_3}-\gamma_R)\right]^2}{I_0(k_R^{EL})} \times e^{k_R^{EL}\cos(\phi_R^{SB_3}-\mu_R^{EL})}d\phi_R^{SB_3}. \tag{5.40b}$$

According to the general relationship in (5.15) and (5.16), the parameter $\phi_T^{SB_3}$ in (5.40a) and (5.40b) can be expressed by $\phi_R^{SB_3}$. Considering the von Mises PDFs for the two-ring model and applying the following equalities $\int_{-\pi}^{\pi} e^{a\sin c+b\cos c}dc=2\pi I_0\left(\sqrt{a^2+b^2}\right)$, $dI_V(z)/dz=[I_{V-1}(z)+I_{V+1}(z)]/2$, and $zI_{V-1}(z)-zI_{V+1}(z)=(V+1)I_V(z)$ [101], where $I_V(\cdot)$ is the V^{th}-order modified Bessel function of the first kind, we can get the following closed-form expressions of the parameters b_m^{DB} $(m=1,2)$

$$b_1^{DB}=b_0^{DB}\left[\frac{2\pi f_{T_{max}}\cos(\gamma_T-\mu_T^{TR})I_1(k_T^{TR})}{I_0(k_T^{TR})}+\frac{2\pi f_{R_{max}}\cos(\gamma_R-\mu_R^{TR})I_1(k_R^{TR})}{I_0(k_R^{TR})}\right] \tag{5.41a}$$

$$b_2^{DB}=b_0^{DB}\Bigg[4\pi^2 f_{T_{max}}^2\frac{1+\cos\left(2\left(\gamma_T-\mu_T^{TR}\right)\right)I_2\left(k_T^{TR}\right)}{2I_0\left(k_T^{TR}\right)}+4\pi^2 f_{R_{max}}^2\frac{1+\cos\left(2\left(\gamma_R-\mu_R^{TR}\right)\right)I_2\left(k_R^{TR}\right)}{2I_0\left(k_R^{TR}\right)}$$

$$+8\pi^2 f_{T_{max}}f_{R_{max}}\cos(\gamma_T-\mu_T^{TR})\cos(\gamma_R-\mu_R^{TR})\frac{I_1(k_T^{TR})I_1(k_R^{TR})}{I_0(k_T^{TR})I_0(k_R^{TR})}\Bigg]. \tag{5.41b}$$

Numerical integration methods are needed to evaluate the integrals in (5.39) and (5.40).

- **Derivation of b_m for Macro- and Micro-cell Scenarios**

For macro- and micro-cell scenarios, the widely used assumption $D\gg\max\{R_T,R_R\}$ can be used in the derivation of b_m. This results in the closed-form solution of the integrals in (5.39), while the expressions of other parameters b_m remain unchanged.

As mentioned in Section 5.2, the application of $D \gg \max\{R_T, R_R\}$ leads to the approximate relationships $\phi_R^{SB_1} \approx \pi - \Delta_T \sin\phi_T^{SB_1}$ and $\phi_T^{SB_2} \approx \Delta_R \sin\phi_R^{SB_2}$. Based on the above two approximate relations and following approximate relations $\sin\chi \approx \chi$ and $\cos\chi \approx 1$ when χ is small, the parameters $b_m^{SB_{1(2)}}$ $(m = 1, 2)$ in (5.39) can be further simplified as

$$b_m^{SB_1} = b_0^{SB_1} \int_{-\pi}^{\pi} \frac{(2\pi)^{m-1}\left[f_{T_{max}}\cos(\phi_T^{SB_1} - \gamma_T) + f_{R_{max}}(\Delta_T \sin\phi_T^{SB_1}\sin\gamma_R - \cos\gamma_R)\right]^m}{I_0(k_T^{TR})} \times e^{k_T^{TR}\cos(\phi_T^{SB_1} - \mu_T^{TR})} d\phi_T^{SB_1} \tag{5.42a}$$

$$b_m^{SB_2} = b_0^{SB_2} \int_{-\pi}^{\pi} \frac{(2\pi)^{m-1}\left[f_{T_{max}}(\Delta_R \sin\phi_R^{SB_2}\sin\gamma_T + \cos\gamma_T) + f_{R_{max}}\cos(\phi_R^{SB_2} - \gamma_R)\right]^m}{I_0(k_R^{TR})} \times e^{k_R^{TR}\cos(\phi_R^{SB_2} - \mu_R^{TR})} d\phi_R^{SB_2}. \tag{5.42b}$$

The integrals in (5.42a) and (5.42b) can be further simplified and thus the closed-form expressions of parameters $b_m^{SB_{1(2)}}$ can be obtained as

$$b_1^{SB_{1(2)}} = b_0^{SB_{1(2)}} \left\{ 2\pi \left[f_{T(R)_{max}} \cos(\gamma_{T(R)} - \mu_{T(R)}^{TR}) + f_{R(T)_{max}} \Delta_{T(R)} \sin\mu_{T(R)}^{TR} \sin\gamma_{R(T)} \right] \times \frac{I_1(k_{T(R)}^{TR})}{I_0(k_{T(R)}^{TR})} \mp 2\pi f_{R(T)_{max}} \cos\gamma_{R(T)} \right\} \tag{5.43a}$$

$$\begin{aligned} b_2^{SB_{1(2)}} = b_0^{SB_{1(2)}} \Big\{ & 2\pi^2 \big(2 f_{R(T)_{max}}^2 \cos^2\gamma_{R(T)} + f_{T(R)_{max}}^2 + f_{R(T)_{max}}^2 \Delta_{T(R)}^2 \sin^2\gamma_{R(T)} \\ & + 2 f_{T_{max}} f_{R_{max}} \Delta_{T(R)} \sin\gamma_T \sin\gamma_R \big) \mp 4\pi^2 \big[2 f_{T_{max}} f_{R_{max}} \cos\gamma_{R(T)} \\ & \times \cos\left(\gamma_{T(R)} - \mu_{T(R)}^{TR}\right) + f_{R(T)_{max}}^2 \Delta_{T(R)} \sin\left(2\gamma_{R(T)}\right) \sin\mu_{T(R)}^{TR} \big] \frac{I_1\left(k_{T(R)}^{TR}\right)}{I_0\left(k_{T(R)}^{TR}\right)} \\ & + 2\pi^2 \big[f_{T(R)_{max}}^2 \cos\left(2\left(\gamma_{T(R)} - \mu_{T(R)}^{TR}\right)\right) - f_{R(T)_{max}}^2 \Delta_{T(R)}^2 \sin^2\gamma_{R(T)} \cos\left(2\mu_{T(R)}^{TR}\right) \\ & + f_{T_{max}} f_{R_{max}} \Delta_{T(R)} \sin\gamma_{R(T)} \sin\left(\gamma_{T(R)} - 2\mu_{T(R)}^{TR}\right) \big] \frac{I_2(k_{T(R)}^{TR})}{I_0(k_{T(R)}^{TR})} \Big\}. \end{aligned} \tag{5.43b}$$

In Appendix I, we only provide a brief outline for the derivation of (5.43b) since the derivations of (5.43a) and (5.43b) are similar. The parameters $b_m^{SB_{1(2)}}$ for 3D narrowband and wideband M2M channels were derived in [96] and [55], respectively. The expressions of $b_m^{SB_{1(2)}}$ in [55] can reduce to the ones in [96] by setting $R_{t(r)1} = R_{t(r)2}$. If we further assume elevation-related parameters $\beta_{T(R)} = \Delta_H = 0$ in the parameters

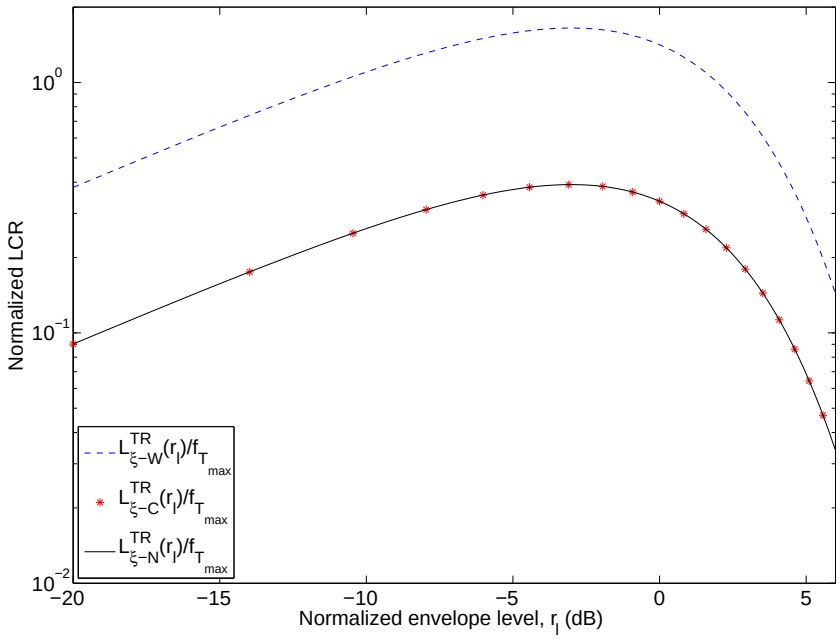

FIGURE 5.3: Comparison of the LCRs $L^{TR}_{\xi-W}(r_l)$, $L^{TR}_{\xi-C}(r_l)$, and $L^{TR}_{\xi-N}(r_l)$.

$b_m^{SB_{1(2)}}$ in [96], the parameters $b_m^{SB_{1(2)}}$ for 2D macro- and micro-cell scenarios can be obtained. To distinguish this from the parameters $b_m^{SB_{1(2)}}$ in (5.43), we denote the parameters $b_m^{SB_{1(2)}}$ obtained from [96] and [55] as $\tilde{b}_m^{SB_{1(2)}}$. The difference between the $b_m^{SB_{1(2)}}$ and $\tilde{b}_m^{SB_{1(2)}}$ motivates us to find which derivations are correct. To this end, in FIGURE 5.3 we compare the LCRs having the same expression (5.35) but with different expressions of parameters $b_m^{SB_{1(2)}}$: 1) $L^{TR}_{\xi-C}(r_l)$ having $b_m^{SB_{1(2)}}$ calculated by (5.43); 2) $L^{TR}_{\xi-W}(r_l)$ having $\tilde{b}_m^{SB_{1(2)}}$; 3) $L^{TR}_{\xi-N}(r_l)$ having the numerically computed $b_m^{SB_{1(2)}}$ in (5.42). The parameters used in FIGURE 5.3 are $f_{T_{max}} = f_{R_{max}} = 500$ Hz, $K = 0$, $\Delta_T = \Delta_R = 0.01$, $\mu_T^{TR} = 31.2°$, $k_T^{TR} = 18.2$, $\mu_R^{TR} = 216.3°$, and $k_R^{TR} = 10.6$. FIGURE 5.3 shows excellent agreement between $L^{TR}_{\xi-C}(r_l)$ and $L^{TR}_{\xi-N}(r_l)$, demonstrating the correctness of our derivations (5.43).

It is worth emphasizing that the LCR, $L^{TR}_{\xi-C}(r_l)$, is obtained based on the assumption $D \gg \max\{R_T, R_R\}$. To fulfill this assumption, the values of parameters Δ_T and Δ_R should be chosen carefully due to the relationships $\Delta_T \approx R_T/D$ and $\Delta_R \approx R_R/D$ (in general, the smaller the better). However, the values of parameters Δ_T and Δ_R are chosen comparatively large (Δ_T=Δ_R=0.6) in [96]. This raises several questions, such

as whether $\Delta_T{=}\Delta_R{=}0.6$ violates the assumption $D{\gg}\max\{R_T, R_R\}$, and if so, how inaccurate the LCR $L^{TR}_{\xi-C}(r_l)$ is, and whether this inaccuracy can be ignored. To address the above questions, we define an error function to measure the error between the LCR, $L^{TR}_{\xi-G}(r_l)$, having the expression of (5.35) with the general expressions of parameters $b_m^{SB_{1(2)}}$ in (5.39), and $L^{TR}_{\xi-C}(r_l)$ as $\varepsilon = L^{-1}\sum_{l=1}^{L}\left|L^{TR}_{\xi-G}(r_l) - L^{TR}_{\xi-C}(r_l)\right| / \left|L^{TR}_{\xi-G}(r_l)\right|$, where L is the total number of the investigated specified level r_l. FIGURE 5.4 illustrates the error ε versus the parameter Δ ($\Delta_T{=}\Delta_R{=}\Delta$) by using the same parameters as in FIGURE 5.3. In FIGURE 5.4, the investigated levels r_l were obtained by taking $L = 200$ equal-distance samples between -20dB and 5dB. As expected, it is shown that the inaccuracy of $L^{TR}_{\xi-C}(r_l)$ increases with the increase of the parameter Δ. From FIGURE 5.4, it is obvious that at $\Delta = 0.6$, we have very high error $\varepsilon = 0.894547$. This demonstrates that the chosen parameters $\Delta_T = \Delta_R = 0.6$ in [96] may result in extremely inaccurate $L^{TR}_{\xi-C}(r_l)$. Therefore, it is desirable to propose a criterion on how to choose the parameters Δ_T and Δ_R to guarantee the accuracy of $L^{TR}_{\xi-C}(r_l)$ is acceptable. In this chapter, we assume the accuracy of $L^{TR}_{\xi-C}(r_l)$ is acceptable if the error $\varepsilon \leq 0.01$. In such a case, the LCR $L^{TR}_{\xi-C}(r_l)$ can be applied under the condition that $\Delta_T = \Delta_R \leq 0.1085$. In other words, when $\Delta_T = \Delta_R > 0.1085$, the LCR $L^{TR}_{\xi-G}(r_l)$ can only be used instead of $L^{TR}_{\xi-C}(r_l)$.

The AFD, $T_{\xi-}(r_l)$, is the average time over which the signal envelope, $\xi(t)$, remains below a certain level r_l. In general, the AFD $T_{\xi-}(r_l)$ for Ricean fading channels is defined by [71]

$$T_{\xi-}(r_l) = \frac{P_{\xi-}(r_l)}{L_{\xi}(r_l)} = \frac{1 - Q\left(\sqrt{2K}, \sqrt{2(K+1)}r_l\right)}{L_{\xi}(r_l)} \tag{5.44}$$

where $P_{\xi-}(r_l)$ indicates a cumulative distribution function of $\xi(t)$ with $Q(\cdot,\cdot)$ denoting the generalized Marcum Q function.

Many existing LCRs and AFDs are special cases of the non-isotropic M2M LCR and AFD in (5.35) and (5.44). The simplest case is Clarke's LCR $\sqrt{2\pi} f_{R_{max}} r_l \exp(-r_l^2)$ and AFD $(\exp(r_l^2) - 1)/(\sqrt{2\pi} f_{R_{max}} r_l)$ [41], which can be obtained from (5.35) and (5.44), respectively, by setting $K = 0$ (NLoS condition), $k_R^{TR} = 0$ (isotropic scattering around

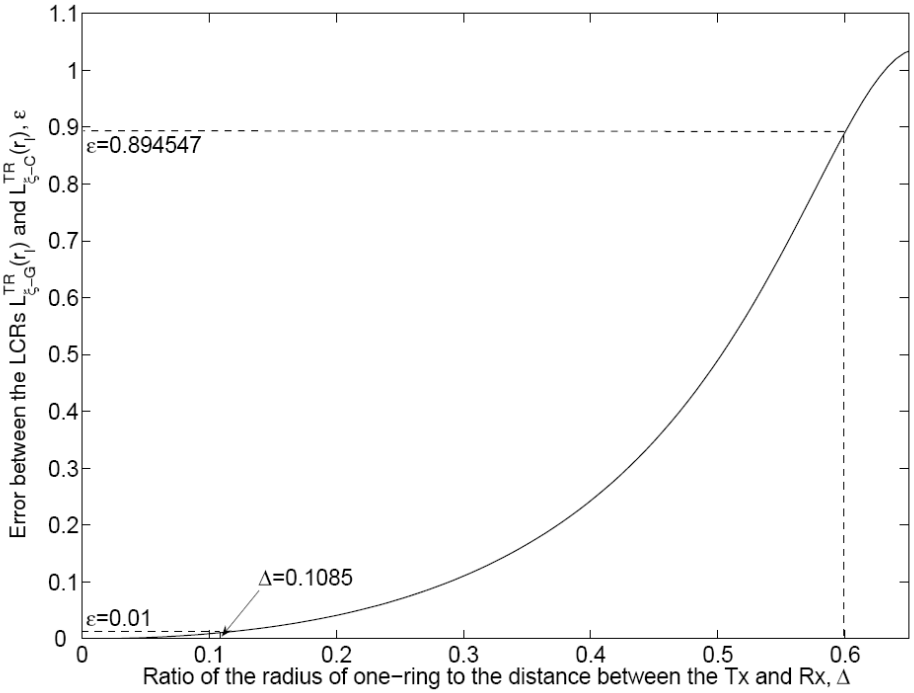

FIGURE 5.4: The error ε between the LCRs $L^{TR}_{\xi-G}(r_l)$ and $L^{TR}_{\xi-C}(r_l)$.

Rx), and $f_{T_{max}} = k_T^{TR} = \eta_{SB_1} = \eta_{SB_3} = \eta_{DB} = 0$ (fixed Tx, no scattering around Tx). Expressions for other LCRs and AFDs based on the isotropic one-ring model only around the Rx, e.g., those in [71] and [102], can be similarly obtained. The LCR and AFD based on the non-isotropic two-ring model with single-bounced rays [95] are obtained from (5.35) and (5.44), respectively, by setting $K = f_{T_{max}} = \eta_{SB_3} = \eta_{DB} = 0$. Finally, the LCR and AFD for isotropic M2M Rayleigh channels [26] are obtained from (5.35) and (5.44), respectively, by setting $K = k_T^{TR} = k_R^{TR} = \eta_{SB_1} = \eta_{SB_2} = \eta_{SB_3} = 0$.

5.5 Numerical Results and Analysis

Unless otherwise specified, all the results presented in this section are obtained using $f_c = 5.9$ GHz, $f_{T_{max}} = f_{R_{max}} = 570$ Hz, $D = 300$ m, $a = 200$ m, and $R_T = R_R = 40$ m.

FIGURES 5.5 and 5.6 illustrate the space and frequency CFs of the single- and double-bounce two-ring model and single-bounce ellipse model for different scenarios. It is

obvious that both the space and frequency CFs vary significantly for different scenarios (Scenario *a* and Scenario *b*, see caption of Fig. 5.5). We also notice that directions of motion (related to the values of γ_T and γ_R) have no impact on the space and frequency CFs.

FIGURE 5.7 shows normalised Doppler PSDs for different scenarios (Scenario *a* and Scenario *b*, see caption of Fig. 5.7). For Scenario *a*, it is clear that no matter what the direction of motion (same or opposite) and the shape of the scattering region (one-ring, two-ring, or ellipse) are, the Doppler PSD of single-bounced rays is similar to the *U*-shaped PSD of F2M cellular channels[2], whereas the Doppler PSD of double-bounced rays has a "rounded" shape having a peak in the middle. This indicates that the *U*-shaped Doppler PSD will appear when high dependency exists between the AoD and AoA, while the "rounded" shaped Doppler PSD will appear when the AoD and AoA are relatively independent. We can also observe that for different directions of motion, the Doppler PSDs of double-bounced rays remain unchanged, while the Doppler PSDs of single-bounced rays change with different ranges of Doppler frequencies. More importantly, we found that the impact of single-bounced rays from different rings (ring around the Tx or Rx) on the Doppler PSD are the same for M2M channels when the Tx and Rx are moving in opposite directions, leading to the *U*-shaped Doppler PSD for the single-bounce two-ring model. When the Tx and Rx are moving in the same direction, the impact of single-bounced rays from different rings on the Doppler PSD are different in terms of the range of Doppler frequencies, which results in the double-*U*-shaped Doppler PSD for the single-bounce two-ring model. Therefore, we can conclude that a more realistic M2M channel model should take into account the different contributions from different rings. However, this has not been considered in all the existing M2M GBSMs, e.g., in [28]. It is worth mentioning that by setting one terminal fixed (i.e., $f_{T_{max}} = 0$), our M2M model can reduce to a F2M model. In this case, we studied the Doppler PSD for the corresponding single- and double-bounce two-ring F2M models and single-bounce ellipse F2M model, and found that they have the same *U*-shaped PSD. For brevity,

[2]Note that when the Tx and Rx move in the same direction, the Doppler PSD of the single-bounce ellipse model is not an exact *U*-shape, but it is reasonable to consider it as an approximate *U*-shape since peaks exist in both the left and right sides of the Doppler PSD instead of in the middle.

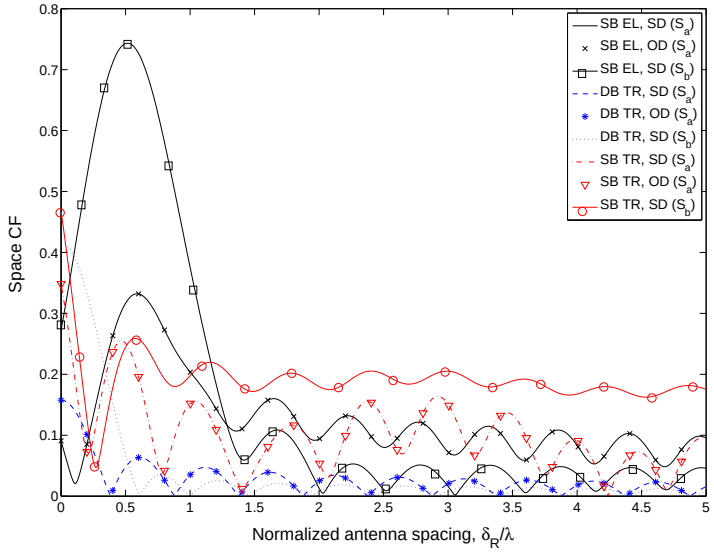

FIGURE 5.5: Space CFs of the single-bounce (SB) ellipse (EL) model, double-bounce (DB) two-ring (TR) model, and SB TR model for different scenarios ($\tau = 0$, $\chi = 0$, and $\delta_T = 2$). SD: same direction ($\gamma_T = \gamma_R = 0$); OD: opposite direction ($\gamma_T = 0$ and $\gamma_R = \pi$); Scenario a (S_a): $k_T^{TR} = k_R^{TR} = k_R^{EL} = 0$ (isotropic environments); Scenario b (S_b): $k_T^{TR} = k_R^{TR} = k_R^{EL} = 3$ (non-isotropic environments), $\mu_T^{TR} = \pi/4$, and $\mu_R^{TR} = \mu_R^{EL} = 3\pi/4$.

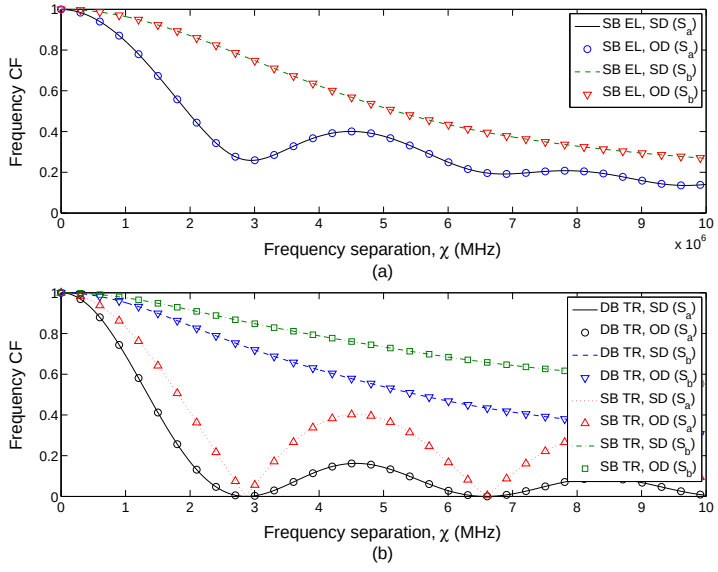

FIGURE 5.6: Frequency CFs of the single-bounce (SB) ellipse (EL) model, double-bounce (DB) two-ring (TR) model, and SB TR model for different scenarios ($\tau = 0$, $\delta_T = \delta_R = 0$). SD: same direction ($\gamma_T = \gamma_R = 0$); OD: opposite direction ($\gamma_T = 0$ and $\gamma_R = \pi$); Scenario a (S_a): $k_T^{TR} = k_R^{TR} = k_R^{EL} = 0$ (isotropic environments); Scenario b (S_b): $k_T^{TR} = k_R^{TR} = k_R^{EL} = 3$ (non-isotropic environments), $\mu_T^{TR} = \pi/4$, and $\mu_R^{TR} = \mu_R^{EL} = 3\pi/4$.

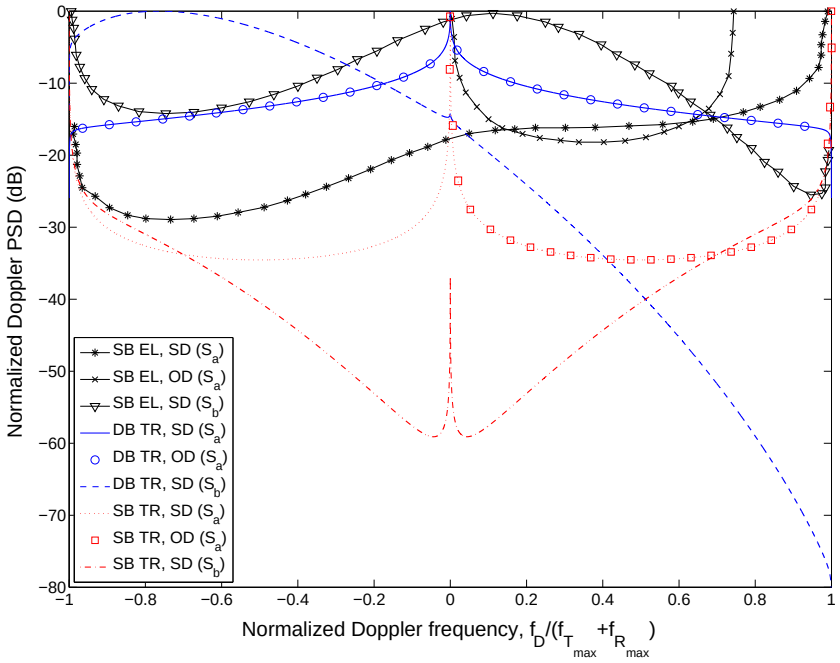

FIGURE 5.7: Normalised Doppler PSDs of the single-bounce (SB) ellipse (EL) model, double-bounce (DB) two-ring (TR) model, and SB TR model for different scenarios ($\delta_T = \delta_R = 0$, $\chi = 0$). SD: same direction ($\gamma_T = \gamma_R = 0$); OD: opposite direction ($\gamma_T = 0$ and $\gamma_R = \pi$); Scenario a (S_a): $k_T^{TR} = k_R^{TR} = k_R^{EL} = 0$ (isotropic environments); Scenario b (S_b): $k_T^{TR} = k_R^{TR} = k_R^{EL} = 3$ (non-isotropic environments), $\mu_T^{TR} = \pi/4$, and $\mu_R^{TR} = \mu_R^{EL} = 3\pi/4$.

the results regarding F2M channels are omitted here. These observations indicate that the impact of single- and double-bounced rays on the Doppler PSD are completely different for M2M channels (U-shaped and "rounded" shaped, respectively), while they are the same for F2M channels (U-shaped). At the end, the comparison of Scenario a and Scenario b illustrates the significant impact of angle spreads (related to the values of k_T^{TR}, k_R^{TR}, and k_R^{EL}) and mean angles (related to the values of μ_T^{TR}, μ_R^{TR}, and μ_R^{EL}) on the Doppler PSD.

FIGURES 5.8 and 5.9 depict the impact of the antenna element spacing and frequency separation on the Doppler PSD, respectively. FIGURE 5.8 shows that the space separation introduces fluctuations in the Doppler PSD no matter what the shape of the scattering region is. FIGURE 5.9 illustrates that the frequency separation only generates fluctuations in the Doppler PSD for the double-bounce two-ring model, while for other cases, the impact of the frequency separation vanishes.

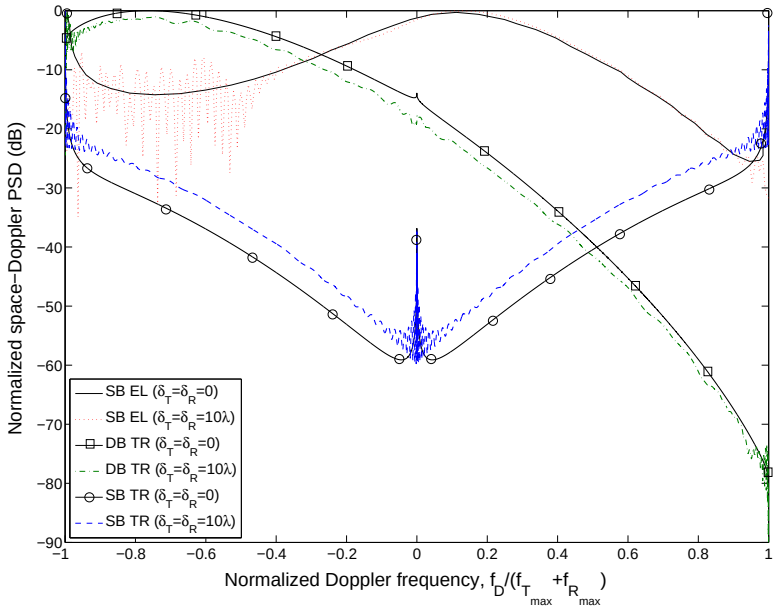

FIGURE 5.8: Normalised space-Doppler PSDs of the single-bounce (SB) ellipse (EL) model, double-bounce (DB) two-ring (TR) model, and SB TR model for different antenna element spacings in a M2M non-isotropic scattering environment ($k_T^{TR} = k_R^{TR} = k_R^{EL} = 3$, $\mu_T^{TR} = \pi/4$, $\mu_R^{TR} = \mu_R^{EL} = 3\pi/4$) with the Tx and Rx moving in the same direction ($\gamma_T = \gamma_R = 0$).

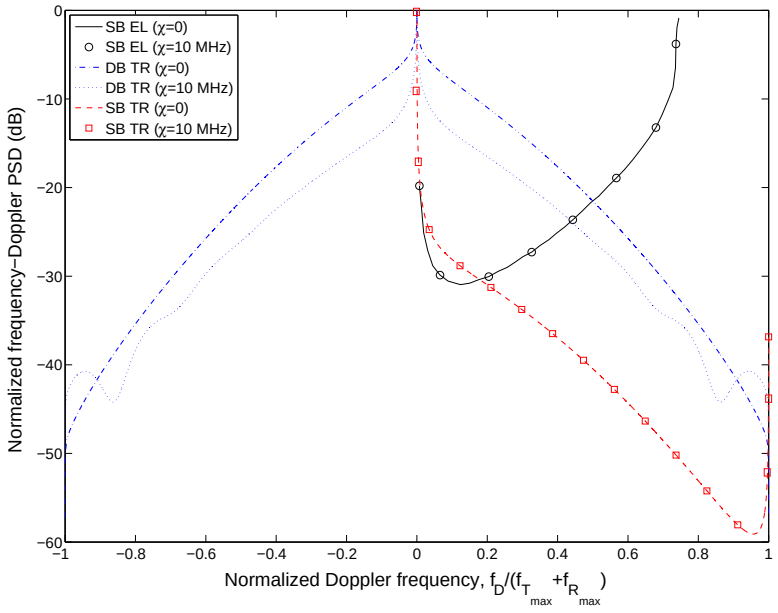

FIGURE 5.9: Normalised frequency-Doppler PSDs of the single-bounce (SB) ellipse (EL) model, double-bounce (DB) two-ring (TR) model, and SB TR model for different frequency separations in a M2M non-isotropic scattering environment ($k_T^{TR} = k_R^{TR} = k_R^{EL} = 3$, $\mu_T^{TR} = \pi/4$, $\mu_R^{TR} = \mu_R^{EL} = 3\pi/4$) with the Tx and Rx moving in the opposite direction ($\gamma_T = 0$ and $\gamma_R = \pi$).

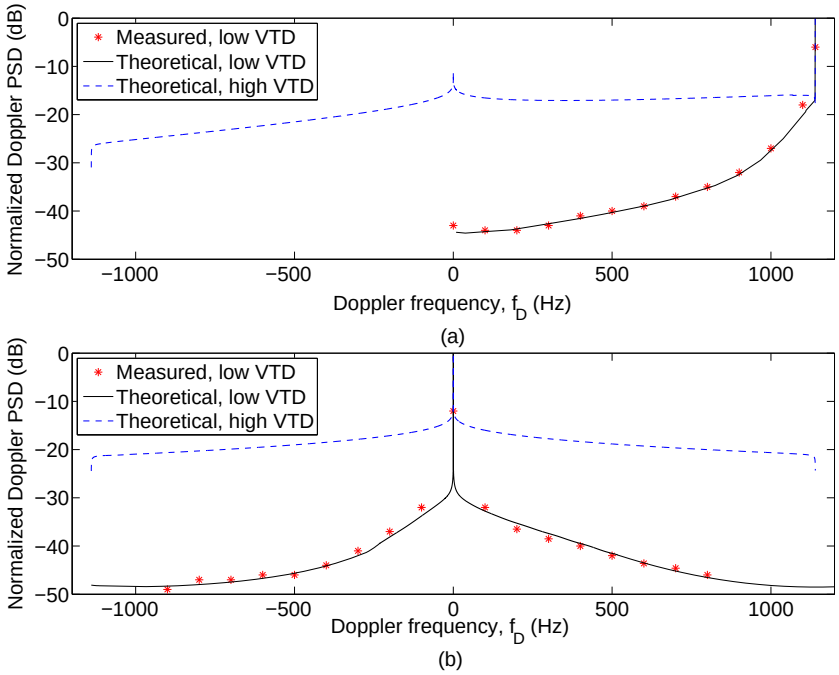

FIGURE 5.10: Normalised Doppler PSDs of the proposed adaptive model for different SISO pico-cell scenarios ($\delta_T = \delta_R = 0$, $\chi = 0$): (a) Tx and Rx are moving in opposite directions, (b) Tx and Rx are moving in the same direction. VTD: vehicular traffic density.

FIGURES 5.10 (a) and (b) show the theoretical Doppler PSDs obtained from the proposed M2M model for different VTDs (low and high) when the Tx and Rx are moving in opposite directions and same direction, respectively. For further comparison, the measured data taken from FIGURES 4 (a) and (c) in [31] are also plotted in FIGURES 5.10 (a) and (b), respectively. In [31], the measurement campaigns were performed at a carrier frequency of 5.9 GHz on an expressway with a low VTD in the metropolitan Atlanta, Georgia area and the maximum Doppler frequencies were $f_{T_{max}} = f_{R_{max}} = 570$ Hz. The distance between the Tx and Rx was approximately $D = 300$ m and the directions of movement were $\gamma_T = 0$, $\gamma_R = \pi$ (opposite direction, shown in FIGURE 4 (a) in [31]) and $\gamma_T = \gamma_R = 0$ (same direction, shown in FIGURE 4 (c) in [31]). Both the Tx and Rx were equipped with one omnidirectional antenna, i.e., SISO case. Based on the measured scenarios in [31], we chose the following environment-related parameters: $k_T^{TR} = 6.6$, $k_R^{TR} = 8.3$, $k_R^{EL} = 5.5$, $\mu_T^{TR} = 12.8°$, $\mu_R^{TR} = 178.7°$, and $\mu_R^{EL} = 131.6°$ for FIGURE 5.10 (a), and $k_T^{TR} = 9.6$, $k_R^{TR} = 3.6$,

k_R^{EL}=11.5, μ_T^{TR}=21.7°, μ_R^{TR}=147.8°, and μ_R^{EL}=171.6° for FIGURE 5.10 (b). Considering the constraints of the Ricean factor and energy-related parameters for different propagation scenarios as mentioned in Section 5.2, we choose the following parameters in order to fit the measured Doppler PSDs reported in [31] for the two scenarios with low VTD: 1) K=2.186, η_{DB}=0.005, η_{SB_1}=0.252, η_{SB_2}=0.262, and η_{SB_3}=0.481 for FIGURE 5.10 (a); 2) K=3.786, η_{DB}=0.051, η_{SB_1}=0.335, η_{SB_2}=0.203, and η_{SB_3}=0.411 for FIGURE 5.10 (b). The excellent agreement between the theoretical results and measured data confirms the utility of the proposed model. The environment-related parameters for high VTD in FIGURES 5.10 (a) and (b) are the same as those for low VTD except $k_T^{TR} = k_R^{TR} = 0.6$, which are related to the distribution of moving cars (normally, the smaller values the more distributed moving cars, i.e., the higher VTD). The Doppler PSDs for high VTD shown in FIGURES 5.10 (a) and (b) were obtained with the parameters $K = 0.2$, $\eta_{DB} = 0.715$, $\eta_{SB_1} = \eta_{SB_2} = 0.115$, and $\eta_{SB_3} = 0.055$. Unfortunately, to the best of the authors' knowledge, no measurement results (e.g., in [31, 32, 33, 34, 35, 55, 103]) were available regarding the impact of high VTD (e.g., a traffic jam) on the Doppler PSD.

Comparing the theoretical Doppler PSDs in FIGURES 5.10 (a) and (b), we observe that the VTD significantly affects both the shape and value of the Doppler PSD for M2M channels. The Doppler PSD tends to be more evenly distributed across all Doppler frequencies with a higher VTD. This is because with a high VTD, the received power mainly comes from the moving cars around the Tx and Rx from all directions, while the power of the LoS component is not that significant. This means that the received power for different Doppler frequencies (directions) is more evenly distributed. With a low VTD, the received power from the LoS component may be significant, while the power from the moving cars may be small. Therefore, the power tends to be concentrated on some Doppler frequencies.

FIGURES 5.11 (a) and (b) depict the theoretical LCRs and AFDs for different VTDs (low or high) in M2M Ricean fading channels when the Tx and Rx are moving in the same direction, respectively. The parameters $f_c = 5.2$ GHz and $f_{T_{max}} = f_{R_{max}} =$ 500 Hz are used in these figures. For a further comparison, the measured results taken

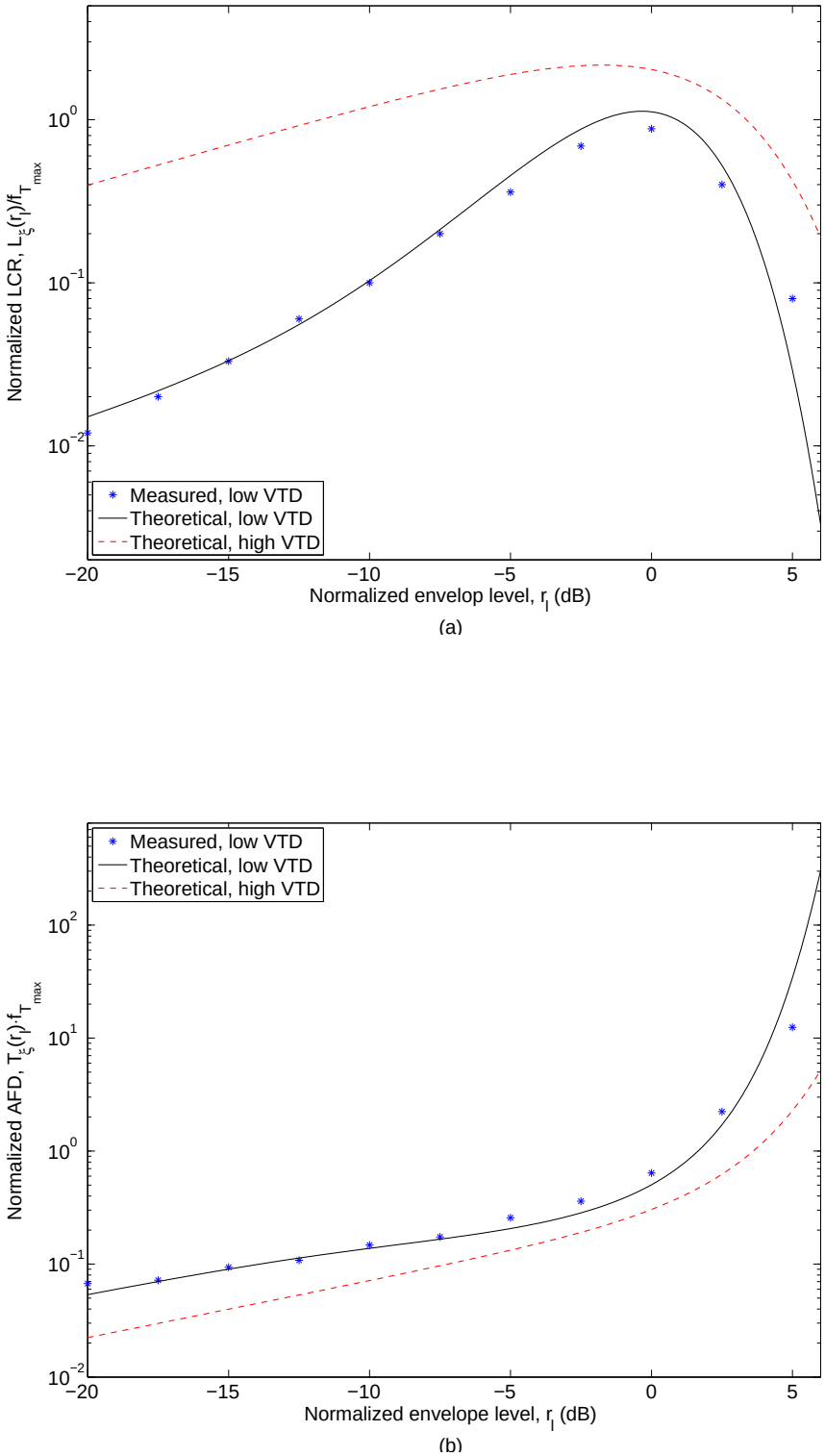

FIGURE 5.11: (a) LCRs and (b) AFDs of the developed M2M channel model with a low or high vehicular traffic density (VTD) when the Tx and Rx are moving in the same direction.

from FIGURE 8 (b) in [103] are also plotted in FIGURES 5.11 (a) and (b). In [103], the measurement campaigns were performed on a highway with a low VTD in Germany and the directions of movement of the Tx and Rx were $\gamma_T = \gamma_R = 0$ (same direction). Based on the measured scenarios in [103], we chose the following environment-related parameters for FIGURES 5.11 (a) and (b): $\mu_T^{TR} = 33.2°$, $k_T^{TR} = 18.2$, $\mu_R^{TR} = 148.6°$, $k_R^{TR} = 13.3$, $\mu_R^{EL} = 148.6°$, and $k_R^{EL} = 8.6$. Considering the constraints of the Ricean factor and energy-related parameters for a propagation scenario with low VTD as mentioned in Section 5.2, we choose the following parameters in order to fit the measured LCR/AFD reported in [103]: $K = 4.26$, $\eta_{DB} = 0.08$, $\eta_{SB_1} = 0.12$, $\eta_{SB_2} = 0.18$, and $\eta_{SB_3} = 0.62$. The excellent agreement between the theoretical results and measured data confirms the utility of the proposed model. The environment-related parameters for a high VTD in FIGURES 5.11 (a) and (b) are the same as those for a low VTD except $k_T^{TR} = k_R^{TR} = 0.6$. The theoretical LCR and AFD for a high VTD shown in FIGURES 5.11 (a) and (b) were obtained with the parameters $K = 0.56$, $\eta_{DB} = 0.58$, $\eta_{SB_1} = 0.1$, $\eta_{SB_2} = 0.18$, $\eta_{SB_3} = 0.14$. Unfortunately, to the best of the authors' knowledge, no measurement results, e.g., [31, 32, 33, 34, 35, 55, 103], were available regarding the impact of high VTD (e.g., a traffic jam) on the LCR and AFD.

Comparing the theoretical LCRs and AFDs in FIGURES 5.11 (a) and (b), respectively, we observe that the VTD significantly affects the LCR and AFD for M2M channels. Moreover, FIGURE 5.11 (a) shows that the fades are shallower when the VTD is lower. We see from FIGURE 5.11 (b) that the AFD tends to be larger with lower VTD. This is because with a high VTD, the received power mainly comes from the moving cars around the TX and Rx from all directions, while for a low VTD the received power concentrates on several directions, e.g., the directions of LoS components and/or large stationary scatterers on the roadside environment.

5.6 Summary

In this chapter, we have proposed a generic and adaptive RS-GBSM for non-isotropic scattering MIMO M2M Ricean fading channels. By adjusting some model parameters

and with the help of the newly derived general relationship between the AoA and AoD, the proposed model is adaptable to a wide variety of M2M propagation environments. In addition, the VTD is for the first time taken into account in the RS-GBSM for modeling M2M channels. From this model, we have derived the STF CF and the corresponding SDF PSD for non-isotropic scattering environments, where the closed-form expressions are available in the case of the single-bounce two-ring model for macro-cell and micro-cell scenarios, and the double-bounce two-ring model for any scenarios. Moreover, the envelope LCR and AFD have been derived in terms of the simplified version (SISO) of the proposed MIMO M2M model. Based on the derived STF CFs and SDF PSDs, we have further investigated the degenerate CFs and PSDs in detail and found that some parameters (e.g., the angle spread, direction of motion, antenna element spacing, etc.) have a great impact on the resulting CFs and PSDs. It has also been demonstrated that for M2M isotropic scattering scenarios, no matter what the direction of motion and shape of the scattering region are, single-bounced rays will result in the U-shaped Doppler PSD, while double-bounced rays will result in the "rounded"-shaped Doppler PSD. More importantly, we have investigated the impact of the VTD on the Doppler PSD, envelope LCR, and AFD and found that with a lower VTD results the Doppler PSD tends to be concentrated on some Doppler frequencies, the envelope LCR is smaller (i.e., the shallower fades) and the AFD tends to be larger. Finally, it has been shown that theoretical Doppler PSDs, envelope LCRs, and AFDs match the measured data in [31, 103], validating the utility of our model.

Chapter 6

Modelling and Simulation of Wideband MIMO Mobile-to-Mobile Channels

6.1 Introduction

In Chapter 5, we have proposed a narrowband MIMO M2M RS-GBSM for non-isotropic scattering Ricean fading channels. However, most potential transmission schemes for M2M communications use relatively wide bandwidths (e.g., approximately 10 MHz for the IEEE 802.11p standard). The underlying M2M channels present frequency-selectivity since the signal bandwidth is larger than the coherence bandwidth of such channels (normally around 4 – 6 MHz [32]). Therefore, wideband M2M channel models are indispensable.

As mentioned in Chapter 2, only one 3D wideband GBSM was proposed in [30] for MIMO M2M Ricean fading channels. However, the model cannot describe the channel statistics for different time delays, which are important for M2M channels as mentioned in [31, 33]. Although the measurement campaign in [32] has demonstrated that the VTD significantly affects the channel statistics for M2M channels, the impact of the VTD is not considered in the wideband model in [30]. In addition, it is non-trivial

to use this model to match any given or measured PDP since many parameters need adjustment via a complicated procedure.

To fill the above gap, in the first part of this chapter, based on the application of the TDL concept, we propose a new 2D wideband M2M RS-GBSM which is an extension of the narrowband model proposed in Chapter 5 with respect to the frequency-selectivity. This wideband model comprises a two-ring model and a multiple confocal ellipses model incorporating LoS, single-, and double-bounced rays. By using the multiple confocal ellipses to construct a TDL structure, the proposed wideband model can investigate the channel statistics for different time delays, i.e., per-tap channel statistics, and can also easily match any specified or measured PDP. In order to take into account the impact of the VTD on channel statistics for every tap in the proposed wideband model while maintaining a similar complexity to that of our narrowband model described in Chapter 5, we first distinguish between the moving cars and the stationary roadside environment, which are described by a two-ring model and a multiple confocal ellipses model, respectively. Then, from the analysis of real environments of M2M communications, we generate a novel and simple approach to incorporate the impact of the VTD into every tap of our wideband model. From the proposed model, we derive the ST CF, the corresponding SD PSD, the frequency CF (FCF), and the corresponding PDP. Finally, the obtained theoretical per-tap Doppler PSDs and measurement data in [31] are compared. Excellent agreement between them demonstrates the utility of the proposed model.

Since the proposed wideband RS-GBSM is actually a mathematical reference model that assumes an infinite number of effective scatterers, it cannot be directly implemented in practice. Therefore, accurate M2M channel simulation models play a major role in the practical simulation and performance evaluation of M2M systems. As addressed in Chapter 2, up to now, many M2M channel simulators [36, 39, 40] are limited to isotropic scattering narrowband SISO channels, while only [27, 29] proposed SoS simulation models for non-isotropic scattering narrowband MIMO M2M channels. So far, only one deterministic SoS simulation model was proposed in [30] for non-isotropic scattering wideband MIMO M2M channels. No stochastic SoS simulation models for

non-isotropic scattering wideband MIMO M2M channels are available in the current literature.

The second part of this chapter derives new deterministic and stochastic wideband MIMO M2M channel simulation models based on the proposed wideband RS-GBSM. First, we propose a new wideband deterministic simulation model. Based on the TDL concept, the proposed deterministic model employs a combination of two-ring and multiple confocal ellipses models that comprise LoS, single-, and double-bounced rays. The statistical properties of our model are verified by simulations. Furthermore, a new parameter computation method, named improved modified method of equal areas (IMMEA), is proposed for deterministic MIMO M2M channel simulators under non-isotropic scattering conditions. Compared to the existing parameter computation methods, i.e., the MMEA in [27] and the method in [29, 30], the IMMEA provides better approximation to the desired properties of the mathematical reference model. By allowing at least one parameter (frequencies and/or gains) to be a random variable, our wideband deterministic model can be further modified to a wideband stochastic model. Numerical results validate the utility of the resulting stochastic model. It is worth stressing that the proposed wideband mathematical reference model can be easily reduced to our narrowband model in Chapter 5 by removing the frequency-selectivity. Therefore, the corresponding narrowband simulation models, whose mathematical reference model is the narrowband MIMO M2M RS-GBSM in Chapter 5, can be obtained by removing the frequency-selectivity from the proposed wideband simulation models.

The remainder of this paper is outlined as follows. Section 6.2 describes the new M2M RS-GBSM for non-isotropic scattering wideband MIMO M2M Ricean fading channels. In Section 6.3, based on the proposed new model, the ST CF, the corresponding SD PSD, the FCF, and the corresponding PDP are derived. Section 6.4 details the proposed deterministic and stochastic SoS simulation models. Numerical results and analysis are presented in Section 6.5. Finally, concluding remarks are drawn in Section 6.6.

6.2 A New Wideband MIMO Mobile-to-Mobile Mathematical Reference Model

Let us now consider a wideband MIMO M2M communication system with M_T transmit and M_R receive omni-directional antenna elements. Both the Tx and Rx are equipped with low elevation antennas. FIGURE 6.1 illustrates the geometry of the proposed RS-GBSM, which is the combination of a two-ring model and a multiple confocal ellipses model incorporating LoS, single- and double-bounced rays. Note that in FIGURE 6.1, we used uniform linear antenna arrays with $M_T = M_R = 2$ as an example. The two-ring model defines two rings of effective scatterers, one around the Tx and the other around the Rx. Suppose there are $N_{1,1}$ effective scatterers around the Tx lying on a ring of radius R_T and the $n_{1,1}$th ($n_{1,1}=1, ..., N_{1,1}$) effective scatterer is denoted by $s^{(n_{1,1})}$. Similarly, assume there are $N_{1,2}$ effective scatterers around the Rx lying on a ring of radius R_R and the $n_{1,2}$th ($n_{1,2}=1, ..., N_{1,2}$) effective scatterer is denoted by $s^{(n_{1,2})}$. The multiple confocal ellipses model with the Tx and Rx located at the foci represents the TDL structure and has $N_{l,3}$ effective scatterers on the lth ellipse (i.e., lth tap), where $l=1, 2, ..., L$ with L being the total number of ellipses or taps. The semi-major axis of the lth ellipse and the $n_{l,3}$th ($n_{l,3}=1, ..., N_{l,3}$) effective scatterer are denoted by a_l and $s^{(n_{l,3})}$, respectively. The distance between the Tx and Rx is $D=2f$ with f denoting the half length of the distance between the two focal points of ellipses. The antenna element spacings at the Tx and Rx are designated by δ_T and δ_R, respectively. The multi-element antenna tilt angles are denoted by β_T and β_R. The Tx and Rx move with speeds υ_T and υ_R in directions determined by the angles of motion γ_T and γ_R, respectively. The AoA of the wave traveling from an effective scatterer $s^{(n_{1,1})}$, $s^{(n_{1,2})}$, and $s^{(n_{l,3})}$ toward the Rx are denoted by $\phi_R^{(n_{1,1})}$, $\phi_R^{(n_{1,2})}$, and $\phi_R^{(n_{l,3})}$, respectively. The AoD of the wave that impinges on the effective scatterer $s^{(n_{1,1})}$, $s^{(n_{1,2})}$, and $s^{(n_{l,3})}$ are designated by $\phi_T^{(n_{1,1})}$, $\phi_T^{(n_{1,2})}$, and $\phi_T^{(n_{l,3})}$, respectively. Note that ϕ^{LoS} denotes the AoA of a LoS path.

The MIMO fading channel can be described by a matrix $\mathbf{H}(t) = [h_{oq}(t, \tau')]_{M_R \times M_T}$ of size $M_R \times M_T$. According to the TDL concept, the complex impulse response

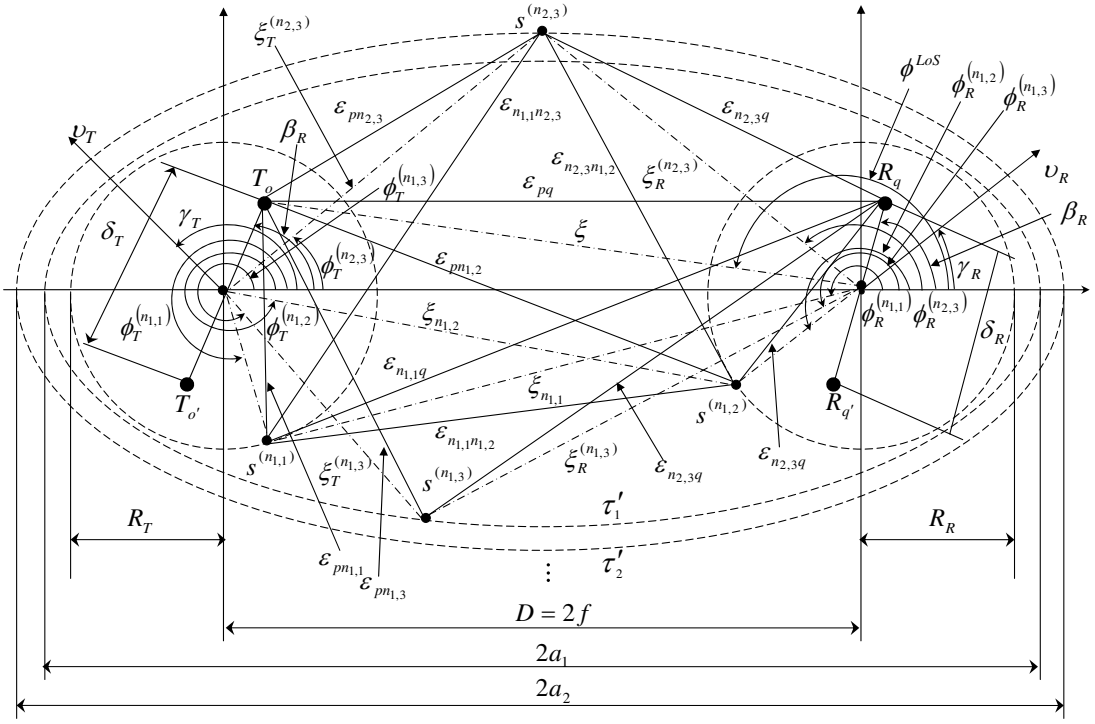

FIGURE 6.1: A geometry-based stochastic channel model combining a two-ring model and a multiple confocal ellipses model with LoS, single- and double-bounced rays for a wideband MIMO M2M channel.

between the oth ($o = 1, ..., M_T$) Tx, T_o, and the qth ($q = 1, ..., M_R$) Rx, R_q, can be expressed as $h_{oq}(t, \tau') = \sum_{l=1}^{L} c_l h_{l,oq}(t)\, \delta(\tau' - \tau_l')$ where c_l represents the gain of the lth tap, $h_{l,oq}(t)$ and τ_l' denote the complex time-variant tap coefficient and the discrete propagation delay of the lth tap, respectively. From the above RS-GBSM, the complex tap coefficient for the first tap of the $T_o - R_q$ link is a superposition of the LoS, single- and double-bounced components, and can be expressed as

$$h_{1,oq}(t) = h_{1,oq}^{LoS}(t) + \sum_{i=1}^{I} h_{1,oq}^{SB_i}(t) + h_{1,oq}^{DB}(t) \tag{6.1}$$

with

$$h_{1,oq}^{LoS}(t) = \sqrt{\frac{K_{oq}}{K_{oq}+1}} e^{-j2\pi f_c \tau_{oq}} e^{j\left[2\pi f_{T_{max}} t \cos\left(\pi - \phi^{LoS} + \gamma_T\right) + 2\pi f_{R_{max}} t \cos\left(\phi^{LoS} - \gamma_R\right)\right]} \tag{6.2a}$$

$$h_{1,oq}^{SB_i}(t) = \sqrt{\frac{\eta_{SB_{1,i}}}{K_{oq}+1}} \lim_{N_{1,i}\to\infty} \sum_{n_{1,i}=1}^{N_{1,i}} \frac{1}{\sqrt{N_{1,i}}} e^{j\left(\psi_{n_{1,i}} - 2\pi f_c \tau_{oq,n_{1,i}}\right)} \times e^{j\left[2\pi f_{T_{max}} t\cos\left(\phi_T^{(n_{1,i})}-\gamma_T\right)+2\pi f_{R_{max}} t\cos\left(\phi_R^{(n_{1,i})}-\gamma_R\right)\right]} \tag{6.2b}$$

$$h_{1,oq}^{DB}(t) = \sqrt{\frac{\eta_{DB_1}}{K_{oq}+1}} \lim_{N_{1,1},N_{1,2}\to\infty} \sum_{n_{1,1},n_{1,2}=1}^{N_{1,1},N_{1,2}} \frac{1}{\sqrt{N_{1,1}N_{1,2}}} e^{j\left(\psi_{n_{1,1},n_{1,2}} - 2\pi f_c \tau_{oq,n_{1,1},n_{1,2}}\right)} \times e^{j\left[2\pi f_{T_{max}} t\cos\left(\phi_T^{(n_{1,1})}-\gamma_T\right)+2\pi f_{R_{max}} t\cos\left(\phi_R^{(n_{1,2})}-\gamma_R\right)\right]}. \tag{6.2c}$$

where $\tau_{oq}=\varepsilon_{oq}/c$, $\tau_{oq,n_{1,i}}=(\varepsilon_{on_{1,i}}+\varepsilon_{n_{1,i}q})/c$, and $\tau_{oq,n_{1,1},n_{1,2}}=(\varepsilon_{on_{1,1}}+\varepsilon_{n_{1,1}n_{1,2}}+\varepsilon_{n_{1,2}q})/c$ are the travel times of the waves through the link T_o-R_q, $T_o-s^{(n_{1,i})}-R_q$, and $T_o-s^{(n_{1,1})}-s^{(n_{1,2})}-R_q$, respectively, as shown in FIGURE 6.1. The symbol $I=3$ and c and K_{oq} designate the speed of light and the Ricean factor, respectively. The complex tap coefficient for other taps ($l'>1$) of the T_o-R_q link is a superposition of the single- and double-bounced components, and can be expressed as

$$h_{l',oq}(t) = h_{l',oq}^{SB_3}(t) + h_{l',oq}^{DB_1}(t) + h_{l',oq}^{DB_2}(t) \tag{6.3}$$

with

$$h_{l',oq}^{SB_3}(t) = \sqrt{\eta_{SB_{l',3}}} \lim_{N_{l',3}\to\infty} \sum_{n_{l',3}=1}^{N_{l',3}} \frac{1}{\sqrt{N_{l',3}}} e^{j\left(\psi_{n_{l',3}} - 2\pi f_c \tau_{oq,n_{l',3}}\right)} \times e^{j\left[2\pi f_{T_{max}} t\cos\left(\phi_T^{(n_{l',3})}-\gamma_T\right)+2\pi f_{R_{max}} t\cos\left(\phi_R^{(n_{l',3})}-\gamma_R\right)\right]} \tag{6.4a}$$

$$h_{l',oq}^{DB_{1(2)}}(t) = \sqrt{\eta_{DB_{l',1(2)}}} \lim_{N_{1,1(2)},N_{l',3}\to\infty} \sum_{n_{1,1(2)},n_{l',3}=1}^{N_{1,1(2)},N_{l',3}} \frac{1}{\sqrt{N_{1,1(2)}N_{l',3}}} e^{j\left(\psi_{n_{1,1(2)},n_{l',3}} - 2\pi f_c \tau_{oq,n_{1,1(2)},n_{l',3}}\right)} \times e^{j2\pi t\left[f_{T_{max}}\cos\left(\phi_T^{(n_{1(l'),1(3)})}-\gamma_T\right)+f_{R_{max}}\cos\left(\phi_R^{(n_{l'(1),3(2)})}-\gamma_R\right)\right]}. \tag{6.4b}$$

$\tau_{oq,n_{l',3}}=(\varepsilon_{on_{l',3}}+\varepsilon_{n_{l',3}q})/c$ and $\tau_{oq,n_{1,1(2)},n_{l',3}}=(\varepsilon_{on_{1(l'),1(3)}}+\varepsilon_{n_{1(l'),1(3)}n_{l'(1),3(2)}}+\varepsilon_{n_{l'(1),3(2)}q})/c$ are the travel times of the waves through the link $T_o-s^{(n_{l',3})}-R_q$ and $T_o-s^{(n_{1,1})}(s^{(n_{l',3})})-s^{(n_{l',3})}(s^{(n_{1,2})})-R_q$, respectively, as illustrated in FIGURE 6.1. Energy-related parameters $\eta_{SB_{1,i}}$, η_{DB_1} and $\eta_{SB_{l',3}}$, $\eta_{DB_{l',1(2)}}$ specify how much the single-, double-bounced rays contribute to the total scattered power of the first tap and other taps, respectively. Note that these energy-related parameters satisfy $\sum_{i=1}^{I}\eta_{SB_{1,i}}+\eta_{DB_1}=1$ and

$\eta_{SB_{l',3}}+\eta_{DB_{l',1}}+\eta_{DB_{l',2}}=1$. The phases $\psi_{n_{1,i}}$, $\psi_{n_{1,1},n_{1,2}}$, $\psi_{n_{l',3}}$, and $\psi_{n_{1,1(2)},n_{l',3}}$ are i.i.d. random variables with uniform distributions over $[-\pi,\pi)$, $f_{T_{max}}$ and $f_{R_{max}}$ are the maximum Doppler frequencies with respect to the Tx and Rx, respectively.

As presented in [32], the VTD significantly affects statistical properties at all taps of a wideband M2M channel. To take the impact of the VTD into account, we first distinguish between the moving cars around the Tx and Rx and the stationary roadside environment by using the two-ring model to mimic the moving cars and the multiple confocal ellipses model to depict the stationary roadside environment. For the first tap, the single-bounced rays are generated from the scatterers located on either of the two rings or the first ellipse, while the double-bounced rays are produced from the scatterers located on both rings. This means that the first tap contains a LoS component, a two-ring model with single- and double-bounced rays, and an ellipse model with single-bounced rays, as shown in FIGURE 6.2. For a low VTD, the value of K_{oq} is large since the LoS component can bear a significant amount of power. Also, the received scattered power is mainly from waves reflected by the stationary roadside environment described by the scatterers located on the first ellipse. The moving cars represented by the scatterers located on the two rings are sparse and thus more likely to be single-bounced, rather than double-bounced. This indicates that $\eta_{SB_{1,3}}>\max\{\eta_{SB_{1,1}},\eta_{SB_{1,2}}\}>\eta_{DB_1}$. For a high VTD, the value of K_{oq} is smaller than the one in the low VTD scenario. Also, due to the large number of moving cars, the double-bounced rays of the two-ring model bear more energy than single-bounced rays of two-ring and ellipse models, i.e, $\eta_{DB_1}>\max\{\eta_{SB_{1,1}},\eta_{SB_{1,2}},\eta_{SB_{1,3}}\}$.

For other taps, we assume that the single-bounced rays are generated only from the scatterers located on the corresponding ellipse, while the double-bounced rays are caused by the scatterers from the combined one ring (either of the two rings) and the corresponding ellipse, as illustrated in FIGURE 6.2. Note that according to the TDL structure, the double-bounced rays in one tap must be smaller in distance than the single-bounced rays on the next ellipse. As shown in Appendix J, this is valid only if the condition $\max\{R_T,R_R\}<\min\{a_{l+1}-a_l\}$ is fulfilled. For many current M2M channel measurement campaigns, e.g., in [31, 32, 33], the resolution in delay is 100 ns.

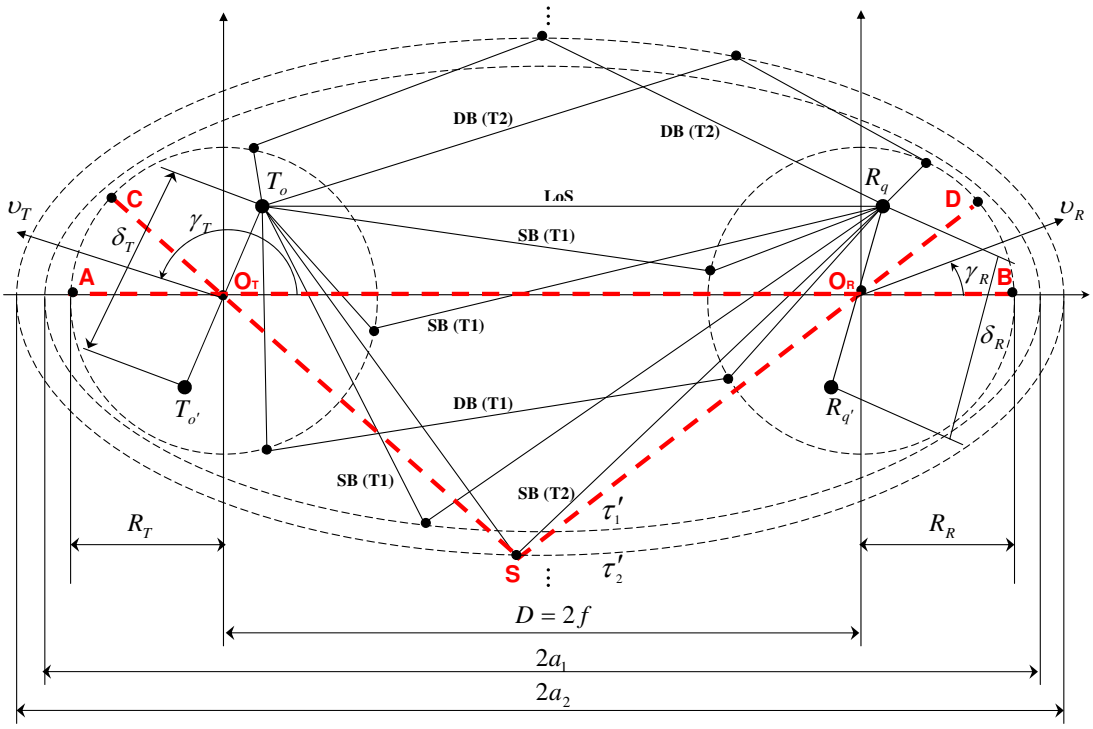

FIGURE 6.2: Geometrical description of the LoS, single- and double-bounced rays for different taps in the proposed wideband MIMO M2M GBSM. SB: single-bounce; DB: double-bounce; T1: tap 1; T2: tap 2.

Then, the above condition can be modified as $\max\{R_T, R_R\} \leq 15$ m by calculating the equality $2(a_l - a_{l-1}) = c \cdot \tau'$ with $c = 3 \times 10^8$ m/s and $\tau' = 100$ ns. This indicates that the maximum acceptable width of the road is 30 m, which is sufficiently large to cover most roads in reality. In other words, the proposed wideband model with the specified TDL structure is valid for different scenarios. For a low VTD, the received scattered power is mainly from waves reflected by the stationary roadside environment described by the scatterers located on the ellipse. This indicates that $\eta_{SB_{l',3}} > \max\{\eta_{DB_{l',1}}, \eta_{DB_{l',2}}\}$. For a high VTD, due to the large number of moving cars, the double-bounced rays from the combined one-ring and ellipse models bear more energy than the single-bounced rays of the ellipse model, i.e, $\min\{\eta_{DB_{l',1}}, \eta_{DB_{l',2}}\} > \eta_{SB_{l',3}}$.

From FIGURE 6.1, based on the application of the law of cosines in triangles and the following assumptions $\min\{R_T, R_R, a - f\} \gg \max\{\delta_T, \delta_R\}$ and $D \gg \max\{R_T, R_R\}$,

and using the approximation $\sqrt{1+x} \approx 1 + x/2$ for small x, we have

$$\varepsilon_{oq} \approx D - k_o\delta_T \cos\beta_T - k_q\delta_R \cos(\phi^{LoS} - \beta_R) \tag{6.5a}$$

$$\varepsilon_{on_{1,1}} \approx R_T - k_o\delta_T \cos(\phi_T^{(n_{1,1})} - \beta_T) \tag{6.5b}$$

$$\varepsilon_{n_{1,1}q} \approx D - R_T \cos\phi_T^{(n_{1,1})} - k_q\delta_R \cos(\phi_R^{(n_{1,1})} - \beta_R) \tag{6.5c}$$

$$\varepsilon_{on_{1,2}} \approx D + R_R \cos\phi_R^{(n_{1,2})} - k_o\delta_T \cos\left(\phi_T^{(n_{1,2})} - \beta_T\right) \tag{6.5d}$$

$$\varepsilon_{n_{1,2}q} \approx R_R - k_q\delta_R \cos\left(\phi_R^{(n_{1,2})} - \beta_R\right) \tag{6.5e}$$

$$\varepsilon_{n_{1,1}n_{1,2}} \approx D - R_T \cos\phi_T^{(n_{1,1})} - R_R \cos\left(\phi_R^{(n_{1,1})} - \phi_R^{(n_{1,2})}\right) \tag{6.5f}$$

$$\varepsilon_{on_{l,3}} \approx \xi_T^{(l,3)} - k_o\delta_T \cos\left(\phi_T^{(n_{l,3})} - \beta_T\right) \tag{6.5g}$$

$$\varepsilon_{n_{l,3}q} \approx \xi_R^{(l,3)} - k_q\delta_R \cos\left(\phi_R^{(n_{l,3})} - \beta_R\right) \tag{6.5h}$$

$$\varepsilon_{n_{1,1}n_{l',3}} = \sqrt{\left(\xi_T^{(l',3)}\right)^2 + R_T^2 - 2\xi_T^{(l',3)} R_T \cos\left(\phi_T^{(n_{l,1})} - \phi_T^{(n_{l',3})}\right)} \tag{6.5i}$$

$$\varepsilon_{n_{l',3}n_{1,2}} = \sqrt{\left(\xi_R^{(l',3)}\right)^2 + R_R^2 - 2\xi_R^{(l',3)} R_R \cos\left(\phi_R^{(n_{l,2})} - \phi_R^{(n_{l',3})}\right)} \tag{6.5j}$$

where $\phi^{LoS} \approx \pi$, $k_o = (M_T - 2o + 1)/2$, $k_q = (M_R - 2q + 1)/2$, $\xi_T^{(n_{l,3})} = (a_l^2 + f^2 + 2a_l f \times \cos\phi_R^{(n_{l,3})}) / (a_l + f\cos\phi_R^{(n_{l,3})})$, and $\xi_R^{(n_{l,3})} = b_l^2 / \left(a_l + f\cos\phi_R^{(n_{l,3})}\right)$ with b_l denoting the semi-minor axis of the lth ellipse. Note that the AoD $\phi_T^{(n_{1,i})}$, $\phi_T^{(n_{l',3})}$ and AoA $\phi_R^{(n_{1,i})}$, $\phi_R^{(n_{l',3})}$ are independent for double-bounced rays, while they are interdependent for single-bounced rays. By using the results in Chapter 5, we can express the relationships between the AoD and AoA for the single-bounced two-ring model as $\phi_R^{(n_{1,1})} \approx \pi - \Delta_T \sin\phi_T^{(n_{1,1})}$ and $\phi_T^{(n_{1,2})} \approx \Delta_R \sin\phi_R^{(n_{1,2})}$ with $\Delta_T \approx R_T/D$ and $\Delta_R \approx R_R/D$ and for the multiple confocal ellipses model as $\phi_T^{(n_{l,3})} = \arcsin[b_l^2 \sin\phi_R^{(n_{l,3})} / (a_l^2 + f^2 + 2a_l f\cos\phi_R^{(n_{l,3})})]$.

Since the numbers of effective scatterers are assumed to be infinite, i.e., $N_{1,i}, N_{l',3} \to \infty$, the proposed model is actually a mathematical reference model and results in either Ricean PDF (the first tap) or Rayleigh PDF (other taps). For our reference model, the discrete AoDs $\phi_T^{(n_{1,i})}$, $\phi_T^{(n_{l',3})}$ and AoAs $\phi_R^{(n_{1,i})}$, $\phi_R^{(n_{l',3})}$, can be replaced by continuous expressions $\phi_T^{(1,i)}$, $\phi_T^{(l',3)}$ and $\phi_R^{(1,i)}$, $\phi_R^{(l',3)}$, respectively. To characterise these AoDs and AoAs, we use the von Mises PDF given in (3.7). Here, we give the expressions of the the von Mises PDF for the AoD $\phi_T^{(1,1)}$ and AoAs $\phi_R^{(1,2)}$, $\phi_R^{(l,3)}$, which will be used in Sections 6.3 and 6.4. Applying the von Mises PDF to the two-ring model, we

obtain $f\left(\phi_T^{(1,1)}\right)=\exp\left[k_T^{(1,1)}\cos\left(\phi_T^{(1,1)}-\mu_T^{(1,1)}\right)\right]/\left[2\pi I_0\left(k_T^{(1,1)}\right)\right]$ for the AoD $\phi_T^{(1,1)}\in[-\pi,\pi)$ and $f\left(\phi_R^{(1,2)}\right)=\exp\left[k_R^{(1,2)}\cos\left(\phi_R^{(1,2)}-\mu_R^{(1,2)}\right)\right]/\left[2\pi I_0\left(k_R^{(1,2)}\right)\right]$ for the AoA $\phi_R^{(1,2)}\in[-\pi,\pi)$. Similarly, applying the von Mises PDF to the multiple confocal ellipses model, we get $f\left(\phi_R^{(l,3)}\right)=\exp\left[k_R^{(l,3)}\cos\left(\phi_R^{(l,3)}-\mu_R^{(l,3)}\right)\right]/\left[2\pi I_0\left(k_R^{(l,3)}\right)\right]$ with $\phi_R^{(l,3)}\in[-\pi,\pi)$.

6.3 Statistical Properties of the Proposed Wideband MIMO Mobile-to-Mobile Reference Model

In this section, based on the proposed wideband channel model, we will derive the ST CF, the corresponding SD PSD, the FCF, and the corresponding PDP for a non-isotropic scattering environment.

6.3.1 Space-Time Correlation Function

Under the WSSUS condition, the correlation properties of two arbitrary channel impulse responses $h_{oq}(t,\tau')$ and $h_{o'q'}(t,\tau')$ of a MIMO M2M channel are completely determined by the correlation properties of $h_{l,oq}(t)$ and $h_{l,o'q'}(t)$ in each tap since no correlations exist between the underlying processes in different taps. Therefore, we can restrict our investigations to the following ST CF

$$\rho_{h_{l,oq}h_{l,o'q'}}(\tau)=\mathbf{E}\left[h_{l,oq}\left(t\right)h_{l,o'q'}^{*}(t-\tau)\right] \tag{6.6}$$

where $(\cdot)^*$ denotes the complex conjugate operation and $\mathbf{E}[\cdot]$ designates the statistical expectation operator. Since the LoS, single-, and double-bounced components are independent of each other, based on (6.1) we have the following ST CF for the first tap

$$\rho_{h_{1,oq}h_{1,o'q'}}(\tau)=\rho_{h_{1,oq}^{LoS}h_{1,o'q'}^{LoS}}(\tau)+\sum_{i=1}^{I}\rho_{h_{1,oq}^{SB_i}h_{1,o'q'}^{SB_i}}(\tau)+\rho_{h_{1,oq}^{DB}h_{1,o'q'}^{DB}}(\tau)\,. \tag{6.7}$$

Whereas for other taps, according to (6.3) we have the ST CF as

$$\rho_{h_{l',oq}h_{l',o'q'}}(\tau)=\rho_{h^{SB_3}_{l',oq}h^{SB_3}_{l',o'q'}}(\tau)+\rho_{h^{DB_1}_{l',oq}h^{DB_1}_{l',o'q'}}(\tau)+\rho_{h^{DB_2}_{l',oq}h^{DB_2}_{l',o'q'}}(\tau)\,. \tag{6.8}$$

Applying the corresponding von Mises distribution, trigonometric transformations, and the equality $\int_{-\pi}^{\pi}\exp\left(a\sin c+b\cos c\right)dc=2\pi I_0\left(\sqrt{a^2+b^2}\right)$ [101], and following the similar reasoning to Chapter 5, we can obtain the ST CF of the LoS, single-, and double-bounced components as follows.

1) In the case of the LoS component,

$$\rho_{h^{LoS}_{1,oq}h^{LoS}_{1,o'q'}}(\tau)=\sqrt{\frac{K_{oq}K_{o'q'}}{(K_{oq}+1)(K_{o'q'}+1)}}e^{j2\pi G+j2\pi\tau H} \tag{6.9}$$

where $G{=}O\cos\beta_T{-}Q\cos\beta_R$ and $H{=}f_{T_{max}}\cos\gamma_T{-}f_{R_{max}}\cos\gamma_R$ with $O{=}(o'{-}o)\,\delta_T/\lambda$, $Q{=}(q'{-}q)\,\delta_R/\lambda$.

2) In terms of the single-bounce two-ring model

$$\rho_{h^{SB_{1(2)}}_{1,oq}h^{SB_{1(2)}}_{1,o'q'}}(\tau)=\eta_{SB_{1,1(2)}}e^{jC^{SB_{1(2)}}_{T(R)}}\frac{I_0\left\{\sqrt{\left(A^{SB_{1(2)}}_{T(R)}\right)^2+\left(B^{SB_{1(2)}}_{T(R)}\right)^2}\right\}}{\sqrt{(K_{oq}+1)(K_{o'q'}+1)}I_0\left(k^{(1,1(2))}_{T(R)}\right)} \tag{6.10}$$

where

$$A^{SB_{1(2)}}_{T(R)}{=}k^{(1,1(2))}_{T(R)}\cos\mu^{(1,1(2))}_{T(R)}{+}j2\pi\tau f_{T(R)_{max}}\cos\gamma_{T(R)}+j2\pi O(Q)\cos\beta_{T(R)} \tag{6.11a}$$

$$\begin{aligned}B^{SB_{1(2)}}_{T(R)}{=}k^{(1,1(2))}_{T(R)}\sin\mu^{(1,1(2))}_{T(R)}{+}j2\pi\tau(f_{T(R)_{max}}\sin\gamma_{T(R)}+f_{R(T)_{max}}\Delta_{T(R)}\sin\gamma_{R(T)})\\ +j2\pi(O(Q)\sin\beta_{T(R)}+Q(O)\Delta_{T(R)}\sin\beta_{R(T)})\end{aligned} \tag{6.11b}$$

$$C^{SB_{1(2)}}_{T(R)}{=}-2\pi\tau f_{R(T)_{max}}\cos\gamma_{R(T)}-2\pi Q(O)\cos\beta_{R(T)}. \tag{6.11c}$$

3) In the case of the single-bounce multiple confocal ellipses model

$$\begin{aligned}\rho_{h^{SB_3}_{l,oq}h^{SB_3}_{l,o'q'}}(\tau)=\frac{\eta_{SB_{l,3}}}{2\pi I_0\left(k^{(l,3)}_R\right)U}\int_{-\pi}^{\pi}e^{j2\pi\left[O\cos\left(\phi^{(l,3)}_T-\beta_T\right)+Q\cos\left(\phi^{(l,3)}_R-\beta_R\right)\right]}\\ \times e^{k^{(l,3)}_R\cos\left(\phi^{(l,3)}_R-\mu^{(l,3)}_R\right)}e^{j2\pi\tau\left[f_{T_{max}}\cos\left(\phi^{(l,3)}_T-\gamma_T\right)+f_{R_{max}}\cos\left(\phi^{(l,3)}_R-\gamma_R\right)\right]}d\phi^{(l,3)}_R\end{aligned} \tag{6.12}$$

where $\phi_T^{(n_{l,3})} = \arcsin[b_l^2 \sin\phi_R^{(n_{l,3})}/(a_l^2+f^2+2a_l f\cos\phi_R^{(n_{l,3})})]$ as mentioned in Section 6.2 and $U = \sqrt{(K_{oq}+1)(K_{o'q'}+1)}$ only appears for the first tap.

4) In terms of the double-bounce component for the first tap

$$\rho_{h_{1,oq}^{DB} h_{1,o'q'}^{DB}}(\tau) = \eta_{DB_1} \frac{I_0\left\{\sqrt{\left(A_T^{DB_1}\right)^2+\left(B_T^{DB_1}\right)^2}\right\} I_0\left\{\sqrt{\left(A_R^{DB_1}\right)^2+\left(B_R^{DB_1}\right)^2}\right\}}{\sqrt{(K_{oq}+1)(K_{o'q'}+1)}\, I_0\left(k_T^{(1,1)}\right) I_0\left(k_R^{(1,2)}\right)} \tag{6.13}$$

where

$$A_{T(R)}^{DB_1} = k_{T(R)}^{(1,1(2))}\cos\mu_{T(R)}^{(1,1(2))} + j2\pi\tau f_{T(R)_{max}}\cos\gamma_{T(R)} + j2\pi O(Q)\cos\beta_{T(R)} \tag{6.14a}$$

$$B_{T(R)}^{DB_1} = k_{T(R)}^{(1,1(2))}\sin\mu_{T(R)}^{(1,1(2))} + j2\pi\tau f_{T(R)_{max}}\sin\gamma_{T(R)} + j2\pi O(Q)\sin\beta_{T(R)}. \tag{6.14b}$$

5) In terms of the double-bounce component for other taps

$$\rho_{h_{l',oq}^{DB_{1(2)}} h_{l',o'q'}^{DB_{1(2)}}}(\tau) = \eta_{DB_{l',1(2)}} \frac{I_0\left\{\sqrt{\left(A_T^{DB_{l',1(2)}}\right)^2+\left(B_T^{DB_{l',1(2)}}\right)^2}\right\} I_0\left\{\sqrt{\left(A_R^{DB_{l',1(2)}}\right)^2+\left(B_R^{DB_{l',1(2)}}\right)^2}\right\}}{I_0\left(k_T^{(1(l'),1(3))}\right) I_0\left(k_R^{(l'(1),3(2))}\right)} \tag{6.15}$$

where

$$A_T^{DB_{l',1(2)}} = k_T^{(1(l'),1(3))}\cos\mu_T^{(1(l'),1(3))} + j2\pi\tau f_{T_{max}}\cos\gamma_T + j2\pi O\cos\beta_T \tag{6.16a}$$

$$B_T^{DB_{l',1(2)}} = k_T^{(1(l'),1(3))}\sin\mu_T^{(1(l'),1(3))} + j2\pi\tau f_{T_{max}}\sin\gamma_T + j2\pi O\sin\beta_T \tag{6.16b}$$

$$A_R^{DB_{l',1(2)}} = k_R^{(l'(1),3(2))}\cos\mu_R^{(1(l'),1(3))} + j2\pi\tau f_{R_{max}}\cos\gamma_R + j2\pi Q\cos\beta_R \tag{6.16c}$$

$$B_R^{DB_{l',1(2)}} = k_R^{(l'(1),3(2))}\sin\mu_R^{(1(l'),1(3))} + j2\pi\tau f_{R_{max}}\sin\gamma_R + j2\pi Q\sin\beta_R. \tag{6.16d}$$

Note that since $k_T^{(l',3)}$, $\mu_T^{(l',3)}$ and $k_R^{(l',3)}$, $\mu_R^{(l',3)}$ refer to the same ellipse, $k_T^{(l',3)} = k_R^{(l',3)}$ and $\mu_T^{(l',3)} = \arcsin[b_{l'}^2 \sin\mu_R^{(l',3)}/(a_{l'}^2+f^2+2a_{l'}f\cos\mu_R^{(l',3)})]$ hold. Finally, the ST CF of the channel impulse responses $h_{oq}(t,\tau')$ and $h_{o'q'}(t,\tau')$ can be expressed as $\rho_{h_{oq}h_{o'q'}}(\tau) = \sum_{l=1}^{L} c_l^2 \rho_{h_{l,oq}h_{l,o'q'}}(\tau)$.

6.3.2 Space-Doppler Power Spectral Density

Applying the Fourier transform to the ST CF $\rho_{h_{l,oq}h_{l,o'q'}}(\tau)$in terms of τ, we can obtain the corresponding SD PSD as

$$S_{h_{l,oq}h_{l,o'q'}}(f_D) = \int_{-\infty}^{\infty} \rho_{h_{l,oq}h_{l,o'q'}}(\tau)\, e^{-j2\pi f_D \tau} d\tau \tag{6.17}$$

where f_D is the Doppler frequency. Therefore, SD PSD for the first tap is

$$S_{h_{1,oq}h_{1,o'q'}}(f_D)=S_{h_{1,oq}^{LoS}h_{1,o'q'}^{LoS}}(f_D)+\sum_{i=1}^{I} S_{h_{1,oq}^{SB_i}h_{1,o'q'}^{SB_i}}(f_D)+S_{h_{1,oq}^{DB}h_{1,o'q'}^{DB}}(f_D)\,. \tag{6.18}$$

Whereas for other taps, we have the SD PSD as

$$S_{h_{l',oq}h_{l',o'q'}}(f_D)=S_{h_{l',oq}^{SB_3}h_{l',o'q'}^{SB_3}}(f_D)+S_{h_{l',oq}^{DB_1}h_{l',o'q'}^{DB_1}}(f_D)+S_{h_{l',oq}^{DB_2}h_{l',o'q'}^{DB_2}}(f_D)\,. \tag{6.19}$$

Note that except for the SD PSD of the single-bounce multiple confocal ellipses model $S_{h_{l',oq}^{SB_3}h_{l',o'q'}^{SB_3}}(f_D)$, which must be evaluated numerically; for other SD PSDs we can derive the following closed-form solutions by using the equality $\int_0^{\infty} I_0\left(j\alpha\sqrt{x^2+y^2}\right)\cos(\beta x)\, dx = \cos\left(y\sqrt{\alpha^2-\beta^2}\right)/\sqrt{\alpha^2-\beta^2}$ [101] and following the similar reasoning to Chapter 5.

1) In the case of the LoS component,

$$S_{h_{1,oq}^{LoS}h_{1,o'q'}^{LoS}}(f_D)=\sqrt{\frac{K_{oq}K_{o'q'}}{(K_{oq}+1)(K_{o'q'}+1)}}e^{j2\pi G}\delta(f_D-H) \tag{6.20}$$

where $\delta(\cdot)$ denotes the Dirac delta function.

2) In terms of the single-bounce two-ring model

$$S_{h_{1,oq}^{SB_{1(2)}}h_{1,o'q'}^{SB_{1(2)}}}(f_D)=\frac{\eta_{SB_{1,1(2)}} 2e^{jU_{T(R)}^{SB_{1(2)}}+j2\pi O_{T(R)}^{SB_{1(2)}}\frac{D_{T(R)}^{SB_{1(2)}}}{W_{T(R)}^{SB_{1(2)}}}}\cos\left[\frac{E_{T(R)}^{SB_{1(2)}}}{W_{T(R)}^{SB_{1(2)}}}\sqrt{W_{T(R)}^{SB_{1(2)}}-4\pi^2\left(O_{T(R)}^{SB_{1(2)}}\right)^2}\right]}{\sqrt{(K_{oq}+1)(K_{o'q'}+1)}I_0\left(k_{T(R)}^{(1,1(2))}\right)\sqrt{W_{T(R)}^{SB_{1(2)}}-4\pi^2\left(O_{T(R)}^{SB_{1(2)}}\right)^2}} \tag{6.21}$$

where $O_{T(R)}^{SB_{1(2)}} = 2\pi\left(f_D \pm f_{R(T)_{max}}\cos\gamma_{R(T)}\right)$, $U_{T(R)}^{SB_{1(2)}} = \mp 2\pi Q(O)\cos\beta_{R(T)}$

$$\begin{aligned} W_{T(R)}^{SB_{1(2)}} &= 4\pi^2 f_{T(R)_{max}}^2 + 4\pi^2 f_{R(T)_{max}}^2 \Delta_{T(R)}^2 \sin^2\gamma_{R(T)} \\ &\quad + 8\pi^2 f_{T_{max}} f_{R_{max}} \Delta_{T(R)} \sin\gamma_T \sin\gamma_R \qquad (6.22a) \\ D_{T(R)}^{SB_{1(2)}} &= -j2\pi k_{T(R)}^{(1,1(2))} J_{T(R)} + 4\pi^2 O(Q)(f_{T(R)_{max}}\cos\left(\beta_{T(R)} - \gamma_{T(R)}\right) \\ &\quad + \Delta_{T(R)} f_{R(T)_{max}} \sin\beta_{T(R)} \sin\gamma_{R(T)}) + 4\pi^2 Q(O)(\Delta_{T(R)} f_{T(R)_{max}} \\ &\quad \times \sin\beta_{R(T)} \sin\gamma_{T(R)} + \Delta_{T(R)}^2 f_{R(T)_{max}} \sin\beta_{R(T)} \sin\gamma_{R(T)}) \qquad (6.22b) \\ E_{T(R)}^{SB_{1(2)}} &= j2\pi k_{T(R)}^{(1,1(2))}(f_{T(R)_{max}} \sin\left(\gamma_{T(R)} - \mu_{T(R)}^{(1,1(2))}\right) + f_{R(T)_{max}} \Delta_{T(R)} \\ &\quad \times \sin\gamma_{R(T)} \cos\mu_{T(R)}^{(1,1(2))}) + 4\pi^2 O(Q)(f_{T(R)_{max}} \sin\left(\beta_{T(R)} - \gamma_{T(R)}\right) - \Delta_{T(R)} f_{R(T)_{max}} \\ &\quad \times \cos\beta_{T(R)} \sin\gamma_{R(T)}) + 4\pi^2 Q(O)\Delta_{T(R)} f_{T(R)_{max}} \sin\beta_{R(T)} \cos\gamma_{T(R)} \qquad (6.22c) \end{aligned}$$

with $J_{T(R)} = f_{T(R)_{max}}\cos\left(\gamma_{T(R)} - \mu_{T(R)}^{(1,1(2))}\right) - f_{R(T)_{max}} \Delta_{T(R)} \sin\gamma_{R(T)} \sin\mu_{T(R)}^{(1,1(2))}$. For the Doppler PSD in (6.21), the range of Doppler frequency is limited by $\left|f_D \pm f_{R(T)_{max}}\cos\gamma_{R(T)}\right| \leq \sqrt{W_{T(R)}^{SB_{1(2)}}}/(2\pi)$.

3) In terms of the double-bounce component for the first tap

$$\begin{aligned} S_{h_{1,oq}^{DB} h_{1,o'q'}^{DB}}(f_D) &= \frac{\eta_{DB_1}}{\sqrt{(K_{oq}+1)(K_{o'q'}+1)} I_0\left(k_T^{(1,1)}\right) I_0\left(k_R^{(1,2)}\right)} 2e^{j2\pi f \frac{D_T^{DB}}{W_T^{DB}}} \\ &\times \frac{cos\left(\frac{E_T^{DB}}{W_T^{DB}}\sqrt{W_T^{DB} - 4\pi^2 f^2}\right)}{\sqrt{W_T^{DB} - 4\pi^2 f^2}} \odot 2e^{j2\pi f \frac{D_R^{DB}}{W_R^{DB}}} \frac{cos\left(\frac{E_R^{DB}}{W_R^{DB}}\sqrt{W_R^{DB} - 4\pi^2 f^2}\right)}{\sqrt{(W_R^{DB} - 4\pi^2 f^2}} \qquad (6.23) \end{aligned}$$

where $\odot$ denotes convolution, $W_{T(R)}^{DB} = 4\pi^2 f_{T(R)_{max}}^2$

$$D_{T(R)}^{DB} = 4\pi^2 O(Q) f_{T(R)_{max}} \cos\left(\beta_{T(R)} - \gamma_{T(R)}\right) - j2\pi k_{T(R)}^{(1,1(2))} f_{T(R)_{max}} \cos\left(\gamma_{T(R)} - \mu_{T(R)}^{(1,1(2))}\right) \qquad (6.24a)$$

$$E_{T(R)}^{DB} = 4\pi^2 O(Q) f_{T(R)_{max}} \sin\left(\beta_{T(R)} + \gamma_{T(R)}\right) - j2\pi k_{T(R)}^{(1,1(2))} f_{T(R)_{max}} \sin\left(\gamma_{T(R)} - \mu_{T(R)}^{(1,1(2))}\right). \qquad (6.24b)$$

For the Doppler PSD in (6.23), the range of Doppler frequency is limited by $|f_D| \leq f_{T_{max}} + f_{R_{max}}$.

4) In the case of the double-bounce component for other taps

$$S_{h_{l',oq}^{DB_{1(2)}} h_{l',o'q'}^{DB_{1(2)}}}(f_D) = \frac{\eta_{DB_{l',1(2)}}}{I_0\left(k_T^{(1(l'),1(3))}\right) I_0\left(k_R^{(l'(1),3(2))}\right)} 2e^{j2\pi f \frac{D_T^{DB_{l',1(2)}}}{W_T^{DB_{l',1(2)}}}} \times \frac{cos\left(\frac{E_T^{DB_{l',1(2)}}}{W_T^{DB_{l',1(2)}}} \sqrt{W_T^{DB_{l',1(2)}} - 4\pi^2 f^2}\right)}{\sqrt{W_T^{DB_{l',1(2)}} - 4\pi^2 f^2}} \odot 2e^{j2\pi f \frac{D_R^{DB_{l',1(2)}}}{W_R^{DB_{l',1(2)}}}} \frac{cos\left(\frac{E_R^{DB_{l',1(2)}}}{W_R^{DB_{l',1(2)}}} \sqrt{W_R^{DB_{l',1(2)}} - 4\pi^2 f^2}\right)}{\sqrt{(W_R^{DB_{l',1(2)}} - 4\pi^2 f^2}} \tag{6.25}$$

where $W_T^{DB_{l',1(2)}} = 4\pi^2 f_{T_{max}}^2$, $W_R^{DB_{l',1(2)}} = 4\pi^2 f_{R_{max}}^2$

$$D_T^{DB_{l',1(2)}} = 4\pi^2 O f_{T_{max}} \cos(\beta_T - \gamma_T) - j2\pi k_T^{(1(l'),1(3))} f_{T_{max}} \cos\left(\gamma_T - \mu_T^{(1(l'),1(3))}\right) \tag{6.26a}$$

$$E_T^{DB_{l',1(2)}} = 4\pi^2 O f_{T_{max}} \sin(\beta_T - \gamma_T) + j2\pi k_T^{(1(l'),1(3))} f_{T_{max}} \sin\left(\gamma_T - \mu_T^{(1(l'),1(3))}\right) \tag{6.26b}$$

$$D_R^{DB_{l',1(2)}} = 4\pi^2 Q f_{R_{max}} \cos(\beta_R - \gamma_R) - j2\pi k_R^{(l'(1),3(2))} f_{R_{max}} \cos\left(\gamma_R - \mu_R^{(l'(1),3(2))}\right) \tag{6.26c}$$

$$E_R^{DB_{l',1(2)}} = 4\pi^2 Q f_{R_{max}} \sin(\beta_R - \gamma_R) + j2\pi k_R^{(l'(1),3(2))} f_{R_{max}} \sin\left(\gamma_R - \mu_R^{(l'(1),3(2))}\right). \tag{6.26d}$$

For the Doppler PSD in (6.25), the range of Doppler frequency is limited by $|f_D| \leq f_{T_{max}} + f_{R_{max}}$. Similar to the ST CF, the SD PSD of the channel impulse responses $h_{oq}(t,\tau')$ and $h_{o'q'}(t,\tau')$ can be expressed as $S_{h_{oq}h_{o'q'}}(f_D) = \sum_{l=1}^{L} c_l^2 S_{h_{l,oq}h_{l,o'q'}}(f_D)$.

6.3.3 Frequency Correlation Function and Power Delay Profile

The FCF $\rho_{H_{oq}H_{o'q'}}(\Delta f')$ of the proposed wideband MIMO M2M RS-GBSM is defined as $\rho_{H_{oq}H_{oq}}(\Delta f') = \mathbf{E}\left[H_{oq}(t,f') H_{oq}^*(t, f' - \Delta f')\right]$. Here, $H_{oq}(t,f')$ denotes the time-variant transfer function, which is the Fourier transform of the channel impulse response $h_{oq}(t,\tau')$ and can be expressed as $H_{oq}(t,f') = \sum_{l=1}^{L} c_l h_{l,oq}(t) e^{-j2\pi f'\tau'}$. Therefore, the FCF can be derived as

$$\rho_{H_{oq}H_{o'q'}}(\Delta f') = \sum_{l=1}^{L} c_l^2 e^{-j2\pi f'\tau_l'}. \tag{6.27}$$

Applying the inverse Fourier transform to the FCF $\rho_{H_{oq}H_{o'q'}}(\Delta f')$ in (6.27), we can obtain the corresponding PDP as $S_{H_{oq}H_{o'q'}}(\tau') = \sum_{l=1}^{L} c_l^2 \delta(\tau' - \tau_l')$. It is obvious that the FCF and the PDP are completely determined by the number of propagation paths L, the path gains c_l, and the propagation delays τ_l'. Appropriate values for these parameters can be found in many measurement campaigns for wideband M2M channels, e.g., those in [31, 32, 33, 34]. This allows us to fit the FCF $\rho_{H_{oq}H_{o'q'}}(\Delta f')$ and the corresponding PDP $S_{H_{oq}H_{o'q'}}(\tau')$ of the proposed model to any specified or measured FCF and PDP characterised by the sets $\{c_l\}_{l=1}^{L}$ and $\{\tau_l'\}_{l=1}^{L}$.

6.4 MIMO Mobile-to-Mobile Simulation Models

The reference models for non-isotropic scattering narrowband and wideband MIMO M2M channels proposed in Section 5.2 and Section 6.2, respectively, assume an infinite number of effective scatterers, and thus cannot be implemented in practice. Note that by by removing the frequency-selectivity and assuming the power $\Omega_{oq} = 1$, the proposed wideband reference model in (6.1) and (6.3) can be reduced to the proposed narrowband reference model in (5.1). Therefore, based on the proposed wideband reference model, this section will design realisable wideband simulation models that have the reasonable complexity. Similarly, the narrowband simulation models can be obtained from the wideband simulation models by removing the frequency-selectivity.

6.4.1 Wideband Simulation Models

Based on the TDL structure, the complex impulse response of our simulation models is again composed of L discrete taps according to $\tilde{h}_{oq}(t, \tau') = \sum_{l=1}^{L} c_l \tilde{h}_{l,oq}(t)\, \delta(\tau' - \tau_l')$, where the complex time-variant tap coefficient $\tilde{h}_{l,oq}(t)$ is modeled by using a finite number of effective scatterers. Assuming 2D non-isotropic scattering and using our reference model in (6.1) and (6.3), we propose the time-variant tap coefficient for the

first tap as

$$\tilde{h}_{1,oq}(t) = \tilde{h}_{1,oq}^{LoS}(t) + \sum_{i=1}^{I} \tilde{h}_{1,oq}^{SB_i}(t) + \tilde{h}_{1,oq}^{DB}(t) \tag{6.28}$$

where

$$\tilde{h}_{1,oq}^{LoS}(t) = \sqrt{\frac{K_{oq}}{K_{oq}+1}} e^{-j2\pi f_c \tau_{oq}} e^{j\left[2\pi f_{T_{max}} t \cos\left(\pi - \phi^{LoS} + \gamma_T\right) + 2\pi f_{R_{max}} t \cos\left(\phi^{LoS} - \gamma_R\right)\right]} \tag{6.29a}$$

$$\tilde{h}_{1,oq}^{SB_i}(t) = \sqrt{\frac{\eta_{SB_{1,i}}}{K_{oq}+1}} \sum_{n_{1,i}=1}^{N_{1,i}} \frac{1}{\sqrt{N_{1,i}}} e^{j\left(\tilde{\psi}_{n_{1,i}} - 2\pi f_c \tau_{oq,n_{1,i}}\right)} \times e^{j\left[2\pi f_{T_{max}} t \cos\left(\tilde{\phi}_T^{(n_{1,i})} - \gamma_T\right) + 2\pi f_{R_{max}} t \cos\left(\tilde{\phi}_R^{(n_{1,i})} - \gamma_R\right)\right]} \tag{6.29b}$$

$$\tilde{h}_{1,oq}^{DB}(t) = \sqrt{\frac{\eta_{DB_1}}{K_{oq}+1}} \sum_{n_{1,1},n_{1,2}=1}^{N_{1,1},N_{1,2}} \frac{1}{\sqrt{N_{1,1}N_{1,2}}} e^{j\left(\tilde{\psi}_{n_{1,1},n_{1,2}} - 2\pi f_c \tau_{oq,n_{1,1},n_{1,2}}\right)} \times e^{j\left[2\pi f_{T_{max}} t \cos\left(\tilde{\phi}_T^{(n_{1,1})} - \gamma_T\right) + 2\pi f_{R_{max}} t \cos\left(\tilde{\phi}_R^{(n_{1,2})} - \gamma_R\right)\right]} \tag{6.29c}$$

and the time-variant tap coefficient for other taps as

$$\tilde{h}_{l',oq}(t) = \tilde{h}_{l',oq}^{SB_3}(t) + \tilde{h}_{l',oq}^{DB_1}(t) + \tilde{h}_{l',oq}^{DB_2}(t) \tag{6.30}$$

where

$$\begin{aligned} \tilde{h}_{l',oq}^{SB_3}(t) &= \sqrt{\eta_{SB_{l',3}}} \sum_{n_{l',3}=1}^{N_{l',3}} \frac{1}{\sqrt{N_{l',3}}} e^{j\left(\tilde{\psi}_{n_{l',3}} - 2\pi f_c \tau_{oq,n_{l',3}}\right)} \\ &\quad \times e^{j\left[2\pi f_{T_{max}} t \cos\left(\tilde{\phi}_T^{(n_{l',3})} - \gamma_T\right) + 2\pi f_{R_{max}} t \cos\left(\tilde{\phi}_R^{(n_{l',3})} - \gamma_R\right)\right]} \end{aligned} \tag{6.31a}$$

$$\begin{aligned} \tilde{h}_{l',oq}^{DB_{1(2)}}(t) &= \sqrt{\eta_{DB_{l',1(2)}}} \sum_{n_{1,1(2)},n_{l',3}=1}^{N_{1,1(2)},N_{l',3}} \frac{1}{\sqrt{N_{1,1(2)}N_{l',3}}} e^{j\left(\tilde{\psi}_{n_{1,1(2)},n_{l',3}} - 2\pi f_c \tau_{oq,n_{1,1(2)},n_{l',3}}\right)} \\ &\quad \times e^{j2\pi t\left[f_{T_{max}} \cos\left(\tilde{\phi}_T^{(n_{1(l'),1(3)})} - \gamma_T\right) + f_{R_{max}} \cos\left(\tilde{\phi}_R^{(n_{l'(1),3(2)})} - \gamma_R\right)\right]}. \end{aligned} \tag{6.31b}$$

In (6.29) and (6.31), the AoDs $\tilde{\phi}_T^{(n_{1,i})}$ and $\tilde{\phi}_T^{(n_{l',3})}$, and AoAs $\tilde{\phi}_R^{(n_{1,i})}$ and $\tilde{\phi}_R^{(n_{l',3})}$ are discrete realisations of the random variables $\phi_T^{(1,i)}$ and $\phi_T^{(l',3)}$, and $\phi_R^{(1,i)}$ and $\phi_R^{(l',3)}$, respectively. Note that from our reference model in Section 6.2, we know that only

the AoD $\tilde{\phi}_T^{(n_{1,1})}$ and AoAs $\tilde{\phi}_R^{(n_{1,2})}$ and $\tilde{\phi}_R^{(n_{l,3})}$ need to be generated based on the corresponding von Mises PDFs. The phases $\tilde{\psi}_{n_{1,i}}$, $\tilde{\psi}_{n_{1,1},n_{1,2}}$, $\tilde{\psi}_{n_{l',3}}$, and $\tilde{\psi}_{n_{1,1(2)},n_{l',3}}$ are i.i.d. random variables with uniform distributions over $[-\pi, \pi)$.

- **New Deterministic Simulation Model**

We first propose a new deterministic simulation model, which has the model parameters that are kept constant during simulation and thus needs only one simulation trial to obtain the desired statistical properties. The complex impulse response is $\tilde{h}_{oq}(t, \tau') = \sum_{l=1}^{L} c_l \tilde{h}_{l,oq}(t)\, \delta(\tau' - \tau_l')$, where the complex time-variant tap coefficient $\tilde{h}_{l,oq}(t)$ is a deterministic function and defined as (6.28) and (6.30). Therefore, the essential issue to design our deterministic simulation model is to find the sets of AoD $\left\{\tilde{\phi}_T^{(n_{1,1})}\right\}_{n=1}^{N_{1,1}}$ and AoAs $\left\{\tilde{\phi}_R^{(n_{1,2})}\right\}_{n=1}^{N_{1,2}}$, $\left\{\tilde{\phi}_R^{(n_{l,3})}\right\}_{n=1}^{N_{l,3}}$ that make the simulation model reproduce the desired statistical properties of the reference model as faithfully as possible with reasonable complexity, i.e., with a finite number of $N_{1,i}$ and $N_{l',3}$. To this end, the following conditions should be met as mentioned in Chapter 4: $\tilde{\phi}_{T(R)}^{(n_{1,1(2)})} \neq \pm\tilde{\phi}_{T(R)}^{(m_{1,1(2)})}$, $n_{1,1(2)} \neq m_{1,1(2)}$ and $\tilde{\phi}_R^{(n_{l,3})} \neq \pm\tilde{\phi}_R^{(m_{l,3})}$, $n_{l,3} \neq m_{l,3}$. However, in Chapter 4 we found that unlike isotropic scattering environments, for non-isotropic scattering environments it is difficult to find the sets of AoDs and AoAs to meet the above conditions. To the best of the authors' knowledge, so far only two parameter computation methods are available in [27, 29, 30] for non-isotropic scattering MIMO M2M channels. However, neither of them solved the difficulty in finding the sets of AoDs and AoAs to meet the conditions. This motivates us to propose a new parameter computation method, named IMMEA, to solve this difficulty. For easy comparison, we first give a brief description of these two existing methods.

The first method is the MMEA in [27], which is first proposed in [93] for F2M cellular channels. The MMEA is originated from the MEA in [13] for isotropic scattering F2M channels. Based on the MMEA in [27], the AoD and AoA of our model can be

designed as

$$\frac{n_{1,1(2)}-1/4}{N_{1,1(2)}} = \int_{\mu_{T(R)}^{(1,1(2))}-\pi}^{\tilde{\phi}_{T(R)}^{(n_{1,1(2)})}} f\left(\phi_{T(R)}^{(1,1(2))}\right) d\phi_{T(R)}^{(1,1(2))}, \quad n_{1,1(2)}=1,2,...,N_{1,1(2)} \tag{6.32a}$$

$$\frac{n_{l,3}-1/4}{N_{l,3}} = \int_{\mu_{R}^{(l,3)}-\pi}^{\tilde{\phi}_{R}^{(n_{l,3})}} f\left(\phi_{R}^{(l,3)}\right) d\phi_{R}^{(l,3)}, \quad n_{l,3}=1,2,...,N_{l,3} \tag{6.32b}$$

where $f\left(\phi_{T(R)}^{(1,1(2))}\right)$ $(\phi_{T(R)}^{(1,1(2))} \in [-\pi,\pi))$ and $f\left(\phi_{R}^{(l,3)}\right)$ $(\phi_{R}^{(l,3)} \in [-\pi,\pi))$ are von Mises PDFs with the mean angles $\mu_{T(R)}^{(1,1(2))}$ and $\mu_{R}^{(l,3)}$, respectively (as mentioned at the end of Section 6.2). If the mean angles $\mu_{T(R)}^{(1,1(2))}$ and $\mu_{R}^{(l,3)}$ are equal to or less than zero, (6.32a) and (6.32b) become

$$\tilde{\phi}_{T(R)}^{(n_{1,1(2)})} = F_{T(R)}^{-1}\left(\frac{n_{1,1(2)}-1/4}{N_{1,1(2)}}\right), \quad \tilde{\phi}_{T(R)}^{(n_{1,1(2)})} \in [-\pi,\pi) \tag{6.33a}$$

$$\tilde{\phi}_{R}^{(n_{l,3})} = F_{R_l}^{-1}\left(\frac{n_{l,3}-1/4}{N_{l,3}}\right), \quad \tilde{\phi}_{R}^{(n_{l,3})} \in [-\pi,\pi) \tag{6.33b}$$

where $F_{T(R)}^{-1}(\cdot)$ and $F_{R_l}^{-1}(\cdot)$ denote the inverse function of the von Mises CDF for $\phi_{T(R)}^{(1,1(2))}$ and $\phi_{R}^{(l,3)}$, respectively. Whereas for $\mu_{T(R)}^{(1,1(2))}>0$ and $\mu_{R}^{(l,3)}>0$, it is clear that the $\tilde{\phi}_{T(R)}^{(n_{1,1}(m_{1,2}))}$ and $\tilde{\phi}_{R}^{(n_{l,3})}$ are designed over the range $\left[\mu_{T(R)}^{(1,1(2))}-\pi,\pi\right)$ and $\left[\mu_{R}^{(l,3)}-\pi,\pi\right)$, respectively, rather than over the whole range $[-\pi,\pi)$, which is necessary to the design of simulation model under the condition of non-isotropic scattering as addressed in Chapter 4 and [93]. Note that as mentioned in [93], the MMEA can only meet the above conditions when $\mu_{T(R)}^{(1,1(2))}$=0 and $\mu_{R}^{(l,3)}$=0.

The other parameter computation method is the method proposed by Zajić and Stüber in [29, 30]. To distinguish this from MMEA, we name this method MMEA2 since it actually originated from the MEA in [13] as well. Following the MMEA2, we have the AoD and AoA of our model as

$$\tilde{\phi}_{T(R)}^{(n_{1,1(2)})} = F_{T(R)}^{-1}\left(\frac{n_{1,1(2)}-1/2}{N_{1,1(2)}}\right), \quad \tilde{\phi}_{T(R)}^{(n_{1,1(2)})} \in [-\pi,\pi) \tag{6.34a}$$

$$\tilde{\phi}_{R}^{(n_{l,3})} = F_{R_l}^{-1}\left(\frac{n_{l,3}-1/2}{N_{l,3}}\right), \quad \tilde{\phi}_{R}^{(n_{l,3})} \in [-\pi,\pi). \tag{6.34b}$$

It is obvious that the MMEA2 chooses the value of 1/2 rather than 1/4 chosen in the MMEA. This is seemly inspired by the modified MEDS in [36] for the simulation of isotropic scattering M2M channels. However, the MMEA2 cannot meet the above conditions.

In the following, we will derive the IMMEA that has the ability to meet the above conditions for any non-isotropic scattering M2M channels. To this end, we first define the random variables $\phi_{T(R)}^{\prime(1,1(2))}$, which fulfill von Mises distribution with the same mean angle $\mu_{T(R)}^{(1,1(2))}$ and parameter $k_{T(R)}^{(1,1(2))}$ as the random variables $\phi_{T(R)}^{(1,1(2))}$, over the range $\left[\mu_{T(R)}^{(1,1(2))}-\pi, \mu_{T(R)}^{(1,1(2))}+\pi\right)$. Similarly, we define the random variables $\phi_R^{\prime(l,3)}$ over the range $\left[\mu_R^{(l,3)}-\pi, \mu_R^{(l,3)}+\pi\right)$ that fulfill von Mises distribution with the same mean angle $\mu_R^{(l,3)}$ and parameter $k_R^{(l,3)}$ as the random variables $\phi_R^{(l,3)}$. The discrete realisations of the new defined random variables $\phi_{T(R)}^{\prime(1,1(2))}$ and $\phi_R^{\prime(l,3)}$ can be designed as

$$\tilde{\phi}_{T(R)}^{\prime(n_{1,1(2)})} = F_{T(R)}^{\prime-1}\left(\frac{n_{1,1(2)}-1/4}{N_{1,1(2)}}\right), \quad \tilde{\phi}_{T(R)}^{\prime(n_{1,1(2)})} \in \left[\mu_{T(R)}^{(1,1(2))}-\pi, \mu_{T(R)}^{(1,1(2))}+\pi\right) \tag{6.35a}$$

$$\tilde{\phi}_R^{\prime(n_{l,3})} = F_{R_l}^{\prime-1}\left(\frac{n_{l,3}-1/4}{N_{l,3}}\right), \quad \tilde{\phi}_R^{\prime(n_{l,3})} \in \left[\mu_R^{(l,3)}-\pi, \mu_R^{(l,3)}+\pi\right) \tag{6.35b}$$

where $F_{T(R)}^{\prime-1}(\cdot)$ and $F_{R_l}^{\prime-1}(\cdot)$ denote the inverse function of the von Mises CDF for $\phi_{T(R)}^{\prime(1,1(2))}$ and $\phi_R^{\prime(l,3)}$, respectively. The AoD and AoAs of our simulation model can be obtained by mapping $\tilde{\phi}_{T(R)}^{\prime(n_{1,1(2)})}$ and $\tilde{\phi}_R^{\prime(n_{l,3})}$ to the range of $[-\pi, \pi)$ as

$$\tilde{\phi}_{T(R)}^{(n_{1,1(2)})} = \begin{cases} \tilde{\phi}_{T(R)}^{\prime(n_{1,1(2)})}+2\pi, & \text{if} \quad \tilde{\phi}_{T(R)}^{\prime(n_{1,1(2)})} < -\pi \\ \tilde{\phi}_{T(R)}^{\prime(n_{1,1(2)})}-2\pi, & \text{if} \quad \tilde{\phi}_{T(R)}^{\prime(n_{1,1(2)})} \geq \pi \\ \tilde{\phi}_{T(R)}^{\prime(n_{1,1(2)})}, & \text{else} \end{cases} \tag{6.36a}$$

$$\tilde{\phi}_R^{(n_{l,3})} = \begin{cases} \tilde{\phi}_R^{\prime(n_{l,3})}+2\pi, & \text{if} \quad \tilde{\phi}_R^{\prime(n_{l,3})} < -\pi \\ \tilde{\phi}_R^{\prime(n_{l,3})}-2\pi, & \text{if} \quad \tilde{\phi}_R^{\prime(n_{l,3})} \geq \pi \\ \tilde{\phi}_R^{\prime(n_{l,3})}, & \text{else.} \end{cases} \tag{6.36b}$$

It is clear that the IMMEA corresponds to the MMEA when $\mu_{T(R)}^{(1,1(2))}=0$ and $\mu_R^{(l,3)}=0$. The IMMEA can meet the above conditions and thus should outperform the MMEA and MMEA2. The validation of the IMMEA and our deterministic simulation model will be given in Section 6.5.

The correlation properties of our simulation model must be analysed by using time averages rather than statistical averages. The ST CF has to be computed according to $\tilde{\rho}_{\tilde{h}_{l,oq}\tilde{h}_{l,o'q'}}(\tau) = \left\langle \tilde{h}_{l,oq}(t)\, \tilde{h}^{*}_{l,o'q'}(t-\tau) \right\rangle$, where $\langle\cdot\rangle$ denotes the time average operator. For brevity, the straightforward derivation of $\tilde{\rho}_{\tilde{h}_{l,oq}\tilde{h}_{l,o'q'}}(\tau)$ is omitted. Note that for $\{N_{1,i}, N_{l',3}\} \to \infty$, the ST CF of our simulation model matches that of the reference model, i.e, $\tilde{\rho}_{\tilde{h}_{l,oq}\tilde{h}_{l,o'q'}}(\tau) = \rho_{h_{l,oq}h_{l,o'q'}}(\tau)$ holds. The FCF of our simulation model can be computed in terms of $\tilde{\rho}_{\tilde{H}_{oq}\tilde{H}_{oq}}(\Delta f') = \left\langle \tilde{H}_{oq}(t, f')\, \tilde{H}^{*}_{oq}(t, f'-\Delta f') \right\rangle$, where $\tilde{H}_{oq}(t, f')$ is the Fourier transform of the complex impulse response $\tilde{h}_{oq}(t, \tau')$ with respect to the propagation delay τ'. Therefore, it is straightforward to obtain the FCF as $\tilde{\rho}_{\tilde{H}_{oq}\tilde{H}_{o'q'}}(\Delta f') = \sum_{l=1}^{L} c_l^2 e^{-j2\pi f' \tau'_l}$, which is equal to the FCF $\rho_{H_{oq}H_{o'q'}}(\Delta f')$ of our reference model in (6.27).

- **New Stochastic Simulation Model**

Our deterministic model can be further modified to a stochastic simulation model by allowing both the phases and frequencies to be random variables. Different from the deterministic model, the properties of the stochastic model vary for each simulation trial, but will converge to the desired ones when averaged over a sufficient number of simulation trials. To distinguish from our deterministic model, we define the complex impulse response of the proposed stochastic model as $\hat{h}_{oq}(t, \tau') = \sum_{l=1}^{L} c_l \hat{h}_{l,oq}(t)\, \delta(\tau' - \tau'_l)$, where the complex time-variant tap coefficient $\hat{h}_{l,oq}(t)$ is non-ergodic random processes and defined as (6.28) and (6.30). Unlike the deterministic simulation model, the AoD $\hat{\phi}_T^{(n_{1,1})}$ and AoAs $\hat{\phi}_R^{(n_{1,2})}$, $\hat{\phi}_R^{(n_{l,3})}$ of our stochastic model are random variable and thus vary for different simulation trials. Therefore, the fundamental issue for the design of the sets of AoD $\left\{\hat{\phi}_T^{(n_{1,1})}\right\}_{n=1}^{N_{1,1}}$ and AoAs $\left\{\hat{\phi}_R^{(n_{1,2})}\right\}_{n=1}^{N_{1,2}}$, $\left\{\hat{\phi}_R^{(n_{l,3})}\right\}_{n=1}^{N_{l,3}}$ is how to incorporate a random term into the AoA and AoD. To deal with this fundamental issue, we apply the method proposed in [67] for isotropic scattering F2M Rayleigh fading channels and design the AoD and AoAs as

$$\hat{\phi}_{T(R)}^{(n_{1,1(2)})} = F_{T(R)}^{-1}\left(\frac{n_{1,1(2)} - 1/2 + \theta_{T(R)}}{N_{1,1(2)}}\right), \qquad \hat{\phi}_{T(R)}^{(n_{1,1(2)})} \in [-\pi, \pi) \tag{6.37a}$$

$$\hat{\phi}_{R}^{(n_{l,3})} = F_{R_l}^{-1}\left(\frac{n_{l,3} - 1/2 + \theta_{R_l}}{N_{l,3}}\right), \qquad \hat{\phi}_{R}^{(n_{l,3})} \in [-\pi, \pi) \tag{6.37b}$$

where $\theta_{T(R)}$ and θ_{R_l} are random variables uniformly distributed in the interval $[-1/2, 1/2)$ and independent to each other. As mentioned in Chapter 4, the interval $[-1/2, 1/2)$ and the constant value $1/2$ are chosen to guarantee that the design of the AoA and AoDs is based on the desired range (here is $[-\pi, \pi)$). Due to the introduction of random variables $\theta_{T(R)}$ and θ_{R_l}, the sets of AoDs and AoAs vary for different simulations.

Unlike the deterministic simulation model, the ST CF of our stochastic model should be computed according to $\hat{\rho}_{\hat{h}_{l,oq}\hat{h}_{l,o'q'}}(\tau) = \mathbf{E}\left[\hat{h}_{l,oq}(t)\,\hat{h}^*_{l,o'q'}(t-\tau)\right]$. It can be shown that the ST CF $\hat{\rho}_{\hat{h}_{l,oq}\hat{h}_{l,o'q'}}(\tau)$ of our stochastic model matches the ST CF $\rho_{h_{l,oq}h_{l,o'q'}}(\tau)$ of the reference model irrespective of the values of $N_{1,i}$ and $N_{l',3}$, i.e., for any $N_{1,i}$ and $N_{l',3}$. The derivation of $\hat{\rho}_{\hat{h}_{l,oq}\hat{h}_{l,o'q'}}(\tau)$ is complicated and lengthy, details are omitted here for brevity. We invite interested readers to refer to Appendix D since one can derive the ST CF $\hat{\rho}_{\hat{h}_{l,oq}\hat{h}_{l,o'q'}}(\tau)$ by following the similar procedure provided there. The FCF of our simulation model can be computed in terms of $\hat{\rho}_{\hat{H}_{oq}\hat{H}_{oq}}(\Delta f') = \mathbf{E}\left[\hat{H}_{oq}(t, f')\,\hat{H}^*_{oq}(t, f'-\Delta f')\right]$, where $\hat{H}_{oq}(t, f')$ is the Fourier transform of the complex impulse response $\hat{h}_{oq}(t, \tau')$ with respect to the propagation delay τ'. Therefore, the FCF is $\hat{\rho}_{\hat{H}_{oq}\hat{H}_{o'q'}}(\Delta f') = \sum_{l=1}^{L} c_l^2 e^{-j2\pi f'\tau'_l}$, which is equal to the FCF $\rho_{H_{oq}H_{o'q'}}(\Delta f')$ of our reference model in (6.27).

6.4.2 Narrowband Simulation Models

If we only consider the first tap (i.e., impose $L = 1$) on the wideband simulation models proposed in the previous subsection, they reduce to narrowband MIMO M2M channel simulators. It follows that $\tilde{h}_{oq}(t, \tau') = \tilde{h}_{oq}(t)\,\delta(\tau')$ holds. Note that due to the similar relationship between the proposed wideband reference model in Section 6.2 and the narrowband reference model in Section 5.2, the reduced narrowband MIMO M2M channel simulators are actually the corresponding simulation models for the proposed narrowband reference in (5.1) and (5.2). The complex fading envelope $\tilde{h}_{oq}(t)$ of the narrowband simulation model can be obtained by removing the subscript $(\cdot)_1$ from

(6.28) and (6.29)

$$\tilde{h}_{oq}(t) = \tilde{h}_{oq}^{LoS}(t) + \sum_{i=1}^{I} \tilde{h}_{oq}^{SB_i}(t) + \tilde{h}_{oq}^{DB}(t) \tag{6.38}$$

where

$$\tilde{h}_{oq}^{LoS}(t) = \sqrt{\frac{K_{oq}}{K_{oq}+1}} e^{-j2\pi f_c \tau_{oq}} e^{j\left[2\pi f_{T_{max}} t \cos\left(\pi - \phi^{LoS} + \gamma_T\right) + 2\pi f_{R_{max}} t \cos\left(\phi^{LoS} - \gamma_R\right)\right]} \tag{6.39a}$$

$$\begin{aligned}\tilde{h}_{oq}^{SB_i}(t) = &\sqrt{\frac{\eta_{SB_i}}{K_{oq}+1}} \sum_{n_i=1}^{N_i} \frac{1}{\sqrt{N_i}} e^{j\left(\tilde{\psi}_{n_i} - 2\pi f_c \tau_{oq,n_i}\right)} \\ &\times e^{j\left[2\pi f_{T_{max}} t \cos\left(\tilde{\phi}_T^{(n_i)} - \gamma_T\right) + 2\pi f_{R_{max}} t \cos\left(\tilde{\phi}_R^{(n_{1,i})} - \gamma_R\right)\right]}\end{aligned} \tag{6.39b}$$

$$\begin{aligned}\tilde{h}_{oq}^{DB}(t) = &\sqrt{\frac{\eta_{DB_1}}{K_{oq}+1}} \sum_{n_1,n_2=1}^{N_1,N_2} \frac{1}{\sqrt{N_1 N_2}} e^{j\left(\tilde{\psi}_{n_1,n_2} - 2\pi f_c \tau_{oq,n_1,n_2}\right)} \\ &\times e^{j\left[2\pi f_{T_{max}} t \cos\left(\tilde{\phi}_T^{(n_1)} - \gamma_T\right) + 2\pi f_{R_{max}} t \cos\left(\tilde{\phi}_R^{(n_2)} - \gamma_R\right)\right]}.\end{aligned} \tag{6.39c}$$

In (6.39), the AoDs $\tilde{\phi}_T^{(n_i)}$ and AoAs $\tilde{\phi}_R^{(n_i)}$ are discrete realisations of the random variables $\phi_T^{SB_i}$ and $\phi_R^{SB_i}$ of the narrowband reference model in Chapter 5, respectively.

We first propose a deterministic simulation model. Analogous to the proposed wideband deterministic simulation model, the key issue to design this narrowband deterministic simulation model is to properly design the AoD $\tilde{\phi}_T^{(n_1)}$, and AoAs $\tilde{\phi}_R^{(n_2)}$ and $\tilde{\phi}_R^{(n_3)}$. Applying the IMMEA in (6.35) and (6.36), we design the AoD and AoAs of our deterministic simulation model as

$$\tilde{\phi}_T^{(n_1)} = \begin{cases} \tilde{\phi}_T^{\prime(n_1)} + 2\pi, & \text{if} \quad \tilde{\phi}_T^{\prime(n_1)} < -\pi \\ \tilde{\phi}_T^{\prime(n_1)} - 2\pi, & \text{if} \quad \tilde{\phi}_T^{\prime(n_1)} \geq \pi \\ \tilde{\phi}_T^{\prime(n_1)}, & \text{else} \end{cases} \tag{6.40a}$$

$$\tilde{\phi}_R^{(n_{2(3)})} = \begin{cases} \tilde{\phi}_R^{\prime(n_{2(3)})} + 2\pi, & \text{if} \quad \tilde{\phi}_R^{\prime(n_{2(3)})} < -\pi \\ \tilde{\phi}_R^{\prime(n_{2(3)})} - 2\pi, & \text{if} \quad \tilde{\phi}_R^{\prime(n_{2(3)})} \geq \pi \\ \tilde{\phi}_R^{\prime(n_{2(3)})}, & \text{else} \end{cases} \tag{6.40b}$$

where $\tilde{\phi}_T^{(n_1)} \in [-\pi, \pi)$, $\tilde{\phi}_R^{(n_{2(3)})} \in [-\pi, \pi)$, and

$$\tilde{\phi}_T'^{(n_1)} = F_T'^{-1}\left(\frac{n_1 - 1/4}{N_1}\right), \qquad \tilde{\phi}_T'^{(n_1)} \in \left[\mu_T^{TR} - \pi, \mu_T^{TR} + \pi\right) \tag{6.41a}$$

$$\tilde{\phi}_R'^{(n_{2(3)})} = F_{R-2(3)}'^{-1}\left(\frac{n_{2(3)} - 1/4}{N_{2(3)}}\right), \quad \tilde{\phi}_R'^{(n_{2(3)})} \in \left[\mu_R^{TR(EL)} - \pi, \mu_R^{TR(EL)} + \pi\right) \tag{6.41b}$$

where $F_T'^{-1}(\cdot)$ and $F_{R-2(3)}'^{-1}(\cdot)$ denote the inverse function of the von Mises CDF for $\phi_T'^{(SB_1)}$ and $\phi_R'^{(SB_{2(3)})}$, respectively. The parameter $\phi_T'^{(SB_1)}$ and $\phi_R'^{(SB_{2(3)})}$ fulfill the same von Mises distributions as $\phi_T^{(SB_1)}$ and $\phi_R^{(SB_{2(3)})}$, respectively, but with different ranges, i.e., $\phi_T'^{(SB_1)} \in \left[\mu_T^{TR} - \pi, \mu_T^{TR} + \pi\right)$ and $\phi_R'^{(SB_{2(3)})} \in \left[\mu_R^{TR(EL)} - \pi, \mu_R^{TR(EL)} + \pi\right)$, while $\phi_T^{(SB_1)} \in [-\pi, \pi)$ and $\phi_R^{(SB_{2(3)})} \in [-\pi, \pi)$.

By allowing both the phases and frequencies to be random variables, Our deterministic model $\tilde{h}_{oq}(t)$ can be further modified to a stochastic simulation model $\hat{h}_{oq}(t)$. The AoD $\hat{\phi}_T^{(n_1)}$, and AoAs $\hat{\phi}_R^{(n_2)}$ and $\hat{\phi}_R^{(n_3)}$ can be designed by using the method described in (6.37)

$$\hat{\phi}_T^{(n_1)} = F_T^{-1}\left(\frac{n_1 - 1/2 + \theta_T}{N_1}\right), \qquad \hat{\phi}_T^{(n_1)} \in [-\pi, \pi) \tag{6.42a}$$

$$\hat{\phi}_R^{(n_{2(3)})} = F_{R-2(3)}^{-1}\left(\frac{n_{2(3)} - 1/2 + \theta_{R-2(3)}}{N_{2(3)}}\right), \qquad \hat{\phi}_R^{(n_{2(3)})} \in [-\pi, \pi) \tag{6.42b}$$

where $F_T^{-1}(\cdot)$ and $F_{R-2(3)}^{-1}(\cdot)$ denote the inverse function of the von Mises CDF for $\phi_T^{SB_1}$ and $\phi_R^{SB_{2(3)}}$, respectively, and θ_T and $\theta_{R-2(3)}$ are random variables uniformly distributed in the interval $[-1/2, 1/2)$ and independent to each other.

6.5 Numerical Results and Analysis

Unless otherwise specified, all the results presented in this section are obtained using f_c=5.9 GHz, $f_{T_{max}}$=$f_{R_{max}}$=570 Hz, D=300 m, a_1=160 m, a_2=175 m, R_T=R_R=6 m, $\beta_T = 60°$, $\beta_R = 45°$ $N_{1,1} = N_{1,2} = N_{1,3} = N_{2,3} = 30$ for the deterministic model, $N_{1,1} = N_{1,2} = N_{1,3} = N_{2,3} = 20$ for the stochastic model, and the normalised sampling period $f_{T_{max}} T_s = 0.005$ (T_s is the sampling period).

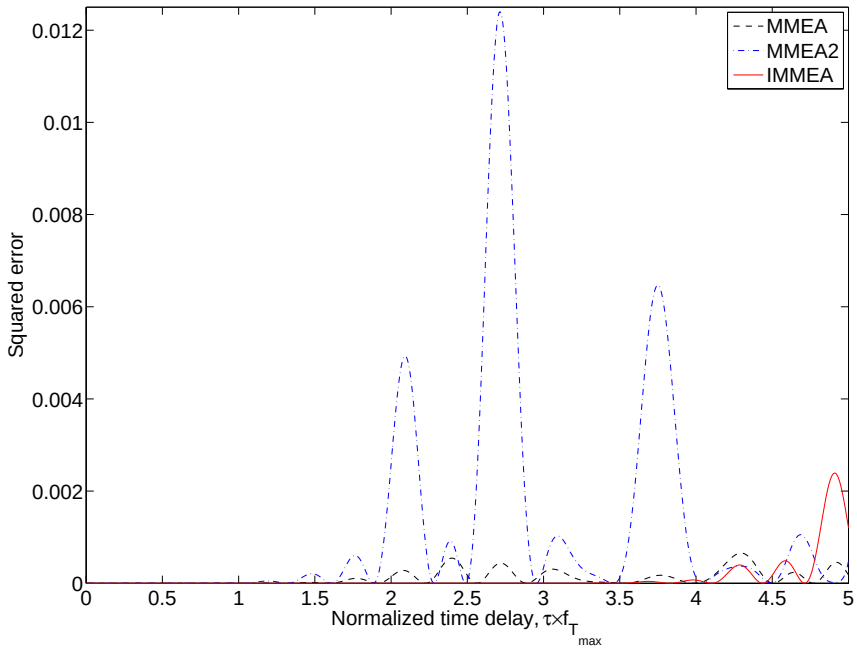

FIGURE 6.3: Squared error in the ST CF of the deterministic simulation model by using the MMEA, MMEA2, and IMMEA for a non-isotropic scattering MIMO M2M channel: $\beta_T = \beta_R = \gamma_T = \gamma_R = \mu_T^{(1,1)} = \mu_R^{(1,2)} = -40°$, $k_T^{(1,1)} = k_R^{(1,2)} = 1$, and $\delta_T = \delta_R = 0.5\lambda$.

FIGURES 6.3–6.5 compare the difference in the ST CF for the deterministic model by using different parameter computation methods (i.e., the MMEA, MMEA2, and IMMEA). Without any loss of generality, here we choose the double-bounce two-ring model as the mathematical reference model for further investigation. Therefore, in FIGURES 6.3–6.5 we compare the difference in the ST CF $\tilde{\rho}_{h_{1,oq}^{DB} h_{1,o'q'}^{DB}}(\tau)$ from the desired $\rho_{h_{1,oq}^{DB} h_{1,o'q'}^{DB}}(\tau)$ by using the squared error $\left|\tilde{\rho}_{h_{1,oq}^{DB} h_{1,o'q'}^{DB}}(\tau) - \rho_{h_{1,oq}^{DB} h_{1,o'q'}^{DB}}(\tau)\right|^2$ for different non-isotropic scattering scenarios. From FIGURES 6.3–6.5, it is clear that the IMMEA outperforms the other two methods (MMEA and MMEA2) for different non-isotropic scattering scenarios. Comparing the MMEA and MMEA2, we can conclude that neither of them consistently outperforms the other for all non-isotropic scattering scenarios. FIGURE 6.5 also shows that the MMEA results in a relatively large difference even in shorter time delays, which are of most interest for most communication systems [36]. This is because that the MMEA designs the AoDs/AoAs in a non-sufficient range when the mean AoDs/AoAs are larger than zero as mentioned in Section 6.4.

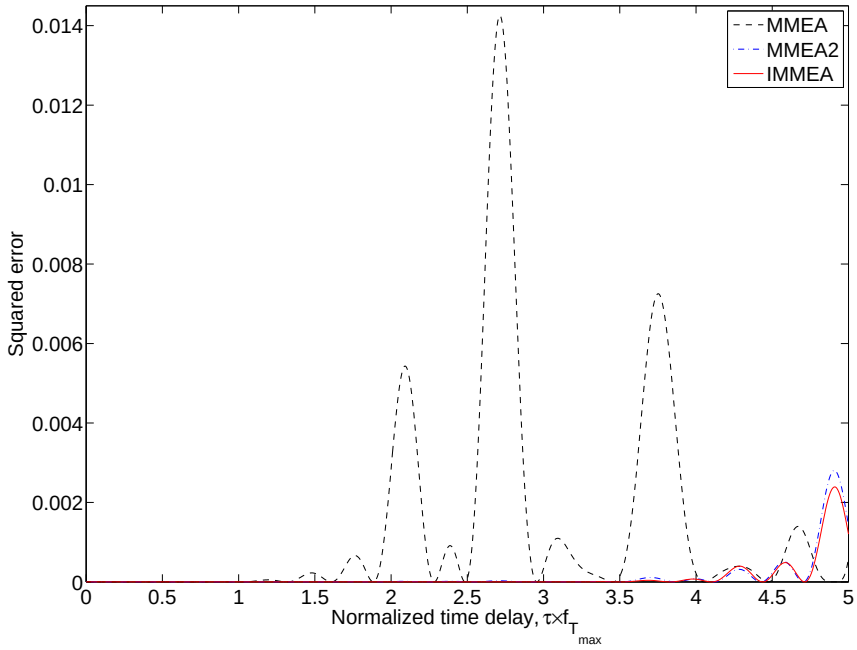

FIGURE 6.4: Squared error in the ST CF of the deterministic simulation model by using the MMEA, MMEA2, and IMMEA for a non-isotropic scattering MIMO M2M channel: $\beta_T = \beta_R = \gamma_T = \gamma_R = \mu_T^{(1,1)} = \mu_R^{(1,2)} = -30°$, $k_T^{(1,1)} = k_R^{(1,2)} = 1$, and $\delta_T = \delta_R = 0.5\lambda$.

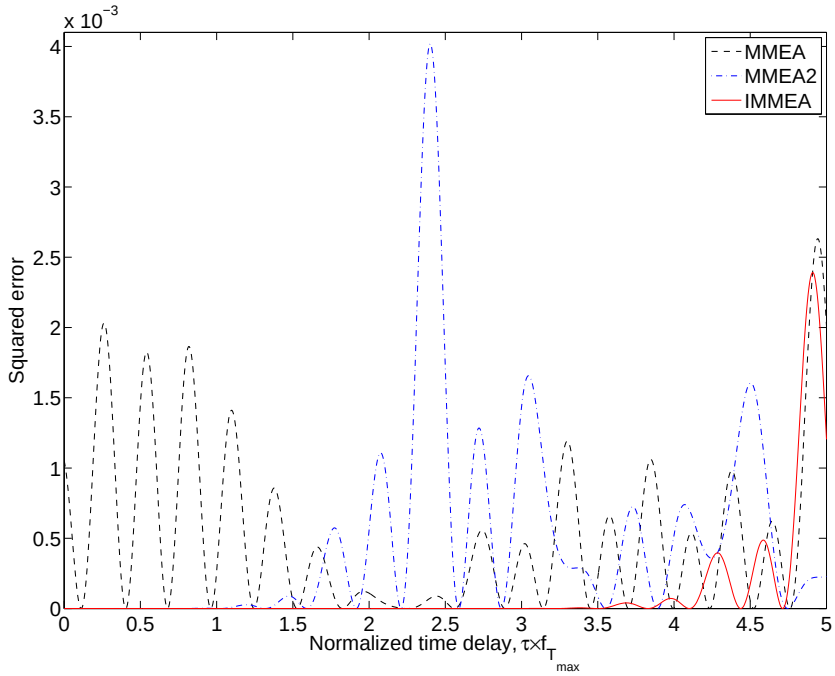

FIGURE 6.5: Squared error in the ST CF of the deterministic simulation model by using the MMEA, MMEA2, and IMMEA for a non-isotropic scattering MIMO M2M channel: $\beta_T = \beta_R = \gamma_T = \gamma_R = \mu_T^{(1,1)} = \mu_R^{(1,2)} = 50°$, $k_T^{(1,1)} = k_R^{(1,2)} = 1$, and $\delta_T = \delta_R = 0.5\lambda$.

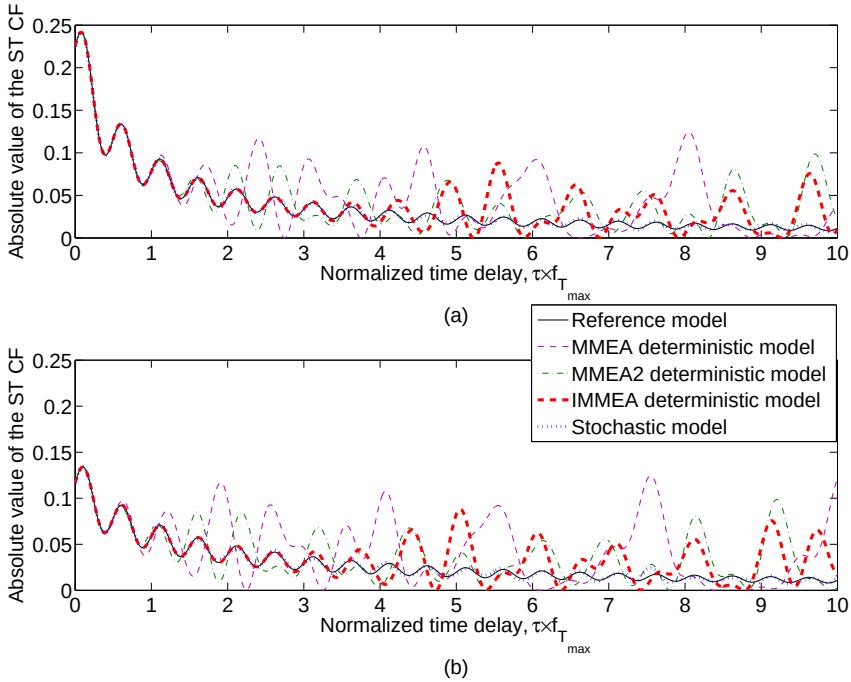

FIGURE 6.6: Absolute value of the ST CF of the mathematical reference model, deterministic simulation models (MMEA model, MMMEA2 model, and IMMEA model), and stochastic simulation model for a non-isotropic scattering MIMO M2M channel ($\beta_T = \beta_R = \gamma_T = \gamma_R = \mu_T^{(1,1)} = \mu_R^{(1,2)} = -70^\circ$ and $k_T^{(1,1)} = k_R^{(1,2)} = 1$) with the antenna spacings (a) $\delta_T = \delta_R = 0.5\lambda$ and (b) $\delta_T = \delta_R = 1\lambda$.

FIGURE 6.6 shows the ST CF of the mathematical reference model, the proposed IMMEA deterministic simulation model, and the proposed stochastic model. For simplicity, we only consider the double-bounced rays of the first tap in our mathematical reference model. In such a case, our model reduces to a double-bounce two-ring mathematical reference model. The results obtained for the stochastic model are averaged over $N_{sto} = 50$ trials. From FIGURE 6.6, it is obvious that the IMMEA model provides a good approximation to the ST CF of the mathematical reference model over a short normalised time delay range $0 \leq \tau f_{T_{max}} \leq 3$, which is typically of interest for most communication systems [36]. The stochastic model presents a good approximation to the desired ST CF over a wider range of normalised time delays with an even smaller number of complex harmonic functions $N_{1,1}$ and $N_{1,2}$. For further comparison, the ST CF of the MMEA and MMEA2 deterministic models are also plotted. Again, it is clear that the IMMEA model outperforms the MMEA and MMEA2 models. In addition, comparing FIGURES 6.6 (a) and (b), we find that the increase of the antenna

element spacings (i.e., the value of δ_T and δ_R) increases the difficulty in approximating the desired ST CF of the mathematical reference model.

FIGURES 6.7 and 6.8 show the theoretical SD PSDs of the proposed M2M model for the first and second tap with different VTDs (low and high) and different antenna separations ($\delta_T = \delta_R = 0$ or 3λ) when the Tx and Rx are moving in the opposite directions and same direction, respectively. Note that when $\delta_T = \delta_R = 0$, the SD PSDs actually reduce to Doppler PSDs. For comparison purposes, the measured Doppler PSDs taken from FIGURES 4 (a)–(d) in [31] are also plotted in FIGURES 6.7 (a), (b) and FIGURES 6.8 (a), (b), respectively. In [31], the measurement campaigns were performed at a carrier frequency of 5.9 GHz on an expressway with a low VTD. The distance between the Tx and Rx was approximately $D = 300$ m and the directions of movement were γ_T=0, γ_R=π (opposite direction) and γ_T=γ_R=0 (same direction). Both the Tx and Rx were equipped with one omnidirectional antenna, i.e., SISO case. Based on the measured scenarios in [31], we chose the following environment-related parameters: 1) $k_T^{(1,1)}$= 6.6, $k_R^{(1,2)}$= 8.3, $k_R^{(1,3)}$= 5.5, $k_R^{(2,3)}$= 7.7, $\mu_T^{(1,1)}$= 12.8°, $\mu_R^{(1,2)}$= 178.7°, $\mu_R^{(1,3)}$= 131.6°, and $\mu_R^{(2,3)}$= 31.3° for FIGURE 6.7 and 2) $k_T^{(1,1)}$= 9.6, $k_R^{(1,2)}$= 3.6, $k_R^{(1,3)}$= 11.5, $k_R^{(2,3)}$= 11.7, $\mu_T^{(1,1)}$= 21.7°, $\mu_R^{(1,2)}$= 147.8°, $\mu_R^{(1,3)}$= 171.6°, and $\mu_R^{(2,3)}$= 177.6° for FIGURE 6.8. Considering the constraints of the Ricean factor and energy-related parameters for different taps as mentioned in Section 6.2, we choose the following parameters in order to fit the measured Doppler PSDs reported in [31] under the condition of low VTD: 1) K_{oq}= 2.186, η_{DB_1}= 0.005, $\eta_{SB_{1,1}}$= 0.252, $\eta_{SB_{1,2}}$= 0.262, and $\eta_{SB_{1,3}}$= 0.481 for FIGURE 6.7 (a); 2) $\eta_{DB_{2,1}}$= $\eta_{DB_{2,2}}$= 0.119 and $\eta_{SB_{2,3}}$= 0.762 for FIGURE 6.7 (b); 3) K_{oq}= 3.786, η_{DB_1}= 0.051, $\eta_{SB_{1,1}}$= 0.335, $\eta_{SB_{1,2}}$= 0.203, and $\eta_{SB_{1,3}}$= 0.411 for FIGURE 6.8 (a); 4) $\eta_{DB_{2,1}}$= $\eta_{DB_{2,2}}$= 0.121 and $\eta_{SB_{2,3}}$= 0.758 for FIGURE 6.8 (b). The excellent agreement between the theoretical and measured Doppler PSDs confirms the utility of the proposed wideband model. The environment-related parameters for high VTD in FIGURES 6.7 and 6.8 are the same as those for low VTD except $k_T^{(1,1)}$=0.6 and $k_R^{(1,2)}$=1.3, which are related to the distribution of moving scatterers. The SD PSDs for high VTD shown in FIGURES 6.7 and 6.8 were obtained with the following parameters 1) K_{oq}= 0.156, η_{DB_1}= 0.685, $\eta_{SB_{1,1}}$= $\eta_{SB_{1,2}}$= 0.126, $\eta_{SB_{1,3}}$=0.063 for the first tap and 2) $\eta_{DB_{2,1}}$=$\eta_{DB_{2,2}}$=0.456, $\eta_{SB_{2,3}}$=0.088 for the second

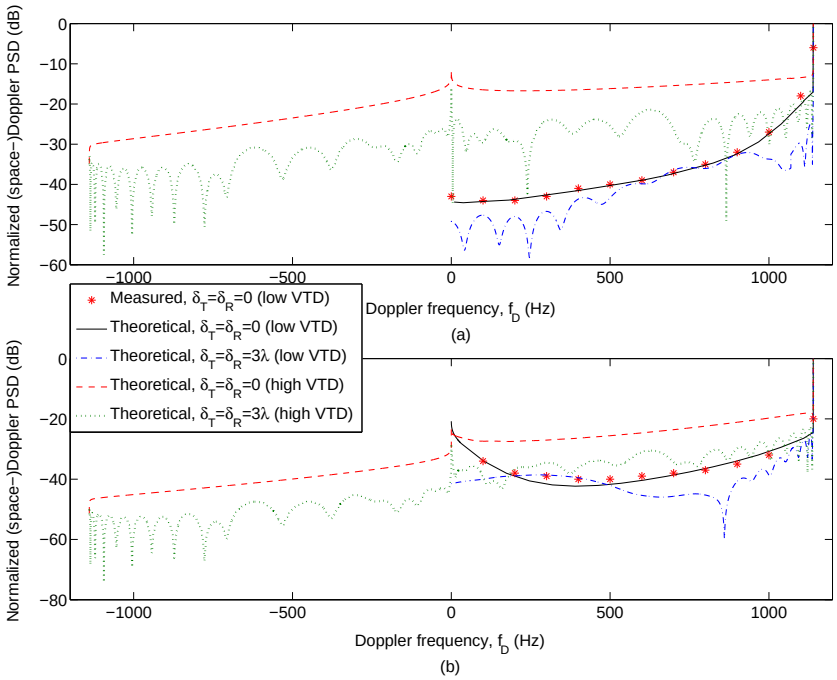

FIGURE 6.7: Normalised (space-)Doppler PSDs of the (a) first tap and (b) second tap of the proposed wideband MIMO M2M channel model with low and high VTDs when the Tx and Rx are moving in opposite directions on an expressway.

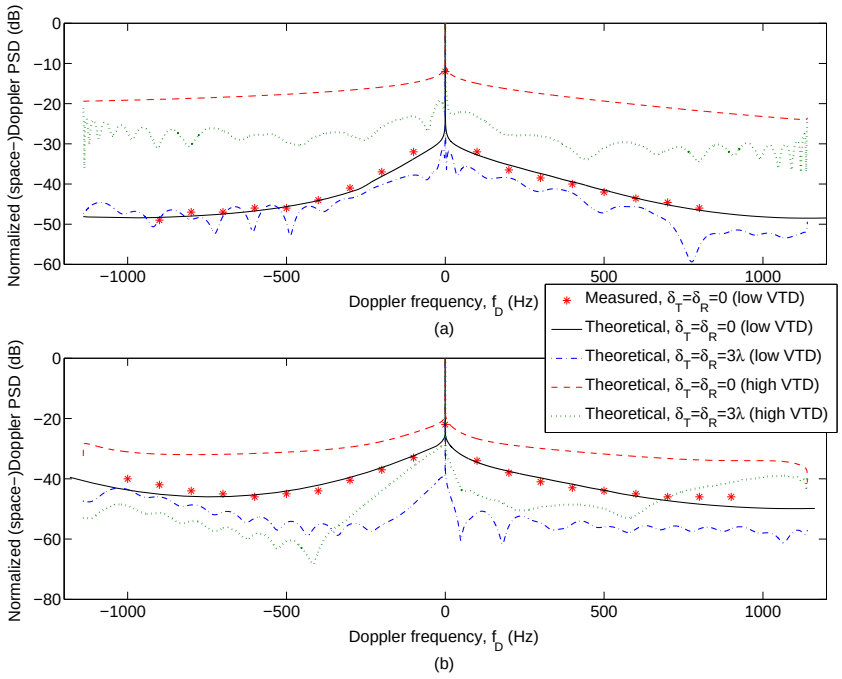

FIGURE 6.8: Normalised (space-)Doppler PSDs of the (a) first tap and (b) second tap of the proposed wideband MIMO M2M channel model with low and high VTDs when the Tx and Rx are moving in the same direction on an expressway.

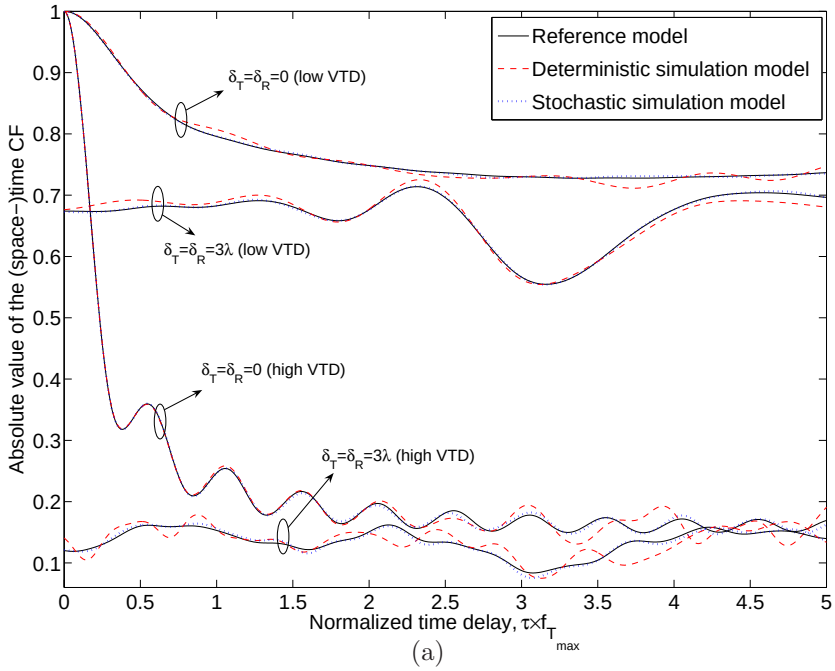

(a)

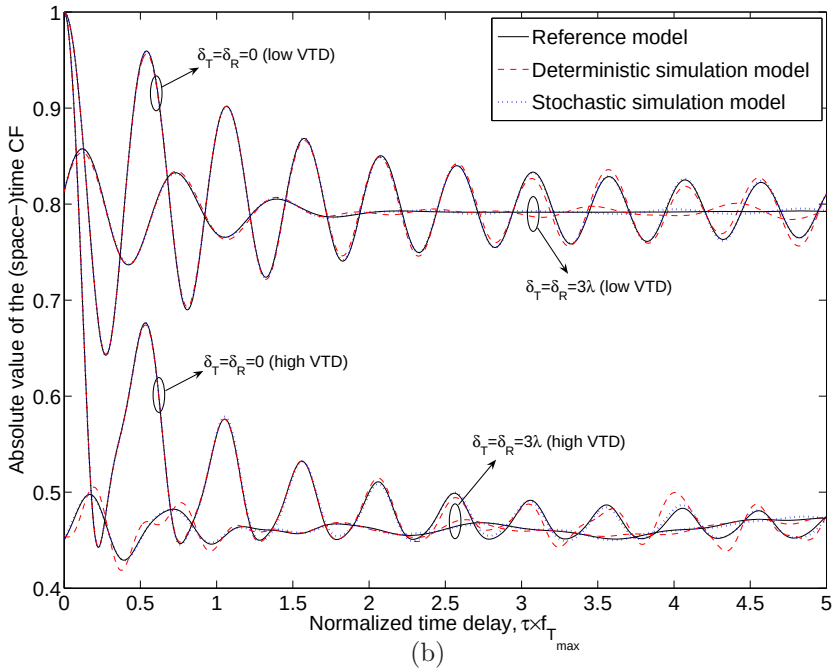

(b)

FIGURE 6.9: Absolute value of the (space-)time CFs of the (a) first tap and (b) second tap of the proposed wideband MIMO M2M channel mathematical reference model and corresponding simulation models with low and high VTDs when the Tx and Rx are moving in opposite directions on an expressway.

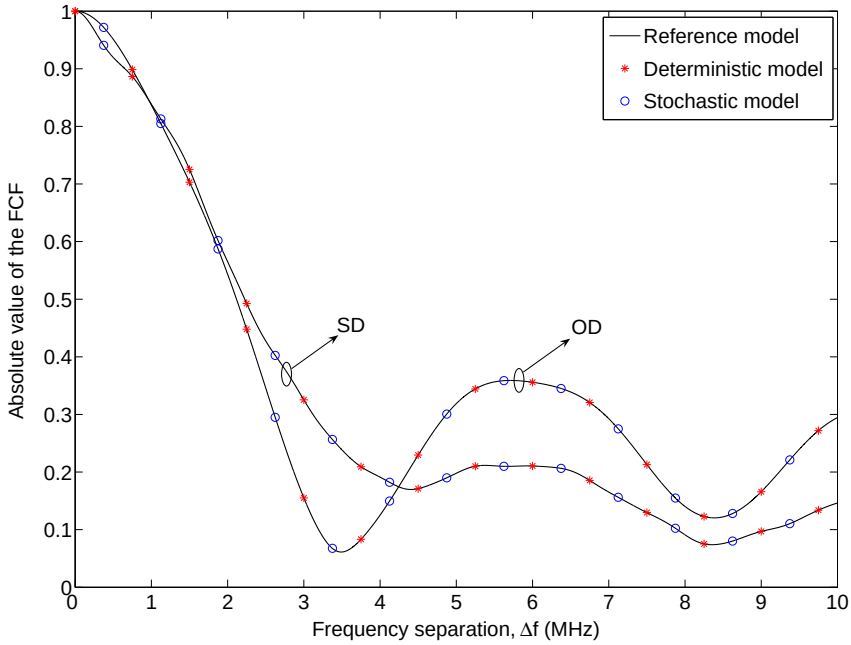

FIGURE 6.10: Absolute value of the FCF for the mathematical reference model, deterministic and stochastic simulation models. SD: same direction; OD: opposite directions.

tap. Unfortunately, to the best of the authors' knowledge, no measurement results (e.g., in [31, 32, 33, 34, 35, 55, 103]) were available regarding the impact of the high VTD (e.g., a traffic jam) on the SD PSD. Comparing the theoretical SD PSDs with different VTDs in FIGURES 6.7 and 6.8, we observe that the VTD significantly affects the SD PSDs at different taps in M2M channels. Moreover, the space separation results in the fluctuations on SD PSDs.

By using the same parameters as FIGURES 6.7 (a) and (b), FIGURES 6.9 (a) and (b) depict the corresponding ST CFs for the first tap and second tap, respectively. Again, the VTD affects greatly the ST correlation properties at different taps. Higher VTDs lead to lower correlation properties. For further comparison, the ST CFs of the proposed IMMEA deterministic and stochastic simulation models are also plotted. The results obtained for the stochastic model are averaged over N_{sto}=30 trials. It is obvious that the deterministic model provides a fairly good approximation to the ST CFs of the mathematical reference model, while the stochastic model presents much better approximation with an even smaller number of complex harmonic functions.

FIGURE 6.10 shows the FCF of our mathematical reference model, IMMEA deterministic and stochastic simulation models. The results are obtained by using the following parameters reported in [31]: 1) the propagation delays $\{\tau'\}_{l=1}^{4}=\{0, 0.1, 0.2, 0.3\}\ \mu s$ and the tap powers $\{c_l^2\}_{l=1}^{4}=\{0, -6.3, -25.1, -22.7\}$ dB when the Tx and Rx are moving in opposite directions; 2) the propagation delays $\{\tau'\}_{l=1}^{8}=\{0, 0.1, 0.2, 0.3, 0.4, 0.5, 0.6, 0.7\}\ \mu s$ and the tap powers $\{c_l^2\}_{l=1}^{8} = \{0, -11.2, -19, -21.9, -25.3, -24.4, -28.0, -26.1\}$ dB when the Tx and Rx are moving in the same direction. It is clear that the FCFs of the simulation models are identical to those of the mathematical reference model.

6.6 Summary

This chapter has proposed a wideband MIMO M2M RS-GBSM, which has the ability to study the channel statistics at different time delays and consider the impact of the VTD on channel statistics. From the proposed mathematical reference model, the ST CF, SD PSD, FCF, and PDP have been derived. Numerical results have demonstrated that the VTD has a great impact on the resulting CFs and PSDs. It has been shown that the theoretical per-tap Doppler PSDs closely match the measured data, which validates the utility of the proposed mathematical reference model. Based on our mathematical reference model, we have proposed new deterministic and stochastic SoS simulation models for wideband MIMO M2M Ricean fading channels. We have demonstrated that by removing the frequency-selectivity, our wideband simulation models can be reduced to the narrowband ones, which are actually the corresponding simulation models for the proposed narrowband MIMO M2M mathematical reference model in Chapter 5. Furthermore, a new parameter computation method for a deterministic simulation model, named IMMEA, has been derived for non-isotropic scattering MIMO M2M channels. It has been demonstrated that IMMEA outperforms other existing methods, i.e., the MMEA and MMEA2. Numerical results have shown that the proposed deterministic model with the IMMEA presents a fairly good approximation to the desired properties of our mathematical reference model, while the proposed stochastic model provides better approximation over a wider range of normalised time delays with even small numbers of complex harmonic functions.

Chapter 7

Conclusions and Outlook

Wireless channel modelling and simulation are crucial for designing and developing wireless communication systems. Knowledge of different propagation channels obtained from channel measurements and corresponding channel models are important for the development of algorithms for reliable communications. Simulation models complement this by reproducing the desired statistical properties of propagation channels in practical simulations and thus providing a platform for designing and testing different algorithms. In this chapter, we summarise the key findings of our research on wireless channel modelling and simulation for MIMO F2M cellular communication systems and SISO/MIMO M2M communication systems. Furthermore, several interesting future research directions are proposed.

7.1 Summary of Results

A. F2M Cellular Channel Models

- Based on the TDL structure, a new wideband multiple-ring based MIMO channel mathematical reference model has been proposed for non-isotropic scattering macro-cell scenarios. The proposed mathematical reference model is actually an extension of the traditional narrowband one-ring model to wideband applications. Moreover, the proposed wideband model has the ability to investigate the

channel statistics for different time delays and to consider the interaction of the AoA, AoD, and ToA. From the new wideband mathematical reference model, a generic STF CF has been derived, which can be reduced to a closed-form STF CF for narrowband MIMO channels by removing the frequency-selectivity. Numerical results have revealed the impact of the environment parameter on frequency correlations and the inherent frequency correlations within spatial correlations.

- From the newly proposed multiple-ring based MIMO channel mathematical reference model, we have developed the corresponding wideband deterministic SoS simulation model. A narrowband deterministic SoS simulator has also been obtained from the developed wideband simulation model by removing the frequency-selectivity. The statistics of the simulation models have been verified by simulations and the results have shown that these simulation models are a good approximation to the mathematical reference models.

B. M2M Channel Models

- Based on a non-isotropic scattering narrowband two-ring SISO M2M mathematical reference model, new SoS simulation models have been proposed. First, a deterministic simulation model has been proposed and the statistical properties of the model have been derived and verified by simulations. The results have shown that the deterministic model provides a fairly good approximation to the desired correlation properties of the mathematical reference model in a shorter normalised time-delay range. In order to approximate the desired properties over a longer time-delay range, a new stochastic simulation model has been developed. Compared to the existing ARA stochastic model, the proposed stochastic model yields a better performance with an even lower complexity.

- A generic and adaptive RS-GBSM has been proposed for non-isotropic scattering narrowband MIMO M2M Ricean fading channels. The proposed model includes a single- and double-bounce two-ring model, a single-bounce ellipse model, and a LoS component and thus is adaptable to a wide variety of M2M scenarios by

adjusting some model parameters. Moreover, the proposed model is the first RS-GBSM that has the ability to consider the impact of the VTD on channel statistics. From the proposed model, we have derived the STF CF and the SDF PSD for non-isotropic scattering environments. Some of the obtained numerical results can serve as a guide for setting some important parameters of our model and building up more purposeful measurement campaigns in the future. It has been shown that the derived theoretical Doppler PSDs closely match the measured data, demonstrating the utility of the proposed model.

- From the corresponding non-isotropic scattering narrowband SISO M2M RS-GBSM, which is a simplified version of the proposed narrowband MIMO M2M RS-GBSM, the envelope LCR and AFD have been derived. Based on the derived LCR and AFD, we have investigated for the first time the impact of the VTD on the LCR and AFD. The results have illustrated that the VTD significantly affects the LCR and AFD for non-isotropic scattering M2M Ricean fading channels. Moreover, the derived LCR and AFD yield an excellent agreement with the measured data.

- In order to extend the developed narrowband MIMO M2M RS-GBSM to wideband applications, we have proposed a novel wideband RS-GBSM that has the ability to investigate the channel statistics at different time delays and consider the impact of the VTD on per-tap channel statistics. Based on the proposed wideband model, the ST CF, SD PSD, FCF, and PDP have been derived. Numerical results have shown that the VTD has a great impact on the resulting CFs and PSDs. In addition, excellent agreement is achieved between the theoretical per-tap Doppler PSDs and the measured data, which validates the utility of the proposed wideband model.

- Based on the proposed wideband MIMO M2M RS-GBSM, we have designed new wideband deterministic and stochastic SoS simulation models for non-isotropic scattering environments. The corresponding narrowband SoS simulation models, whose mathematical reference model is the proposed narrowband MIMO

M2M RS-GBSM, can be easily obtained from the proposed wideband simulation models by removing the frequency-selectivity. Moreover, a new parameter computation method for a deterministic simulation model, namely IMMEA, has been proposed for non-isotropic scattering MIMO M2M channels. Compared to other existing methods (e.g., the MMEA and MMEA2), the IMMEA yields better performance in terms of fitting the correlation properties of the mathematical reference models. Numerical results have shown that the developed simulation models provide a close agreement with the desired statistical properties of the corresponding mathematical reference models.

7.2 Future Research Directions

There are several directions of this thesis that can be expanded at a future stage. Some of these deserve more thorough investigations and are outlined below.

- **Measurements:** Due to a lack of channel measurement capabilities, our contributions have been limited to proposing theoretical RS-GBSMs and simulation models of MIMO F2M channels and M2M channels. Although the developed narrowband and wideband MIMO M2M RS-GBSMs have been validated by comparing with some available measurement data, the complete verification of these proposed RS-GBSMs still needs the comparison with more purposeful measurement data, such as the measurement data for high VTD scenarios as noted in Chapters 5 and 6. Therefore, future research efforts may be devoted to conducting measurement campaigns cooperated with Professor Sana Salous in Durham University and proposing channel models from these measurements.

  In this case, other modelling approaches, such as non-geometrical stochastic modelling approach and irregular-shaped geometry-based stochastic modelling approach, can also be applied to propose novel M2M channel models. Furthermore, it is desirable to compare the proposed different types of M2M models, i.e., NGSM, RS-GBSM, and IS-GBSM, in order to obtain a deeper understanding of

them. This may be useful for the development of a new type of M2M channel model that offers better trade-off between the model accuracy and complexity.

- **Non-stationarity of M2M channels:** Due to the high velocity of the Tx/Rx and the existence of many moving scatterers around the Tx/Rx in M2M environments, the time variation in M2M channels can be more rapid than that in F2M channels. This essentially means that M2M channels are in most cases statistically non-stationary, since the stationarity conditions pertain to a much shorter time period than in F2M channels. However, the proposed narrowband and wideband MIMO M2M RS-GBSMs assume that all effective scatterers are stationary and thus cannot capture the non-stationarity of M2M channels. Therefore, it is desirable to extend the proposed M2M models to be capable of capturing the non-stationarity of M2M channels.

  The discussion in Chapter 2 showed that the non-stationary nature of M2M channels has been considered in NGSMs [32] by using a birth/death process to account for the appearance and disappearance of taps, and in IS-GBSMs [59] by prescribing the motion of the Tx, Rx, and mobile scatterers. However, the trade-off between the model accuracy and complexity of the NGSMs and IS-GBSMs in capturing the non-stationarity still needs more comprehensive investigations. For example, it is interesting to investigate whether the effect of the drift of scatterers into different delay bins on the non-stationarity of M2M channels is significant, and whether it is worth sacrificing the complexity for capturing this effect by using IS-GBSMs.

  In summary, how to properly incorporate the non-stationarity into M2M channel models is still an open problem. Based on the conducted measurement campaigns in the future, it is extremely important to comprehensively investigate the features of different types of M2M channel models, i.e., NGSM, RS-GBSM, and IS-GBSM, in capturing the non-stationarity of M2M channels in order to find a sensible approach to fill this gap.

- **Impact of the elevation angle on channel statistics:** In practical M2M channels, waves travel in three dimensions, instead of two dimensions. This

means that 3D channel models are necessary, especially for urban canyon scenarios and some expressways with high walls or sound blockers on both edges. Therefore, another research direction is to extend the proposed 2D M2M models to 3D models and then further investigate the impact of the elevation angle on various channel statistics in different M2M scenarios.

- **Relay channels:** Relay channels are encountered in systems that utilise cooperative diversity or virtual antenna arrays. Depending on the mobility of the relay, the overall channel from the source to the destination via the relay in amplify and forward systems is either a cascade of F2M and M2M links or a cascade of F2M and mobile-to-fixed links. Therefore, the statistical properties of relay channels are quite different from those of F2M or M2M channels. A possible extension of our work is the development of channel models for relay channels.

Appendix A

Derivation of (3.11)

Substituting (3.5), (3.6), and (3.9) into (3.10) and after some mathematical manipulation, we have

$$\rho_{l,oq;l,o'q'}(\tau,\chi)=\frac{1}{2\pi I_0(k)}\sum_{i=0}^{\Lambda_l-1}\sum_{r=1}^{R_c}Q_{l,i,r}e^{jC_{l,i}}\int_{\mu_{l,i,r}-\Delta\mu_{l,i}}^{\mu_{l,i,r}+\Delta\mu_{l,i}}e^{A_{l,i,r}\cos\phi^R_{l,i,r}}e^{B_{l,i,r}\sin\phi^R_{l,i,r}}d\phi^R_{l,i,r}. \tag{A.1}$$

Considering the periodic property of trigonometric function and the relationship between the sine and cosine functions, the well-known series $e^{z\sin\theta}=I_0(z)+2\sum_{k=0}^{\infty}(-)^k I_{2k+1}(z)\sin[(2k+1)\theta]+2\sum_{k=1}^{\infty}(-)^k I_{2k}(z)\cos(2k\theta)$ in [104] can be further simplified as

$$e^{z\sin\theta}=I_0(z)+2\sum_{\ell=1}^{\infty}(-1)^{\ell}I_{\ell}(z)\cos[\ell\theta+\ell\pi/2]. \tag{A.2}$$

By making use of another well-known series $e^{z\cos\theta}=I_0(z)+2\sum_{k=1}^{\infty}I_k(z)\cos(k\theta)$ in [104] and the further simplified series in (A.2), $\rho_{l,oq;l,o'q'}(\tau,\chi)$ can be further expressed as

$$\begin{aligned}\rho_{l,oq;l,o'q'}(\tau,\chi)=\frac{1}{2\pi I_0(k)}\sum_{i=0}^{\Lambda_l-1}\sum_{r=1}^{R_c}Q_{l,i,r}e^{jC_{l,i}}\int_{\mu_{l,i,r}-\Delta e_{l,i}}^{\mu_{l,i,r}+\Delta e_{l,i}}\left[I_0(A_{l,i,r})+2\sum_{\ell=1}^{\infty}I_{\ell}(A_{l,i,r})\cos\left(\ell\phi^R_{l,i,r}\right)\right]\\ \times\left[I_0(B_{l,i,r})+2\sum_{\ell'=1}^{\infty}(-1)^{\ell'}I_{\ell'}(B_{l,i,r})\cos\left(\ell'\phi^R_{l,i,r}+\ell'\pi/2\right)\right]d\phi^R_{l,i,r}.\end{aligned} \tag{A.3}$$

To obtain the closed-form expression of (3.11), the following definite integral functions in [101] are used:

$$\int_{\mu-\Delta\mu}^{\mu+\Delta\mu} \cos(\ell\phi)d\phi = \frac{2\sin(\ell\Delta\mu)\cos(\ell\mu)}{\ell} \tag{A.4a}$$

$$\int_{\mu-\Delta\mu}^{\mu+\Delta\mu} \cos(\ell'\phi + \ell'\pi/2)d\phi = \frac{2\sin(\ell'\Delta\mu)\cos(\ell'\mu + \ell'\pi/2)}{\ell'} \tag{A.4b}$$

$$\int_{\mu-\Delta\mu}^{\mu+\Delta\mu} \cos(\ell\phi + \ell\pi/2)\cos(\ell\phi)d\phi = \Delta\mu\cos(\ell\pi/2) + \frac{\sin(2\ell\Delta\mu)\cos(2\ell\mu + \ell\pi/2)}{2\ell} \tag{A.4c}$$

$$\int_{\mu-\Delta\mu}^{\mu+\Delta\mu} \sin[\ell'\phi + (\ell'-1)\pi/2]\cos(\ell\phi)d\phi = \frac{\sin[(\ell+\ell')\Delta\mu]\cos[(\ell+\ell')\mu + \ell'\pi/2]}{\ell+\ell'} + \frac{\sin[(\ell-\ell')\Delta\mu]\cos[(\ell-\ell')\mu - \ell'\pi/2]}{\ell-\ell'}. \tag{A.4d}$$

Appendix B

Derivation of (3.16)

Substituting $\Delta\mu_{l,i}=\pi$ and $\Lambda_l=R_c=1$ into (3.11), we have

$$\rho_{l,oq;l,o'q'}(\tau,\chi)=\frac{e^{jC}\left[I_0(A)\,I_0(B)+2\sum_{\ell=1}^{\infty}(-1)^{\ell}\,I_{2\ell}(A)\,I_{2\ell}(B)\right]}{I_0(k)} \tag{B.1}$$

By making use of the Neumann's addition theorem [105], the following equation can be obtained by further considering $J_\ell(jz)=j^\ell I_\ell(z)$, where ℓ is integral, and setting the angle $\phi=\pi/2$ in the theorem

$$I_0\left[\left(Z^2+z^2\right)\right]=I_0(Z)\,I_0(z)+2\sum_{\ell=1}^{\infty}(-1)^{\ell}\,I_{2\ell}(Z)\,I_{2\ell}(z). \tag{B.2}$$

With the help of (B.1) and (B.2), (3.16) can be easily obtained.

Appendix C

Derivation of (4.13a) and (4.13b)

In this appendix, we first derive the time-average autocorrelation function $\tilde{\rho}_{\tilde{h}_i\tilde{h}_i}(\tau)$ of the in-phase component $\tilde{h}_i(t)$ (4.5) of the proposed deterministic simulation model

$$
\begin{aligned}
\tilde{\rho}_{\tilde{h}_i\tilde{h}_i}(\tau) &= \left\langle \tilde{h}_i(t)\,\tilde{h}_i(t-\tau) \right\rangle = \lim_{T\to\infty}\frac{1}{2T}\int_{-T}^{T}\tilde{h}_i(t)\,\tilde{h}_i(t-\tau)\,dt \\
&= \lim_{T\to\infty}\frac{1}{2T}\int_{-T}^{T}\frac{1}{N_iM_i}\sum_{n_i,m_i=1}^{N_i,M_i}\sum_{n_i',m_i'=1}^{N_iM_i}\cos\Big[\tilde{\psi}_{n_im_i}+2\pi f_{T_{max}}t\cos(\tilde{\phi}_T^{m_i}-\gamma_T) \\
&\quad +2\pi f_{R_{max}}t\cos(\tilde{\phi}_R^{n_i}-\gamma_R)\Big]\cos\Big[\tilde{\psi}_{n_i'm_i'}+2\pi f_{T_{max}}(t-\tau)\cos(\tilde{\phi}_T^{m_i'}-\gamma_T) \\
&\quad +2\pi f_{R_{max}}(t-\tau)\cos(\tilde{\phi}_R^{n_i'}-\gamma_R)\Big]\,dt \\
&= \lim_{T\to\infty}\frac{1}{2T}\int_{-T}^{T}\frac{1}{N_iM_i}\sum_{n_i,m_i=1}^{N_i,M_i}\cos\Big[\tilde{\psi}_{n_im_i}+2\pi f_{T_{max}}t\cos(\tilde{\phi}_T^{m_i}-\gamma_T)+2\pi f_{R_{max}}t \\
&\quad \times\cos(\tilde{\phi}_R^{n_i}-\gamma_R)\Big]\cos\Big[\tilde{\psi}_{n_im_i}+2\pi f_{T_{max}}(t-\tau)\cos(\tilde{\phi}_T^{m_i}-\gamma_T)+2\pi f_{R_{max}} \\
&\quad \times(t-\tau)\cos(\tilde{\phi}_R^{n_i}-\gamma_R)\Big]\,dt \\
&\quad (\text{since } n_i\neq n_i' \text{ and/or } m_i\neq m_i',\ \tilde{\rho}_{\tilde{h}_i\tilde{h}_i}(\tau)=0) \\
&= \lim_{T\to\infty}\frac{1}{2T}\int_{-T}^{T}\frac{1}{2N_iM_i}\sum_{n_i,m_i=1}^{N_i,M_i}\cos\Big[2\pi f_{T_{max}}\tau\cos(\tilde{\phi}_T^{m_i}-\gamma_T) \\
&\quad +2\pi f_{R_{max}}\tau\cos(\tilde{\phi}_R^{n_i}-\gamma_R)\Big]\,dt. \qquad \text{(C.1)}
\end{aligned}
$$

The integral of (C.1) is trivial as the integrand does not contain the variable of integration. Therefore, the expression of $\tilde{\rho}_{\tilde{h}_i\tilde{h}_i}(\tau)$ in (4.13a) can be easily obtained from (C.1).

The derivation of the time-average cross-correlation function $\tilde{\rho}_{\tilde{h}_i\tilde{h}_q}(\tau)$ between the in-phase component $\tilde{h}_i(t)$ (4.5) and the quadrature component $\tilde{h}_q(t)$ (4.6) of the proposed deterministic simulation model is outlined as follows

$$
\begin{aligned}
\tilde{\rho}_{\tilde{h}_i\tilde{h}_q}(\tau) &= \left\langle \tilde{h}_i(t)\,\tilde{h}_q(t-\tau)\right\rangle = \lim_{T\to\infty}\frac{1}{2T}\int_{-T}^{T}\tilde{h}_i(t)\,\tilde{h}_q(t-\tau)\,dt \\
&= \lim_{T\to\infty}\frac{1}{2T}\int_{-T}^{T}\frac{1}{\sqrt{N_iM_i}\sqrt{N_qM_q}}\sum_{n_i,m_i=1}^{N_i,M_i}\sum_{n_q,m_q=1}^{N_q,M_q}\cos\Big[\tilde{\psi}_{n_im_i}+2\pi f_{T_{max}}t\cos(\tilde{\phi}_T^{m_i}-\gamma_T) \\
&\quad +2\pi f_{R_{max}}t\cos(\tilde{\phi}_R^{n_i}-\gamma_R)\Big]\sin\Big[\tilde{\psi}_{n_qm_q}+2\pi f_{T_{max}}(t-\tau)\cos(\tilde{\phi}_T^{m_q}-\gamma_T) \\
&\quad +2\pi f_{R_{max}}(t-\tau)\cos(\tilde{\phi}_R^{n_q}-\gamma_R)\Big]\,dt \\
&= \begin{cases} -\lim_{T\to\infty}\frac{1}{2T}\int_{-T}^{T}\frac{1}{2NM}\sum_{n,m=1}^{N,M}\sin\Big[2\pi f_{T_{max}}\tau\cos(\tilde{\phi}_T^{m}-\gamma_T)+2\pi f_{R_{max}}\tau\cos(\tilde{\phi}_R^{n}-\gamma_R)\Big]dt\,, \\ \qquad\qquad N_i{=}N_q{=}N \text{and } M_i{=}M_q{=}M\ (\textit{Cases I and III}) \\ 0\,, \qquad\qquad N_i{\neq}N_q \text{ and } M_i{\neq}M_q\ (\textit{Case II}) \end{cases}
\end{aligned}
\tag{C.2}
$$

where at the third equality of (C.2), setting $N_i \neq N_q$ and $M_i \neq M_q$ results in the integrand for *Case II* containing the variable of integration t unlike the integrand for other cases.

Appendix D

Derivation of the CF $\hat{\rho}_{\hat{h}\hat{h}}(\tau)$

In this appendix, we derive the CF $\hat{\rho}_{\hat{h}\hat{h}}(\tau)$ for the stochastic simulation model in (4.14)

$$\hat{\rho}_{\hat{h}\hat{h}}(\tau)=E\left[\hat{h}(t)\,\hat{h}^{*}(t-\tau)\right]$$

$$=\begin{cases}\dfrac{1}{NM}\displaystyle\sum_{n,m=1}^{N,M}\int_{\frac{-1}{2}}^{\frac{1}{2}}\int_{\frac{-1}{2}}^{\frac{1}{2}} e^{j2\pi\tau\left\{f_{T_{max}}\cos\left[F^{-1}\left(\frac{m-1/2+\theta_T}{vM}\right)-\gamma_T\right]+f_{R_{max}}\cos\left[F^{-1}\left(\frac{n-1/2+\theta_R}{uN}\right)-\gamma_R\right]\right\}} \\ \qquad\qquad \times d\theta_T d\theta_R\,, \quad N_i{=}N_q{=}N \text{ and } M_i{=}M_q{=}M \qquad (\textit{Cases I} \text{ and } \textit{III}) \\ \dfrac{1}{2N_iM_i}\displaystyle\sum_{n_i,m_i=1}^{N_i,M_i}\int_{\frac{-1}{2}}^{\frac{1}{2}}\int_{\frac{-1}{2}}^{\frac{1}{2}}\cos\Bigg\{2\pi\tau\Bigg(f_{T_{max}}\cos\left[F^{-1}\left(\frac{m_i-1/2+\theta_T}{M_i}\right)-\gamma_T\right]+f_{R_{max}} \\ \times\cos\left[F^{-1}\left(\frac{n_i-1/2+\theta_R}{N_i}\right)-\gamma_R\right]\Bigg)\Bigg\}\,d\theta_T d\theta_R+\dfrac{1}{2N_qM_q}\displaystyle\sum_{n_q,m_q=1}^{N_q,M_q}\int_{\frac{-1}{2}}^{\frac{1}{2}}\int_{\frac{-1}{2}}^{\frac{1}{2}}\cos\{2\pi\tau(f_{T_{max}} \\ \times\cos\left[F^{-1}\left(\frac{m_q-1/2+\theta_T}{M_q}\right)-\gamma_T\right]+f_{R_{max}}\cos\left[F^{-1}\left(\frac{n_q-1/2+\theta_R}{N_q}\right)-\gamma_R\right]\Bigg)\Bigg\}\,d\theta_T d\theta_R\,, \\ (\textit{Case II})\end{cases}$$

$$
=\begin{cases}
\dfrac{NM}{NM}\displaystyle\sum_{n,m=1}^{N,M}\int_{F^{-1}\left(\frac{n-1}{uN}\right)}^{F^{-1}\left(\frac{n}{uN}\right)}\int_{F^{-1}\left(\frac{m-1}{vM}\right)}^{F^{-1}\left(\frac{m}{vM}\right)} e^{j2\pi\tau\left[f_{T_{max}}\cos\left(\beta_T^m-\gamma_T\right)+f_{R_{max}}\cos\left(\beta_R^n-\gamma_R\right)\right]}\dfrac{e^{k_T\cos(\beta_T^m-\mu_T)+k_R\cos(\beta_R^n-\mu_R)}}{4\pi^2 I_0(k_T)I_0(k_R)} \\
\qquad\qquad \times d\beta_T^m d\beta_R^n \qquad N_i{=}N_q{=}N \text{ and } M_i{=}M_q{=}M \qquad (\textit{Cases I and III}) \\
\dfrac{N_iM_i}{2N_iM_i}\displaystyle\sum_{n_i,m_i=1}^{N_i,M_i}\int_{F^{-1}\left(\frac{n_i-1}{N_i}\right)}^{F^{-1}\left(\frac{n_i}{N_i}\right)}\int_{F^{-1}\left(\frac{m_i-1}{M_i}\right)}^{F^{-1}\left(\frac{m_i}{M_i}\right)}\cos\{2\pi\tau[f_{T_{max}}\cos\left(\beta_T^{m_i}-\gamma_T\right)+f_{R_{max}}\cos(\beta_R^{n_i}-\gamma_R)]\} \\
\times\dfrac{e^{k_T\cos(\beta_T^{m_i}-\mu_T)+k_R\cos(\beta_R^{n_i}-\mu_R)}}{4\pi^2 I_0(k_T)I_0(k_R)}d\beta_T^{m_i}d\beta_R^{n_i}+\dfrac{N_qM_q}{2N_qM_q}\displaystyle\sum_{n_q,m_q=1}^{N_q,M_q}\int_{F^{-1}\left(\frac{n_q-1}{N_q}\right)}^{F^{-1}\left(\frac{n_q}{N_q}\right)}\int_{F^{-1}\left(\frac{m_q-1}{M_q}\right)}^{F^{-1}\left(\frac{m_q}{M_q}\right)}\cos\{2\pi\tau[f_{T_{max}} \\
\times\cos\left(\beta_T^{m_q}-\gamma_T\right)+f_{R_{max}}\cos\left(\beta_R^{n_q}-\gamma_R\right)]\}\dfrac{e^{k_T\cos(\beta_T^{m_q}-\mu_T)+k_R\cos(\beta_R^{n_q}-\mu_R)}}{4\pi^2 I_0(k_T)I_0(k_R)}d\beta_T^{m_q}d\beta_R^{n_q} \\
\qquad\qquad (\textit{Case II})
\end{cases}
$$

$$
=\begin{cases}
\dfrac{1}{2\pi^2 I_0(k_T)I_0(k_R)}\displaystyle\int_0^{\pi}\int_0^{\pi} e^{j2\pi\tau[f_{T_{max}}\cos(\beta_T-\gamma_T)+f_{R_{max}}\cos(\beta_R-\gamma_R)]} \\
\qquad\qquad \times e^{k_T\cos(\beta_T^m-\mu_T)+k_R\cos(\beta_R^n-\mu_R)}d\beta_T d\beta_R\,, \qquad (\textit{Case I}) \\
\dfrac{1}{4\pi^2 I_0(k_T)I_0(k_R)}\displaystyle\int_{-\pi}^{\pi}\int_{-\pi}^{\pi}\cos\{2\pi\tau[f_{T_{max}}\cos(\beta_T-\gamma_T)+f_{R_{max}}\cos(\beta_R-\gamma_R)]\} \\
\qquad\qquad \times e^{k_T\cos(\beta_T-\mu_T)+k_R\cos(\beta_R-\mu_R)}d\beta_T d\beta_R\,, \qquad (\textit{Case II}) \\
\dfrac{1}{4\pi^2 I_0(k_T)I_0(k_R)}\displaystyle\int_{-\pi}^{\pi}\int_{-\pi}^{\pi} e^{j2\pi\tau[f_{T_{max}}\cos(\beta_T-\gamma_T)+f_{R_{max}}\cos(\beta_R-\gamma_R)]} \\
\qquad\qquad \times e^{k_T\cos(\beta_T^m-\mu_T)+k_R\cos(\beta_R^n-\mu_R)}d\beta_T d\beta_R\,, \qquad (\textit{Case III})
\end{cases}
$$

(D.1)

where at the third equality of (D.1), the integration variables θ_T and θ_R were replaced by $\beta_T^{m_{i/q}} = F^{-1}\left(\frac{m_{i/q}-1/2+\theta_T}{M_{i/q}}\right)$, $d\theta_T = \frac{M_{i/q} e^{k_T \cos\left(\beta_T^{m_{i/q}} - \mu_T\right)}}{2\pi I_0(k_T)} d\beta_T^{m_{i/q}}$, $\beta_R^{n_{i/q}} = F^{-1}\left(\frac{n_{i/q}-1/2+\theta_R}{N_{i/q}}\right)$, $d\theta_R = \frac{N_{i/q} e^{k_R \cos\left(\beta_R^{n_{i/q}} - \mu_R\right)}}{2\pi I_0(k_R)} d\beta_R^{n_{i/q}}$, $\beta_T^m = F^{-1}\left(\frac{m-1/2+\theta_T}{M}\right)$, $d\theta_T = \frac{M e^{k_T \cos(\beta_T^m - \mu_T)}}{2\pi I_0(k_T)} d\beta_T^m$, $\beta_R^n = F^{-1}\left(\frac{n-1/2+\theta_R}{N}\right)$, and $d\theta_R = \frac{N e^{k_R \cos(\beta_R^n - \mu_R)}}{2\pi I_0(k_R)} d\beta_R^n$. The two single definite integrals in the last equality of (D.1) can be solved by using the equality $\int_{-\pi}^{\pi} e^{a \sin c + b \cos c} dc = 2\pi I_0\left(\sqrt{a^2+b^2}\right)$ [101]. After some manipulation, the closed-form expression of the CF $\hat{\rho}_{\hat{h}\hat{h}}(\tau)$ can be obtained and is the same as $\rho_{hh}(\tau)$ in (4.2).

Appendix E

Derivation of (5.11)–(5.16)

In this appendix, following the same derivation procedure (i.e., the same newly proposed method), we will derive these general relationships for the two-ring model in (5.11)–(5.14) and the ellipse model in (5.15) and (5.16). In FIGURE E.1, applying the laws of cosines and sines to the triangle $O_T s^{(n_1)} O_R$, we obtain

$$\xi_{n_1}^2 = R_T^2 + D^2 - 2DR_T \cos\phi_T^{(n_1)} \tag{E.1}$$

$$R_T^2 = \xi_{n_1}^2 + D^2 + 2D\xi_{n_1} \cos\phi_R^{(n_1)} \tag{E.2}$$

$$\frac{R_T}{\sin\phi_R^{(n_1)}} = \frac{\xi_{n_1}}{\sin\phi_T^{(n_1)}}. \tag{E.3}$$

From the above expressions, we can easily obtain (5.11) and (5.12). Similarly, applying the laws of cosines and sines to the triangle $O_T s^{(n_2)} O_R$, we have

$$\xi_{n_2}^2 = R_R^2 + D^2 + 2DR_R \cos\phi_R^{(n_2)} \tag{E.4}$$

$$R_R^2 = \xi_{n_2}^2 + D^2 - 2D\xi_{n_2} \cos\phi_T^{(n_2)} \tag{E.5}$$

$$\frac{R_R}{\sin\phi_T^{(n_2)}} = \frac{\xi_{n_2}}{\sin\phi_R^{(n_2)}}. \tag{E.6}$$

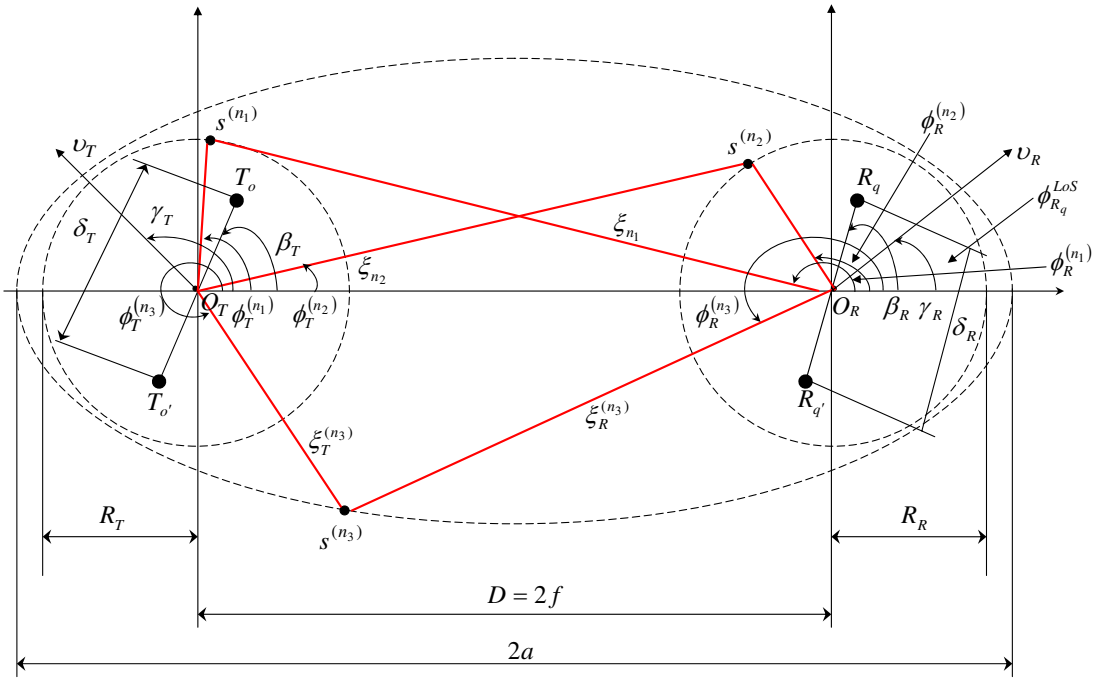

FIGURE E.1: Relationships between the AoA and AoD for single-bounced rays.

We can easily obtain (5.13) and (5.14) from these expressions. Analogously, applying the laws of cosines and sines to the triangle $O_T s^{(n_3)} O_R$, we get

$$\left(\xi_T^{(n_3)}\right)^2 = \left(\xi_R^{(n_3)}\right)^2 + D^2 + 2D\xi_R^{(n_3)} \cos\phi_R^{(n_3)} \tag{E.7}$$

$$\left(\xi_R^{(n_3)}\right)^2 = \left(\xi_T^{(n_3)}\right)^2 + D^2 - 2D\xi_T^{(n_3)} \cos\phi_T^{(n_3)} \tag{E.8}$$

$$\frac{\xi_R^{(n_3)}}{\sin\phi_T^{(n_3)}} = \frac{\xi_T^{(n_3)}}{\sin\phi_R^{(n_3)}}. \tag{E.9}$$

Based on the above expressions, and the following equalities $D{=}2f$ and $\xi_T^{(n_3)}{+}\xi_R^{(n_3)}{=}2a$, we can get (5.15) and (5.16).

Appendix F

Derivation of (5.21)

Considering the von Mises PDF for the two-ring model, applying the following approximate relationships $\phi_R^{(n_1)} \approx \pi - \Delta_T \sin \phi_T^{(n_1)}$ and $\phi_T^{(n_2)} \approx \Delta_R \sin \phi_R^{(n_2)}$, and substituting (5.2b) and (5.4)–(5.7) into (5.17), we have

$$\rho_{h_{oq}^{SB_{1(2)}} h_{o'q'}^{\prime SB_{1(2)}}}(\tau, \chi) = \frac{\left[2\pi I_0\left(k_{T(R)}^{SB_{1(2)}}\right)\right]^{-1} e^{jC_{T(R)}^{SB_{1(2)}}}}{\sqrt{(K_{oq}+1)(K_{o'q'}+1)}} \times \int_{-\pi}^{\pi} e^{\left(A_{T(R)}^{SB_{1(2)}} \cos\phi_{T(R)}^{SB_{1(2)}} + B_{T(R)}^{SB_{1(2)}} \sin\phi_{T(R)}^{SB_{1(2)}}\right)} d\phi_{T(R)}^{SB_{1(2)}} \quad \text{(F.1)}$$

where $A_{T(R)}^{SB_{1(2)}}$, $B_{T(R)}^{SB_{1(2)}}$, and $C_{T(R)}^{SB_{1(2)}}$ have been given in (5.22a)–(5.22c). The definite integrals in the right hand side of (F.1) can be solved by using the equality $\int_{-\pi}^{\pi} e^{a\sin c + b\cos c} dc = 2\pi I_0\left(\sqrt{a^2+b^2}\right)$ [101]. After some manipulation, we can get the closed-form expression (5.21).

Appendix G

Derivation of (5.28)

Given $a^2+b^2=c(d^2+e^2)$, after some complex manipulation, we can rewrite $I_0\left[\sqrt{\left(A_{T(R)}^{SB_{1(2)}}\right)^2+\left(B_{T(R)}^{SB_{1(2)}}\right)^2}\right]$ as

$$I_0\left[j\sqrt{W_{T(R)}^{SB_{1(2)}}}\sqrt{\left(\tau+\frac{D_{T(R)}^{SB_{1(2)}}}{W_{T(R)}^{SB_{1(2)}}}\right)^2+\left(\frac{E_{T(R)}^{SB_{1(2)}}}{W_{T(R)}^{SB_{1(2)}}}\right)^2}\right] \tag{G.1}$$

where $W_{T(R)}^{SB_{1(2)}}$, $D_{T(R)}^{SB_{1(2)}}$, and $E_{T(R)}^{SB_{1(2)}}$ have been given in (5.29b)–(5.29d). Note that the expression (G.1) corrects the expressions (38) and (39) in [28]. By applying the Fourier transform to (5.21) in terms of the time separation τ, and using (G.1) and the equality $\int_0^\infty I_0\left(j\alpha\sqrt{x^2+y^2}\right)\cos(\beta x)\,dx=\cos\left(y\sqrt{\alpha^2-\beta^2}\right)/\sqrt{\alpha^2-\beta^2}$ [101], we can obtain (5.28).

Appendix H

Comparison between the Doppler PSDs with different CFs (5.17) and (5.18)

To further clarify which CF definition, (5.17) or (5.18), results in the correct Doppler PSD to accurately reflect the underlying physical phenomena of real channels, we first derive the relationship between the Doppler PSD based on the CF (5.17), $S_{h_{oq}h_{oq}}(f_D)$, and the Doppler PSD based on the CF (5.18), $\tilde{S}_{h_{oq}h_{oq}}(f_D)$. Considering the equality $\tilde{\rho}_{h_{oq}h_{oq}}(\tau) = \rho^*_{h_{oq}h_{oq}}(\tau)$ and the Fourier transform relation between the CF and Doppler PSD, we have

$$\tilde{S}_{h_{oq}h_{oq}}(f_D) = S^*_{h_{oq}h_{oq}}(-f_D)\,. \tag{H.1}$$

From (H.1), it is clear that only if $S_{h_{oq}h_{oq}}(f_D)$ is a real function and symmetrical to the origin, the equality $\tilde{S}_{h_{oq}h_{oq}}(f_D) = S_{h_{oq}h_{oq}}(f_D)$ holds. Note that due to the Fourier transform relationship, the equality $\tilde{S}_{h_{oq}h_{oq}}(f_D) = S_{h_{oq}h_{oq}}(f_D)$ leads to the equality $\tilde{\rho}_{h_{oq}h_{oq}}(\tau) = \rho_{h_{oq}h_{oq}}(\tau)$ and vice versa. We now proceed the comparison of $S_{h_{oq}h_{oq}}(f_D)$ and $\tilde{S}_{h_{oq}h_{oq}}(f_D)$ in the following two typical scenarios.

The first typical scenario, *Scenario1*, is a non-isotropic F2M macro-cell propagation environment ($f_{T_{max}} = 0$), as shown in FIGURE H.1(a). We use a one-ring model to

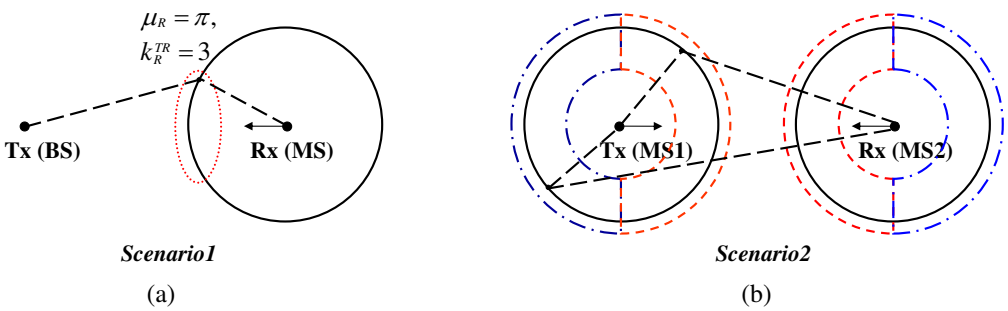

FIGURE H.1: Graphical description of (a) *Scenario1* and (b) *Scenario2*.

represent this scenario, where the ring of scatterers is around the Rx, i.e., MS, and the MS moves toward the direction of the Tx, i.e., $\gamma_R{=}\pi$. Note that the major amount of scatterers are located in a small part of the ring facing the motion of the MS, i.e., $\mu_R{=}\pi$. The second scenario, *Scenario2*, is an isotropic M2M propagation environment ($k_T^{TR}{=}k_R^{TR}{=}0$), where the Tx and Rx move in opposite directions ($\gamma_T{=}0$ and $\gamma_R{=}\pi$), as shown in FIGURE H.1(b). Here, a single-bounce two-ring model is used to represent this scenario. For *Scenario1*, based on (H.1), the opposite results for the Doppler PSD are expected as shown in FIGURE H.2, where $k_R^{TR} = 3$. Since the MS moves toward the majority of received signals, the maximum Doppler PSD should appear at $f_D{=}f_{R_{max}}{=}570$ Hz. From FIGURE H.2, it is clear that the $S_{h_{oq}h_{oq}}(f_D)$ presents the underlying physical phenomena for *Scenario1*. For *Scenario2*, as expected from (H.1), the opposite results of the Doppler PSD with respect to the range of Doppler frequencies are illustrated in FIGURE H.2, where $f_{T_{max}}{=}f_{R_{max}}{=}570$ Hz were used. Since the Tx and Rx are moving in opposite directions, the Doppler PSD should be limited to the range of Doppler frequencies $0 \leq f_D \leq 1140$ Hz, whereas the maximum Doppler PSD exists at $f_D{=}0$ and $f_D{=}f_{T_{max}}{+}f_{R_{max}}{=}1140$ Hz. Again, from FIGURE H.2, it is obvious that $S_{h_{oq}h_{oq}}(f_D)$ reflects the underlying physical phenomenon for *Scenario2*.

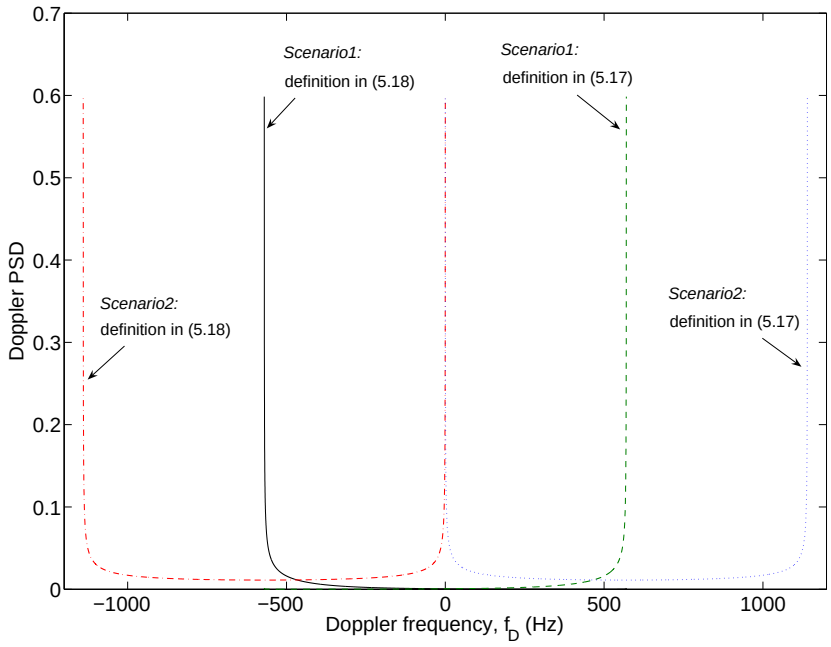

FIGURE H.2: Comparison of the Doppler PSDs of *Scenario1* and *Scenario2* based on the CF definitions in (5.17) and (5.18).

Therefore, we can conclude that $S_{h_{oq}h_{oq}}(f_D)$ is able to accurately capture the underlying physical phenomena of real channels for any scenario, while $\tilde{S}_{h_{oq}h_{oq}}(f_D)$ cannot. It is worth stressing that for an isotropic F2M macro-cell scenario (Clarke's scenario), where no scatterers are around the Tx, we find that the difference of the Doppler PSD caused by two CF definitions vanishes, i.e., $\tilde{S}_{h_{oq}h_{oq}}(f_D) = S_{h_{oq}h_{oq}}(f_D)$. This is because Clarke's scenario has the U-shape Doppler PSD, which is a real function and symmetrical to the origin. This seems to be the reason why the CF (5.18) was widely misapplied.

Appendix I

Derivation of (5.43b)

Note that (5.43b) includes two formulas regarding parameters $b_2^{SB_1}$ and $b_2^{SB_2}$. In this appendix, we only derive the parameter $b_2^{SB_1}$ since the derivation of the parameter $b_2^{SB_2}$ is exactly the same. From the general expression of $b_2^{SB_1}$ in (5.42a) with $m = 2$, we have

$$
\begin{aligned}
b_2^{SB_1} &= \frac{b_0^{SB_1} 2\pi}{I_0(k_T^{TR})} \int_{-\pi}^{\pi} e^{k_T^{TR}\cos(\phi_T^{SB_1}-\mu_T^{TR})} \Bigg(\frac{f_{T_{max}}^2}{2} + \frac{f_{R_{max}}^2 \Delta_T^2 \sin^2\gamma_R}{2} + f_{R_{max}}^2 \cos^2\gamma_R + f_{T_{max}} f_{R_{max}} \\
&\quad \times \Delta_T \sin\gamma_T \sin\gamma_R \Bigg) d\phi_T^{SB_1} - \Bigg[\frac{b_0^{SB_1} 2\pi}{I_0(k_T^{TR})} \int_{-\pi}^{\pi} e^{k_T^{TR}\cos(\phi_T^{SB_1}-\mu_T^{TR})} 2 f_{T_{max}} f_{R_{max}} \cos\gamma_R \cos(\phi_T^{SB_1} \\
&\quad - \gamma_T) d\phi_T^{SB_1} + \frac{b_0^{SB_1} 2\pi}{I_0(k_T^{TR})} \int_{-\pi}^{\pi} e^{k_T^{TR}\cos(\phi_T^{SB_1}-\mu_T^{TR})} f_{R_{max}}^2 \Delta_T \sin(2\gamma_R) \sin\phi_T^{SB_1} d\phi_T^{SB_1} \Bigg] \\
&\quad + \Bigg[\frac{b_0^{SB_1} 2\pi}{I_0(k_T^{TR})} \int_{-\pi}^{\pi} e^{k_T^{TR}\cos(\phi_T^{SB_1}-\mu_T^{TR})} f_{T_{max}}^2 \frac{\cos\left(2\left(\phi_T^{SB_1}-\gamma_T\right)\right)}{2} d\phi_T^{SB_1} - \frac{b_0^{SB_1} 2\pi}{I_0(k_T^{TR})} \int_{-\pi}^{\pi} e^{k_T^{TR}} \\
&\quad \times e^{\cos(\phi_T^{SB_1}-\mu_T^{TR})} \frac{f_{R_{max}}^2 \Delta_T^2 \sin^2\gamma_R \cos(2\phi_T^{SB_1})}{2} d\phi_T^{SB_1} + \frac{b_0^{SB_1} 2\pi}{I_0(k_T^{TR})} \int_{-\pi}^{\pi} e^{k_T^{TR}\cos(\phi_T^{SB_1}-\mu_T^{TR})} \\
&\quad \times f_{T_{max}} f_{R_{max}} \Delta_T \sin\gamma_R \sin\left(\gamma_T - 2\phi_T^{SB_1}\right) d\phi_T^{SB_1} \Bigg] \\
&= X_1 - [X_2 + X_3] + [X_4 - X_5 + X_6] \,. \qquad \text{(I.1)}
\end{aligned}
$$

For the above equation, the first term X_1 can be readily obtained as the following closed-form expression based on the equality $\int_{-\pi}^{\pi} e^{a\sin c+b\cos c}dc = 2\pi I_0\left(\sqrt{a^2+b^2}\right)$ [101]

$$X_1 = b_0^{SB_1} 4\pi^2 \left(\frac{f_{T_{max}}^2}{2} + \frac{f_{R_{max}}^2 \Delta_T^2 \sin^2\gamma_R}{2} + f_{R_{max}}^2 \cos^2\gamma_R + f_{T_{max}} f_{R_{max}} \Delta_T \sin\gamma_T \sin\gamma_R \right). \tag{I.2}$$

The second term X_2 is given as follows

$$\begin{aligned} X_2 &= \frac{b_0^{SB_1} 4\pi f_{T_{max}} f_{R_{max}} \cos\gamma_R}{I_0(k_T^{TR})} \int_{-\pi}^{\pi} e^{k_T^{TR}\cos(\phi_T^{SB_1}-\mu_T^{TR})} \frac{e^{j\left(\phi_T^{SB_1}-\gamma_T\right)} + e^{-j\left(\phi_T^{SB_1}-\gamma_T\right)}}{2} d\phi_T^{SB_1} \\ &= \frac{b_0^{SB_1} 2\pi f_{T_{max}} f_{R_{max}} \cos\gamma_R}{I_0(k_T^{TR})} \Bigg[e^{j(\pi/2+\mu_T^{TR}-\gamma_T)} \int_{-\pi/2+\mu_T^{TR}}^{3\pi/2+\mu_T^{TR}} e^{-j\beta_T + k_T^{TR}\sin\beta_T} d\beta_T \\ &\quad + e^{j(\pi/2-\mu_T^{TR}+\gamma_T)} \int_{-\pi/2-\mu_T^{TR}}^{3\pi/2-\mu_T^{TR}} e^{-j\theta_T + k_T^{TR}\sin\theta_T} d\theta_T \Bigg] \end{aligned} \tag{I.3}$$

where in the second equality we have used the following equalities $\phi_T^{SB_1} = \pi/2 - \beta_T + \mu_T^{TR}$ and $\phi_T^{SB_1} = -\pi/2 + \theta_T + \mu_T^{TR}$, so that $d\phi_T^{SB_1} = -d\beta_T$ and $d\phi_T^{SB_1} = d\theta_T$, respectively. Based on the modified equality $\int_{\alpha_l}^{\alpha_u} e^{-jV\theta + z\sin\theta} d\theta = 2\pi(-j)^V I_V(z)$ with $\alpha_u - \alpha_l = 2\pi$ obtained from [101], (I.3) becomes

$$X_2 = b_0^{SB_1} 8\pi^2 f_{T_{max}} f_{R_{max}} \cos\gamma_R \cos\left(\gamma_T - \mu_T^{TR}\right) \frac{I_1\left(k_T^{TR}\right)}{I_0\left(k_T^{TR}\right)}. \tag{I.4}$$

Using the same procedure shown above, the closed-form expressions of other terms X_3, X_4, X_5, and X_6 can be obtained similarly. The substitution of $X_1, X_2, ..., X_6$ into (I.1) gives the final result of $b_2^{SB_1}$, as shown in (5.43b).

Appendix J

Derivation of the condition $\max\{R_T, R_R\} < \min\{a_{l+1} - a_l\}$ that guarantees the TDL structure of our model

For the first tap, FIGURE 6.2 clearly shows that the longest distance caused by the double-bounced rays is the link $O_T{-}A{-}B{-}O_R$, which is equal to $2R_T{+}2R_R{+}2f$. According to the TDL structure, the inequality $2R_T{+}2R_R{+}2f{<}2a_2$ should be fulfilled. Considering $R_T{+}R_R{+}2f{<}2a_1$ (as shown in FIGURE 2) and based on the transitivity of inequalities, we know that if $R_T{+}R_R{+}2a_1{<}2a_2$ then $2R_T{+}2R_R{+}2f{<}2a_2$. Therefore, we can conclude that the condition $R_T{+}R_R{<}2a_2{-}2a_1$ guarantees the fulfillment of the TDL structure for the first tap.

For other taps ($l' > 1$), since the derivations of the condition that guarantees the fulfillment of the TDL structure are the same, here we only detail the derivation of the condition for the second tap. From FIGURE 6.2, it is clear that the longest distance in the second tap caused by the double-bounced rays is either the link $O_T{-}C{-}S{-}O_R$, which is equal to $2R_T{+}2a_2$, or the link $O_T{-}S{-}D{-}O_R$, which is equal to $2R_R{+}2a_2$. In terms of the TDL structure, the inequality $\max\{R_T, R_R\} < \{a_3{-}a_2\}$ should be

fulfilled. Therefore, we can conclude that the condition $\max\{R_T, R_R\} < \min\{a_{l'+1} - a_{l'}\}$ guarantees the fulfillment of the TDL structure for other taps.

Since the condition $R_T + R_R < 2a_2 - 2a_1$ for the first tap can be rewritten as $R_T < a_2 - a_1$ (if $R_T \geq R_R$) and $R_R < a_2 - a_1$ (if $R_R \geq R_T$), we can obtain the general condition $\max\{R_T, R_R\} < \min\{a_{l+1} - a_l\}$ that guarantees the fulfillment of the TDL structure of our model.

Bibliography

[1] W. C. Y. Lee, *Mobile Communications Engineering*, New York: McGraw Hill, 1982.

[2] R. Steele, *Mobile Radio Communications*, London, UK: Pentech Press, 1992.

[3] R. Wang and D. Cox, "Channel modeling for ad hoc mobile wireless networks," *Proc. IEEE VTC'02-Spring*, , Birmingham, USA, May 2002, pp. 21–25.

[4] F. Kojima, H. Harada, and M. Fujise, "Inter-vehicle communication network with an autonomous relay access scheme," *IEICE Trans. Commun.* vol. E83-B, no. 3, pp. 566–575, Mar. 2001.

[5] IEEE P802.11p/D2.01, "Standard for wireless local area networks providing wireless communications while in vehicular environment,"Tech. Rep., Mar. 2007.

[6] G. J. Foschini, "Layered space-time architecture for wireless communication in a fading environment when using multiple antennas," *Bell Laboratories Technical Journal*, vol. 1, no. 2, pp. 41-59, 1996.

[7] G. J. Foschini, and M. J. Gans, "On limits of wireless communications in a fading environment," *Wireless Personal Communications*, vol. 6, pp. 311-335, 1998.

[8] I. E. Telatar, "Capacity of multi-antenna Gaussian channels," *European Trans. Telecommunications*, vol. 6, pp. 585-595, Dec. 1999.

[9] A. F. Molisch, M. Steinbauer, M. Toeltsch, E. Bonek, and R. S. Thomä, "Capacity of MIMO systems based on measured wireless channels," *IEEE J. Selected Areas Commun.*, vol. 20, no. 3, pp. 539–549, Apr. 2002.

[10] J. B. Anderson, T. S. Rappaport, and S. Yoshida, "Propagation measurements and modeling for wireless communication channels," *IEEE Commun. Mag.*, vol. 33, pp. 42–49, Jan. 1995.

[11] P. Almers, E. Bonek, A. Burr, N. Czink, M. Debbah, V. Degli-Esposti, H. Hofstetter, P. Kyösti, D. Laurenson, G. Matz, A. F. Molisch, C. Oestges, and H. Özcelik, "Survey of channel and radio propagtion models for wireless MIMO systems", *EURASIP Journal on Wireless Communications and Networking* , vol. 2007, no. 1, pp. 1–19, 2007.

[12] P. Hoeher, "A statistical discrete-time model for the WSSUS multipath channel," *IEEE Trans. Veh. Technol.*, vol. 41, pp. 461–468, Nov. 1992.

[13] M. Pätzold, *Mobile Fading Channels*. Chichester: John Wiley & Sons, 2002.

[14] L. M. Correia, Ed., *Wireless Flexible Personalised Communications (COST 259 Final Report)*, Chichester (UK): Wiley, 2001.

[15] A. F. Molisch, H. Asplund, R. Heddergott, M. Steinbauer, and T. Zwickg, "The COST 259 directional channel model– Part I overview and methodology," *IEEE Trans. Wireless Comm.*, vol. 5, no. 12, pp. 3421–3433, Dec. 2006.

[16] H. Asplund, A. A. Glazunov, A. F. Molisch, K. I. Pedersen, and M. Steinbauer, "The COST 259 directional channel model– Part II macrocells," *IEEE Trans. Wireless Comm.*, vol. 5, no. 12, pp. 3434–3450, Dec. 2006.

[17] A. F. Molisch, H. Hofstetter, et al., "The COST273 channel model," *COST 273 Final Report*, L. Correia, Ed., Springer, New York, NY, USA, 2006.

[18] 3GPP, R1-02-0181, "MIMO discussion summary," *Tech. Rep.*, Jan. 2002.

[19] 3GPP, TR 25.996, "Spatial channel model for multiple input multiple output (MIMO) simulations (Rel. 6)," *Tech. Rep.*, Sept. 2003.

[20] 3GPP, R1-050586, "Wideband SCM," *Tech. Rep.*, 2005.

[21] http://www.ist-winner.org/.

[22] A. Abdi, and M. Kaveh, "A space-time correlation model for multielement antenna systems in mobile fading channels", *IEEE J. Select. Areas Commun.*, vol. 20, no. 3, pp. 550–560, Apr. 2002.

[23] T. A. Chen, M. P. Fitz, W. Y. Kuo, M. D. Zoltowski, and J. H. Grimm, "A space-time model for frequency nonselective Rayleigh fading channels with applications to space-time modems", *IEEE J. Sel. Areas Commun.*, vol. 18, no. 7, pp. 1175–1190, Jul. 2000.

[24] A. Abdi, J. A. Barger, and M. Kaveh, "A parametric model for the distribution of the angle of arrival and the associated correlation function and power spectrum at the mobile station," *IEEE Trans. Veh. Technol.*,vol. 51, no. 3, pp. 425–434, 2002.

[25] A. S. Akki and F. Haber, "A statistical model for mobile-to-mobile land communication channel," *IEEE Trans. Veh. Technol.*, vol. 35, no. 1, pp. 2–10, Feb. 1986.

[26] A. S. Akki, "Statistical properties of mobile-to-mobile land communication channels," *IEEE Trans. Veh. Technol.*, vol. 43, no. 4, pp. 826–831, Nov. 1994.

[27] M. Pätzold, B. O. Hogstad, and N. Youssef, "Modeling, analysis, and simulation of MIMO mobile-to-mobile fading channels," *IEEE Trans. Wireless Commun.*, vol. 7, no. 2, pp. 510–520, Feb. 2008.

[28] A. G. Zajić and G. L. Stüber, "Space-time correlated mobile-to-mobile channels: modeling and simulation," *IEEE Trans. Veh. Technol.*, vol. 57, no. 2, pp. 715–726, Mar. 2008.

[29] A. G. Zajić and G. L. Stüber, "Three-dimensional modeling, simulation, and capacity analysis of space-time correlated mobile-to-mobile channels," *IEEE Trans. Veh. Technol.*, vol. 57, no. 4, pp. 2042-2054, Jul. 2008.

[30] A. G. Zajić and G. L. Stüber, "Three-dimensional modeling and simulation of wideband MIMO mobile-to-mobile channels," *IEEE Trans. Wireless Commun.*, vol. 8, no. 3, pp. 1260–1275, Mar. 2009.

[31] G. Acosta and M. A. Ingram, "Six time- and frequency-selective empirical channel models for vehicular wireless LANs," *IEEE Veh. Technol. Mag.*, vol. 2, no. 4, pp. 4–11, Dec. 2007.

[32] I. Sen and D. W. Matolak, "Vehicle-vehicle channel models for the 5-GHz band," *IEEE Trans. Intell. Transp. Syst.*, vol. 9, no. 2, pp. 235–245, Jun. 2008.

[33] G. Acosta, K. Tokuda, and M. A. Ingram, "Measured joint Doppler-delay power profiles for vehicle-to-vehicle communications at 2.4 GHz," *Proc. IEEE GLOBECOM'04*, Dallas, USA, Nov. 2004, pp. 3813–3817.

[34] A. Paier, J. Karedal, N. Czink, C. Dumard, T. Zemen, F. Tufvesson, A. F. Molisch, and C. F. Mecklenbräuker, "Characterization of vehicle-to-vehicle radio channels from measurements at 5.2 GHz," *Wireless Pers. Commun.*, Jun. 2008, [Online] http://dx.doi.org/10.1007/s11277-008-9546-6.

[35] L. Cheng, B. E. Henty, D. D. Stancil, F. Bai, and P. Mudalige, "Mobile vehicle-to-vehicle narrowband channel measurement and characterization of the 5.9 GHz dedicated short range communication (DSRC) frequency band," *IEEE J. Sel. Areas Commun.*, vol. 25, no. 8, pp. 1501–1516, Oct. 2007.

[36] C. S. Patel, G. L. Stüber, and T. G. Pratt, "Simulation of Rayleigh-faded mobile-to-mobile communication channels," *IEEE Trans. Commun.*, 53(11):1876–1884, Nov. 2005.

[37] M. Pätzold, B. O. Hogstad, N. Youssef, and D. Kim, "A MIMO mobile-to-mobile channel model: Part I–the reference model," *Proc. IEEE PIMRC'05*, Berlin, Germany, Sept. 2005, pp. 573–578.

[38] M. Pätzold, B. O. Hogstad, N. Youssef, and D. Kim, "A MIMO mobile-to-mobile channel model: Part I–the simulation model," *Proc. IEEE PIMRC'05*, Berlin, Germany, Sept. 2005, pp. 562–567.

[39] A. G. Zajić and G. L. Stüber, "A new simulation model for mobile-to-mobile Rayleigh fading channels," *IEEE WCNC'06*, Las Vegas, USA, Apr. 2006, pp. 1266–1270.

[40] L. C. Wang, W. C. Liu, and Y. H. Cheng, "Statistical analysis of a mobile-to-mobile Rician fading channel model," *IEEE Trans. Veh. Technol.*, vol. 58, no. 1, pp. 32–38, Jan. 2009.

[41] G. L. Stüber, *Principles of Mobile Communication*. 2nd ed. Boston: Kluwer Academic Publishers, 2001.

[42] M. Hata and T. Nagatsu, "Mobile location using signal strength measurements in a cellular system," *IEEE Trans. Veh. Technol.*, vol. 29, no. 2, pp. 245-251, May 1980.

[43] Y. Okumura, E. Ohmuri, T. Kawano, and K. Fukuda, "Field strength and its variability in VHP and UHF land mobile radio service," *Rev. of the ECL*, vol. 16, pp. 825-873, 1968.

[44] W. C. Y. Lee, *Mobile Communications Design Fundamentals*, Indianapolis, IN: Sams, 1986.

[45] COST 231 TD(973)119-REV 2 (WG2):, "Urban transmission loss models for mobile radio in the 900- and 1,800-MHz bands," *Tech. Rep.*, Sept. 1991.

[46] P. A. Bello, "Characterization of randomly time-variant linear channels", *IEEE Trans. Commun. Systems*, vol. 11, no. 4, pp. 360–393, Dec. 1963.

[47] R. Kattenbach, "Statistical Modeling of Small-Scale Fading in Directional Radio Channels", *IEEE J. Selected Areas Commun.*, vol. 20, no. 3, pp. 584–592, Apr. 2002.

[48] B. H. Fleury, "First and second order characterization of direction dispersion and space selectivity in the radio channel", *IEEE Trans. Inform. Theory*, vol. 46, no. 6, pp. 2027–2044, Sept. 2000.

[49] P. A. Bello, "Time-frequency duality", *IEEE Trans. Inform. Theory*, vol. 10, no. 1, pp. 18–33, Jan. 1964.

[50] R. B. Ertel, P. Cardieri, K. W. Sowerby, T. S. Rappaport, and J. H. Reed, "Overview of spatial channel models for antenna array communication systems", *IEEE Pers. Commun.*, vol. 5, no. 2, pp. 10–22, 1998.

[51] K. Yu and B. Ottersten, "Modeling of MIMO propagation channels, a review", *Wiley Journal on Wireless Commun. and Mobile Computing*, vol. 2, no. 7, pp. 653–666, Nov. 2002.

[52] C.-X. Wang, X. Hong, H. Wu, and W. Xu, "Spatial temporal correlation properties of the 3GPP spatial channel model and the Kronecker MIMO channel model", *EURASIP Journal on Wireless Communications and Networking, Special Issue on Space-Time Channel Modeling for Wireless Communications*, vol. 2007, no. 39871, pp. 1–9, 2007.

[53] J. C. Liberti and T. S. Rappaport, *Smart Antennas for Wireless Communication: IS-95 and Third Generation CDMA Applications*. Englewood Cliffs, NJ: Prentice-Hall, 1999.

[54] Z. Latinovic, A. Abdi, and Y. Bar-Ness, "A wideband space-time model for MIMO mobile fading channels," *IEEE WCNC 2003*,New Orleans, LA, USA, Mar. 2003, pp. 338–342.

[55] A. G. Zajić, G. L. Stüber, T. G. Pratt, and S. Nguyen, "Wideband MIMO mobile-to-mobile channels: geometry-based statistical modeling with experimental verification," *IEEE Trans. Veh. Technol.*, vol. 58, no. 2, pp. 517–634, Feb. 2009.

[56] T. Kosch and W. Franz "Technical concept and prerequisites of car-to-car communication," *Proc. 5th Eur. Congr. Exhib. Intell. Transp. Syst. Serv.*, Hannover, Germany, Jun. 2005. pp. 1–12.

[57] D. W. Matolak, "Channel modeling for vehicle-to-vehicle communications," *IEEE Commun. Mag.*, vol. 46, no. 5, pp. 76–83, May 2008.

[58] J. Maurer, T. Fügen, M. Porebska, T. Zwick, and W. Wisebeck, "A ray-optical channel model for mobile to mobile communications," *COST 2100 4th MCM*, COST 2100 TD(08) 430, Wroclaw, Poland, 6-8 Feb. 2008.

[59] J. Karedal, F. Tufvesson, N. Czink, A. Paier, C. Dumard, T. Zemen, C. F. Mecklenbräuker, and A. F. Molisch, "A geometry-based stochastic MIMO model

for vehicle-to-vehicle communications,“ *IEEE Trans. Wireless Commun.*, vol. 8, no. 7, Jul. 2009, pp. 3646–3657.

[60] D. J. Young and N. C. Beaulieu, “A quantitative evaluation of generation methods for correlated Rayleigh random variates”, *Proc. IEEE GLOBECOM'98*, Sydney, Australia, November, 1998, pp. 3332–3337.

[61] D. J. Young and N. C. Beaulieu, “The generation of correlated Rayleigh random variates by inverse discrete Fourier transform,” *IEEE Trans. Commun.*,vol. 48, pp. 1114–1127, Jul. 2000.

[62] D. Verdin and T. C. Tozer, “Generating a fading process for the simulation of land-mobile radio communications,” *Electronics Lett.*, vol. 29, no. 23, pp. 2011–2012, Nov. 1993.

[63] S. A. Fechtel, “A novel approach to modeling and efficient simulation of frequency-selective fading radio channels,” *IEEE J. Sel. Area Commun.*, vol. 11, no. 3, pp 422–431, Apr. 1993.

[64] R. H. Clarke, “A statistical theory of mobile-radio reception,” Proc. Bell Syst. Tech. J., pp 957–1000, Jul. 1968.

[65] W. C. Jakes, *Microwave Mobile Communications*, 2nd ed. Piscataway, NJ: Wiley-IEEE Press, 1994.

[66] M. F. Pop and N. C. Beaulieu, “Limitations of sum-of-sinusoids fading channel simulators“, *IEEE Trans. Commun.*, vol. 49, pp. 699–708, Apr. 2001.

[67] Y. R. Zheng and C. S. Xiao, “Improved models for the generation of multiple uncorrelated Rayleigh fading waveforms“, *IEEE Commun. Lett.*, vol. 6, no. 6, pp. 256–258, Jun. 2002.

[68] Y. R. Zheng and C. S. Xiao, “Simulation models with correct statistical properties for Rayleigh fading channels“, *IEEE Trans. Commun.*, vol. 51, pp. 920–928, Jun. 2003.

[69] C.-X. Wang, M. Pätzold, and D. Yuan, "Accurate and efficient simulation of multiple uncorrelated Rayleigh fading waveforms", *IEEE Trans. Wireless Commun.*, vol. 6, no. 3, pp. 833–839, Mar. 2007.

[70] C.-X. Wang, D. Yuan, H. H. Chen, and W. Xu, "An improved deterministic SoS channel simulator for efficient simulation of multiple uncorrelated Rayleigh fading channels", *IEEE Trans. Wireless Commun.*, vol. 7, no. 9, pp. 3307–3311, Sept. 2008.

[71] M. Pätzold and F. Laue, "Statistical properties of Jakes' fading channel simulator," *Proc. IEEE VTC'98-Spring*, Ottawa, Canada, May 1998, pp. 712–718.

[72] M. Pätzold U. Killat, and F. Laue, "A deterministic model for a shadowed Rayleigh land mobile radio channel," *Proc. IEEE PIMRC'94*, Hague, Netherlands, Sept. 1994, pp. 1202–1210.

[73] M. Pätzold U. Killat, and F. Laue, "A deterministic digital simulation model for Suzuki processes with application to a shadowed Rayleigh land mobile radio channel," *IEEE Trans. Veh. Technol.*, vol. 45, no. 2, pp. 318–331, May 1996.

[74] M. Pätzold U. Killat, F. Laue, and Y. Li, "A new and optimal method for the derivation of deterministic simulation models for mobile radio channels," *Proc. IEEE VTC'96-Spring*, Atlanta, Georgia, USA, Apr. 1996, pp. 1423–1427.

[75] M. Pätzold U. Killat, F. Laue, and Y. Li, "On the statistical properties of deterministic simulation models for mobile fading channels," *IEEE Trans. Veh. Technol.*, vol. 47, no. 1, pp. 254–269, Feb. 1998.

[76] M. Pätzold, C.-X. Wang, and B. O. Hogstad, "Two new sum-of-sinusoids-based methods for the efficient generation of multiple uncorrelated Rayleigh fading waveforms", *IEEE Trans. Wireless Commun.*, accepted for publication.

[77] C. S. Xiao, Y. R. Zheng, and N. Beaulieu, "Novel Sum-of-Sinusoids Simulators for Ricean Fading Channels," *IEEE Trans. Wireless Commun.*, vol. 5, no. 12, pp. 3667–3679, Dec. 2006.

[78] C. S. Patel, G. L. Stüber, and T. G. Pratt, "Comparative analysis of statistical models for the simulation of Rayleigh faded cellular channels," *IEEE Trans. Commun.*, vol. 53, no. 6, pp. 1017–1026, Jun. 2005.

[79] M. Pätzold and B. O. Hogstad, "A space-time channel simulator for MIMO channels based on the geometrical one-ring scattering model," *Proc. IEEE VTC'04-Fall*, Los Angeles, CA, USA, Sept. 2004, pp. 144–149.

[80] B. O. Hogstad, M. Pätzold, A. Chopra, D. Kim, and K. B. Yeom, "A wideband MIMO channel simulation model based on the geometrical elliptical scattering model," *Proc. IEEE WWRF'05*, Paris, France, Dec. 2005, pp. 1–6.

[81] M. Pätzold and B. O. Hogstad, "A Wideband Space-Time MIMO Channel Simulator Based on the Geometrical One-Ring Model," *IEEE VTC'06-Fall*, Montreal, Canada, Sept. 2006, pp. 1–6.

[82] Y. R. Zheng, "A non-isotropic model for mobile-to-mobile fading channel simulations," *IEEE MCC'06*, Washington, USA, Oct. 2006, pp. 1–6.

[83] C. C. Chong, C. M. Tan, D. I. Laurenson, S. McLaughlin, M. A. Beach, and A. R. Nix, "A new statistical wideband spatio-temporal channel model for 5-GHz band WLAN systems," *IEEE J. Select. Areas Commun.*, vol. 21, no. 2, pp. 139–150, Feb. 2003.

[84] J. Foersler, "Channel modeling sub-committee reprot (final)," *IEEE P802.15-02/490r1-SG3a*, Feb. 2003.

[85] H. Bölcskei, M. Borgmann, and A. Paulraj, "Impact of the propagation environment on the performance of space-frequency code MIMO-OFDM," *IEEE Journal on Selected Areas in Commun.*, vol. 21, no. 3, pp. 427–439, 2003.

[86] M. Kalkan and R. H. Clarke, "Prediction of the space-frequency correlation function for base station diversity reception," *IEEE Trans. Veh. Technol.*, vol. 46, no. 1, pp. 176–184, Feb. 1997.

[87] T. Fulghum and K. Molnar, "The Jakes fading model incorporating angular spread for a disk of scatterers," *IEEE VTC'98-Spring*, Ottawa, ON, Canada, May 1998, pp. 489–493.

[88] W. C. L. Lee, "Level crossing rates of an equal-gain predetection diversity combiner," *IEEE Trans. Commun. Technol.*, vol. 18, no. 4, pp. 417–426, Aug. 1970.

[89] J. Salz, and J. H. Winters, "Effect of fading correlation on adaptive arrays in digital mobile radio," *IEEE Trans. Veh. Technol.*, vol. 43, no. 4, pp. 1049–1057, Nov. 1994.

[90] F. Adachi, M. T. Feeney, A. G. Williamson, and J. D. Parsons, "Cross-correlation between the envelopes of 900 MHz signals received at a mobile radio base station site," *IEE Proc. F, Commun., Radar, Signal Processing*, vol. 133, pp. 506–512, 1986.

[91] L. Schumacher, K. I. Pedersen, and P. E. Mogensen, "From antenna spacings to theoretical capacities – guidelines for simulating MIMO systems," *IEEE PIMRC'02*, Lisbon, Portugal, Sept 2002, pp. 587–592.

[92] G. J. Byers, and F. Takawira, "Spatially and temporally correlated MIMO channels: modeling and capacity analysis," *IEEE Trans. Veh. Technol.*, vol. 53, no. 3, pp. 634–643, May 2004.

[93] C. A. Gutiérrez and M. Pätzold, "Sum-of-sinusoid-based simulation of flat fading wireless propagation channels under non-isotropic scattering conditions," *IEEE GLOBECOM'07*, Washington, D.C., USA, Nov. 2007, pp. 3842–3846.

[94] A. Papoulis and S. U. Pillai, *Probability, Random Variables and Stochastic Processes*. 4th ed. New York: McGraw Hill, 2002.

[95] S. Wang, A. Abdi, J. Salo, H. M. EL-Sallabi, J. W. Wallace, P. Vainikainen, and M. A. Jensen, "Time-varying MIMO channels: parametric statistical modeling and experimental results," *IEEE Trans. Veh. Technol.*, vol. 56, no. 4, pp. 1949–1963, July 2007.

[96] A. G. Zajić, G. L. Stüber, T. G. Pratt, and S. Nguyen, "Envelope level crossing rate and average fade duration in mobile-to-mobile fading channels," *Proc. IEEE ICC'08*, Beijing, China, May 2008, pp. 4446–4450.

[97] M. Pätzold and N. Youssef, "Modeling and simulation of direction-selective and frequency-selective mobile radio channels," *International Journal of Electronics and Communications, AEUE*, vol. 55, no. 6, pp. 433–442, Nov. 2001.

[98] P. Y. Chen and H. J. Li, "Modeling and applications of space-time correlation for MIMO fading signals," *IEEE Trans. Veh. Technol.*, vol. 56, no. 4, pp. 1580–1590, Jul. 2007.

[99] N. Youssef, C.-X. Wang, and M. Pätzold, "A study on the second order statistics of Nakagami-Hoyt mobile fading channels," *IEEE Trans. Veh. Technol.*, vol. 54, no. 4, pp. 1259–1265, Jul. 2005.

[100] M. Pätzold, U. Killat, and F. Laue, "An extended Suzuki model for land mobile satellite channels and its statistical properties," *IEEE Trans. Veh. Technol.*, vol. 47, no. 2, pp. 617–630, May 1998.

[101] I. S. Gradshteyn, and I. M. Ryzhik, *Table of Integrals, Series, and Products*. 6th ed, Boston: Academic, 2000.

[102] S. O. Rice, "Distribution of the duration of fades in radio transmission: Gaussian noise model," *Bell Syst. Tech. J.*, vol. 37, pp. 581–635, 1958.

[103] J. Maurer, T. Fügen, and W. Wisebeck, "Narrow-band measurement and analysis of the inter-vehicle transmission channel at 5.2 GHz," *Proc. IEEE VTC'02-Spring*, Birmingham, USA, May 2002, pp. 1274–1278.

[104] M. Abramowitz and I. A. Stegun, *Handbook of Mathematical Functions with Formulas, Graphs and Mathematical Tables*. New York: Dover, 1965.

[105] G. N. Watson, *A Treatise of the Theory of Bessel Functions*. 2nd ed. Cambridge, 1952.